Les kites comme propulsion axillaire pour les navires : système expérimental, campagnes de mesures, analyse des données et identification des performances des kites

Morgan Behrel

To cite this version:

Morgan Behrel. Les kites comme propulsion axillaire pour les navires : système expérimental, campagnes de mesures, analyse des données et identification des performances des kites. Fluid mechanics [physics.class-ph]. Université de Bretagne occidentale - Brest, 2017. English. NNT : 2017BRES0132 . tel-03081135

HAL Id: tel-03081135
https://theses.hal.science/tel-03081135v1

Submitted on 18 Dec 2020

UBO
université de bretagne
occidentale

UNIVERSITE
BRETAGNE
LOIRE

Ph.D. Thesis / UNIVERSITÉ DE BRETAGNE OCCIDENTALE
part of Université européenne de Bretagne
for the degree of
DOCTOR AT UNIVERSITÉ DE BRETAGNE OCCIDENTALE
Specialized in mechanics
École Doctorale Sciences Pour l'Ingénieur

Submitted by

Morgan BEHREL

Completed at ENSTA Bretagne, in the Dupuy de Lôme Research Institute (IRDL - CNRS FRE 3744)

Investigation of kites for auxiliary ship propulsion: experimental set-up, trials, data analysis and kite specs novel identification approach

Les kites comme propulsion axillaire pour les navires : système expérimental, campagnes de mesures, analyse des données et identification des performances des kites

Invited

Dr. Sime Malenica
Deputy Director of the Research Department of Bureau Veritas, France

Dr. Serge Sutulo
Associate Professor at University of Lisbon

Dr. Frédéric Hauville
Associate Professor, IRENAV, French Naval Academy

Co-supervisors

Dr. Jean-Baptiste Leroux
Associate Professor, IRDL, ENSTA Bretagne

Dr. Alain Nême
Associate Professor, IRDL, ENSTA Bretagne

Dr. Kostia Roncin
Associate Professor, IRDL, ENSTA Bretagne

Ph. D. thesis examined
on 15th December 2017

Committee members

Prof. Sandrine Aubrun
Professor at Centrales Nantes, LHEEA / *Reviewer*

Dr. Lorenzo Fagiano
Associate professor at Politecnico Di Milano / *Reviewer*

Prof. Xavier Carton
Professor at University of Western Brittany / *Examiner*

Prof. Dominic A. Hudson
Shell Professor of Ship Safety and Efficiency at the University of Southampton / *Examiner*

Dr.-Ing. Richard Leloup
Research and Development Director at beyond the sea / *Examiner*

Dr. -Ing. Gian Mauro Maneia
Senior Researcher at Centro Studi Industriali Srl / *Examiner*

Prof. Carlos Guedes Soares
Distinguished professor at University of Lisbon / *Examiner*

Dr.-Ing. habil. Christian Jochum
Associate Professor, ENSTA Bretagne / *Primary Supervisor*

INVESTISSEMENTS D'AVENIR

ADEME

beyond the sea®
by Yves Parlier

ENSTA
Bretagne

Remerciement

Ce manuscrit de thèse est le fruit d'un travail personnel mené sur trois ans, mais qui ne peut aboutir que grâce au soutient de nombreuses personnes. Mais bien avant d'attaquer la moindre tache dans une thèse, il faut déjà la commencer. Pour cela il faut un élément déclencheur présentant la chose comme une superbe expérience à vivre absolument, et permettant d'aller au fond des choses. Dans mon cas, ce fut celui qui deviendra ensuite mon directeur de thèse, Christian Jochum, qui officia en ce sens, et qui me convainquis de me lancer dans un tel projet. Pour cela je le remercie grandement une première fois, car il se trouve qu'il avait entièrement raison.

Mais que serait une thèse sans l'encadrement d'enseignant chercheurs, motivés à avancer et à transmettre leur connaissance, toujours prêts à aider pour surmonter un point difficile, et regorgeant d'idées, de suggestions et de solutions ? Je n'ai pas la réponse à cette question, et cela me convient. Je remercie donc chaleureusement mon directeur de thèse Christian Jochum pour une seconde fois, ainsi que les trois co-encadrants, Jean-Baptiste Leroux, Alain Nême et Kostia Roncin. C'est grâce à eux quatre que le travail a abouti.

Une étude expérimentale demande bien sur un système d'essais et de mesures complexe, et la mise au point de celui-ci ne peut pas aboutir sans les conseils précieux de personnes expérimentées dans le domaine. Un grand merci donc à Frédéric Montel qui a suivi de bout en bout l'évolution du systeme, et merci aussi à Didier Penchenat, Sebastien Bourc'his, Yvon Gallou, Bruno Mecucci-Minucci et Pierre Simon.

Un système expérimental, c'est aussi beaucoup d'achats de matériel, qu'il faut faire rentrer dans des lignes de dépenses pas toujours prévues. Pour cela je souhaite remercier les services administratifs de l'ENSTA Bretagne qui ont toujours réussi à trouver des solutions pour que le matériel soit disponible à temps. Merci en particulier au secrétaire général Jean Pierre Baudu, ainsi qu'à Michel Le Bras, Martine Inizan, Marilyne Pochard et Anne Predour. Merci aussi aux autres services comme le bureau des missions, en la personne de Genevièvre Guen et Christelle Le Duff, qui gèrent la planification des divers déplacements à merveille. Merci aussi au service communication de l'ENSTA Bretagne, à savoir Ingrid Le Toutouze, Julie Quéau et Nadège Le Clainche.

Mais en première ligne pour recevoir et traiter toutes les demandes administratives se trouve Nathalie Leal, qui gère ça à merveille. Un très grand merci à elle !

Que pourrions-nous faire de nos jours sans ordinateur ? Certainement pas cette thèse, et si mes ordinateurs ont parfaitement rempli leur rôle, c'est grâce au support sans faille du service informatique, toujours disponible pour répondre à une simple question ou pour régler un problème. Merci en particulier à Cédric Gaudron, Philipe Bruno et Tanguy Bars avec qui j'ai le plus interagi.

Cette étude a été réalisée au sein d'un projet d'envergure, et je souhaite donc aussi remercier les acteurs du projet, à commencer par Yves Parlier qui a mis sur pied ce programme, et merci aussi à Richard Leloup et Fabien Griffon, à tous les partenaires du projet, et l'ADEME pour le financement. Merci également aux deux étudiants de l'ENSTA Bretagne Victor Jubert et Yohann Leslé qui ont dessiné le kiteboat au cours de leur projet de troisième année.

Un grand merci aux deux rapporteurs, Sandrine Aubrun et Lorenzo Fagiano, qui ont lu de façon détaillée ce document en préparation de la soutenance, et merci à l'ensemble des membres du jury qui ont porté un jugement élogieux sur le travail effectué au cours de ces trois dernières années : Xavier Carton, Carlos Guedes Soares, Dominic Hudson, Richard Leloup, Gian Mauro Maneia, Serge Sutulo et Sime Malenica. Merci aussi à Frederic Hauville qui a participé au comité de suivi à mi-parcours.

Mon passé de sportif de haut niveau en planche à voile a très clairement contribué à la réussite de cette thèse et à faire ce que je suis maintenant. Pour cela je souhaite remercier les personnes qui m'ont accompagné et aidé dans ce parcours sportif, allant du lycée en sport étude jusqu'à mes années en école d'ingénieur. La liste serait trop longue, mais je souhaite citer nominativement, Christophe Boutet, Stephane Jaouen et Olivier Le Gouic qui ont été mes coachs, et aussi François Jaouen et Damien Coadour.

Je souhaite aussi remercier les différentes personnes de l'école avec qui j'ai toujours eu plaisir à discuter, dans un bureau ou autour d'un café, que cela soit sur un sujet scientifique ou simplement une conversation ouverte. Merci donc, entre autres, à Yves Marie Scolan, Jean-Yves Pradillon, Guilhem Bles, Jean-Marc Laurens, Michel Arrigoni, Steven Kerampran, Hélène Klucik, Christianne Gilet...

Comment puis-je écrire des remerciements pour Nedeleg Bigi ? Je ne pense pas que des mots puissent suffire, à la vue du parcours scolaire, du parcours sportif, et bien plus important encore, de l'amitié qui nous lie. Je vais donc faire simple, et opter pour l'unique mot entièrement en lettre capitale de cette partie : MERCI.

Une thèse serai aussi beaucoup plus compliquée sans le soutien sans faille de la famille et des amis. Il n'est évidemment pas possible de remercier nominativement tout le monde en détaillant les contributions de chacun, je finirai donc par un grand merci général pour tous les très bons moments passés ces trois dernières années. Que ce soit au bureau, sur l'eau, au bar ou ailleurs, je sais que les personnes visées par ces derniers mots sauront se reconnaître !

Abstract

This Ph. D. study is part of a global research project aiming to develop the use of kites as auxiliary propulsion devices for ships, in order to reduce polluting emissions and save fuel. This project is made of academical and private partners, and is funded by the French environment and energy management agency (ADEME). This Ph. D. study is one of the three research programs undertaken at ENSTA Bretagne to develop the scientific knowledge associated with wind-assisted ships. Precisely, this study is an experimental analysis, that aims to provide experimental measurements for the benchmark of numerical models developped by other resarch programs.

To complete this objective, an experimental set-up has been developed, allowing the steering of the kite and the acquisition of data, for the performance assessment like the towing force for instance. A kite automatic pilot has also been developed, based on previous published works. It is able to fly the kite in a dynamic mode, and in a repeatable way. This experimental set-up was deployed for three major experimental campaigns, preceeded by periods of development and adjustment.

The first campaign was achieved on a 13-meter-long fishing vessel, fitted with a 50-square-meter kite. The aim of this work was to measure the influence of the kite on the propulsive chain of the boat, thanks to an engine room already well equipped with sensors. However, the initial program of the trials could not be completed due to several issues, and only a few data dealing with kite flight were collected. These data were processed to estimate the aerodynamic specifications of the kite, leading to kite specs making sense with other published works. This campaign was however very instructive, showing the importance of wind measurements for such works. The feedback has therefore been taken into account for the next steps of this study.

The second experimental campaign was carried out onshore, and was focused on the estimation of kite aerodynamic specs along an eight-pattern trajectory. So far in the literature, these parameters were considered as being constant, but this can be problematical. Indeed, in this case, the amplitude of forces is underestimated, and a larger amplitude could affect numerous parts of the project, as the structural strength of the kite fabrics or of the tethers, or the stability of the ship. To measure the wind at the altitude of the kite, a wind profiler was used based on a sonic technology. Plenty of eight-pattern trajectories were recorded, leading to a post processing based on a conditional phase averaging method. This process shows a clear evolution of aerodynamic specs of the kite along a trajectory, however no repeatable scheme fitting the entire set of data could have been pointed out. Nevertheless

linear law for specs evolution was proposed, associating the lift to drag ratio and the lift coefficient of the kite with the rotation rate of the kite velocity vector around the axis of the tethers.

The last campaign of measurements was carried out on a 6-meter-long boat, specially designed to fit expectations for kite trials, and fully available. After a period of development and tests, measurement works were done, during a four week period in April 2017.The wind at kite altitude was this time estimated using a meteorological model provided by a specialized company, associated with numerous on site measurements. Data obtained were processed at first using simple means, and performances of the boat towed by a kite have been obtained, for various true wind angles. The conditional phase averaging method was adapted from previous works, and boat motions associated with a towing kite were highlighted. All acquired data has not been processed, and further work is possible. However the data set collected represents a good first database for numerical model validations.

Plenty of other tracks are also open regarding other possibilities for the measurements of kite specs, as for example the photogrammetry process. Such a tehnique applied to the existing set-up could lead to a useful measurement of the flying shape of kites towing a boat, and then feed fluid-structure-interaction modeling approaches.

Résumé

Cette thèse s'inscrit dans un projet de recherche global, visant à développer la traction de navire de commerce par des ailes de kites, afin de réduire les émissions de polluant, tout en réduisant la consommation de carburant. Ce projet associe des entreprises du secteur privé et des partenaires académiques, et est financé par l'agence de l'environnement et de la maitrise de l'énergie (ADEME). Cette thèse fait partie des trois actions de recherches engagées pour affiner les connaissances liées aux problématiques des navires tractées par kite. Plus précisément, l'objectif de cette thèse est de réaliser une étude expérimentale sur le sujet, permettant de confronter des modélisations numériques développées par ailleurs avec des mesures au réel.

Dans la cadre de cette étude, un banc d'essais et de mesures a donc été développé, permettant de contrôler le kite et d'en enregistrer les performances, en particulier les efforts. Un pilote automatique a aussi été implémenté, en se basant sur des travaux publiés par d'autres équipes de recherche. Ce pilote automatique permet de faire fonctionner le kite en vol dynamique, avec une bonne répétabilité. Le retour de position du kite est réalisé avec une cellule d'efforts tri dimensionnelle. Ce banc d'essais, dans ses différentes versions, a été déployé à l'occasion de trois campagnes de mesures, chaque campagne de mesures étant précédée par une phase de mise au point et d'amélioration du banc.

La première campagne de mesures réalisée dans le cadre de cette thèse s'est déroulée sur un chalutier québécois, en septembre 2015. Cette campagne était l'occasion de mesurer l'influence de la traction d'un kite sur la chaine propulsive d'un navire, car le chalutier était initialement particulièrement bien instrumenté. Cependant, plusieurs facteurs ont empêché la réalisation du programme de mesure, et seules quelques données de tractions du kite ont été obtenues. Celles-ci ont été traitées pour en extraire les performances aérodynamiques du kite, et ces performances ont pu être confrontées à d'autres données présentes dans la littérature. Cependant cette campagne a apporté un retour d'expérience important, en pointant notamment l'importance de l'estimation du vent à l'altitude du kite. Cette information a donc orienté les choix pour la campagne suivante.

La seconde campagne expérimentale a été menée à terre et visait en particulier à mesurer l'influence de la trajectoire du kite sur les paramètres aérodynamiques. En effet ceux-ci étaient jusqu'à présent considérés comme constant le long d'une trajectoire en huit par le modèle zero-mass. Cependant cela peut être problématique car, l'amplitude des efforts est alors minorée, et cela peut poser des problèmes au niveau de la résistance structurelle du kite, des lignes et des points d'attache, mais aussi avoir un impact sur la stabilité du

navire. Pour mesurer le vent à l'altitude du kite, un profileur vertical basé sur une technologie sonique a été utilisé. De très nombreuses trajectoires en huit ont été effectuées et enregistrées, avec une bonne répétabilité. Cela a donc permis de réaliser un post traitement par moyenne de phases, et ce poste traitement met clairement en évidence une évolutions des paramètres aérodynamiques le long d'une trajectoire. Cependant, aucun schéma systématique d'évolution n'a pu être établi au regard de l'ensemble des données obtenues. Une évolution en fonction de la vitesse de rotation du vecteur vitesse du kite autour de l'axe des lignes est tout de même proposé dans l'attente de futures mesures.

La troisième campagne de mesure était à nouveau axée sur des essais en mer, mais cette fois depuis un bateau de six mètres spécialement conçu dans ce but, et ainsi entièrement disponible pour les opérations de développements et de mesures. Après une phase de test du système de contrôle lorsque que celui-ci est embarqué sur le bateau, une phase de mesure de plusieurs semaines a été réalisée en baie de Quiberon en avril 2017. La problématique de la mesure du vent a cette fois été abordée en multipliant les moyens de mesures sur la zone de navigation, et en mettant en place un partenariat avec une entreprise spécialisée dans la modélisation météorologique à petite échelle. Les données acquises sur cette période a été post traitées dans un premier temps par simple moyenne, ce qui permet par exemple d'obtenir les performances de ce navire tracté par un kite, en fonction de l'angle vent réel. Le post traitement par moyenne de phase a pu aussi être adapté à cette campagne, et mettre ainsi en avant les mouvements du bateau induits par un chargement cyclique généré par une kite réalisant une trajectoire en huit. L'ensemble des données n'a pas été traité entièrement, et de futures actions sont possibles. Cependant cela constitue tout de même une bonne première base de données pour la validation de modèles numériques.

De nombreuses autres pistes sont aussi ouvertes concernant la mesures des performances des kites, comme la photogrammétrie qui pourrait permettre de capturer la déformée du kite en vol, et donc de qualifier des modèles d'interactions fluides structures.

Nomenclature

Underlined letter, as $\underline{X}$, denotes a space vector, usually belonging to $\mathbb{R}^3$. Double underlined letter, as $\underline{\underline{X}}$, denotes a matrix. Over-right-arrowed letter, as $\overrightarrow{X}$, denotes a time-series, belonging to $\mathbb{R}^n$, with n the number of time step. Therefore, $\overrightarrow{\underline{X}}$ denotes the time-series of a space vector, and then belongs to $\mathbb{R}^3 \times \mathbb{R}^n$. When index of vectors or matrices need to be used, they are denoted in the subscript, after a comma if a subscript notation already exists. Thus, the i^{th}component of $\underline{X}_b$ will be denoted as $X_{b,i}$. Moreover, the following notations are used:

$$X = \|\underline{X}\| = \sqrt{X_1^2 + X_2^2 + X_3^2}$$

$$\mu_{\overrightarrow{X}} = \mathrm{mean}(\overrightarrow{X}) = \frac{1}{n}\sum_{i=1}^{n} X_i$$

$$\sigma_{\overrightarrow{X}} = \mathrm{std}(\overrightarrow{X}) = \sqrt{\frac{1}{n-1}\sum_{i=1}^{n} |X_i - \mu_{\overrightarrow{X}}|}$$

$$\lceil \underline{X} \rfloor = \mathrm{abs}(\underline{X}) = \begin{pmatrix} |X_1| \\ |X_2| \\ |X_3| \end{pmatrix}$$

$$\lceil \underline{\underline{X}} \rfloor = \mathrm{abs}(\underline{\underline{X}}) = \begin{pmatrix} |X_{11}| & |X_{12}| & |X_{13}| \\ |X_{21}| & |X_{22}| & |X_{23}| \\ |X_{31}| & |X_{32}| & |X_{33}| \end{pmatrix}$$

$$\triangle X = \max(\overrightarrow{X}) - \min(\overrightarrow{X})$$

As for programming languages, the function **atan2** is defined:

$$\operatorname{atan2}(y, x) = \arctan\left(\frac{y}{\sqrt{y^2 + x^2} + x}\right)$$

Roman Symbols

A_k	Kite area	(m^2)
AR	Kite aspect ratio	$(-)$
C	Fuel consumption	$(L \cdot h^{-1})$
C_k	Kite force coefficient	$(-)$
C_l	Lift coefficient of the kite	$(-)$
f	Lift to drag ratio of the kite	$(-)$
f_γ	Cutoff frequency	(Hz)
$\underline{F}_a$	Aerodynamic kite force vector	(N)
F_{bl}	Left back tether force	(N)
F_{br}	Right back tether force	(N)
$\underline{F}_f$	Force vector into front tethers	(N)
$\underline{F}_k$	Total kite force vector	(N)
$\underline{F}_m$	Front tether force vector at attachment point	(N)
L_t	Tether length	(m)
Lat	Lattitude of the experimental setup	(°)
Lon	Longitude of the experimental setup	(°)
m	Mass of the kite	(kg)
$\underline{P}_k$	Kite Position vector	(m)
$\underline{p}_k$	Weight vector of the kite	(N)
Px	X-coordinate of kite position vector	(m)

Py	Y-coordinate of kite position vector	(m)
Pz	Z-coordinate of kite position vector	(m)
Q	Torque on the propeller shaft	$(N \cdot m)$
r	Radial coordinate of kite position vector	(m)
r_a	Amplitude ratio of kite force	$(-)$
r_b	Back tether ratio	$(-)$
r_{prop}	Propulsive Ratio	$(-)$
r_p	Power Ratio	$(-)$
r_s	Boat Speed Ratio	$(-)$
S_d	Phase averaging method detection signal	$(-)$
t_a	Phase duration (phase averaging method)	(s)
t_r	Duration of the measurement run	(s)
$\underline{V}_a$	Apparent Wind velocity vector on kite	$(m \cdot s^{-1})$
$\underline{V}_k$	Kite velocity vector	$(m \cdot s^{-1})$
$\underline{V}_s$	Velocity vector of the ship	$(m \cdot s^{-1})$
$\underline{V}_{WM}$	Measured Wind velocity vector at measurement point	$(m \cdot s^{-1})$
$\underline{V}_{WR,z}$	Relative wind velocity vector at altitude z	$(m \cdot s^{-1})$
$\underline{V}_{WR}$	Relative wind velocity vector at kite altitude	$(m \cdot s^{-1})$
$\underline{V}_{WT,z}$	True wind velocity vector at altitude z	$(m \cdot s^{-1})$
z_0	Altitude of wind measurement point	(m)

Greek Symbols

α_R	Return angle of back tethers	$(^\circ)$
β_{WD}	Horizontal True Wind Direction (TWD)	$(^\circ)$
β_{WR}	Relative Wind angle at kite altitude	$(^\circ)$
β_{WT}	Horizontal True Wind Angle (TWA)	$(^\circ)$

χ_{wr}	Horizontal Relative Wind angle at kite altitude	$(^{\circ})$
δ	Measured steering command apllied to kite	(m)
$\Delta\theta_{tgt}$	Angular elevation deviation between left and right target points	$(^{\circ})$
δ_r	Rudder angle	$(^{\circ})$
δ_{set}	Kite steering setpoint	(m)
ϵ	Lift to drag angle of the kite	$(^{\circ})$
γ	Angle between the kite velocity vector and the local meridian at kite position	$(^{\circ})$
$\underline{\Gamma}_k$	Kite acceleration vector	$(m \cdot s^{-2})$
γ_{ref}	Angle between the objective vector and the local meridian at kite position	$(^{\circ})$
$\lambda 1$	Measured position of actuator 1	(m)
$\lambda 1_{set}$	Position setpoint for actuator 1	(m)
$\lambda 2$	Measured position of actuator 2	(m)
$\lambda 2_{set}$	Position setpoint for actuator 2	(m)
ω	Rotation speed of the propeller shaft	$(rad \cdot s^{-1})$
$\underline{\Omega}_s$	Boat rotation speed vector	$(rad \cdot s^{-1})$
ϕ	Azimuth coordinate of kite position vector	$(^{\circ})$
ϕ_P	Azimuth angle of trajectory target point P_{tgt}	$(^{\circ})$
ϕ_{swt}	Switch azimuth angle (kite trajectory definition)	$(^{\circ})$
ϕ_s	Roll angle of the boat or of the experimental setup	$(^{\circ})$
ϕ_{tgt}	Target point azimuth angle (kite trajectory definition)	$(^{\circ})$
ϕ_{traj}	Expected center of the autopiloted 8-pattern trajectory	$(^{\circ})$
ϕ_{ws}	Bank Euler angle of onshore wind measurement device	$(^{\circ})$
ϕ_w	Bank Euler angle of wind measurement device	$(^{\circ})$
ψ	True heading angle of the boat or of or of the experimental setup	$(^{\circ})$
ψ_{ws}	Heading Euler angle of onshore wind measurement device	$(^{\circ})$

ψ_w	Heading Euler angle of wind measurement device	$(°)$
ρ	Density of the air	$(kg \cdot m^3)$
τ	Measured trim of the kite	(m)
τ_{set}	Kite trim setpoint	(m)
θ	Elevation coordinate of kite position vector	$(°)$
θ_P	Elevation angle of trajectory target point P_{tgt}	$(°)$
θ_s	Pitch angle of the boat or of the experimental setup	$(°)$
θ_{tgt}	Target point elevation angle (kite trajectory definition)	$(°)$
θ_{ws}	Elevation Euler angle of onshore wind measurement device	$(°)$
θ_w	Elevation Euler angle of wind measurement device	$(°)$
ζ_{wr}	Vertical Relative Wind angle at kite altitude	$(°)$

Abbreviations

2D	2 Dimensions
3D	3 Dimensions
GPS	Global Positioning System (sensor based on)
IITC	International Towing Tank Conference
IMU	Inertial Measurement Unit
LEI	Leading Edge Inflatable
MEMs	Mirco Electro Mechanical Systems
NaN	Not a Number
RIB	Rigid-hulled inflatable boat
TWA	True Wind Angle
TWD	True Wind Direction
TWS	True Wind Speed

Reference Frames

Reference frames used in this study are introduced below and detailed with drawings in the following sections. They are identified with one or two letters, printed in subscript under the normalized vectors $(\underline{x}, \underline{y}, \underline{z})$ forming the axis system. When the considered reference frame needs to be precised , this one is then printed under parenthesis in upperscript above the variable: for example, if the vector $\underline{A}_b$ is expressed in the reference frame R_{ref}, it will be denoted as $\underline{A}_b^{(ref)}$. In the following section, “body” stands for the ground station used onshore or for the boat used during see trials

List of reference frames

$R_{ned}(o, \underline{x}_{ned}, \underline{y}_{ned}, \underline{z}_{ned})$	North East Down reference frame.
$R_{\psi}(o, \underline{x}_{\psi}, \underline{y}_{\psi}, \underline{z}_{\psi})$	True Heading reference frame.
$R_s(o, \underline{x}_s, \underline{y}_s, \underline{z}_s)$	Ship reference frame.
$R_{ws}(W, \underline{x}_{ws}, \underline{y}_{ws}, \underline{z}_{ws})$	Onshore Wind Measurement reference frame.
$R_{wm}(W, \underline{x}_{wm}, \underline{y}_{wm}, \underline{z}_{wm})$	Wind Measurement reference frame.
$R_{wr}(A, \underline{x}_{wr}, \underline{y}_{wr}, \underline{z}_{wr})$	Relative Wind reference frame at kite altitude.
$R_a(K, \underline{x}_a, \underline{y}_a, \underline{z}_a)$	Aerodynamic reference frame at kite altitude.

Euler Angles Definition All the different Euler angles used in this study are (yaw,pitch,roll), or $(\psi_{euler}, \theta_{euler}, \phi_{euler})$ as draft in Fig. 1, referred to in the literature as Cardan/Tait-Bryan angles. The sequence of rotations follows the aerospace convention (z-y’-x” sequence) for rotation from the global reference axis system R_{ref} to the new axis system R_{new}.

The transfer matrix to rotate a vector from R_{new} to R_{ref} is obtained from Eq. 1.

$$\underline{\underline{M}}_{R_{new} \rightarrow R_{ref}} = \underline{\underline{M}}_{\psi_{euler}} \underline{\underline{M}}_{\theta_{euler}} \underline{\underline{M}}_{\phi_{euler}} \tag{1}$$

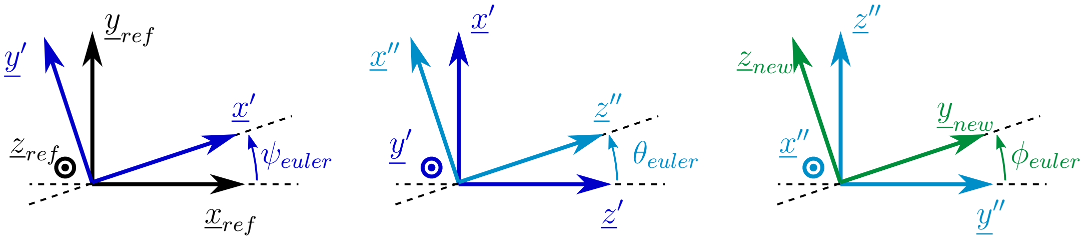

Figure 1.: Euler angles definition, following the aerospace convention (z-y'-x" sequence).

$$\underline{\underline{M}}_{\psi_{euler}} = \begin{pmatrix} \cos(\psi_{euler}) & -\sin(\psi_{euler}) & 0 \\ \sin(\psi_{euler}) & \cos(\psi_{euler}) & 0 \\ 0 & 0 & 1 \end{pmatrix} \tag{2}$$

$$\underline{\underline{M}}_{\theta_{euler}} = \begin{pmatrix} \cos(\theta_{euler}) & 0 & \sin(\theta_{euler}) \\ 0 & 1 & 0 \\ -\sin(\theta_{euler}) & 0 & \cos(\theta_{euler}) \end{pmatrix} \tag{3}$$

$$\underline{\underline{M}}_{\phi_{euler}} = \begin{pmatrix} 1 & 0 & 0 \\ 0 & \cos(\phi_{euler}) & -\sin(\phi_{euler}) \\ 0 & \sin(\phi_{euler}) & \cos(\phi_{euler}) \end{pmatrix} \tag{4}$$

The rotation vector $\underline{\Omega}$ of the reference frame R_{new} in R_{ref} is as following:

$$\underline{\Omega}_{new}^{(ref)} = \dot{\psi}_{euler}\underline{z}_{ref} + \dot{\theta}_{euler}\underline{y}' + \dot{\phi}_{euler}\underline{x}''$$

North East Down (NED) Reference Frame

As presented in Fig. 2, the earth-fixed reference frame used in this study is the North East Down axis system, defined with the x-axis pointing to the north pole of the planet, the y-axis pointing to the East and the z-axis pointing towards the center of the planet. The origin of the frame is the center of gravity of the body.

Heading Reference Frame

The second reference frame is based on the heading angle ψ of the body relatively to the true North direction. It is the result of a rotation about $\underline{z}_{ned}$ of angle ψ applied to frame R_{ned}, as shown in Fig. 3. ψ is the first of the three Euler angles.

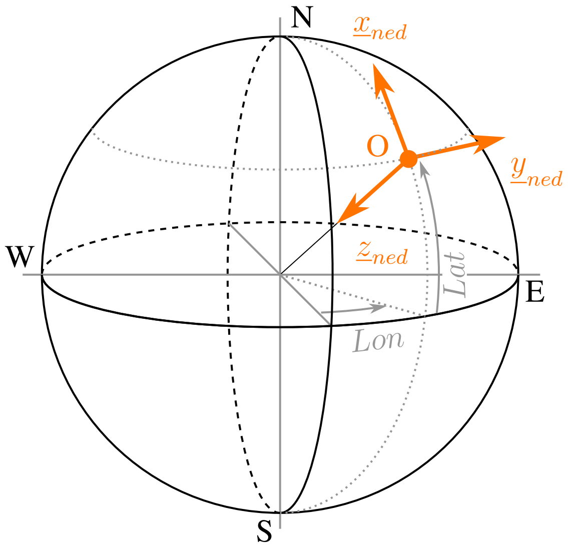

Figure 2.: Drawing of the North East Down R_{ned} reference frame.

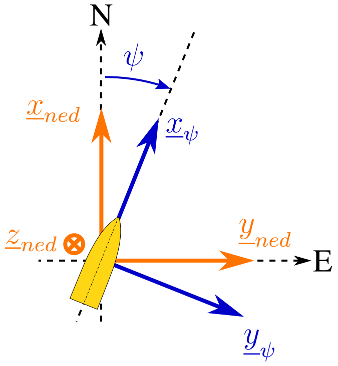

Figure 3.: Drawing of the Heading R_{ψ} refrence frame. ψ is the true heading of the boat (using true North reference).

Ship Reference Frame

The Ship reference frame is rigidly fixed to the body, and is the result of the two other rotations remaining from the two other Euler angles: the pitch θ_s and the roll ϕ_s. At first, a rotation about $\underline{y}_{\psi}$ of an angle θ_s is applied, followed by a rotation about $\underline{x}_s$ of an angle ϕ_s, as visible in Fig. 4.

Onboard Measurement Wind Reference Frame

The Measurement Wind Reference R_{wm} Frame is the axis system of the wind measurement device settled on board. Thus wind measurements are output in this reference frame.

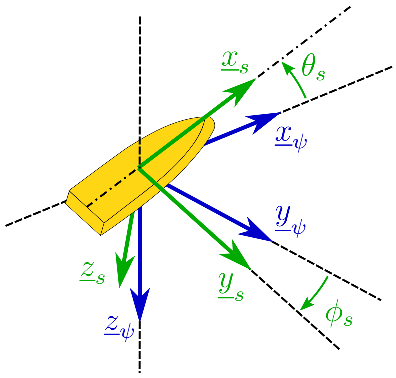

Figure 4.: Drawing of the Ship R_s reference frame.

This frame is the result of a triple rotation of Wind Euler angles $(\psi_w, \theta_w, \phi_w)$ applied to Ship Reference Frame. It origin is located at wind measurement point W. Considering the anemometer is rigidly fixed to the ship, $(\psi_w, \theta_w, \phi_w)$ are constant in time.

Onshore Measurement Wind Reference Frame

The Onshore Measurement Wind Reference R_{ws} Frame is the axis system of the wind measurement device when deployed onshore, and not rigidly fixed to the experimental setup. Thus wind measurements are output in this reference frame. This frame is the result of a triple rotation of onshore Wind Euler angles $(\psi_{ws}, \theta_{ws}, \phi_{ws})$ applied to the Heading Reference Frame R_ψ. It origin is located at wind measurement point W.

Relative Wind Reference Frame

For a known relative wind velocity vector $\underline{V}_{WR}$, the Relative Wind reference frame is defined with the x_{wr}-axis co-linear to $\underline{V}_{WR}$ (see Fig. 5). Thus the R_{wr} reference frame is the result of a first rotation about $\underline{z}_\psi$ of an angle χ_{wr} , followed by a second one about $\underline{y}_{wr}$ of an angle ζ_{wr} . Therefore, χ_{wr} and ζ_{wr} angles are the two first Euler angles as defined previously, and transfer matrices $\underline{\underline{M}}_{\chi_{WR}}$ and $\underline{\underline{M}}_{\zeta_{WR}}$ can also be defined. The relative wind angle β_{WR} generally used by sailors, and also used in this study, is related to the angle χ_{wr} with the following formula:

$$\beta_{WR} = \chi_{wr} + \pi \tag{5}$$

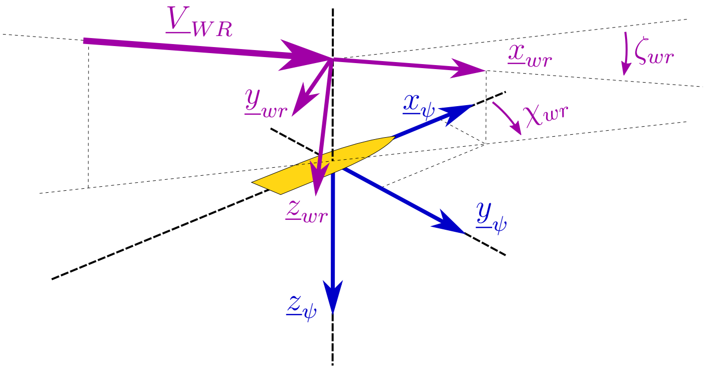

Figure 5.: Drawing of the Relative Wind R_{wr} reference frame. The y_{wr}-axis and z_{wr}-axis are not shown, but are the results of a triple rotation of angles $(\chi_{wr}, \zeta_{wr}, 0)$, following Euler convention, applied to the heading reference frame R_{ψ}.

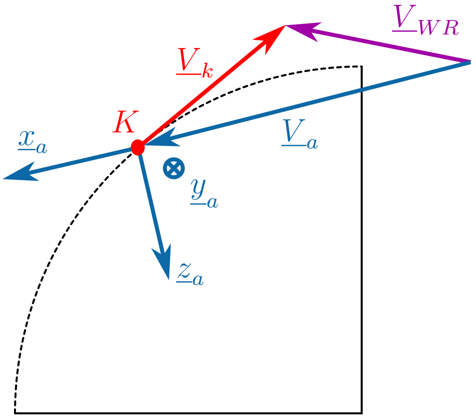

Figure 6.: Drawing of the Aerodynamic R_a reference frame. Kite tethers and kite attachment point are not necessarily contained in the plane of the figure.

Aerodynamic Reference Frame

The Aerodynamic reference frame is also defined from the apparent wind on kite, as shown in Fig. 6. The y_a-axis is orthogonal to the plane formed by the vectors $\underline{V}_a$ and $\underline{V}_k$, and the z_a-axis is completing the axis system, pointing down. Kite tethers and kite attachment point are not necessarily contained in this plane.

Kite Positioning

Kite position is denoted by the point K. The position vector $\underline{P}_k$ can be expressed in one of the reference frame presented previously. Thus the Fig. 7 is no related to a particular axis system, and presents kite position in a generic reference frame. For the bulk of this

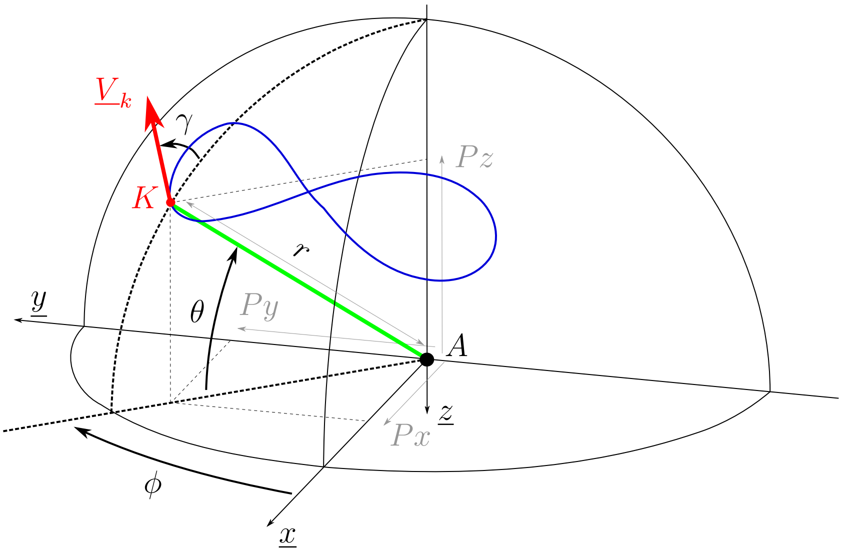

Figure 7.: Drawing of the two kite positioning systems: Cartesian or spherical. The axis system used for positioning kite can vary depending on application.

study, only kite seen as a point is considered, with no motions of rigid body. Therefore, three variables only are requested to positioned the kite. Because kite is nearly flying on a sphere, spherical coordinates (r, θ, ϕ) are particularly suitable. However Cartesian coordinate (Px, Py, Pz) are sometimes necessary.

Contents

List of Figures

List of Tables

Introduction

The globalization of our economy has never been greater than today. With the exponential development of the means of communication, exchanges between the different part of the Earth become more and more easy, as soon as these exchanges are non-material. Thus it is possible today to buy in few minutes a product stored in a country half a world away. However, this product will need to be shipped, and this will most likely be done by ship. As a consequence, the maritime transport sector is permanently growing. Nowadays, all transport ships use engines running on fossil fuel, and the world commercial fleet takes a non-negligible part in the emissions of greenhouse gas or other pollutants, and this is the same thing for the main part of the world fishing fleet. However, the wind is a large source of renewable energy, and furthermore the wind at seas is stronger and more consistent than on lands. Thereupon, some innovative projects have been conducting for the last decades in order to develop wind-assisted ship. In this context, the use of kite instead of classical sails is one of the most promising solutions, regarding the power generated by kite compared with sails for the same area. Kites also demand limited room on the deck, and can induce smaller motion of the ship. For all these reasons, a research project has been launched to develop kite as an auxiliary propulsion device for ship, organized around a consortium of academic partners and private companies. The project is called beyond the sea, and was launched in the middle of 2014.

The scope of such a project is very large and complex. As a matter of fact, numerous elements need to be addressed to obtain a final marketable system. Thus, all the operation of the kite, and particularly the launch and recovery procedures, need to be fully automated, in order not to increase the workload of the crew. Moreover, the structural design of the kite and the tethers have to be achieved, and this implies to precisely define the aerodynamic load on the kite. For giant and nonexistent kites, this load can only be simulated with complex modelings, that need to be built. New fabrics have also to be developed, capable of withstanding these loads, with a mass as light as possible and with life cycle as long as possible. In addition, the interaction between the ship and the kite has to be considered. At first, this is a part of the process aiming to optimize the performance of the kite. Secondly this study also leads to draft the operational limits of the kite and then to provide content for a sailor learning program dedicated to kite use.

All these research and development tasks have been split between the member of the consortium. In this way, the graduate and post-graduate engineering school and research center ENSTA Bretagne has been mandated to carry out the scientific research program. This follows a previous and first research action dealing with kites, ended in 2014 with the achievement of the Ph. D. study of Richard Leloup. This study was the ever first one carried out in France, and it investigated multiple tracks related to the use of kites on ships. It allowed also to define the main directions of the scientific work for the beyond the sea project. Among them, the need of experimental data became obvious, leading to the present study, centered on the experimental analysis of the flight of the kite, when deployed on ships. The objective of this work is therefore to acquire the necessary data that are suitable for benchmarking numerical modelings that have already been developed, or on on-going work. A secondary goal is to propose some basic evolution laws suitable for feeding other new modeling approaches. Before any step of data acquisition and data analysis could be achieved, an experimental set up has to be developed, fitting the specifications for kite trials.

This document is consequently structured around three distinctive parts. The first chapter is a detailed presentation of the context of the study, including a state of the art on kite experiments, and followed by the presentation of the main scientific issues associated with kites and kite experiments. The second part, formed by Chap. 2 and Chap. 3, is a presentation of the experimental set up used all along the study. Finally the last three chapters deal with experimental campaigns achieved in the scope of this study. The first is about trials on a fishing vessel. The second presents a work focused on kite performances and therefore carried out onshore. Finally, the last campaign concerns sea trials using a small boat specifically built for this purpose.

1. Position of the Problem

Résumé

Ce chapitre constitue une introduction étendue du sujet présentant les différents acteurs impliqués dans le projet, les problématiques globales, un état de l'art des études et analyses expérimentales faites sur les kites ainsi qu'une présentation des problématiques scientifiques.

Le projet de recherche beyond the sea est un consortium composé de partenaires privés et académiques, organisé autour de la société éponyme. Celle-ci a été fondée par l'ancien navigateur Yves Parlier, et vise à développer la traction de navire par des kites. Cela doit permettre de réduire la consommation de carburant et donc faire des économies, tout en réduisant les émissions de gaz à effet de serre et autres polluants. En plus de l'entreprise pilote, le consortium se compose d'un fabricant de tissus et d'un fabricant de cordages, en charge de la recherche et du développement sur les matériaux constituant le système. Un spécialiste des apparaux de pont est lui aussi impliqué pour développer les treuils de contrôles. Enfin, l'ENSTA Bretagne, école d'ingénieur avec son centre de recherche faisaint partie de l'IRDL[1], est en charge des aspects scientifiques. Trois thèses sur le sujet sont donc en cours, en comptant celle-ci. Les sujets des deux autres actions de recherche sont une étude d'interaction fluide structure au niveau du kite, et une étude d'interaction entre le kite et le navire. Le projet se concentre sur des kites à boudins gonflables, en particulier pour leur capacité à avoir une forme en l'absence de tout chargement aérodynamique, ce qui peut faciliter les opérations de lancement et de récupération.

Ce projet vise donc à développer la propulsion auxiliaire en utilisant le vent comme source d'énergie. Bien que l'idée ne soit pas nouvelle (les kites pour faire avancer des embarcations sur l'eau sont apparues il y a des centaines d'années), un tel système n'a pour le moment pas été véritablement commercialisé. Le marché est particulièrement vaste, en effet la flotte de navires de commerce est particulièrement grande avec plus de 90 000 navires évoluant autour du monde. Encore plus conséquente, la flotte de pêche mondiale atteint 4.6 millions d'unités, mais toutes ne sont pas motorisées.

Plusieurs équipes de recherches se sont intéressé aux kites, mais elles se sont principalement concentrées sur la production d'énergie électrique à terre, plutôt que la propulsion axillaire des navires. Un seul groupe (la compagnie allemande SkySails) a travaillé de façon soutenue sur le problème de la traction des navires, et a réalisé des essais sur un navire de plus de 100 m, équipé d'un kite à caisson de 320 m². Cependant, quel que soit l'objectif du système, tous les démonstrateurs expérimentaux sont basés sur une architecture relativement commune. La position du kite est généralement obtenue grâce à un capteur d'angle des lignes au sol, et éventuellement complété par des mesures embarqués dans le kite. Le vent est lui aussi mesuré, le plus souvent quelques mètres au-dessus de la surface.

---

[1] Institut de Recherche Dupuy de Lôme

Un des éléments les plus importants dans le cadre d'un tel projet est de démontrer la viabilité économique du système. En effet, si le kite ne permet pas aux armateurs de réaliser des économies, il ne sera pas utilisé. Ainsi, les différentes actions de recherche doivent toute contribuer à estimer la rentabilité du système. Dans le cadre d'une étude précédente (thèse de Richard Leloup (2014)), un outil de de prédiction des économies de carburant a été développé, outil qui a été amélioré par la suite. Cette outil est basé sur la modélisation du vol du kite faisant l'hypothèse que le kite est un unique point sans masse, et est donc appelé le modèle zéro-masse. Ce modèle prend en entrée les paramètres aérodynamiques du kite et prédit les efforts que celui-ci peut générer. Deux cas peuvent être différenciés concernant le vol du kite : le cas statique et le cas dynamique. Dans le premier cas, le kite est simplement une voile relié au navire par ses lignes. Dans le second cas le kite de par sa trajectoire, créé son propre vent apparent, ce qui augmente considérablement la puissance. Avec ce modèle, le problème d'optimisation de la taille de la trajectoire n'a pas pu être mené précédemment, car aucune variation des paramètres aérodynamiques en fonction de la trajectoire n'était prise en compte. Un des objectifs de cette étude est donc d'apporter une démarche et des mesures permettant d'estimer ces variations. Les lignes du kite sont des éléments importants car elles font l'interface entre le kite et le système de contrôle. Des études réalisées dans le cadre du projet ont montrées que l'hypothèse de lignes parfaitement droites et indéformables était largement acceptable dans la majorité des cas. De ce fait cette hypothèse fut retenue pour l'ensemble de cette étude.

L'estimation du vent à l'altitude du kite est aussi un élément important contribuant à l'estimation des économies associables aux kites, car la puissance que peut fournir le kite est bien sur directement liée à l'intensité du vent à la position du kite. Le vent que perçoit le kite est la composition du vent généré par sa propre vitesse et du vent réel. La vitesse du kite peut être calculée en connaissant la vitesse du navire. Cependant connaitre le vent à l'altitude d'évolution du kite est une chose plus complexe. En effet, l'écoulement de l'air le long de la surface de la planète entraine l'apparition d'une couche limite atmosphérique, ce qui génère un gradient de vitesse du vent. De plus, du fait de la rotation de la terre, des effets de Coriolis peuvent entrer en compte, et ainsi générer un vrillage de la direction du vent réel en fonction de l'altitude.

La structure de cette thèse s'articule autour de six chapitres. Les deux premiers, volontairement très techniques, présente le système expérimental qui a été utilisé pendant cette étude. Les trois autres chapitres présentent les trois campagnes expérimentales qui ont été menées, ainsi que les résultats associés. L'ordre de présentation suit l'ordre chronologique de réalisation, car chaque campagne a entrainé un retour d'expérience qui a été pris en compte pour la campagne suivante.

1.1. Context of the study

1.1.1. The beyond-the-sea Project

1.1.1.1. General Overview

This Ph. D. study is integrated in a global project named beyond-the-sea. This project brings together manufacturers from the private sector and academic partners and aims to develop an innovative wind-assisted propulsion for ship, based on kites. It was initiated by the former offshore sailor Yves Parlier during the first decade of 21st century. At the time Yves Parlier was engaged in offshore solo racing, which led him to sail in contact with giant commercial ships, polluting the atmosphere with the exhaust gas of engines whereas he was rounding the world using only the wind as source of energy. Therefore, the idea of assisting vessels by wind caught on in his mind to reduce the environmental impact of maritime transport. In this context, the use of kites appears as being the best solution for four main reasons:

- The required room on deck is limited compared with classic rigs.
- The point of application of forces is located at kite attachment, and not at mid-height of the mast in case of a classic rig. Therefore, the heeling moment generated by kite is lower than the one generated by a sail rig on a mast.
- Kites can fly at high altitude, looking for wind and then catch stronger and more stable winds.
- Kites can fly using dynamic mode and then increased their apparent wind. Therefore the towing power generated is stronger.

For wind-assisted ship by kites, only one research group has really been involved. The project was carried out by the German company SkySails, and led to a prototype of kite control system mounted on a 132-meter long vessel, able to control a ram air kite up to 320-square-meter (Erhard and Strauch (2012)). However, the SkySails company had to refocus its business activity on power generation instead of wind-assisted ship due to the bankruptcy of their main ship owner partner providing the test ship. Nevertheless, in 2017, SkySails had equipped another vessel with their system set on a 40-square-meter kite, and a few images can be seen in YouTube[2]. The vessel is a 35-meter-long catamaran, named Race For Water, with scientific missions. Some other trials has been conducted to tow boat with kite, as the ones done by Fagiano et al. (2010) and also visible in YouTube[3].

The scope of the beyond-the-sea project is focused on leading edge inflatable (LEI) kites instead of ram air kites as used by the SkySails company. Indeed, LEI kites have their own

---

[2] https://www.youtube.com/watch?v=26FCrNtDgGo

[3] https://www.youtube.com/watch?v=DfI1HpnvjWA

shape without any aerodynamic load, which makes the launch step easier. As a matter of fact, at deck level the wind can be weak and really disturbed by superstructures around. In this context, kites with their own shape can catch this disturbed wind more easily to get lifted. As for control system, the choice between multiple-tether kites with control at ship level or single-tether kites with a control pod just below the kite will depend on situation and kite size. Large kites will probably use control pod located underneath the kite, whereas smaller one will be steered from the deck level using control tethers. This project in its first stages deals with kites under 100 m², therefore only kites with 4 tethers and controlled from the deck level are used. This Ph. D. study only focuses on these types of kites, which are, as being controlled from the main deck, totally different in their steering concept compared to existing well known remote control solutions such as developed by Skysails. Moreover, for small LEI kites, an important market exists dedicated to recreation, as kitesurf or kiteboard. This allows to easily buy some kite wings. Thus early trials carried out in this Ph. D. study were done with commercial kites bought at a local specialized shop.

1.1.1.2. The Consortium

The project is structured around the beyond-the-sea company, under the leadership of Yves Parlier. In addition to the general project management mandate, the beyond-the-sea company is mainly focused on kites designs and kite control, including the automated launch and recover procedures. These problematic has led to a Ph. D. study by Du Pontavice (2016). Six other partners are involved in the project, as presented in Fig. 1.1 for their various skills:

Porcher Industries is a weaver manufacturing technical fabrics usually for parts of construction of airbags, para gliders, parachutes, sails... In the beyond-the-sea project, this company is in charge of research and innovation on future kite material in order to provide fabric as light as possible and able to resist to tough solicitations, like large aerodynamic loads and permanent sun exposure in a salty and wet environment.

Cousin Trestec is a technical synthetic rope manufacturer, with a large range of products going from kitesurf lines with diameters of a few millimeters to synthetic cable for towing vessels or holding heavy submarine sensors under boat. In the beyond-the-sea project, this company is in charge of research and innovation on future kite tethers in order to provide tethers as light as possible and able to resist to tough solicitations, as large loads and permanent sun exposure in a salty and wet environment.

CMA CGM is the third biggest ship owner in the world, with a fleet of container ships over 400 units (UNCTAD (2016)). This company will be part of the full scale trials providing a suitable container ship.

Figure 1.1.: Structure of the beyond-the-sea project.

DAAM is a company handling a fleet of competition sailing boats, located near the beyond-the-sea company. DAAM is in charge of trials carried out at sea, buy providing suitable vessels, and by mounting kite control device developed by beyond-the-sea.

BOPP is a leader in designing and manufacturing hydraulic and electrical systems for marine applications. Therefore, this company is in charge of research and development of suitable winches for launching and controlling kite.

ENSTA Bretagne is a graduate and post-graduate engineering school and a research center, with a wide range of knowledge, and in particular a naval architecture department. ENSTA Bretagne is also a long term partner of Yves Parlier, with a few joint research actions carried out in the early 2010s, and leading to the Ph D. program of Richard Leloup (2014). For this project ENSTA Bretagne, as an accademic partner, is in charge of all research aspects. This includes a scientific support to the other companies of the consortium, and especially Porcher Industries and Cousin Trestec about fabrics and ropes specs . Moreover three Ph. D. studies has been launched, including the present one. The two others are focused on interactions between the kite and the ship for the first one, and fluid-structure interaction on soft material forming kites.

The overall budget of the project is 16 millions of euros for a five-year program (2014-2019). The project is funded at 27.5 % by the French environment and energy management agency (ADEME), thanks to repayable advances or subsidies. ENSTA Bretagne funding is only made of subsidies, capped at 1.2 millions of euros for the 5 years. Besides the salaries of the three Ph. D. students and the associated research costs, this budget also includes the salaries of two research engineers in charge of the transfer of knowledge towards industrial partners. Moreover, four associated professors are dedicated to the project, with supervising and project managing mandates.

1.1.2. Some Historical Points on Kites for Sailing

Obviously, the use of wind for moving on the water is absolutely not a new thing. About 3500 years BC, Egyptians already used sailing to carry goods and people on the Nils, thanks to very consistent winds always blowing in the same direction to climb up the river, the current ensuring the other way. Although lesser known and probably not quite as old, kite sailing can also be considered as an ancient practice, with the existence of kite to propel raft across lagoons in Polynesia islands (Henry (1998)) at least 500 years ago. Otherwise, kites were also present in Polynesia culture for example in religion and legend, or for fishing and war. Kites for war were also present in China and this seems to be the first appearance of kite in the History, with elements dating back to hundred years BC.

In our modern history, kites were mainly used for leisure or to carry instruments, like Alexander Wilson in 1740's (J.C. Stevenson (2003)), who seems to be the first European starting using kite. For the specific case of towing kites, George Pocock built kites to tow a carriage, named by himself Charvolant, and had already imagined kite for towing ship, and doing some trials (Pocock (1827)). His Charvolant reached 20 mp/h (32 km/h) with 6 people on board, which was a very good performance at that time. Few years later, Samuel Franklin Cody was the first one to cross the English channel with a little tiny boat towed by a kite in November the 5th of 1903. S. F. Cody was also one of the European pioneer of kite used for military purpose, like manned kites for observations, or antenna kite for increasing radio range. During the main part of the 20th century kite for sailing were marginal, with only a few pioneer trying to adapt parachute for recreation sailing. However the complexity of launching ram air kites above the water, and the consequences after a crash made access to customers difficult.

The real start of sailing with kite was due to two French brothers, Bruno and Dominique Legaignoux, with their wing specially developed for kitesurfing, and made of an inflatable leading edge. Their invention led to a patent published in November 1987. This is then the birth of a new sport, the kitesurf. This new sport spread around the world, and became popular during the first decade of 21st century, despite an initial reputation of dangerous sport due to some fatal accidents. Nowadays, kite designs and safety quick release systems have considerably increased the safeness of the activity, and each year sees new kite-surfers. The actual worldwide kitebaording market is estimated about $250M according to the CEO of a French brand, and kiteboard should become an Olympic sport in 2024. In an irony of history, professional kiteboarder are now using ram air kite instead of leading edge inflatable kite, due to their better performance. Until 2012, kiteboard was also for years the fastest wind propulsed device on water, with a best speed recorded at 55.65 kts over 500 m.

In spite of a number of kiteboarders increasing year after year, kites as towing assistance for boat have not followed the same development. Only a small part of pleasure boat owners seems to be interested in innovation. For professional boat, only potential income or saving associated to kite are considered, and until 2008 and the financial crisis, with a temporary but real rise in the price of oil, kite technology were not seen as a sufficiently good investment.

1.1.3. Overview of the World Commercial Fleet

According to the Review of Maritime Transport 2016 (UNCTAD (2016)), the world commercial fleet consists of more than 90 000 vessels, with combined 1.8 billion dead-weight tons (dwt). It is expending at a rate of 3.48% for the last year, which is the lowest rate in the last decade, but the demand for maritime trade only increases by 2.1% on the same period. Therefore, the worldwide situation of maritime trade is a global overcapacity. The fleet distribution by vessel type (regarding combined dwt) is dominated by bulk carriers (43.6%), followed by oil tankers (27.9%) and container ships (13.5%). The rest of the fleet (15.0%) is divided between general cargos, gas carriers, chemical tankers, offshore units and passenger ships. All categories are in constant growth over the last years, but the percentage of container ship and bulk carriers capacity increases whereas oil tanker capacity percentage goes down. This trend can be also noticed looking at the age distribution of the world fleet. Indeed, more than 50% of container ships are under 10 year old, and this percentage even grows to 67% regarding dwt capacity. Same thing for bulk carriers, with respectively 68% of the ships under 10 year old, and 72% in capacity. A higher percentage of recent ship regarding capacity in comparison to number of units denotes also an augmentation of the size of the vessels in the last decade. Concerning oil tankers, the fleet seems much older, with only 39% of units under 10 year old, and 39% older than 20 year. However, very old oil tankers are relatively small unit because they represent only 4% in terms of capacity, whereas under-10-year old oil tanker capacity reaches 58 %.

Some detailed element on container ship needs to be regarded, as this type of ship is directly targeted by the kite project. The largest company in container trade is Maersk with a market share of 15.1% (in term of twenty-foot equivalent unit (TEU) capacity), followed by Mediterranean Shipping Company (13.4 %) and CMA CGM (9.2 %). These ship owners have started few years ago to order ships more and more bigger, with capacity exceeding now 21 000 TEUs for the latest built, the OOCL Hong Kong, and launched in 2017. This participates to the global overcapacity of the market. Therefore transport costs are lowered. For example the rate for a TEU between Shanghai and Northern Europe was $629 in 2015, still according to UNCTAD (2016), with a rate evolution over the previous year of -45.8 %. Moreover, the increase of ship size was initiated expecting a better market growth than happened, and savings associated to larger ship thanks to economies of scale can quickly become loss if ships are not filled. Larger ships also bring additional cost to logistic partners as ports, which need to invest on larger equipment for loading and offloading, and these investments affect the ship owner. In this context, the economic pressure on ship owners is important, and competition is tough. Thus, in 2016 the owner Hanjin Shipping (8th liner shipping company in the world in number of ship) had been declared bankrupt.

New regulations to increase energy efficiency and to reduce emissions of greenhouse were adopted in 2011 by the International Maritime Organization (IMO) and new engagements were taken in December 2015 during the Paris Agreement at the 21st session of the Conference of the Parties, under the United Nations Framework Convention on Climate Change. These elements lead to measures becoming progressively mandatory, as for example the use of fuel producing nitrogen oxide (NO_x) below certain levels, or requirements on sulfur oxide (SO_x) emissions, requiring the use of scrubbers to clean exhaust gas, or the changeover to liquefied natural gas engines.

Consequently, these various measures increase the operational cost of ship owners, and with income declining due to the overcapacity, they need to find solutions to keep positive financial results. Slow steaming is one of them, because by reducing operation speed, fuel costs decreases, the ship call frequency at a given port decreases and then the port fees, and occupancy rates increases. This method has been in used since 2008 where the maritime trade market, as a lot of other businesses were affected by the financial crisis, and speed was reduced from 20-25 kt to 16-19 kt (Boersma et al. (2015)). This method is however not totally free of charge for ship owners because propulsion system are usually optimized for one operational speed, and a speed reduction of about 30 % can require an engine refit and/or a hull refit for ship launched before 2008. Nowadays, carriers even start to use super slow steaming with cruising speed about 12 kt.

1.1.4. Overview of the World Fishing Fleet

Based on the Food and Agriculture Organization report on the state of world fisheries and aquaculture (FAO (2016)), the total number of fishing vessels in the world in 2014 was estimated about 4.6 million. Therefore the market for mounting kites on fishing vessels seems huge. However, almost 80% of the world fleet is located in Asia and Africa, and these two continents are home for a population mostly poor. Fishing vessels in this areas are then small and sometime not motorized. Thus, no engine powered vessels, using sails or paddle, represent 35 % of the world fleet. The fishing fleet in Europe and North America is estimated to 182 000 ships (4 % of the world fleet), but the very large majority of them are motorized. Moreover, these areas undergo strong regulations about fishing quotas and fleet size. For example the European Union (EU) policy is to not increase fishing fleet size, and the public support for decommissioning vessels is encouraged by EU laws (European Commission (2016)). This policy leads to significant results, with a decrease about 20% in EU fleet size over the last 20 years. However this policy also leads to a very old fleet, with an average age over 20 years. Therefore, vessels do not take advantage of recent technological developments, like improvements on hull hydrodynamics. Hence, the economic pressure on ship owner is getting important, with on one side old vessels with important operating cost, and on the other side limited profits due to quotas.

1.2. State of the Art on Kite Experiments

The use of kites as source of energy is not a recent research field, as first related scientific publications date from the 80s. A good example is the work of Loyd (1980), presenting the concept of kites flying at high speed and carrying power generator. However, the evolution of the global energy situation leads to a raise of research efforts in the field of renewable energy in the last decades. Therefore a number of research groups focused on kite potential, with various organization: some of them are teams part of academic laboratories and others are totally private companies. The third option is a mix of the the first two options, with a private company associated with a laboratory, which is the case of the beyond-the-sea project. In the case of a fully private organization, to respect industrial confidentiality few scientific publications are available and only some patents can be found.

In the specific case of kites, two possibilities exist to capture the energy of the wind. The first one is to transform the mechanical energy into electrical energy, and the second one is to use directly the mechanical energy for moving loads, like ships. A third possible solution is to mix the first two possibilities, leading to a hybrid concept which has been investigated by Fagiano et al. (2012). An overview of the main concepts associated with kite flight and electricity production is given by Fagiano and Milanese (2012). Numerous technology are available for building kite: rigid or soft material, ram air kite or inflatable leading edge kite, one, two or four tethers. A non exhaustive overview of these various types of kite was written by Cherubini et al. (2015). These various technologies have been mainly tested for electricity generation, with various ways available to achieve this purpose as exposed by Diehl (2013).

Solutions for kite control can be sorted in two categories: onboard control or ground control, and both have pros and cons. The first one includes the case of kites controlled thanks to a control pod located under the kite. This is the solution adopted by SkySails (Erhard and Strauch (2013b)) and also the research group of the Delft University of Technology (Vlugt et al. (2013)). The first solution includes also the kites controlled through control surfaces located at the end of the trailing edge of the wing, as it is commonly done for planes. This is the choice of the Ampyx Power Company, but it is devoted principally to rigid kites. Some trials were also carried out byLozano (2014) to control LEI kite with onboard actuators, however this solution seems complicated for this type of kites. The second solution relates to kites controlled from the ground. In this case, at least two tethers need to link the kite to the control system located at ground. This option is particularly suitable for small kites, like the prototype developed by Fagiano and Marks (2015), but it is also the choice of some research groups like EnerKite for their demonstrator EK30 (Bormann et al. (2013)). All these teams have their own experimental set up, generally developed for autopilot testing in order to obtain a robust algorithm suitable for operational use, and for bringing reproducibility as a proof of the concept.

Whatever the aim of a kite experimental set-up, the common data which is the most important is the kite position. Indeed, no autopilot can work without a feedback on current object position. To deal with this issue, several solutions are available. At first, Inertial Measurement Unit (IMU) can be embedded on the kite. If such a device was particularly expensive few decades ago, it is now more affordable thanks to a new technology called MEMS (for Micro Electro Mechanical Systems), and combining little accelerometers and gyroscopes. However, this technology is not as precise as the expensive one, and so a 3D tracking of an object using only MEMS sensors is not really possible Hol (2011). Nevertheless, with additional sensors, some good results can be get, as for example an attitude and heading reference system (AHRS). Such a system is obtained by running a sensor fusion algorithm on data coming from accelerometers, gyroscopes and magnetometers (Islam et al. (2016)). On a simplified basis, by integrating the gyroscopes values, it becomes possible to get the Euler angles of the sensor. Magnetometers and accelerometers are then used to provide the orientation of the reference frame, with the measurement of the earth gravity vector and magnetic field vector. Therefore with an AHRS providing the attitude of the kite, it should be sufficient to deduce kite position with the assumption that the kite can only move on a sphere. However, with a kite flying in dynamic mode, acceleration and deceleration are permanent, and then the gravity vector can not be measured with accuracy. AHRSs are then not sufficient for accuracy position measurement, but the data provided can be used in combination with other sensor outputs, and with specific fusion algorithms, as Fagiano et al. (2014) or Erhard and Strauch (2013a). The most common other solution for measuring position of the kite is the measure of the tether angle at ground level. This is done thanks to a mechanical system tracking the tether axis based on optical encoders or potentiometers (Fagiano and Marks (2015),Erhard and Strauch (2013b),Dadd (2012)Vlugt et al. (2013)). Bormann et al. (2013) also use a tether angle sensor, but without any sensor on kite to avoid problem with data transmission from onboard sensors to ground control device. Some trials with onboard GPS were also carried out by the TU Delft team (Vlugt et al. (2013)), but the kinematic of the kite was problematic for the GPS device, leading to satellite signal loss. Lansdorp et al. (2007) also measure tether angle a tethers attachment point but thanks to 3 load cells mounted on three different axes. with this method, the force generated by the kite is also known. Another way to measure the force of the kite is to add a simple load cell between tethers and attachment point (Dadd (2012); Breukels and Ockels (2008)), or to measure the force after a pulley (Fagiano and Marks (2015)).

A relevant information for research works on fluid structure interaction is the flying shape of the kite. When a sufficient large wind tunnel is available, flying shape of the kite can be measured in such facilities, with laser sensors or with several cameras, as it is done by de Wachter (2008). Indeed with many pictures of the same object under several axis taken at the same time at known location, it is possible to rebuilt the 3D shape with a good accuracy. This process is called photogrammetry, and a good introduction is given by Luhmann (2010). If such a method is really feasible with laboratory facilities like wind tunnels, it becomes much more complicated to carry out this type of measurement during outside trials. This work was however carried out by Deparday et al. (2016) in the case of a sport-boat for measuring flying shape of spinnakers. In the case of kite flying in dynamic mode, an interesting study were carried out by the Australian Maritime College, University of Tasmania, by Infanzon (2013), with three GoPro cameras. Here the problem is slightly different because, the interesting object (the kite) is small in comparison with the area it can range, and cameras are consequently located on the ground and then far from the kite. For that reason, the resolution of the part of the picture showing the kite is poor, and the induced accuracy of the 3D reconstruction is low. However, with better camera, and by targeting a reduced part of the flight domain and with adapted lenses, better results could be expected.

As every airborne energy, wind is the cornerstone of the concept, and wind measurement is essential. In the various experimental set ups operated by kite research groups, several possibilities exist. At first an isolated point of measurement is located near the ground station. The sensor can be an ultrasonic one or a cup anemometer. The EnerKite team has also used LIDAR remote sensing to obtain high altitude wind magnitude and orientation (Bormann et al. (2013)) . Teams with control architecture made of a control pod under the kite embedded on the pod an anemometer: a classic impeller anemometer for SkySails (Erhard and Strauch (2013b)) and a pitot tube for TU Delft team (Vlugt et al. (2013))

1.3. Main Scientific Issues

As many other industrial development of new products, money is the crux. Therefore, to market kites as auxiliary propulsion devices at a large scale, only one point needs to be achieve: kites have to be profitable for ship owners. In this context, all research actions of this project must participate in the demonstration of the economic viability of the kite concept, and each suitable solution considered needs to be carefully analyzed regarding the associated production or operative costs.

To convince ship owner of the economic viability of kites, some figures about associated savings must be provided, and solid scientific studies have to support these figures. The estimation of the savings provided by kites is based on various elements listed below:

1. Average power generated by kites
2. Impact of kites on operations (how kites impact maneuverability, seakeeping, safety)
3. Impact of kites on engines (conversion from kite power to fuel savings)
4. Fuel prices (depending on regulations of allowed fuel type - heavy or refined)
5. Operating life of kites, tethers, control system

Points 1. and 3. have already been partially investigated during the Ph. D. study of Leloup (2014), and showed for example a possible saving up to 26% of fuel consumption for a favorable maritime route (North Atlantic, west to east), for a 232-meter vessel with a 320-square-meter kite. In this study kite power was calculated with a kite modeling based on a zero-mass approach, and detailed in the following subsection. Thereafter, a complementary tool was developed by Podeur et al. (2016), to estimated savings of kites operated on various maritime routes and based on a statistical approach using worldwide weather databases over the last 30 years. Points 4. is totally independent of the project. Point 2. and 5. are partially investigated by the two other Ph. D. studies running at ENSTA Bretagne, and by the industrial partners of the consortium. However, getting an overview of deterioration of kites and tethers over the time is not an easy task, as new materials are specially developed, requiring new studies to be started.

Nevertheless, if a global and complete estimation of savings is not possible so far, some basic calculations can be done, as for example:

- If a kite can save 5% of fuel per year for a all routes (assuming the kite can intermittently produce far more savings, because some parts of the routes will be necessarily upwind routes with no possible saving)

- For a vessel consuming 150 metric tons of fuel per day at sea (that seems to be a classic value for the largest container ships)

- For 240 days of navigation per year (in the case of the Europe-Asia-Europe maritime loop, completed in 77 days, with 12 stopovers, leading to approximately 50 days at sea for a full loop)

- For a fuel price of $300 per metric ton, as it is in 2017

With these estimations, a kite system can then generate $540k per year. At first, the amortization part of the installation of kite control system have to be subtracted from this result. This part can be taken equal to $100k per year, which accounts for a kite control system costing $1M and a payback period of 10 years. Secondly, the minimum savings expected by ship owners have also to be withdrawn from the global kite savings. It seems that this part is about 2% of the fuel cost of the vessel, meaning $216k. That leaves $224k per year for consumables as kite and tethers. In other words, with the earlier assumptions, the price of a kite and tethers must not exceed $224k, if they need to be replaced only once a year, or $112k if they need to be replaced twice a year. These numbers give some overview and allow to point out the main elements affecting the economic viability of the project. However this example does not take account any additional costs, as crew training, insurances, certifications...

1.3.1. Kite Modeling

Kite flight modeling is an important element for predicting the power generated by the kite and transmitted to the ship. Various models were developed by different kite research groups. On the present case, the model in use for the fuel saving prediction tool is the zero-mass model, initially proposed by Wellicome and Wilkinson (1984), and also used by Dadd (2012), but rewritten by Leloup (2014) improving the calculation of the kite velocity, without iterative process. Therefore, the following equations are directly stemmed from Leloup et al. (2016), but only main results are presented here. This model considers the kite as a single point without any mass. Thus, no inertial forces (resulting from the product of acceleration with mass) are taken into account, assuming they are negligible in comparison with aerodynamic forces generated by the kite.

1.3.1.1. Dynamic Flight Force Prediction

One of the main element for calculating kite power is the relative wind at kite altitude $\underline{V}_{WR}$. The estimation of this value will be discussed later. After that, with the zero-mass assumptions, apparent wind seen by the kite can be calculated as follows:

$$V_a = \frac{V_{WR}\cos(\phi_{WR})\cos(\theta_{WR})}{\sin(\epsilon)} \tag{1.1}$$

Knowing the apparent wind, the aerodynamic force generated by the kite can be immediately written as:

$$F_a = \frac{1}{2}\frac{C_l \rho A_k V_a^2}{\cos(\epsilon)} \tag{1.2}$$

The lift to drag angle ϵ and the kite lift coefficient C_l are the parameters characterizing the kite performances,ρ is the density of the air and A_k is the area of the kite. In the current model, tethers are assumed to be straight with constant lengths, therefore the aerodynamic force is along the kite position vector, as defined in the Kite Positioning section (p. xix). With the hypothesis of a constant relative wind, the aerodynamic force reaches a peak when the apparent wind is maximum, and this happens when ϕ_{WR} and θ_{WR} are equal to 0. This corresponds to a kite position vector and relative wind vector being collinear, and this point is so-called maximum power point, and denoted P.

Knowing the apparent wind, the kite velocity can also be computed. Indeed, the kite velocity vector is equal to:

$$\underline{V}_k = \underline{V}_{WR} - \underline{V}_a \tag{1.3}$$

The relative wind vector is perfectly known or at least estimated. The apparent wind vector direction is unknown, but the value has already been calculated. Therefore, Eq. 1.3 is not sufficient to get the kite velocity vector. However, the direction of the kite velocity vector is known because it is given by the trajectory of the kite, and the later is an input of the zero-mass model. Thus, Eq. 1.3 allows to find simultaneously the apparent wind vector orientation and the kite velocity vector magnitude. With the kite velocity known along the given trajectory, it becomes possible to calculate the time required by the kite to go through the whole trajectory. At that time, the total average force generated by the kite along the trajectory can also be calculated by using a temporal integration of the instantaneous force along the trajectory.

Forces generated by the kite can be then projected into ship axis system to get the propulsive force, the side force and the vertical force. The propulsive force will then be taken into account by the propulsion computations to get an estimation of fuel savings related to the given trajectory. The side force needs to be analyzed to measure the impact on ship course, and this could also affect the propulsion part. For example a large side force can lead to a significant rudder angle increasing the hydrodynamic drag of the hull, and consequently affecting the possible fuel savings. The vertical forces can be generally neglected in comparison to the ship weight.

1.3.1.2. Static Flight Case

In the case of static flight, the kite has no velocity in the wind relative reference frame. Thus, the apparent wind on kite equals the relative wind. Introducing this in Eq. 1.2 leads to a new equation ruling the possible positions of the kite in static flight mode:

$$\cos(\phi_{WR})\cos(\theta_{WR}) = \sin(\epsilon) \tag{1.4}$$

The force of the kite flying in static mode is easy to compute because, for a given position, this force is constant over time. The value is given by Eq. 1.2, replacing V_a by V_{WR}.

1.3.1.3. Dynamic Flight Trajectory Definition

With perfectly straight tethers with constant lengths, the kite can only fly on a sphere centered on tethers attachment point. In the case of a kite flying over the sea or over the ground, the available flying area becomes approximately a half-sphere. Moreover, the kite is flying thanks to the relative wind, therefore it can only reach the part of the half sphere located downwind of the attachment point. Finally the kite can fly only on an area being approximately a quarter sphere, and named wind window. The bottom limit is the sea, and the zero-mass model provides a definition of the limit of the flying area towards the wind direction. This limit is named wind window edge, and is formed by all the positions of the kite where it can only fly in static mode. This limit is then also defined with Eq. 1.4.

Every trajectory being contained in the wind window can be used with the zero-mass model, however some operational constraints require trajectories with particularities. Indeed, most of the kite control systems (multiple tethers or control pod) can not support multiple rotations in the same direction along the tethers axis, which will lead to several twists between tethers that might block the steering. Therefore, circle trajectories or equivalent can not be repeated, and then the most common trajectory has the shape of an eight, and is so called eight-pattern trajectory.

Two mathematical definitions of this type of trajectory were given by Wellicome and Wilkinson (1984) and Argatov et al. (2009), based on parts of circle for the first one and on a trigonometric parametric function for the second one. In this model the definition proposed by Argatov is considered. At first trajectory size is fixed, with an angular parameter, considering that the trajectory size is proportional to the tether length. The original orientation of the trajectory is horizontal. Then the trajectory is positioned in the wind window, by defining the position of the center and the rotation of the trajectory around the tether axis. As shown in Fig. 1.2, when the rotation angle equals 0, the trajectory is horizontal. In this case, the kite is going upward when it is on the external part of the 8-pattern, and is getting away from the maximum power point of the wind window. This type of trajectory is named up-loop. When the rotation angle equals 90°, the trajectory is vertical. When the rotation angle equals 180°, the trajectory is again horizontal but this time the kite is getting closer to point P at the external part of the 8-pattern. This trajectory is then named down-loop. As shown with Eq.1.1 and 1.2, instantaneous kite force predicted by the zero-mass model depends solely on kite position, and not on kite course. So instantaneous force in up-loop case and down-loop case are identical. However the kite velocity depends on kite course, and then the duration of the pattern is slightly different in the both cases, with a down-loop trajectory a bit faster. This leads to small differences when computing the time integration to get the average force on a trajectory. These differences for the average force on a trajectory are in the range of 1%. In real situation, when a kite is doing down-loops, it is also helped by gravity in its motion in external part of the pattern. According to kite-surfers, in this situation the kite can turn faster, and the average force generated by the kite is then higher than for the up-loop case. Obviously, this phenomenon can not be seen with the zero-mass model.

1.3.1.4. Dynamic Flight Optimization

To feed a realistic fuel saving prediction tool, the force generated by the kite need to be optimized. This problem is large and ruled by numerous elements, which can be sorted in three categories: the fixed parameters, the optimization variables and the objective variable(s). In the study of Leloup (2014), fixed parameters are the ship course, the ship

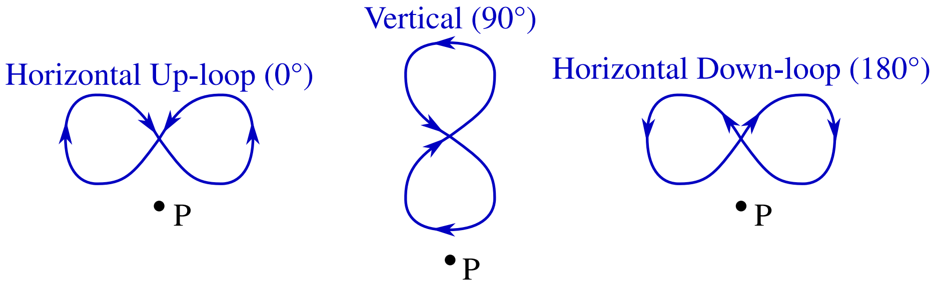

Figure 1.2.: The different possible orientations of the eight-pattern trajectories and the associated names. Arrows denote the running direction of the kite along the trajectories. The point P is the point of maximum power.

speed, the true wind magnitude and orientation in relation to ship axis, the kite size, the kite parameters, tether lengths and eight-pattern size. The optimization variables are the position of the center of the eight-pattern trajectory and its orientation. The objective function is to maximize the propulsive force generated by the ship, in other words to maximize the projection of the kite force on the longitudinal ship axis.

A noteworthy element is that the trajectory size is not optimized, and the perfect eight-pattern with arbitrary size has no reason to be the best solution. Therefore, better result should be expected with changing trajectory, but keeping the principle of “eight” with an equal number of turns done in both directions to avoid tangles in tethers. However, an optimization process on trajectory shape and trajectory size can not be carried out in the present case, because kite parameters (lift coefficient and lift to drag angle) are constant whatever the kite position and the turn rate. Consequently, the optimization will result in very small trajectories as close as possible of the maximum power point P. In real situation, turns with too small radius of curvature are difficult to achieve and require large steering command leading to large deformation of the kite and then probably a loss of aerodynamic performances. One of the objectives of this study will be then to estimate the loss of performances depending on turn rate.

1.3.1.5. Straight Tethers Assumptions

The whole zero-mass model assumes that tethers are perfectly straight all the time, consequently the kite can only fly on a surface (the wind window quarter of sphere). Without this assumption the flight domain of the kite becomes a volume, and the problem is far more complex. Indeed tether deformations need to be calculated for each position, but these deformations depend on the tension generated by the kite, and also on the kite velocity affecting the aerodynamic load on the tethers. Hence, the resolution of the zero-mass model is no longer direct but implies an iterative process.

To estimate the effect of tether deformations, a three dimensional analytical model of tether deformation was developed at ENSTA Bretagne in the scope of the kite-ship interaction Ph. D. study, and it is presented in the third chapter of the 2017 edition of the Airborne Wind Energy book (Bigi et al. (2017)). This study takes into account gravity and aerodynamic loads on tethers. In the case of static flight, it shows that the impact of the straight tether assumption is under 10% of the predicted propulsive force generated by the kite, with a relative wind speed of 5 m/s. At higher wind speed (above 16 m/s), the value even drops below 2%. Consequently, in the case of dynamic flight, with an apparent wind on kite above 20 m/s, the assumptions of straight tethers is acceptable.

1.3.2. Wind at the Altitude of the Kite

1.3.2.1. General Case

The true wind speed is the wind velocity with respect to the Earth. For convenience, the true wind velocity vector can be expressed in polar coordinates, the magnitude of the vector is then named the True Wind Speed (TWS), and the angle between the ship axis and the opposite of the wind vector is named the True Wind Angle (TWA), and is denoted β_{WT}. More precisely, to compute the true wind angle, the vertical component of the true wind is neglected, and the ship axis is taken equal to the x-axis of the heading reference frame. Therefore, the true wind angle computation is done in the horizontal plane:

$$\beta_{WT} = \mathrm{atan2}\left(-V^{(\psi)}_{WT,2}, -V^{(\psi)}_{WT,1}\right) \tag{1.5}$$

Sometimes the the True Wind Direction (TWD) needs to be investigated. It is the angle between the projection of the wind in the horizontal plane and the x-axis of the NED reference frame, and it is denoted β_{WD}. The true wind direction can be calculated following two methods:

$$\beta_{WD} = \mathrm{atan2}\left(-V^{(ned)}_{WT,2}, -V^{(ned)}_{WT,1}\right) = \beta_{WT} + \psi \tag{1.6}$$

In the general case of a kite deployed over a moving ship, the apparent wind vector seen by the kite is equal to the sum of the true wind speed at kite altitude and the wind induced by the kite velocity, or in other word, the velocity of the point K, with respect to the Earth:

$$\underline{V}_a = \underline{V}_{WT} - \underline{V}_{K|R_{ned}} \tag{1.7}$$

This velocity of K with respect to the Earth is given by:

$$\underline{V}_{K|R_{ned}} = \underline{V}_{O|R_{ned}} + \underline{\Omega}_{R_s/R_{ned}} \wedge \underline{OA} + \frac{d\underline{AK}}{dt}_{|R_{\psi}} + \underline{\Omega}_{R_{\psi}/R_{ned}} \wedge \underline{AK} \tag{1.8}$$

From there, and to be consistent with previous work as the one introduced before, the kite velocity vector $\underline{V}_k$ is defined as the velocity of the point K, with respect to the heading reference frame, and the ship velocity vector $\underline{V}_s$ is defined as the velocity of the point O, with respect to the Earth reference frame

$$\underline{V}_k = \frac{d\underline{AK}}{dt}_{|R_\psi} = \underline{V}_{K|R_\psi} = \tag{1.9}$$

$$\underline{V}_s = \underline{V}_{O|R_{ned}} \tag{1.10}$$

Moreover, following notations are used:

$$\underline{\Omega}_s = \underline{\Omega}_{R_s/R_{ned}} \tag{1.11}$$

$$\underline{\Omega}_\psi = \underline{\Omega}_{R_\psi/R_{ned}} \tag{1.12}$$

Therefore, it is also possible to write the velocity of the kite attachment point A as as the sum of the velocity of the ship and the velocity vector induced by ship motions:

$$\underline{V}_{A|R_{ned}} = \underline{V}_s + \underline{\Omega}_s \wedge \underline{OA} \tag{1.13}$$

Finally, combining the previous equations:

$$\underline{V}_a = \underline{V}_{WT} - \underline{V}_s - \underline{\Omega}_s \wedge \underline{OA} - \underline{V}_k - \underline{\Omega}_\psi \wedge \underline{AK} \tag{1.14}$$

The first three elements constitute the relative wind at kite altitude $\underline{V}_{WR}$, and this constitutes the wind triangle as presented in Fig. 1.3.

$$\underline{V}_{WR} = \underline{V}_{WT} - \underline{V}_s - \underline{\Omega}_s \wedge \underline{OA} \tag{1.15}$$

$$\underline{V}_a = \underline{V}_{WR} - \underline{V}_k - \underline{\Omega}_\psi \wedge \underline{AK} \tag{1.16}$$

Depending on situation, ship velocity and ship motions could be neglected or equal to 0 (in particular in the case of onshore experiments with no displacement of the ground station). For example, in a case of a ship with a constant heading (which is the case considered by Leloup (2014)), $\underline{\Omega}_\psi = \underline{0}$, and this is consistent with the Eq. 1.3.

The kite velocity with respect to the heading reference frame and the ship velocity with respect to the Earth can be measured with acceptable accuracy as shown in Chap. 2. On

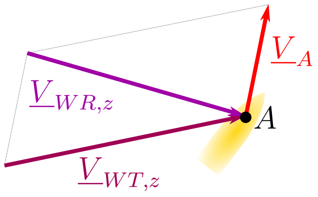

Figure 1.3.: Calculation of the relative wind vector from the true wind vector and the velocity vector of the attachment point. The plane of the figure has no reason to be perfectly horizontal.

the contrary, get an estimation of the true wind speed and the true wind direction at kite altitude is a far more complex task, especially with a kite that can fly between altitudes of 10 to 80 m in the case of the present study.

1.3.2.2. True Wind Velocity Estimation

The measurement of the wind at a given point can be achieved using anemometers. However the measurement of the true wind at any point of a given volume is more complicated because, in this case, anemometers can not be used. Indeed, the replication of many measurement units with their fixation system will completely disturb the wind flow. Two solutions are then possible: extrapolate 3D wind field from some fixed measurement points, or use other technology based on sonic or light principles. Both approaches were carried out in this study, therefore some background elements are given in the following paragraphs.

For wind extrapolation, several cases should be differentiated: horizontal extrapolation, vertical extrapolation and time interpolation. For flow above a uniform surface as sea water, horizontal wind variations can be neglected in first approximation. On the contrary, vertical variations must be taken into account. These variations are due to the roughness of the sea surface, creating a boundary layer above the surface. This layer is called Marine Atmospheric Boundary Layer (MABL). If some models give a good estimation of the flow in the layer of fluid near a wall, the atmospheric boundary layer is more complex for two reasons. At first, the surface roughness depends on sea state, that depends on wind speed and many other parameters (as air temperature, sea temperature, sea currents, clouds...Stull (1988)). Therefore, a coupled resolution atmosphere-ocean needs to be achieved, to get a sensible estimation of wind gradient in the MABL. Secondly, the earth rotation, and more precisely the Coriolis effect, impacts the upper part of the MABL (called Ekman Layer), leading to a twist of the flow along the vertical direction. Because the Coriolis effect varies depending on latitude, the twist of the flow is not the same everywhere on the earth. Therefore, no simple formula gives an estimation of the twist of the flow. If such information could be really important in kite flight optimization for larger unit with tether length over 100 m, it seems reasonable to neglect it in the case of the current study with tether lengths under 80 m. Indeed, the height of the beginning of the Ekman layer where twist flow occurs seems to be above 100 m Stull (1988)). For wind magnitude evolution along altitude, the International Towing Tank Conference ITTC (2014) provides a statistical formula based on previous works like the one carried out by Peterson and Hennessey (1978):

$$\underline{V}_{WT,z} = \left(\frac{z}{z_0}\right)^{1/7} \underline{V}_{WT,z_0} s \tag{1.17}$$

z_0 is the altitude of the wind measurement, and z is the altitude of the point where the wind needs to be estimated. Such a power law seems to give good results for general use, but for instantaneous estimation, its relevance is very questionable, and other laws (as logarithmic law) or other values for the exponent of the power law can be found depending on measurements site (Hadi (2015); Masters (2004)). Moreover, hourly, daily or seasonal effects can distort the vertical profile and modify the MABL height (Arche (2013)). However, when no other solution is available, this formula will be used, as it was done by Leloup (2014).

Time interpolation of wind can be done when several sensors are spread over a measurement field. Thus, variation in time of the wind, like the arrival of a gust, are measured at different time by sensors. It becomes then possible to interpolate during post processing to get an estimation of the wind field in the area located between the sensors.

Another way to deal with wind estimation at a given moving point is to use remote measurements. In the case of wind, this is possible with one of the two following systems: LIDAR devices (Light Detection And Ranging) or SODAR devices (Sound Detection And Ranging). Both of them emit waves (electromagnetic or sound), and receive a reflected part of the original signal. The Doppler frequency shift of the received signal is then used to deduce wind speed. With several axis of emission it becomes possible to rebuilt the 3 components of the wind, at the height of the measurement point.

1.3.3. Acceleration of the Kite

When using the zero-mass model, the acceleration of the kite does not need to be regarded, because forces do not depend on acceleration. However, it is possible to consider the point-mass model, where the entire mass of the kite is concentrated on a single point. Therefore, the acceleration of the kite affects the force generated by the kite, and it has to be calculated. This computation needs to be made with respect to an inertial reference frame. However a ship can not be considered as an inertial frame, excepted if she has a constant speed with no motion. Therefore, the acceleration of the point K which denotes the kite needs to be computed with respect to the Earth (denoted $\underline{\Gamma}_{K|R_{ned}}$). This is done by taking into account additional elements:

$$
\begin{aligned}
\underline{\Gamma}_{K|R_{ned}} &= \underline{\Gamma}_{K|R_\psi} \\
&\quad + \underline{\Gamma}_{A|R_{ned}} + \frac{d\underline{\Omega}_{R_\psi/R_{ned}}}{dt} \wedge \underline{AK} + \underline{\Omega}_{R_\psi/R_{ned}} \wedge (\underline{\Omega}_{R_\psi/R_{ned}} \wedge \underline{AK}) \\
&\quad + 2\underline{\Omega}_{R_\psi/R_{ned}} \wedge \underline{V}_{K|R_\psi}
\end{aligned}
\tag{1.18}
$$

$$
\begin{aligned}
\underline{\Gamma}_{A|R_{ned}} &= \underline{\Gamma}_{O|R_{ned}} \\
&\quad + \frac{d\underline{\Omega}_{R_s/R_{ned}}}{dt} \wedge \underline{OA} + \underline{\Omega}_{R_s/R_{ned}} \wedge (\underline{\Omega}_{R_s/R_{ned}} \wedge \underline{OA})
\end{aligned}
\tag{1.19}
$$

The kite acceleration vector $\underline{\Gamma}_k$ is defined with respect to the heading reference frame:

$$
\underline{\Gamma}_k = \underline{\Gamma}_{K|R_\psi} = \frac{d\underline{V}_k}{dt}_{|R_\psi} = \frac{d^2\underline{AK}}{dt^2}_{|R_\psi}
\tag{1.20}
$$

The ship acceleration vector $\underline{\Gamma}_s$ is defined at point O with respect to the NED reference frame:

$$
\underline{\Gamma}_s = \underline{\Gamma}_{O|R_{ned}} = \frac{d\underline{V}_s}{dt}_{|R_{ned}}
\tag{1.21}
$$

Moreover the following notations are used:

$$
\dot{\underline{\Omega}}_\psi = \frac{d\underline{\Omega}_\psi}{dt}
\tag{1.22}
$$

$$
\dot{\underline{\Omega}}_s = \frac{d\underline{\Omega}_s}{dt}
\tag{1.23}
$$

From there and with using the previous definition of $\underline{V}_k$, the final expression of the acceleration of the kite with respect to the Earth is:

$$
\begin{aligned}
\underline{\Gamma}_{K|R_{ned}} &= \underline{\Gamma}_k \\
&\quad + \underline{\Gamma}_s + \dot{\underline{\Omega}}_s \wedge \underline{OA} + \underline{\Omega}_s \wedge (\underline{\Omega}_s \wedge \underline{OA}) \\
&\quad + \dot{\underline{\Omega}}_\psi \wedge \underline{AK} + \underline{\Omega}_\psi \wedge (\underline{\Omega}_\psi \wedge \underline{AK}) \\
&\quad + 2\underline{\Omega}_\psi \wedge \underline{V}_k
\end{aligned}
\tag{1.24}
$$

1.4. Structure of the Thesis

The present document is organized around five main chapters, which can be sorted into two parts. The first one is very a technical one and provides details of the experimental set-up. The second part deals with the experimental fieldwork, and presents for each one the trials conduct, the post processing strategy and the results.

In Chap. 2, the last version of the hardware part of the experimental set-up is presented, and Chap. 3 deals with the software part of the set up involving in data acquisition and kite automatic control. It is the result of many improvements coming from the feedback of the fieldwork carried all along this study. Therefore the presented system is far more complex from the initial one, but also far more complete. The first experimental works could be then repeated with the final set-up. These two chapters are deliberately technical to provide to the reader a single document with a detailed overview of the system and enough information for future research works to execute the system.

The three other chapters focus on fieldwork:

- Chapter 4 presents the fieldwork carried out in Gaspésie, province of Quebec, Canada, on board a 13-meter-long trawler.
- Chapter 5 focuses on kite specs assessment from onshore trials.
- Chapter 6 deals with the sea trials conducted on the kiteboat, the experimental platform specially designed for kite experiments at sea.

The presentation of these experimental work follows the chronological order of achievement. Indeed, each experimental campaign has led to some feedback, which has been taken into account for the next campaign.

Except the design of the kiteboat, the entire experimental set-up presented in this document was developed by the author, as a part of his Ph. D. study. That means various steps going from drawings of the system, component selection and purchase, mechanical assembly, sensor installation, wiring of electrical components, wiring of sensors, sea water protection, programming of data and control acquisition system, test phases...

2. Experimental Set Up

Résumé

Ce chapitre a pour but de présenter en détail le système expérimental utilisé durant cette étude. Ce système a bien sur évolué au cours des travaux, et c'est donc la version la plus aboutie qui est exposée ici.

Ce système est composé de trois éléments principaux visible Fig. 2.1. Premièrement, un bâti principal contient les actionneurs du kite ainsi que les capteurs directement associés au kite. C'est l'élément d'interface avec le kite. Ce bâti est connecté à une première valise étanche, contenant le système d'acquisition des données et de contrôle du kite, système qui est détaillé dans le chapitre suivant. Ce dispositif est alimenté par une batterie dédiée. Enfin, une seconde valise étanche contient les batteries chargées d'alimenter les actionneurs. Ceux-ci fonctionnent en 24 V, et les capacités des batteries permettent une autonomie d'une journée complète.

Les éléments permettant de contrôler le kite sont deux motoréducteurs d'une puissance de 800 W chacun. Ils sont reliés à des tambours permettant l'enroulement des lignes arrières, comme montré sur le schéma de la Fig. 2.4. Par ailleurs des codeurs incrémentaux optiques permettent d'envoyer au système de contrôle du kite un retour d'information de la position des moteurs. Les moteurs permettent de générer une différence de longueur des lignes arrières, avec une vitesse maximale de 1.4 m/s. Par ailleurs un système de contrôle, basé principalement sur deux joysticks, permet de contrôler les moteurs manuellement.

Les capteurs associés au kite sont principalement des cellules de force à jauges de déformation, chargées de mesurer l'effort généré par le kite. Une cellule d'effort 1D est affectée à la mesure de chaque ligne arrière, par l'intermédiaire d'un circuit de poulie autorisant ainsi l'enroulement des lignes (Fig. 2.9). Une troisième cellule de force permet de mesurer la tension dans les lignes avants, mais aussi l'orientation de celles-ci. (Fig. 2.6). En effet cette cellule est tridimensionnelle, et mesure donc l'effort suivant trois axes. Avec, une hypothèse de lignes parfaitement droites et indéformables, il devient possible d'estimer la position du kite. C'est cette solution qui a été retenue pour l'ensemble de cette étude pour mesurer la position du kite dans sa fenêtre de vol. Ce capteur est donc l'un des plus importants de toute cette étude. Les données de calibrations fournies par le constructeur ont été utilisées, mais une vérification de la validité de celle-ci a été menée en laboratoire.

Par ailleurs, des capteurs étaient spécifiques à chacune des campagnes de mesures effectuées, en particulier en ce qui concerne la mesure du vent ou la mesure des mouvements de plateforme dans le cadre d'essais en mer. Ainsi lors des essais réalisés sur le chalutier québécois, et présenté Chap. 4, le bateau était équipé d'une centrale inertielle, de capteurs en chambre des machines (couple sur l'arbre d'hélice et vitesse de rotation de celui-ci, et débitmètre sur l'arrivée du carburant), d'un capteur d'angle de barre et d'un anémomètre ultrasonique. L'équipement du kiteboat utilisé lors des essais présentés au Chap. 6, est relativement similaire, avec centrale inertielle et capteur d'angle de barre, et un dispositif plus conséquent pour mesurer le vent, avec cette fois 3 anémomètres ultrasoniques. Aucune instrumentation du moteur n'a été effectuée, puisque celui-ci n'était volontairement pas en fonctionnement pendant les essais.

La mesure du vent à l'altitude du kite est un élément crucial pour l'estimation des performances de celui-ci. De ce fait, une attention particulière a été apportée à ce sujet, et des dispositifs complémentaires de mesure du vent sont venus s'ajouter aux systèmes déjà introduits. Pour la campagne de mesures à terre du Chap. 5, un profileur vertical de type SODAR (voir Fig. 2.13(a)) a été utilisé, permettant de remonter au champ de vent dans les 3 dimensions dans la couche d'aire au-dessus de l'instrument. Pour la campagne de mesure associée au kiteboat, des points fixes de mesure du vent étaient repartis dans la zone de navigation. Ceux-ci étaient constitués d'anémomètre ultrasoniques, montés sur des mats installées sur des plateforme flottantes. Ces plateformes étaient à l'ancre dans la baie (voir Fig. 2.15).

2.1. Acquisition Hardware

The whole data acquisition and control system is based on a National Instruments (NI) compactRIO platform. It consists of 3 main parts: a set of I/O modules (NI C-series modules) depending on sensor technology and plugged on a 8-slot-chassis, a Field-Programmable Gate Array (FPGA, NI CRIO-9114) and a Real-Time processor (NI CRIO-9024). All I/O modules are connected to the FPGA, and the very accurate clock of the FPGA ensures a good synchronization between the channels, and precise acquisition frequencies. The Real-Time processor logs all data coming from sensors through the FPGA on a non-volatile memory. All acquisition and control programs have been developed with LabVIEW and will be presented in part. 3.1. Six I/O modules were used for the whole study and are presented in Tab. 2.1. The compactRIO was powered by its own 12V battery having a capacity of 42Ah, ensuring easily a full day of measurement. All the acquisition system was contained in a waterproof box.

Module	Description	Nbr of Channel	Example of Connected Devices
2 x NI 9870	Serial Ports	8	GPS devices, Anemometers, Power Card
1 x NI 9411	Digital Inputs	6	Encoders
2 x NI 9237	Bridge Analog Inputs	8	Load cells
1 x NI 9205	Analog Inputs	16	Kite Control Device (joystick...)

Table 2.1.: Description of the NI C-series I/O modules used during this study

2.2. Kite Control System

Before the beginning of this Ph. D. study, an experimental set up had already been developed by the beyond the sea company in Arcachon. For consistency reasons it was then decided to replicate this set up at ENSTA Bretagne and so a few components were bought, as the gear-motors and the encoder presented in part 2.2.2. Drawings of the set up were also provided, and had been used as a starting point to draw the frame where actuators and sensors have to take place. An update version of these drawings is given in App. 191. The diagram presented in Fig. 2.1 gives an overview of the set up.

2.2.1. Main Frame

The main frame of the set up has been designed to meet following expectations : contain the actuators, provide solid attachment points for the kite, be able to be deploy onshore

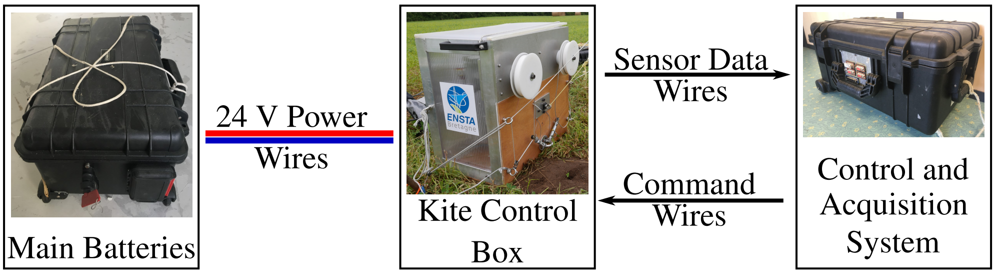

Figure 2.1.: Overview of the experimental set up.

or onboard and handheld by two people . These elements have led to a construction with aluminum plates and profiles welded and screwed. Wood or plastic plates enclose the system, especially for water protection. The 3D modeling using CATIA and a picture of the frame deployed onshore are given in Fig. 2.2.

The frame is 0.63 m large by 0.45 m long and 0.55 m high, and weights 60 kg. When deployed onshore, the frame is rigidly fixed to the ground by dyneema ropes attached to miner's bars driven deep into the ground (visible in Fig. 2.2). In this case, this system is named "Ground Station". When deployed onboard, the system is also fixed to the boat with dyneema ropes but this time attached to specifically designed attachment points on the boat (see Chap. 6).

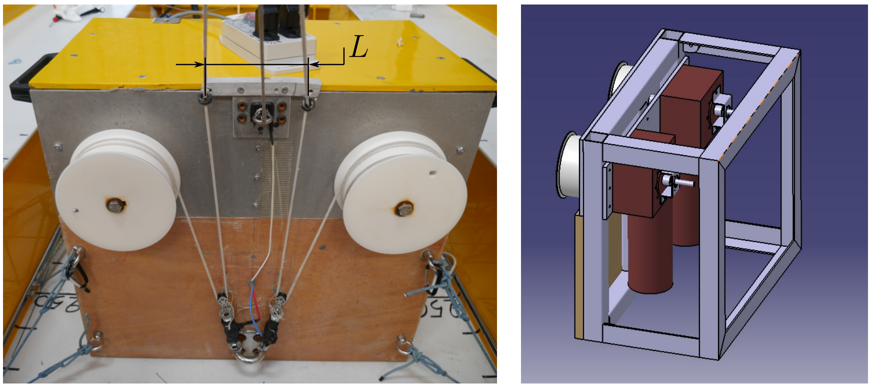

(a) (b)

Figure 2.2.: Picture and drawing of the main frame of the experimental set up. The distance L drawn in picture (a) is added to illustrate a specific point of Part 3.1.5

2.2.2. Actuators

The kite can be steered by applying a difference between the back tether lengths. For this purpose, each back tether is linked to a winch powered by a 800 W permanent magnets D.C. gear-motor. These gear motors are designed to provide a two-side output shaft, with one side suitable for encoders assembly. On the other side a 0.075 m radius winch drum is mounted, and the back tethers are attached on it. A picture of one gear motor with its encoder is given in Fig. 2.3. The initially maximum output speed of the gear-motor was 50 rpm, leading to a maximum winch speed of 0.4 m.s^{-1}. However this speed was too low to ensure an good control of the kite in manual mode. Thus, one stage of the gear reducer with a ratio of 3 has been taken out, leading to a new reducer with a ratio of 60, and an output speed of 90 rpm. Each tether can then be rolled in or rolled out at a maximum speed of 0.7 m.s^{-1}. For a given differential steering setpoint δ, one winch shall shift by a value $\delta/2$ and the other winch by a value of $-\delta/2$. The maximum differential speed is then 1.4 m.s^{-1}. The gear-motor manufacturer was Transtecno, and the product reference was ECMP600/063 U.

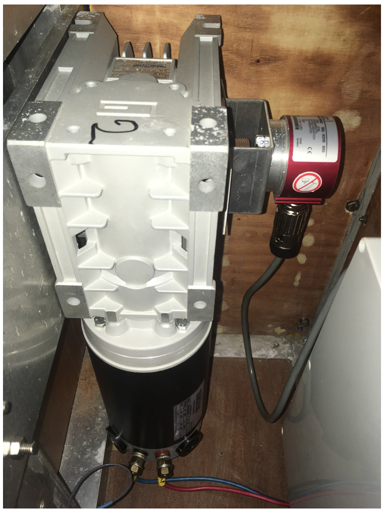

Figure 2.3.: Picture of one of the two gear-motors used for kite control, with the encoder measuring the actuator position (red device).

Optical encoders, with an accuracy of 4096 counts per revolution, are mounted on the encoder side of each gear-motors . These encoders are used to provide to the control system a feedback on winch positions. These encoders are no absolute ones, meaning that the initial position of the winches need to be given by the user at start up. Each encoder needs a 5 V power input, and outputs data position through two digital channels. Thus, they are connected to the digital input module of the compactRIO platform, in a differential mode. The manufacturer was TRelectronic, and the product reference was IEH58.

Gear-motors are powered with 24 V direct current provided by two 12 V lead acid batteries connected in series, with a capacity of 42 Ah. This capacity enables two full days of measurement. A two-channel power card interfaces the two gear-motors and the batteries to ensure the control of the actuators. This card is connected to the compactRIO platform through a serial link. This link also provided information about voltage of the batteries and the consumption of the gear-motors. The manufacturer was RoboteQ, and the product reference was MDC2250C. The two main batteries were contained in a second waterproof box same as the one used for acquisition system, and visible in Fig 2.1.

2.2.3. Tether System

As it has been described in Chap. 1, all experiments carried out during this study have been done using leading edge inflatable kites, with 4 tethers: 2 front ones with constant lengths, and two back ones with variable lengths for control purpose. On kite side the two front tethers are connected to the bridle system of the kite. On the other side, the two front tethers merge on the end of the front leader line, as drawn in Fig. 2.4, and this leader line is then attached to the ground station. Each back tether is attached on the kite side to the back bridle, and on the other end to a back leader line going through one or several pulleys. It is then connected to one of the two winches used for steering. Bridle lines are part of the kite, and were provided by the kite manufacturer. Main tethers are Dyneema SK78 1.5 mm². Leader lines (back and front) are also Dyneema but with a section of 3 mm².

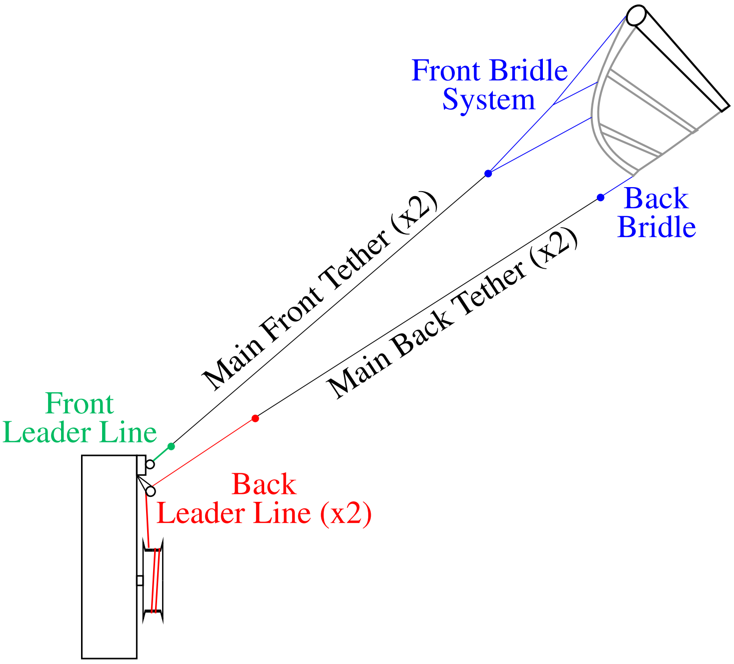

Figure 2.4.: 2D generic diagram of the tethers system. Only one of the two front tethers, and one of the two back tethers are shown. Drawing does not represent faithfully the real kite bridle arrangement.

2.2.4. Control Device

To control the actuators and then the kite, a remote device is used, and a picture is given in Fig. 2.5. Two one-axis joysticks are mounted on it, and also a mode selector. The various modes will be presented in part 3.1.5. The joysticks are linear potentiometers, with an input voltage of 5V and an output voltage between 0.5V and 4.5V. Each output lines are connected to an analog input channel of the NI 9205 module (Tab. 2.1). The mode selector is a combination of switches and resistors: when powered by a 5V voltage, the various position of the switches changed the global resistance, and then the output voltage. The output line is also linked to a channel of the NI 9205 module. A drawing of the circuit is given in App. B.

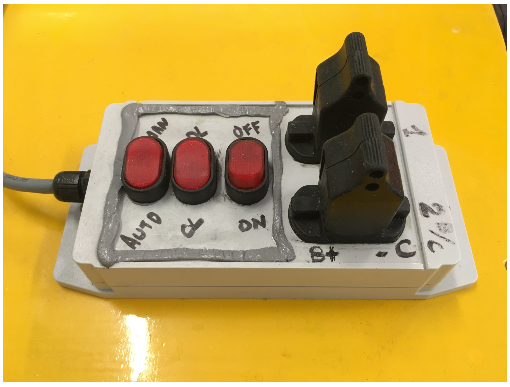

Figure 2.5.: Picture of the remote device used for kite control.

2.3. Kite Specific Sensors

Kite specific sensors are mainly based on load cells measuring forces in tethers.

2.3.1. 3D Load Cells

2.3.1.1. General Information

The measurement of the inensity anf the direction of the force generated by the kite is major element of this study. This can be achieved using 3D load cells. The selection of such a kind of product is oriented through three elements. The first one is that a load cell accuracy is given in accordance to the full scale output of the sensor, also called Rated Outputs (RO). For example with a full scale of 1000N and an accuracy of 1% of the full scale output, the accuracy is 10 N. If the load cell load is about 100 N (10% of RO), the accuracy is still 10N, but it represents 10% of the measured value. That means that a load cell should be used as close as possible of the full scale output. However, in our specific case of outside measurement in uncontrolled environmental conditions, it is not possible to ensure the load applied on the sensor to remain under the full scale output. Nevertheless, these sensors have a safe over load range. For the present case, a safe over load range as big as possible is required. The third element of the list is that the kite can pull on the load cell in all directions. In the case of the a three directional load cell, the scale output on the three axis of the load cell must be equal.

These elements led to only one manufacturer, Michigan Scientific, with the product TR3D-B. Two various ranges were bought, depending on the kite size, and so the expected force. This force has been estimated using the zero-mass model introduced in Chap. 1. The first one has a full scale range of 4Klbs (17800 N) and has been used for the experimental fieldwork on the Steven Paul. A second load cell has been bought for smaller kite, to be used during the onshore fieldwork or onboard the kiteboat, and has a range of 1Klbs (4450 N). The specification sheet is given in App. A, and pictures of these cells are given in Fig. 2.6. The front tethers leader line is attached to the load cell through a ringbolt screwed on the load cell. During the trial when the kite was flying in dynamic flight mode, it has been noticed that the kite succeeded in unscrewing the ringbolt. Then the axis of the screw was working in shear only, resulting in a breakage of the screw. To avoid the problem, a high class screw was employed with a lock washer, and a different rigging process of the leader line on the ring bolt was made to reduce as much as possible the loosening torque effect applied by the kite on the ringbolt.

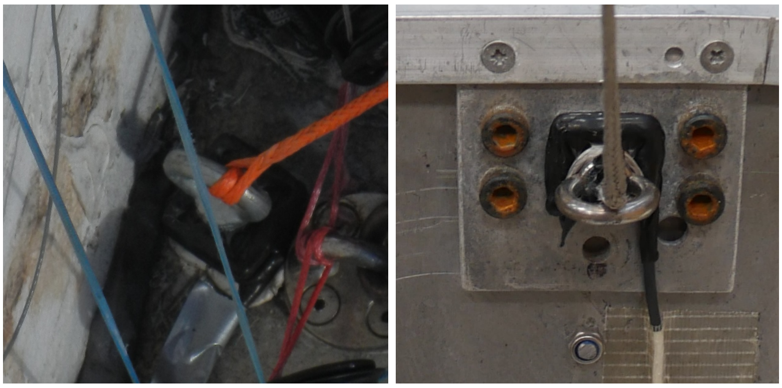
(a) (b)

Figure 2.6.: Pictures of the load cells used during this study. Picture (a) shows the mounting on the boat of the large one and picture (b) shows the small one mounted on the frame detailed Sec. 2.2.1.

Each three dimensional load cell can be seen as three one dimensional load cells, and so there are three channels to acquire. The three axis of a load cell are then linked to three bridge analog inputs of the NI 9237 modules. Each channel has its own sensitivity, and crosstalk effects between channel are limited according to calibration certificate provided by the manufacturer (under 1% of full load output). Sensitivities provided by manufacturer were used during measurement, but some checks have been carried out in laboratory (see Part 2.3.1.3). These load cells are made with a rugged construction, and no issue of waterproof failure was noticed. However during one trial, the plastic seal protecting the strain gauges were damaged by one of the two back tethers, and one of the gauge cable was broken. To ensure a good reparation, the load cell was sent back to manufacturer, and a new factory calibration has been done.

2.3.1.2. Mounting considerations

The measurement of fore done by the 3D load cell is always relatively to the load cell axes. However these load cell axes did not fit with the boat axes. Thus a calibration matrix needs to be applied on measurements to get values in the boat axis system.

In the case of the Steven Paul, the load cell is mounted on the fore deck. This one has a slope of +7° (measured with the IMU presented Part 2.4.1). The load cell is rotated due to mounting consideration by an angle of -67° between the X-axis of the load cell and the X-axis of the boat (measured with a picture of the system taken from the top).

Concerning the mounting case of the kiteboat, the axes of the boat and the axes of the load cell are identical, but permutations needs to be done between axes. Detail of this calibration can be seen in the calibration procedure subsection (Part 3.2.2).

2.3.1.3. Verification of the Sensitivities

The verification of the calibration of a 3D load cell is not an easy task without a device specifically designed. Therefore, all data coming from the 3D load cells are calibrated using the sensitivities provided by the manufacturer. However one of the three 3D load cells has been benchmarked with other load cells of the laboratory. Thus, another 3D balance based on piezoresistive technology has been used as reference. The system was fixed on a perfectly plane table able to withstand high loads. The force was applied thanks to a chain hoist. One side of the chain hoist was attached on the load cell, fitted with the same ringbolt which is used for trials, by means of Dyneema rope. The other side of the chain hoist was fixed at various locations in order to test the load cell in several directions, for example soliciting one channel only, or several. Each time, the orientation of the rope fixed on the ringbolt was measured in relation to the table. Therefore, the quality of the measure of the kite direction made by the load cell is also regarded. To benchmark the value of the magnitude of the force, another 1D load cell was added, as presented in Fig. 2.7.

Ten directions of the load have been tested, by changing the location of the attachment point of the chain hoist. For each direction, the load was increased gradually, with two or three stages, to exceed at least 3 000 N for one channel. Then, the unloading was done,

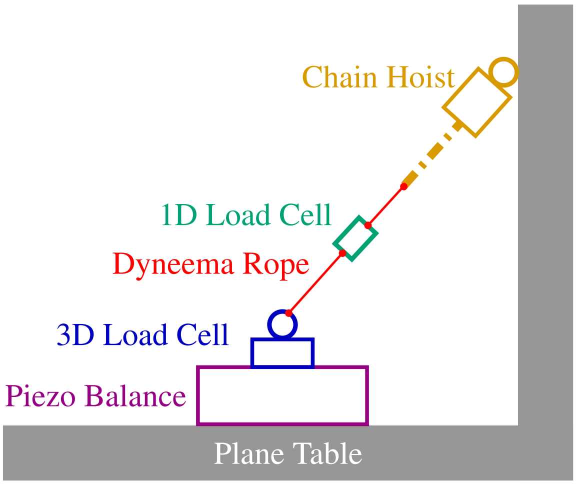

Figure 2.7.: Diagram of the set up used for benchmarking the 3D load cell. The diagram is only drawn in 2D, but measurements were 3D.

eventually with one intermediary stage, to finally go back to the zero load configuration. At each stage, a period of time with no load modification has been kept, to obtain a nearly stabilized load. All the test was recorded, and an overview of the evolution of the total load during one case is given in Fig. 2.7(a). The phases when the load was increased using the chain hoist are clearly visible, with the presence of spikes. The variation of the three different measured loads are in line, however the 3D load cell seems to overestimate the load, in comparison to the two other cells, which fit well together. The three other plots deal with the comparison of the load measurement, axis by axis (X, Y and Z), for the 3D load cell and the piezo balance. In these cases, only the phase with almost stabilized loads has been kept, and the transition periods have been removed from the analysis. Results show a good linearity, even if the return to zero after a cycle of loading is not perfect for the 3D load cell. However, these plots show sensitivities deviations, with a linear coefficient of the regression line close but not equal to 1. This makes sense with the differences in terms of total load observed in plot (a).

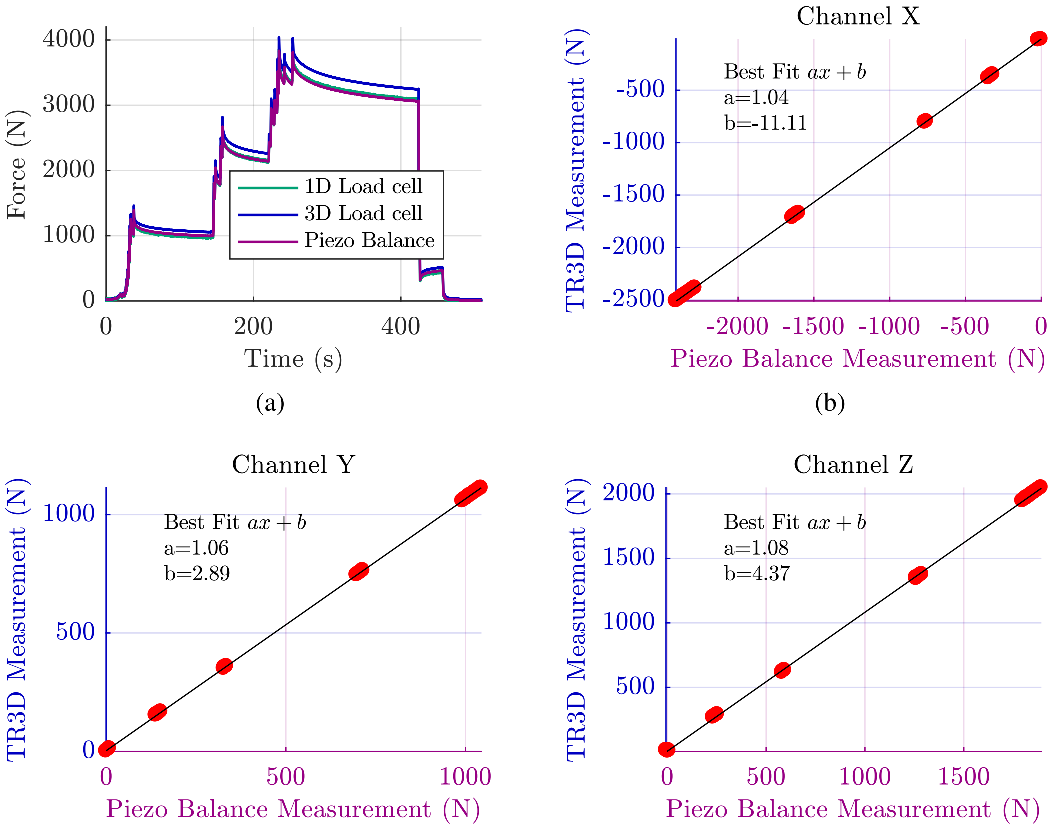

(a) (b)

(c) (d)

Figure 2.8.: Results of one of the load case applied on the set up used for benchmarking the 3D load cell (TR3D). Plot (a) shows the global load measured by the three load cells. Plots (b) to (c) shows the load of each channel, during almost stabilized phase, measured by the 3D load cell, with respect to the measurement achieved by the piezo balance.

2.3.2. 1D Load Cell

The 1D load cells that have been chosen for measuring force passing through back tethers are Futek LCM200. They were taken on because of their very light weight (17g without fixation system), with the idea to measure the force directly in the tether without interference effect on tether behaviors due to additional mass. However this solution appears to be complicated and potentially dangerous for the measurement cable. Then it was decided to measure forces after a return pulley. Various set-ups for return pulley have been tested, leading to various return angles, as shown in Fig. 2.9, where picture (a) shows a return angle α_R of 119° and case (b) a return angle α_R of 10°. These angles were all the time carefully measured to be able to retrieve the real load in tethers. This load is given by Eq. 2.1, where $F_{calibrated}$ is the load in the tether, $F_{measured}$ is the load measured by the load cell, and α_R is the return angle, as shown in Fig. 2.9.

$$F_{calibrated} = \frac{1}{2 * cos(\frac{\alpha_R}{2})} * F_{measured} \qquad (2.1)$$

Thus for the example of Fig. 2.9, calibration factors are respectively 1.01 and 0.51 for case (a) and (b). For the second one, a calibration factor of 0.51 means that the load cell measures nearly twice the load of the tether. The full scale range of the load cell needs to be chosen accordingly. Thus, three couple of load cells were bought, with three different full scale ranges: 250 lbs (1112 N), 500 lbs (2225 N) and 1000 lbs (4450 N). The load cell range is chosen accordingly to the kite and the return angle. Thus the Steven Paul fieldwork has been carried out using the biggest range, and the other works were done at first with the other ranges.

However during the trials carried out on the kiteboat, it has been noticed that these load cells were not enough protected from the sea water. Indeed after important sea water projection, data provided by the load cells became inaccurate with a very large shift of the zero values over time (shift in the order of the full scale range). After such a failure, it was possible sometimes to recover proper functioning of the load cell by drying it using electrical heating, but not all the time. In this later case, load cells were changed, but then the full scale range was not the most suitable. After noticing this problem, all load cells have been protected from sea water with a plastic seal, called Rotabomb. This product has been identified as being the best one for this purpose by previous works carried out at the laboratory.

The Futek LCM200 load cells have a non-linearity error and an hysteresis error under 0.5% of the full scale output, according to specification sheet (given in App. A).

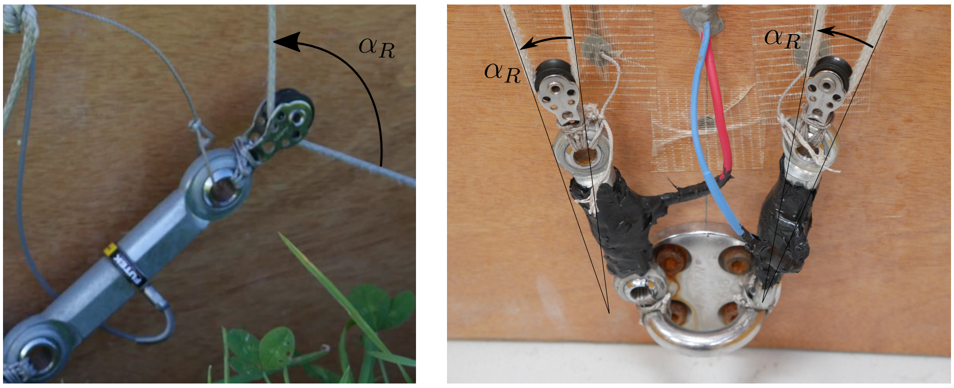

(a) (b)

Figure 2.9.: Pictures of the LCM load cells used for measuring force in back tether. Picture (a) was the onshore system, with no protection, whereas (b) is the onboard version, with plastic protective seal.

2.3.3. Embedded Inertial Measurement Unit (IMU)

In keeping with work started in Arcachon, it was tested to embed an IMU on the kite. The system was made up with a IMU PX4 based on MEMs technology, a battery and a Xbee radio transmitter. The idea was to retrieve the position of the kite with the hypothesis that the IMU is moving on the tangent plane of the sphere on which the kite is flying. However first trials did not give sensible results in comparison with the position measurement achieved by the 3D load cell. Moreover, embedded sensors on the kite connected through radio transmitter is complicated from an operational point of view, and devices can be easily destroyed in the unfortunate event of a kite crash. Thus, two systems were fully damaged during trials. For this reason, this approach has been given up. However, this approach could be a good way to obtain the yaw angle of the kite, independently from the kite velocity and then to retrieve the drift angle of the kite. Further developments to get an easy implemented system are nevertheless required, with analyses of MEMs sensor abilities in the specific case of a kite under dynamic flight.

2.4. Fishing Boat Specific Sensors

In addition to load cells which have been presented previously, other sensors are on the fishing boat Steven Paul. Some of them are onboard all the time, and others have been mounted specifically for the kite experimental fieldwork.

2.4.1. IMU GPS

To measure motions and velocities of the boat, an IMU coupled with a GPS is set up (Xsens MTi-G-700). This unit includes a microprocessor able to realize data fusion, based on an extended Kalman filter providing roll and pitch information. Manufacturer ensures dynamic errors for roll and pitch under 1° with a 1σ RMS error of 0.1°. The acquisition frequencies of the Xsens are 50 Hz for inertial sensors (gyroscope and accelerometer), 20 Hz for roll and pitch, and 5 Hz for all data regarding GPS technology (position and velocity). The Xsens is directly linked to a serial port of the compactRIO. It is fixed in the wheelhouse, just behind the forward bulkhead, a few centimeters behind the attachment point of the kite, located ahead of this bulkhead.

2.4.2. Compass GPS

To avoid complex and uncertain calibration procedure of magnetometers, it has been decided to use an existing onboard sensor to get the yaw information, based on a dual antenna

GPS, instead of yaw information provided by the magnetometers of the Xsens. The sensor is a Si-Tex Vector Pro, with a 1σ RMS error under 0.3°. This sensor, providing the true heading of the boat regardless the boat velocity, is also used by the onboard autopilot. Therefore, a serial link has been established between the autopilot and the compactRIO to recover these data. The maximum update rate of the Si-Tex Vector Pro is up to 20 Hz, according to the manufacturer. However, because the information goes through the autopilot before reaching the data acquisition system, the final update rate is 1 Hz. This could not be modified during the trials.

2.4.3. Rudder Angle

A rudder angle sensor is part of the autopilot system to provide feedback (Fig. 2.10), and is mounted near the hydraulic actuator of the steering system. These data have been retrieved using the existing serial link used for GPS compass acquisition, with a resolution of 1°, and a sampling frequency of 1 Hz. A 3° offset have been noticed during sailing: with a constant steering input, the autopilot always converged to a rudder angle of 3° at any speed and any heading.

Figure 2.10.: Steven Paul's steering system and rudder angle sensor

2.4.4. Engine room sensors

A double flowmeter has been installed previously on the engine, to measure the fuel feed and fuel return, and so provide fuel consumption (Maretron M2RSP-2R-E8). This sensor is connected to the onboard NMEA 2000 network. A conversion device on the NMEA2000 network provided a serial output with NMEA183 protocol. This output is connected to another serial port of the NI 9870 module, and so the fuel flow is logged at 1Hz. A device measuring the torque on the propeller shaft, developed by the company UpDaq, has also been installed previously on board. A strain gauge has been stuck on the shaft and is linked to an amplifier, sending wireless data to a receiver in the wheelhouse. The later is connected to the acquisition system through a serial link. The torque on the shaft is logged at 20 Hz. The measurement of rotational speed of the shaft propeller is carried out thanks to a digital tachometer, the sensor is directly linked to the Digital Input module NI 9411 of the compactRIO system (Tab. 2.1). The rotational speed of the shaft is logged at 20 Hz.

2.5. Kiteboat Specific Sensors

As introduced in Chap. 1, the kiteboat is a specifically developed platform, designed to embed the frame containing actuators and load cells presented in Part 2.2. Thus, only two additional sensors are needed onboard: the first one is the IMU device recording motions and velocity of the boat, which needs to be rigidly fixed to the boat. The second is the rudder angle sensor. Onboard anemometers will be presented in Part 2.6.

2.5.1. GPS

An IMU combined with a two GPS receivers provides boat orientations and velocities. This sensor is a VectorNav VN-300 Rugged. Thanks to the MEMs inertial sensors, associated to advanced Kalman filtering algorithms provided by the manufacturer, the heel and pitch orientation can be obtained. Data from MEMs (angular rate and acceleration) are also recorded at any time. The two GPS receivers, in addition to provide position and velocities of the boat, give also an accurate heading measurement, apart from any magnetic interference. With this accurate measurement of heading, it becomes possible to estimate the drift of the boat, relatively to the ground, comparing heading of the boat and course over ground obtained from GPS receivers. The drift relatively to the sea water can be estimated by taking into account currents. According to the specification sheet (App. A), the orientation static accuracy is under 0.5° RMS, and under 0.3° RMS in dynamic case. Velocity accuracy is 0.05 $m.s^{-1}$. All data are recorded with a flow rate of 50 Hz.

2.5.2. Rudder Angle

A rudder angle based on a rotating potentiometer is included into the steering system (Fig. 2.11). The potentiometer is a Vishay PE30 linear, fully sealed, with a full resistance range of 470 Ω. The input voltage of the system is the voltage of the acquisition system battery, around 12 V, reduced with a 250 Ω resistor placed on the circuit, to get an input tension permanently under 10 V (maximum input voltage of the measurement device). The input voltage of the potentiometer and the output voltage of the potentiometer are measured using two channels of the NI 9205 module (Tab. 2.1). Calibrations were carried out at the laboratory, and zero balance is done and checked several times a day, by locking in neutral position the rudder using a constant length piece of rope attached at the end of the helm on one side, and on a fixed point on the boat. Despite the "military and professional grade" of the product mentionned by the manufacturer, the potentiometer did not perfectly support the assault of the water (due to its position, the potentiometer underwent very important sea water assaults). Indeed after 15 days of operation, data became corrupted, probably due to sea water absorption, affecting the main resistance value of the potentiometer. It had been replaced by the same product to finish the experimental fieldwork.

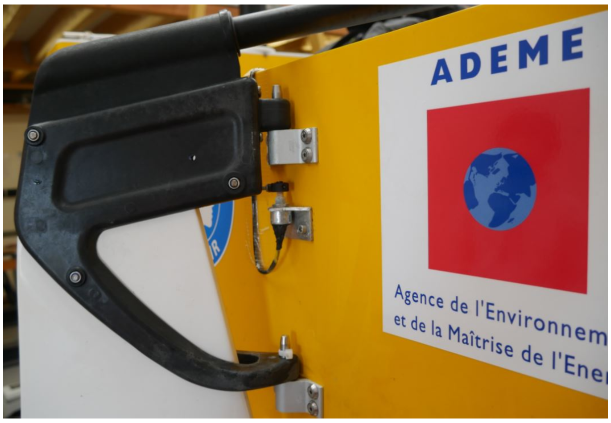

Figure 2.11.: Kiteboat's steering system and rudder angle sensor

2.6. Wind Measurements

Wind measurements are one of the most important aspects to compute sensible post processing, as it has been shown in Chap. 1. However, obtaining a good estimation of wind velocity at kite altitude is a complex task, particularly when measurements are done at sea. Thus, the wind measurement system evolved during the study to improve results.

2.6.1. Fishing Vessel Systems

The fishing vessel Steven Paul was initially fitted with an ultrasonic anemometer, however its location was near the exhaust funnel and it provided data which seemed to be corrupted by fumes or by fumes residue covering the sensor (see Fig. 2.12). Another sensor has been mounted on board, at higher location. It was fixed on one of the VHF antenna, as it can be seen Fig. 2.12. This sensor is an ultrasonic CV7 made by LCJ Capteurs, connected to the acquisition system to the NI 9870 module (serial link, see Tab. 2.1), and using NMEA183 protocol. The frequency of the sensor is 4 Hz, and the measurement altitude was 9.0 m above mean sea level.

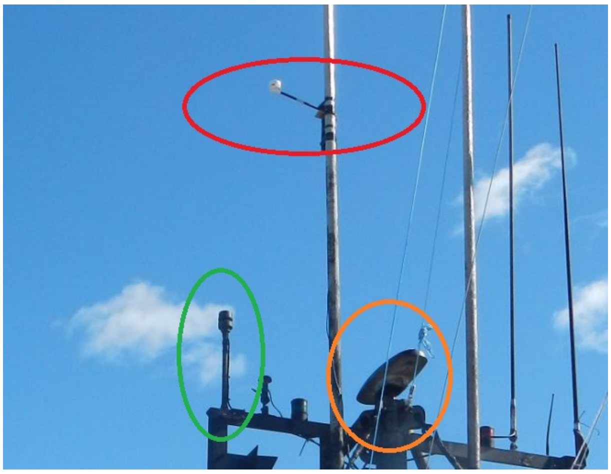

Figure 2.12.: Steven Paul's wind measurement system. The CV7 specifically mounted is cercled in red. The original CV3 is circled in green. The GPS compass antenna is also visible (orange circle)

2.6.2. Onshore Systems

The feedback of Canadian experimental fieldwork has shown how important it is to know the wind gradient along the vertical direction. Moreover, in the present case of experimental work done onshore, the variability of wind profile is expected to be more fluctuating than profiles that can be observed above the sea. However with a kite flying between 10 and 80 meters above the ground, it is difficult to get a wind measurement with a good accuracy at any position of the kite. To deal with this issue, it has been decided to use a wind profiler, based on sonic technology (see Fig. 2.13, picture (a)). This type of device is called SODAR, for SOnic Detection And Ranging. In our case, the SODAR is able to measure a wind profile ranging from 13 meters to 108 meters above the ground , with one point measured every five meters, and provides averaged data over a 5-minute-period. For each point of measurement, the direction, the intensity and the vertical component are available, but also the standard deviation for each data. It is particularly important to have a wind profiler for these onshore measurements because of the topographic configuration of the field where the trials have been carried out. Indeed, it has been observed some variations of the intensity and/or direction and/or vertical intensity of the wind along the altitude that could not have been easy to model. The device was rented to a local society EXWECS. The SODAR device has its own acquisition system, with an onboard clock synchronized with the absolute time of the mobile phone network.


(a) (b) (c)

Figure 2.13.: Onshore wind measurement experimental set-up, based on a SOnic Detection And Ranging wind profiler (picture (a)), a 2D ultrasonic anemometer located on a mast, at 4 m above the ground (picture (b)), and a 3D ultrasonic anemometer located on a mast, at 8 m above the ground (picture (c)).

To get higher frequency wind variations, two others sonic anemometers are used, during the campaign. The first one is the CV7 which was mounted on the Steven Paul. It is located near the kite ground control system (see picture (b)), and is oriented in the same direction as the ground station. The sensor altitude was 4 m above ground level. The second anemometer has been mounted only at the end of the fieldwork, and is a 3D ultrasonic one (Metek USA-1, see picture (c)). Its elevation is 8 m, and its location is fixed in the field. A wireless serial link, based on Xbee devices, has been set up between the sensor and the acquisition system. Data are then acquired through serial port NI 9870 modules, at a rate of 20 Hz.

2.6.3. Kiteboat Sytems

As it has been recalled previously, wind estimation at kite altitude is one of the most important data required to get proper post processed data. However during sea trials, it is not possible to embed the SODAR onboard, due to insufficient room and technological issues (the SODAR needs to be set up in a perfect horizontal position for a accurate measurements). Moreover, due to operational constraints, it was not relevant to set up a wind measurement mast higher than 5 m on the boat. However, the wind gradient above the sea surface is less disturbed than onshore, and can be reasonably estimated using power laws. To get the wind over the kiteboat, three ultrasonic anemometers are fixed on the mast at three different elevations. This assembly provides a redundancy of the wind measurement. The three sonic anemometer are manufactured by Gill, but are different models. The higher one, with a measurement altitude of 5.5 m above the sea level is a WindMaster, a three dimensional anemometer, fixed on the head of the mast, with a data flow rate of 20 Hz. The second one is a 2D anemometer WindSonic placed at 4.2 m above the sea level and deported from the mast by 0.6 m, with a data flow rate of 4 Hz. The last anemometer is a MaxiMet 500. This is also a 2D anemometer, and combines wind measurements with pressure, temperature and relative humidity measurements. This last sensor is also fitted with a GPS sensor and a compass, and can output the true velocity of the wind into the axis system attached to the Earth, corrected from the velocity of the boat. This measurement is redundant when the measurement mast is set up on the kiteboat. The MaxiMet is located at 3.0 m above sea level, and is also deported from the mast by 0.6 m. The Maximet frequency is 1 Hz. A picture of the wind measurement mast mounted on the kiteboat is given in Fig. 2.14. The three anemometers were connected to the serial ports of NI 9870 modules (Tab. 2.1).

The misalignment angles of the sensors with respect to the axis of the mast have been measured in laboratory with a portable tilt sensor, as well as the misalignment angle of the mast with respect to the longitudinal boat axis. Data were then corrected accordingly during post processing.

Figure 2.14.: Kiteboat's wind measurement experimental set-up based on three sonic anemometers located at different altitude above sea level.

2.6.4. Bay of Quiberon Systems

To ensure an even more accurate estimation of wind at kite position, a set of fixed measurement points was deployed in the bay of Quiberon, inspired from the work previously done by Roncin et al. (2005). The system is based on 3 catamarans KL15, fitted with a five-meter mast with a 2D ultrasonic anemometer at the top. The sensor is a CV3F by LCJ Capteurs. A compass provides the heading of the platform, to be able to retrieve the true wind angle relatively to the axis of the North. A GPS provides position, even if platform location has not been changed during the whole fieldwork and are in accordance with Fig. 2.15 (b). The GPS also provides absolute time, and it is used to synchronize data with the kiteboat acquisition system. Data loggers, made with NI myRIO devices, are recording data. A fourth catamaran KL15 is moored in the middle of the triangle formed by the three other catamarans. This one is fitted with the same wind measurement mast than the one mounted on the kiteboat and presented in Part 2.6.3. The GPS and compass devices of the MaxiMet sensor are used to get wind in the NED axis system as well as platform position and absolute time for data synchronization.

(a) (b)

Figure 2.15.: Fixed wind measurement points deployed over the Bay of Quiberon. Picture (a) shows the 4 measurement platforms moored in front of ENVSN. Picture (b) is a GoogleEarth screenshot showing position of the 4 measurement points during trials (white circle); the central one is always occupied by the platform fitted with the 3-anemometer mast (the more on the right on picture (a)); the external locations are occupied by the other platforms fitted with the single-anemometer masts (picture (a), the first three from the right). The red circle shows the limit of the area of measurement (0.7nm radius).

3. Kite Control and Data Acquisition Software

Résumé

Ce chapitre présente de façon détaillée le coté logiciel du système expérimental. Celui-ci peut être divisé en deux parties, une première centrée sur le programme embarqué dans le système expérimental et permettant l'enregistrement des données et le contrôle du kite, et une seconde détaillant la gestion des données acquises. Ce chapitre est volontairement très technique pour permettre à une personne nouvelle de prendre en main tous le système expérimental dans les meilleures conditions.

Le système de contrôle du kite et d'acquisition des données est basé sur du matériel National Instrument (NI), et la gamme de systèmes déployés compactRIO. Ces systèmes ce composent de modules d'entrée et de sortie pour les données, de circuits intégrés FPGA, d'un processeur et d'une mémoire non volatile. Le système est totalement autonome et ne nécessite pas d'ordinateur extérieur pour fonctionner. La programmation s'effectue avec le logiciel propriétaire NI LabVIEW. Le principe de fonctionnement peut être séquencé de la façon suivante. Tout d'abord, les données sont acquises par les modules spécifiques propres aux types des capteurs, et à leur connectivité (analogique ou numérique, via une liaison série ou non). Les données transitent ensuite à travers le FPGA, où elles peuvent être éventuellement traitées. Le processeur se charge alors d'enregistrer ces données dans la mémoire, ou de les utiliser pour contrôler le kite. Dans ce cas, des commandes sont renvoyées vers les actionneurs, via le même chemin. Les données sont aussi envoyées en temps réel vers des afficheurs, ce qui permet de vérifier le bon fonctionnement global du système, et ainsi de détecter rapidement tout disfonctionnement d'un des capteurs.

Le contrôle du kite peut être fait de deux façons : manuellement en contrôlant directement les actionneurs via des joysticks, ou automatiquement grâce à un pilote automatique chargé de définir la consigne à envoyer aux actionneurs. Le contrôle de la direction du kite peut se faire en appliquant un simple différentiel de longueur sur les lignes arrières, c'est ce que permet de faire le joystick principal ou le pilote automatique. La puissance du kite peut être réglée en ajustant la longueur moyenne des lignes arrières par rapport à celle des avants. Cette valeur peut être ajustée grâce au second joystick.

Dans le cadre de cette étude, le pilote automatique a été programmé en se basant entièrement sur des travaux précédemment publiés par d'autres chercheurs impliqués dans le développement des kites comme sources d'énergie. Seules des adaptations mineures ont été apportées afin de satisfaire aux besoins spécifiques du système expérimental. Ce pilote automatique est de ce fait capable de réaliser des trajectoires en huit de façon très répétables, en utilisant une stratégie de type bang-bang et non un suivi de trajectoire point par point. La taille, l'orientation et la position de la trajectoire peuvent être ajustés, en particulier dans le cas d'un navire, afin de placer cette dernière dans une position propulsive. Cependant ces réglages sont manuels, et la trajectoire n'est pas optimisée pour produire un effort maximal.

Toutes les données acquises sont enregistrées dans leur format brut, c'est-à-dire non calibré, bien que cette calibration soit déjà réalisée en temps réel pour permettre l'affichage

de contrôle. De ce fait une nouvelle calibration est effectuée lors du post traitement des données. Celui-ci est réalisé sous MATLAB®. Ce fonctionnement en double calibration et en utilisant deux langages de programmation différents permet une validation croisée des procédures de calibration. Par la suite, des routines spécifiquement développées permettent facilement d'isoler les données intéressantes, de visualiser des résultats préliminaires, en de générer automatiquement des rapports d'essais. Le post traitement fin de ces données est lui détaillé dans les chapitres concernés.

Deux des campagnes d'essais présentées par la suite ont utilisée des capteurs tiers, non relié physiquement au système principal. De ce fait, les données étaient enregistrées sur des supports distants, et un travail de regroupement des données a été mené. La synchronisation temporelle de données venant des différentes sources est basée sur les signaux GPS fournissant l'heure absolue.

3.1. Real-time Software

3.1.1. Overview

A draft of the system is sketched in Fig. 3.1. Three main parts can be identified: the user side (computer and tablet), the hardware side (the sensors and actuators presented Chap. 2), and the control and acquisition device. This whole system is based on a compactRIO platform, developed by National Instruments. The code is developed on a PC using LabVIEW, and then fully deployed on the compactRIO. Then PCs or iPads are only used for controlling settings or monitoring data through network connections. They can be disconnected or switched off without affecting the proper work of the system. Thus the system is totally Windows free, enabling a really good reliability even with high refresh rate (higher than 10kHz for some loops).

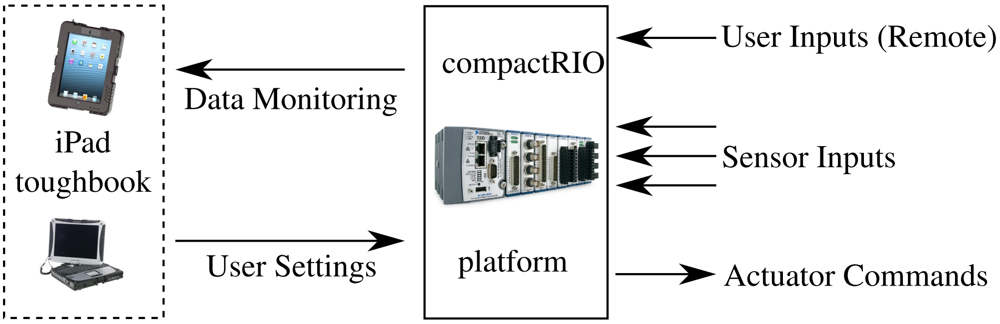

Figure 3.1.: Overview of the acquisition and control system.

The compactRIO system is also made of three main parts: a set of inputs (IN) and outputs (OUT) modules plugged on a chassis, a Field Programmable Gate Array (FPGA) integrated circuit (also named FPGA TARGET) and a Real Time (RT) processor (also named HOST). The FPGA is the link between the I/O modules and the HOST. This device is made of a finite number of predefined resources with programmable interconnects. The global capacity of FPGAs are then limited by the number of these ressources, and some operation can not be run or should be avoided due to their important cost. With these particularities, FPGAs have the capability of true parallelism, high reliability, high determinism and are re-configurable. FPGA programming is a complicated task, but the LabVIEW FPGA compiler ensures all the work to go from LabVIEW graphical code to implementation into FPGA. Thus, for a user knowing LabVIEW graphical programming, the FPGA programming will not be complicated, even if the specificities of such devices need to be known to use their full potential . Thus, FPGAs are very adapted tools to acquire data with accurate rate, and eventually realize simple processing. However, data recording cannot be carried out in FPGAs, thus data are transmitted to the HOST of the compactRIO, which have non volatile memory part. Depending on data frequency and data significance, data are transmitted through First In First Out stacks (FIFOs) or through direct access. For the first case, on the FPGA side, data are written into the FIFO element by element at very high speed, and on the HOST side, data are read by block. For example, if the FPGA writes 1 element every 1ms, and if the refresh period of the HOST loop reading the FIFO is 1000ms, the HOST would have to read blocks of 1000 elements to ensure the emptying of the stack without creating overflow. In the second case of direct access of data, the FPGA writes data into a register, and the register is read by the HOST loop when possible depending on work in queue. In addition to data recording process, HOST processor runs also the kite control system, with sensors feedback or user input, and flows a stream of data to monitoring system. These various tasks are summarized in Fig. 3.2. Ffollowing subsections focus on these various tasks. Detailed explanations about compactRIO functioning can be found in the the technical documentation provided by National Instruments (2014).

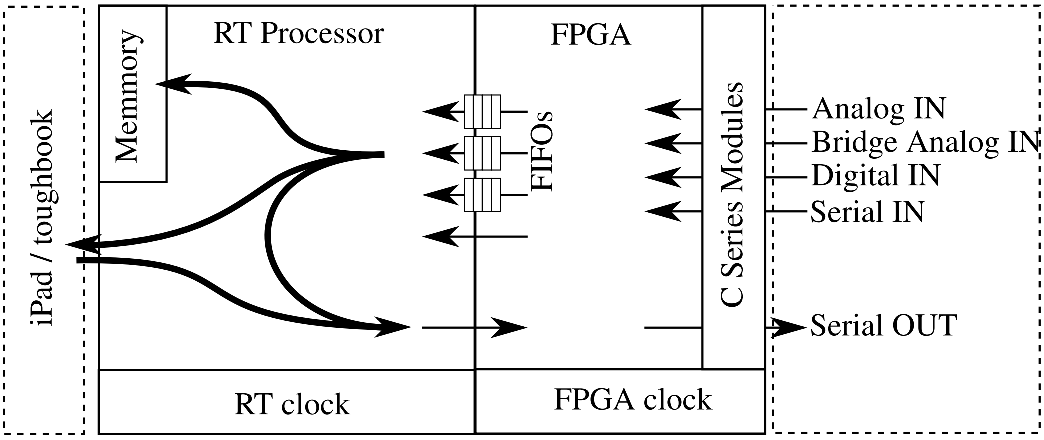

Figure 3.2.: Overview of the compactRIO plateform.

3.1.1.1. FPGA Target

The FPGA code is made of various parallel loops, running at various rates, as shown in Fig. 3.3. The main objective of the FPGA is to acquire data at fixed rate and then transfer these data to HOST part of the compactRIO. The FPGA can access to all IN or OUT ports of each module plugged in the chassis.

The compactRIO FPGA devices can be programmed in both ways. The first one is the Scan Interface Mode, which means that the FPGA is in this case transparent for users, where LabVIEW is automatically programming it to transfer data to the HOST. The second way is the one that has been used in our case. It consists to program manually the FPGA, which is more fastidious at first, but allows a better use of the FPGA capabilities. Moreover, the second possibility also leads to a fine understanding of numeric data types, and their usages. This choice needs to be done at the beginning of the LabVIEW project, and affects all the system in a way it can not be changed after.

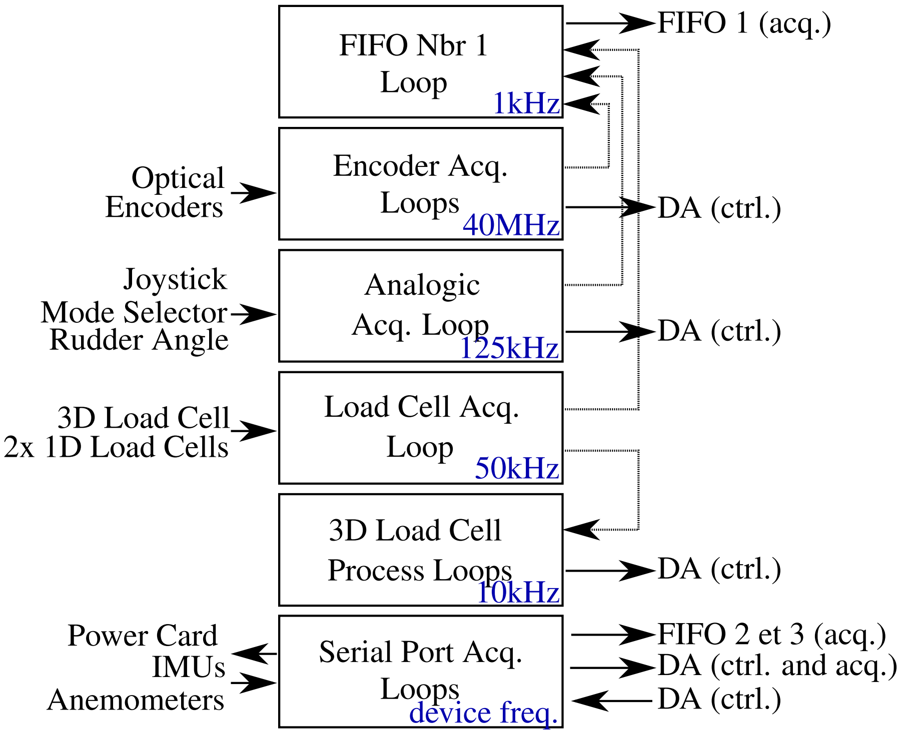

Figure 3.3.: Operating diagram of the FPGA part of the compactRIO. DA stands for “Direct Access”. The arrows of the right side represent data flow to or from the HOST part of the compactRIO. Left side arrows represent data flow from sensors or to the actuators.

3.1.1.2. Real Time HOST

The real time HOST code is made of various parallel loops, running at various rates, with various priorities. A diagram showing these loops, and their inter connections is given in Fig. 3.4. The code presented here is the last one deployed on the kiteboat acquisition and control system, and it is an improved release of all other codes used in the previous experimenatal works.

Data coming from FPGA through FIFOs or the Direct Access (DA) are processing in the HOST in two ways. The main part of data directly arrives into the record loop and then is written on the Non-Volatile Memory (NVM). Only raw data are recorded. Moreover all these data are also calibrated and sent to the Display loop, and then broadcasted to the network to be displayed on the computer or on the iPads. The data which are important for the kite control and the actuator control are processed into one of the two Data Processing Loops. The fastest one computes the kite position and the kite velocity from the 3D load cell measurement, and also computes the actuators feedback and joystick calibration. The frequency of this loop is 200Hz. The second processing loop runs at 10Hz, and computes mainly wind data and boat motions. These calibrated data are then used in the

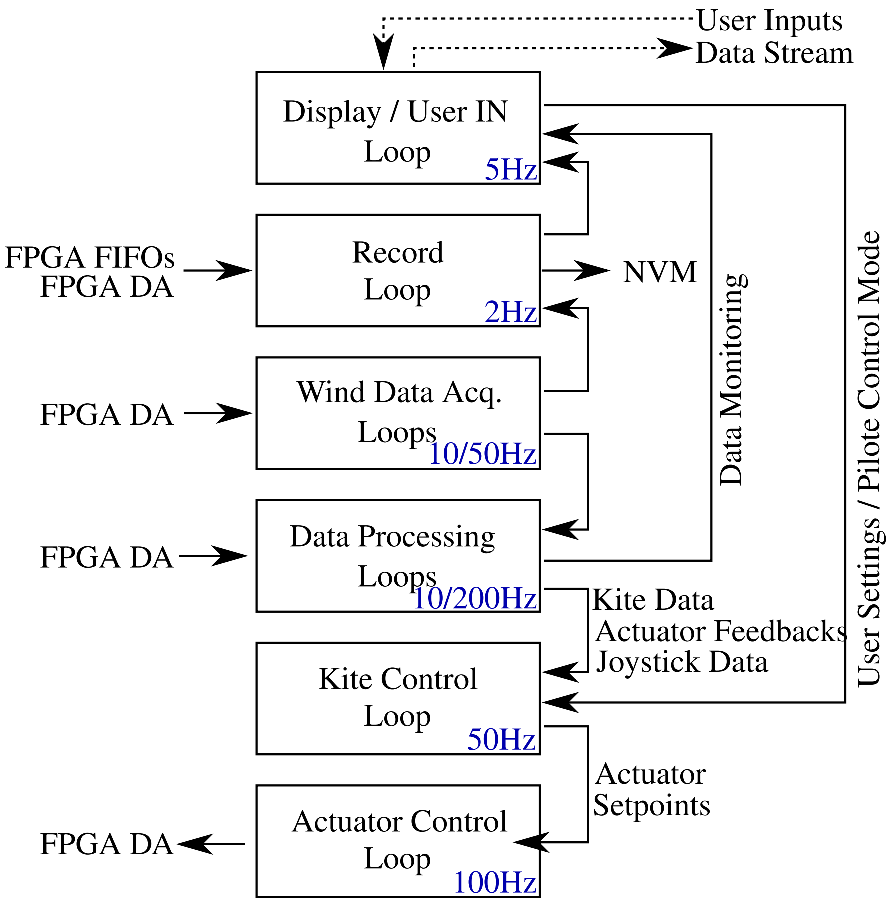

Figure 3.4.: Operating diagram of the HOST part of the compactRIO. NVM stands for “Non-Volatile Memory” and DA stands for “Direct Access”.

Kite Control Loop to define the steering inputs the actuators have to do. Depending on a user choice, the Kite Control Loop runs the automatic pilot performing kite dynamic flight or transforms the joysticks input into actuators setpoints. Finally these setpoints are sent back to the actuators through the Actuator Control Loop and then the FPGA.

Because the HOST is only made of one processor, tasks cannot run in a parallel way. Due to the number of parallel loops, it is important that the time needed to complete tasks of a loop is far under the loop period. Indeed, between the moment the processor ends the last task of a loop and the beginning of the next loop, the processor will run tasks of other loops. That means that every task in each loop is done one by one, and then loops with critical time need to be prioritized. To ensure a proper operation of the system, loop periods have been settled to have a CPU load of the compactRIO under 70% in any case. This 30% safety margin allows that all critical loops always finish on time. Sometimes the Display Loop, the less critical one, can finish late, but this does not affect the whole system.

3.1.2. FPGA Data Acquisition

3.1.2.1. Serial Devices Acquisition

Anemometer and IMU devices are connected to the system through serial link. The communication mode was identical for all these devices, and is based on binary sentences. Each piece of data is streamed within a well defined packets of bytes, starting always with the same start-byte-combination, followed by information about the streamed data, as payload and packet identifiers, and finally the packets of data. Checksum bytes and end sentence byte(s) end the sentence. Data types and lengths vary, and can be for example Unsigned 32 bits (U32), or Float Double (64 bits) or Single (32 bits) precision (DBL or SGL). These sentences and their streaming rates have been defined to fit expectations of the system. This programming is done using the configuration software provided by the manufacturer .

This type of data flow can be read in a LabVIEW FPGA code, however the LabVIEW FPGA tool for serial communication is a Property Node reading only one byte after another. Moreover, FPGA does not support various size array. That means a specific adapted code need to be build for acquiring each sentence of each device. Thus, one loop is dedicated to each devices, as shown in Fig. 3.3. When deploying the code into the FPGA, the properties of the considered serial port are firstly defined. For all devices, the configuration is : 8 data bits, 1 stop bit, no parity. The port rate depends on the device, varying between 4800 baud/s and 115200 baud/s. The recording rates of data coming from these devices are equal to the rate of the streamed data, defined by devices settings.

3.1.2.2. Power Card Serial Communication

The power card used for controlling actuators is also linked to the system through a serial link, but the communication protocol is different for two reasons. The first one is that this link is working in both ways, meaning that actuator commands are sent to the card, and the card sends back data as battery voltage, intensity per channel, or fault messages. The second one is that data are exchanged using ASCII format instead of binary sentences. Thus messages are easily understandable by human, but FPGA part does not support string of characters, thus messages have to be translated into array of Unsigned 8 bits (U8). The ASCII communication protocol is detailed in the power card user manual.

3.1.2.3. Remote Device and Rudder Angle Sensor (Analog Inputs)

The two joysticks, the mode selector, and the rudder angle are devices with variable resistors. Thus an input voltage is applied, and an output voltage is measured by an analog input channel depending on the position of the device. All channels are acquired in the same loop at a rate equal to the frequency refreshment of the module. Control data are sent to the HOST with direct access way, whereas the two rudder angle measurements are sent two the FIFO number 1. The recording rate of these two measurements is then the rate of the loop of the FIFO number 1.

3.1.2.4. Optical Encoders (Digital Inputs)

Each optical encoder outputs three digital channels (A, B and C). The objective of the FPGA encoder loops is to count the number of edges seen on Channel A and Channel B. Knowing the number of counts per revolution, and thus the number of edges (one count has two edges per channel, therefore one count leads to four edges), it becomes possible to compute the angular position of the shaft of the encoder, relatively to the angular positoin. More details about optical encoder functioning can be found in the user manual TR Electronic (2005).

3.1.2.5. Load Cells (Bridge Analog Inputs)

Each load cell channel is connected to one of the 8 bridge analog inputs of the system. The acquisition loop runs at the module rate. Data are written into register, and read into the FIFO number 1 loop. The recording rate of these data is then the rate of the loop of the FIFO number 1. Moreover, the 3 registers coming from the 3D load cell channels are also read in another loop running at 10kHz, and processing an average over 50 elements. Thus the signal noise is really limited. The outputs of this loop are sent to the HOST through a direct access and are then used for kite control purpose.

3.1.3. Data Logging

All data are recorded into TDMS files, a specific format developed for LabVIEW. TDMS files are divided in groups, each group having the same frequency. The recording loop runs at 4Hz. Each piece of data sampled at higher frequency comes from FIFOs, directly from the FPGA or from the wind acquisition loops. Block of data are then written into files. For 4Hz signal, data are directly sent to TDMS file at each iteration of the loop. For 1Hz signal, data are sent to the files only every 4 loop iterations, but this mainly concerned kite control settings.

At the beginning of each new files, a few elements are first written into the header group of the files, as the zero values of unbalanced sensors or kite name and tether lengths. During kiteboat operations, wind data and boat motions are permanently recorded. When the kite measurements start, the current file is closed and a new one is started, containing kite data, and particularly kite forces. The end of kite measurements starts a new file for boat motions and wind.

3.1.4. Live Data Processing for Control Purpose

A few computed data are needed for kite control purpose, like the kite position and the kite velocity vector, the actuator positions, the joystick positions, wind data... Kite position can be computed in various axis system: the one attached to the boat is the direct one, because the 3D load cell providing the kite position is rigidly fixed to the boat. However the heading reference frame, the true wind reference frame, the relative wind reference, or the north east done reference frame can also be used. In this case the change of reference frame is computed in real time.

This process computed in real time is equivalent to the one done thereafter during post processing using MATLAB®, thus it will be not presented in this part but will be detailed in Part 3.2.2.These computations are done into two loops depending on the frequency of refreshment required.

3.1.5. Kite Control

3.1.5.1. Overview

The kite command is based on 2 variables affecting back tether lengths. The first one is the Trim, and is equal to the length difference between back and front tethers, named τ. The second one is the steering and is equal to the length difference between the right and the left back tethers, named δ. Denoting $\lambda 1$ and $\lambda 2$ the real position of actuators coming from encoder measurements, δ and τ are get using Eq. 3.1. An overview of kite control architecture is given in Fig. 3.5.

$$\begin{cases} \delta = \lambda 1 - \lambda 2 \\ \tau = \frac{\lambda 1 + \lambda 2}{2} \end{cases} \tag{3.1}$$

The trim command is manually adjusted with one of the two joysticks, set in power control mode, meaning that the joystick is completely pushed to side, the motors roll-in or roll-out back tethers at maximum available power, but by keeping a synchronization between the two actuators to avoid appearance of a length difference. However some automatic trim adjustments can be added depending on the kite position on its wind window (gray block “Window Adjust.” in Fig. 3.5).

The steering command can be adjusted with the second joystick, set in this case in position mode, meaning that an extreme position of the joystick corresponds to a maximum steering command. This command can be also adjusted by the kite automatic pilot, presented later in this part. The initial steering command can be modified by two optional modules. The first one aims to take into account the change of the length difference between back

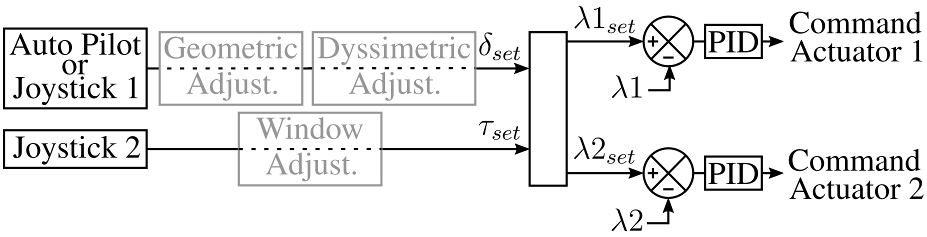

Figure 3.5.: Diagram of the functioning of the kite control part. δ_{set} is the steering set-point of the kite and τ_{set} is the trim set-point. $\lambda 1$ and $\lambda 2$ are the current actuator positions, whereas $\lambda 1_{set}$ and $\lambda 2_{set}$are the setpoints. Grey colored blocks are optional and can be deactivated.

tethers when kite flies on the side of the main frame, due to the distance between the attachment point of the return pulley of the two back tethers. Thus, the steering set-point is corrected by an additional quantity:

$$\delta_{cor} = L * sin(\phi^{(s)}) * cos(\theta^{(s)}) \tag{3.2}$$

with $\phi^{(s)}$ and $\theta^{(s)}$ the azimuth and elevation angle of the kite in the boat axis system, and L the distance between the two attachment points of the return pulley of the two back tethers, as shown in Fig. 2.2. The second optional module is made for adding an offset on the steering command to deal with symmetry issues of the kite or of the tethers.

At any time, the setpoints exist for the trim and the steering commands. Then these commands are processed to output the setpoints needed for each actuator. Steering command can be eventually dyssymmetric, using a specific parameter: for a steering input δ_{set}, instead of an applied $\pm\delta_{set}/2$ on each actuator, one will apply for example $-2\delta_{set}/3$ whereas the other will applied $+\delta_{set}/3$. In this case, the trim does not remain constant This part has been implemented to try to avoid a kite buckling phenomena during a kite turn. However, results were no significant, and this functionality has not been used during measurement.

Finally, the two setpoints $\lambda 1_{set}$ and $\lambda 2_{set}$ are compared with the effective position of actuators $\lambda 1$ and $\lambda 2$, and two PID controllers rule the commands to send to each actuator. In our case, the controllers show satisfactory results with derivative and integral gain set to 0, leading to controllers based only on a proportional gain.

3.1.5.2. Automatic Pilot

The automatic pilot part aims to produce a steering command δ_{set} in place of the user. In the present case the autopilot is only able to perform eight pattern trajectories, using a bang-bang strategy and not by following a track point by point. The autopilot implementation is totally inspired by the one proposed by Fagiano et al. (2014), with some improvements added to deal with the specific case of boat applications. However, parameters identification was done experimentally and not by the use of kite and actuator modelings, as Fagiano did.

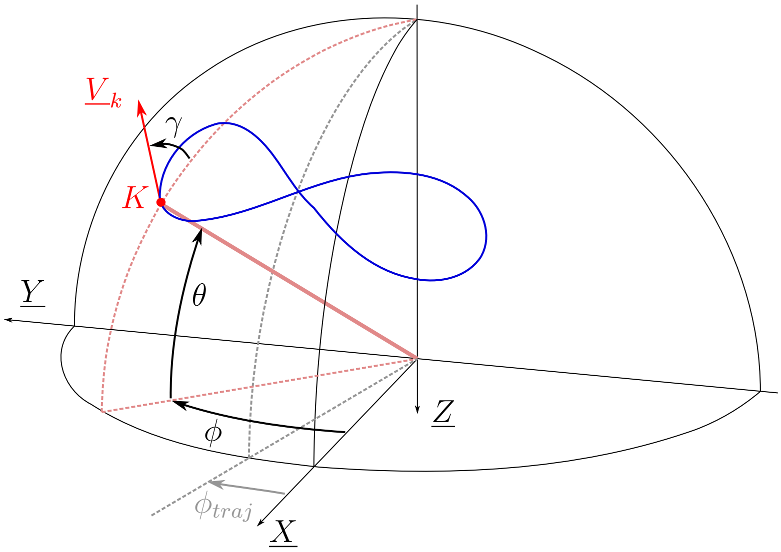

Figure 3.6.: Kite position and velocity variables used in autopilot process

To compute an automatic control of the kite, controller needs a feedback on kite position in the wind window. This feedback comes from the 3D load cell measurement, expressed in spherical coordinate (r, θ, ϕ). With the assumption of straight tethers with constant lengths, r equals to the tether length L_t. The kite position can be expressed in various axis systems, and thus auto piloted trajectories can be defined in these various axis systems. For the following explanations of the autopilot functioning, we consider a generic axis system, with no subscript as presented in Fig. 3.6. The 8-pattern trajectory can be shiftted in the reference frame by an angle ϕ_{traj}, this angle is therefore the expected azimuth of the center of the trajectory. The main variable used by the autopilot is the angleγ defined as the angle between the kite velocity vector and the local meridian at kite position K, as visible in Fig. 3.6. This angle γ is obtained using the following formula (the **atan2** formula is given in the Nomenclature chapter):

$$\gamma = \text{atan2}\Big(cos(\theta)\dot{\phi}, \dot{\theta}\Big) \tag{3.3}$$

This equation uses the time derivatives $\dot{\phi}$ and $\dot{\theta}$ of kite position, and is computed in real time. Because numerical differentiation generates noise, signals are filtered before and after differentiation, using running mean on a 200 ms period. This causes a delay of 200 ms on the output signals, but with no significant effects on the autopilot functioning.

The principle of the autopilot is to compare the angle γ with a reference angle denoted γ_{ref} and defined as the angle between the local meridian at kite position and an objective

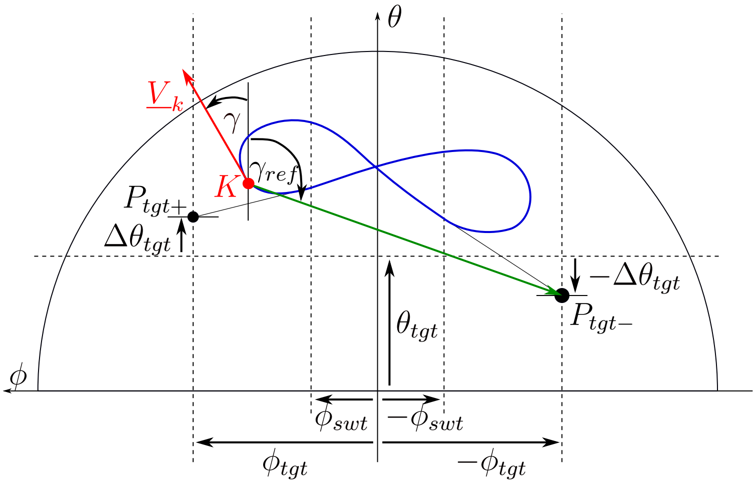

Figure 3.7.: Parametrization of the the eight-pattern trajectory for autopilot purpose, expressed in a 2D symbolic projection of the 3D quarter of sphere, visible in Fig. 3.6.

vector defined as the vector going from the kite position to an active target point P_{tgt} (draft in green in Fig. 3.7). This target point P_{tgt} is defined with its azimuth ϕ_P and its elevation θ_P. Then γ_{ref} can be processed, using Eq. 3.4.

$$\gamma_{ref} = \text{atan2}\left(cos(\theta)(\phi_P - \phi), (\theta_P - \theta)\right) \tag{3.4}$$

Depending on kite position, the active target point is one of the two defined target points: P_{tgt+} and P_{tgt-}. Their positions are respectively $(\theta_{tgt}+\Delta\theta_{tgt}, \phi_{tgt})$ and $(\theta_{tgt}-\Delta\theta_{tgt}, -\phi_{tgt})$. The active point P_{tgt} switches from one target point to another using the parameter ϕ_{swt} and the guidance strategy given in Eq. 3.5. The parameters θ_{tgt}, $\Delta\theta_{tgt}$, ϕ_{tgt} and ϕ_{swt} are user inputs and affect shape and position of the expected trajectory.

$$\begin{cases} if \quad \phi > \phi_{swt} & then \quad P_{tgt} = P_{tgt-} \\ if \quad \phi < -\phi_{swt} & then \quad P_{tgt} = P_{tgt+} \\ & else \quad P_{tgt}(t) = P_{tgt}(t-dt) \end{cases} \tag{3.5}$$

Due to the switch from one target point to another, γ_{ref} is discontinuous, jumping for example from a value close to π to a value close to $-\pi$ when azimuth of kite ϕ reaches ϕ_{swt}. This jump is incompatible with a control purpose, because it will generates sudden jumps in the actuators setpoints and then in the actuators behavior. Therefore a filter is added to smooth the evolution of γ_{ref}. It is a Butteworth filter with a cutoff frequency f_γ. The value of f_γ were found experimentally, and no large variations were tested. Thus f_γ range was between $0.22\ Hz$ and $0.27\ Hz$. Then the filtered $\tilde{\gamma_{ref}}$ is compared with the real angle γ of the kite, and then a PID controller computes the command δ_{set} to apply to the kite through actuators (Fig. 3.5). Here again, the controller shows satisfactory results with derivative and integral gain set to 0, leading to a controller based only on a proportional gain K_γ.

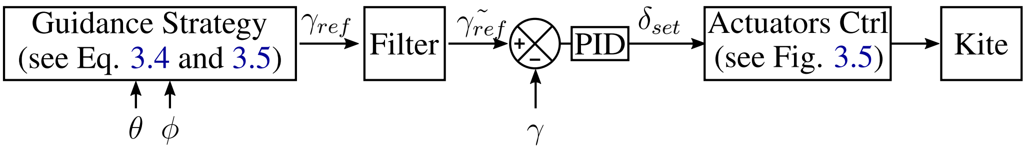

Figure 3.8.: Autopilot functioning diagram . The output of the autopilot is the steering setpoint δ_{set} used as input in the kite control part presented in Fig. 3.5.

The main differences between the autopilot presented here and the one initially proposed by Fagiano et al. (2014) are about position of target point and switching strategy. In Fagiano work, the switch from a target point to another is done when kite reaches its azimuth target. However this leads to a fast variation of γ_{ref} value when the kite arrives close of the target, with opposite sign if the kite is above or under the target. In spite of the presence of the filter, these variations can be a source of instability, it has been then decided to separate target point from switching area. Thus kite can never reach its targets, as the switch operates far before. The second difference is the ability to have the two target points at different elevations, and then rotate the trajectory. This is necessary to fly the kite near the wind window edge, for example when sailing is around 100° of true wind angle. However, the switching procedure has not been modified, using only azimuth ϕ of the kite. Thus full vertical trajectory can not be performed. This alteration of the trajectory has nevertheless already been implemented by other teams, such as Zgraggen et al. (2015). The last improvement was done to be able to realize down-loops instead of up-loops, as introduced in Fig. 1.2. That means that the kite goes down during turns instead of going up (as drawn in Fig. 3.6 and 3.7). This is made using new values of γ and γ_{ref}, denoted with upper-script inv in Eq. 3.6.

$$\begin{aligned} \gamma^{inv} &= \gamma - sign(\gamma)\pi \\ \gamma^{inv}_{ref} &= \gamma_{ref} - sign(\gamma_{ref})\pi \end{aligned} \tag{3.6}$$

It is important to note than, in down-loop case, the target points are located above the trajectory instead of under as for the up-loop case. Therefore, the elevation of these points needs to be increased to have enough clearance to avoid any collision between the kite and the ground or sea surface.

In summary, the draft of a trajectory is based on a set of parameters, with specific influences :

- ϕ_{traj} defines the azimuth of center of the trajectory with respect to the chosen reference frame
- ϕ_{swt} affects the width of the trajectory

- ϕ_{tgt} has a limited effect if sufficiently larger than ϕ_{swt}
- θ_{tgt} affects the global elevation of the trajectory
- $\Delta\theta_{tgt}$ affects the rotation of the trajectory around the tether axis, but rotation higher than about 20° can not be done
- f_γ and K_γ affects the bend radius of the turns.

3.1.6. Data Monitoring

Because measurements were conducted out outside in a particularly tough environment, numerous systems can fail, and it is important to identify these issues early. Thus, during experiments, data signals are monitored using iPads, with a specific application developed by National Instruments, named Data Dashboard for LabVIEW, an available on the Apple Store. The application works on other tablets running other operating systems, but with less functionalities than the iPad release. All important data are then streamed from the compactRIO to a WiFi network specially settled for this purpose. Precisely, the compactRIO is connected to an Ubiquiti Bullet WiFi device, which can be set as WiFi access point, and data are streamed with specific LabVIEW tools, named Shared Variable, used in the HOST display loop (see Fig. 3.4). Kite control parameters and record commands are also set with the tablets. A screen shot of one of the tablet pages used for monitoring data is given in Fig. 3.9.

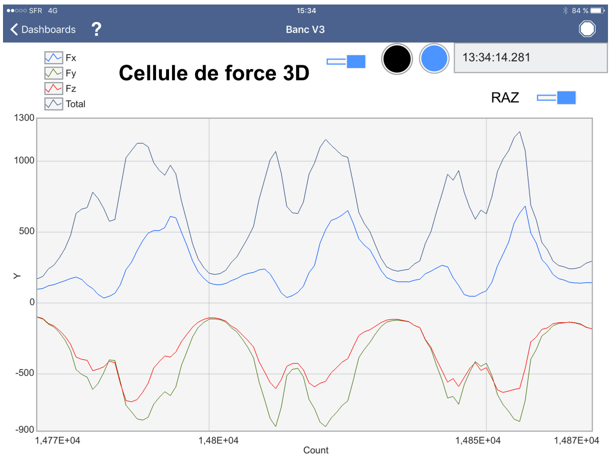

Figure 3.9.: Screen shot of one of the page of the tablet app used for monitoring data of the 3D load cell.

3.2. Data Calibration And Storage

As introduced before, data are recorded in specific LabVIEW files, named TDMS file. To process these data a set of procedures has been developed, and the outline is given in Fig. 3.10. At first, data are imported to MATLAB®, and then put in MATLAB® structure and saved into MAT files. Then data are calibrated, preserving the file format, and saved again in other MAT files. From there a MATLAB® routine specifically written for this purpose plots the most suitable data and gives the user the opportunity to select relevant period of time. Thereafter these selected data are put into new structures, still following the same file format, and saved into new files. These files can then be used in specific post processing works, presented in the dedicated parts of this study. Otherwise, data contained in these files can be exported in PDF reports automatically generated by others routines. These reports are an easy and quick way to share preliminary results of a day of trials, and are useful to improve the experimental set up or the experimental program for next trials. The files generated at each step are kept into separated folders, therefore if a mistake is made at one stage, data can be easily restored using files of the previous stage.

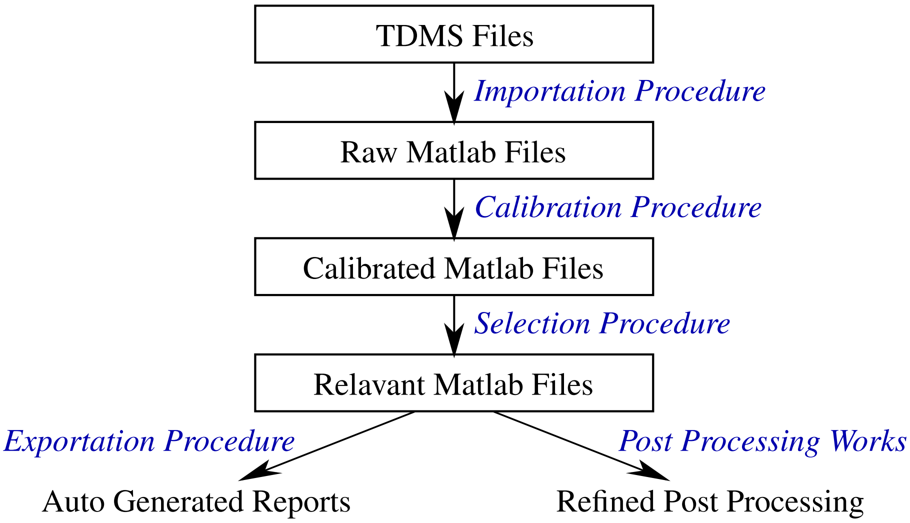

Figure 3.10.: Outline of data processing from acquisition to result presentation.

3.2.1. Importation into MATLAB®

A few MATLAB® toolboxes for importing TDMS files are available on MathWorks website, however a few of them did not work properly with our experimental files for unknown reasons, and another toolbox leads to an extremely long process duration. However, a good Excel adds-on is provided by NI to open TDMS files with Microsoft Excel. Moreover, routines are available in MATLAB® to import data from Excel. Thus a specific routine has been implemented to automatically open the TDMS file with Excel, and then import data into MATLAB® workspace. Data are then stored into a structure, and this structure is saved into a .MAT file. This procedure is limited by the number of rows than an Excel worksheet can handle. Currently, this limit is 1,048,576 rows for the latest releases, according to Microsoft Office Support website. With a maximum sampling frequency of 1kHz in TDMS files, this lead to a record duration no longer than 1048 seconds, or 17 minutes. Thus it has been decided to do runs of record no longer than 10 minutes for onshore fieldwork. For onboard trials, this period is reduced to 5 minutes for space considerations (see Chap 6). For specific reasons, some records were longer than 17 minutes. In this case, data were imported into MATLAB® using the other toolbox, with a longer processing time.

3.2.2. Calibration Procedures

All data recorded are raw, meaning the stored value is directly the value output given by the sensor or the device. Thus a calibration procedure needs to be performed. This procedure evolves with the changes in recorded data, and with the sensors making up the system. For instance, when a load cell is replaced, the procedure changes, because the sensibilities of the two load cells are different. The procedure is written in a MATLAB® routine. Each new version of the procedure leads to a new routine file, with an indexation number. Moreover the changes from the precedent version are written as comments at the beginning of the file. This calibration procedure is also made in real time processing. That means that the calibration procedure has been implemented in two different computer languages. Doing this is a redundancy preventing mistakes. Indeed if monitored data are not apparently consistent with post processed data, that means that one of the two calibration procedure is wrong, and both of them need a control check.

In the following, some specific details of the calibration procedure are given, but it will not provide a full coverage of the routine. To have a complete view of the procedure, the reader should refer directly to the MATLAB® routines. The variable coming from the RAW files are denoted with the subscript IN, whereas the calibrated variable are denoted with the subscript OUT. The calibration actions can be sorted in two groups: value calibrations, for instance to go from the volt measurement to the newton value of the load applied on a load cell. The second group is the geometric calibration, to go for instance from the axis system of the sensor to the axis system of the boat.

Time

The Time value is recorded in milliseconds from the start of the system. Two clock are available in the compactRIO: the FPGA one and the HOST one. It has been decided to record only the FPGA one. In the RT device, time is encoded on an integer unsigned 32bits. However, data are recorded on a single-float format (also 32 bits), and only 2^{23}integer can be encoded with a single-float. Thus, only about 8,388,000 milliseconds (2.3 hours) can be fully described with an integer, and this is not enough in the case of a day of measurement without resetting the system. Therefore, time is stored on two single-floats : the first one $Time1_{IN}$ matches the seconds whereas the second $Time2_{IN}$ matches the milliseconds. Finally time $Time_{OUT}$ is calibrated with the following equation:

$$Time_{OUT} = Time1_{IN} + Time2_{IN} * 1000$$

Load Cells

Each channel of the 3D load cell, and the two 1D load cells need to be calibrated separately. Two values are important for calibrating load cells: the sensibility value of the load cell coming from the certificate of calibration, and the Zero value S_{zero} output by the load cell when no load is applied. Zero value checks are done every day, checked several times a day, and recorded in the header of the TDMS file. $S_{calibration}$ is the value output by the cell when a load equals to $F_{calibration}$ is applied. The factor 1000 reflects the fact that $S_{calibration}$ is given in mV/V whereas the raw signal S_{IN} coming from the conditioner is given in V/V.

$$F_{OUT} = (S_{IN} - S_{zero}) \frac{F_{calibration}}{S_{calibration}} 1000$$

Then, the force vector given by the 3D load cell is expressed in the boat axis system instead of the load cell axis system. For the 1D load cell, the Eq. 2.1 is applied to get the real load of the line.

Encoders

Encoders position are given as a number of pulse between the current angular position and the angular position at start. An offset can be adjusted during experiments to define a new origin position. These offsets are also stored in the the header of the TDMS file. By knowing that the winches have a radius of $R_{winch} = 75\, mm$, and the encoder have $N = 4096$ pulses per revolution (leading to $4N$ edges per revolution, see 3.1.2.4), the length of the lines can be obtained by applying a calibration equation as follows:

$$L_{OUT} = (S_{IN} - S_{zero}) \frac{2\pi R_{winch}}{4N}$$

Rudder Angle

As it has been described in part 2.5.2, the rudder angle sensor is based on a potentiometer. Two voltage measurements are recorded: the input voltage at potentiometer input terminals $V_{ref,IN}$, and the output voltage of the potentiometer V_{IN}. The first measurement depends only on battery voltage, whereas the second one depends on battery voltage and rudder position. It has been assumed than the battery voltage variation is sufficiently low and does not affect the sensibility $\delta_{R,calibration}$ of the potentiometer.

$$\delta_R = (V_{IN} - V_{zero})\frac{\delta_{R,calibration}}{V_{ref,IN}}$$

Speed Over Ground and Course Over Ground

With the point U denoting the location of the IMU, the velocity vector $\underline{V}_U$ of this point is directly outputted by the coupled system IMU and GPS, but in the R_{ned} axis system. However these values are not really convenient, and they are completed by the Speed Over Ground (SOG) and the Course Over Ground (COG).

$$\begin{aligned} SOG &= \|\underline{V}_{U,IN}\| \\ COG &= \operatorname{atan2}(V^{(ned)}_{U,IN,1}, V^{(ned)}_{U,IN,2}) \end{aligned}$$

Onboard Wind Measurements Anemometers output directly calibrated data, but in their own axis system. When possible, this axis system is aligned with the boat one, but this is not always possible. Moreover, because the assembly between the boat and the sensor needs to be rigid, the accuracy of the alignment is not perfect and alignment defaults appear. The calibration of anemometers is then an axis-system change, based on Euler angles $(\psi_W, \theta_W, \phi_W)$, coming from the measurements of misalignment carried out at the laboratory (see part 2.6.3).

$$\underline{V}_{WM,OUT} = \underline{\underline{M}}_{\psi_W}\underline{\underline{M}}_{\theta_W}\underline{\underline{M}}_{\phi_W}\underline{V}_{WM,IN} = \underline{V}^{(s)}_{WM}$$

3.2.3. Data Selection Procedures

The outside measurement of kite performances sometimes leads to unexpected behavior of the kite during recording, ending eventually by a crash, especially during the automatic pilot development period. Recordings were not stopped in this cases, or not immediately, resulting in periods of recording with irrelevant data. To quickly deal with these cases, another MATLAB® routine has been implemented. The principle of this routine is to graphically select on a plot an interesting time range window, using cursor (see Fig. 3.11). Then, this window is named, and saved into the data structure. Thereafter, another routine reads multiple data files, and cuts them into pieces, following the window characteristics previously defined by the user.

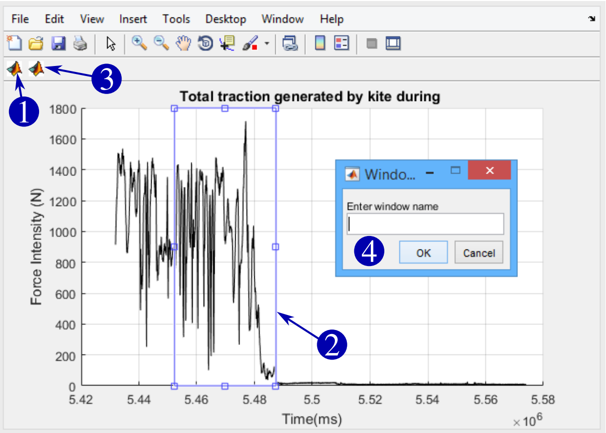

Figure 3.11.: Screenshot of a data plot during cutting procedure. Marker 1 indicates the button that generates the cursor window (marker 2). The marker 3 points out the saving button for generating the pop-up window (marker 4) used to name the data window.

3.2.4. Plotting and Specific Post Processing Procedure

Data can then be plotted, using a MATLAB® script. This script needs at first the name of the file to process, and then the list of data to plot. This list can vary from one work to another, but a main part of it is common, like the total force generated by the kite, the evolution of back tether lengths or the kite position.

3.2.5. Exporting PDF reports

All these plots can be automatically exported in PDF format, for multiple data filed at the same time. A Latex script is also automatically written to include these figures. These latex script is then included in a master document containing description of the day of trials, important features observed during the day, and also element to improve for next trials. An overview of the beginning of such a report is given in Fig. 3.12.

3.3. SODAR Data Procedure

SODAR data are written in ASCII text files, with one new files each day. The new file is first downloaded from the SODAR online server. Thereafter, it is read by MATLAB® routines and then data are converted into numeric format, stored into MATLAB® structure and saved into a new .MAT file. One point of measurement is made of a header and a table containing wind data (see an example in Fig. 3.13(a). Each line of the table matches

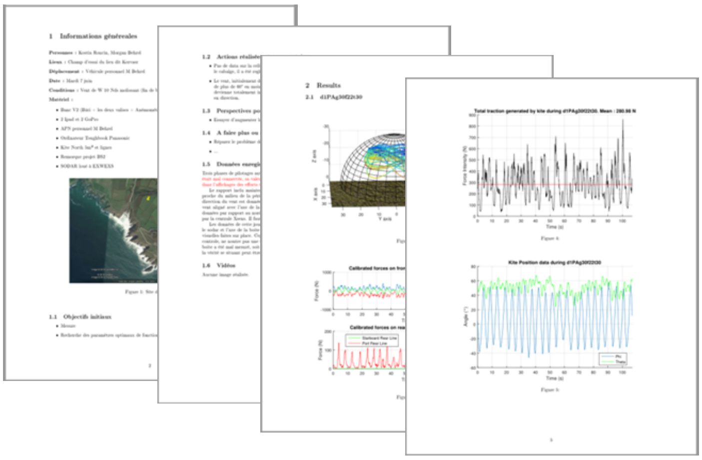

Figure 3.12.: Example of a PDF report with experimental results automatically added.

with the altitude of measurement, indicated in the first column. The most important data in the header is the date of the measurement, and more precisely the date of the end of measurement period. In the current example, the date is July 8th, 2016 at 12:05 UTC, meaning the data are related to the period from 12:00 to 12:05 (because the time step was 5 minutes).

3.4. Bay of Quiberon Weather Data Procedure

The experimental fieldwork carried out in the Bay of Quiberon during the month of April 2017 involved a specific organization for measuring and estimating wind at kite altitude. As presented in Part 2.6.4, 4 fixed measurement platforms were spread out over the navigation area. However these platforms could not be linked to the KiteLab acquisition device, and independent recording systems had to be organized.

3.4.1. Fixed Point Wind Measurement

3.4.1.1. Data Importation from Central Measurement Point

The central point is supplied with anemometers identical with the ones mounted on the kiteboat. Therefore, the acquisition device is duplicated from the kiteboat's one, and based on a second compactRIO. Recording files were also TDMS files, with exactly the same structure. The acquisition software runs automatically when the system is powered. To avoid too large files, a new one is started every hour. At the end of each day of measurement, data were downloaded into a computer.

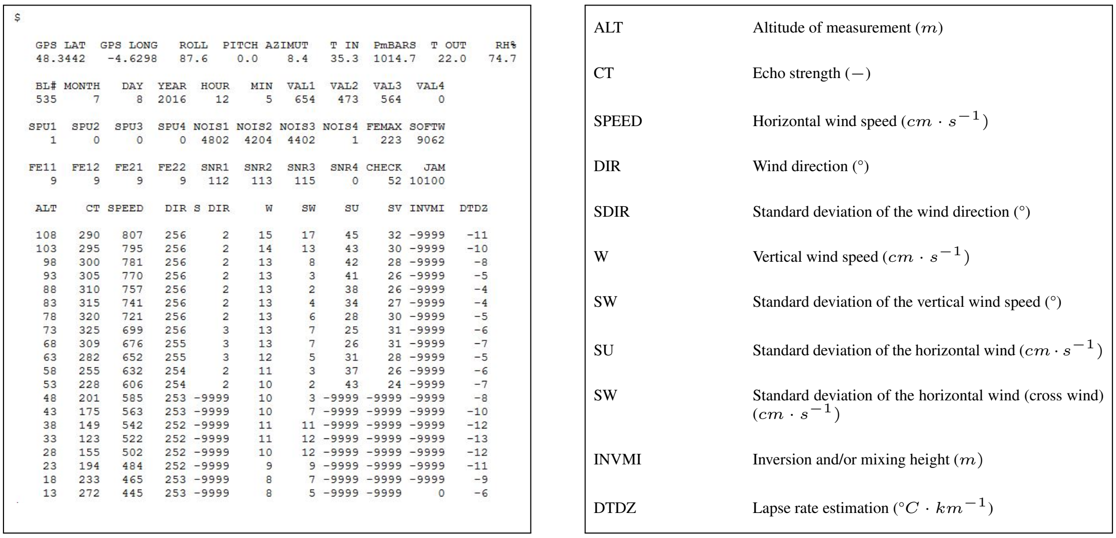

```
$

  GPS LAT  GPS LONG   ROLL  PITCH AZIMUT   T IN  PmBARS  T OUT    RH%
  48.3442   -4.6298   87.6    0.0    8.4   35.3  1014.7   22.0   74.7

  BL# MONTH    DAY  YEAR  HOUR    MIN   VAL1   VAL2   VAL3   VAL4
  535     7      8  2016    12      5    654    473    564      0

 SPU1   SPU2   SPU3   SPU4 NOIS1 NOIS2 NOIS3 NOIS4 FEMAX SOFTW
    1      0      0      0  4802  4204  4402     1   223  9062

 FE11   FE12   FE21   FE22  SNR1  SNR2  SNR3  SNR4 CHECK   JAM
    9      9      9      9   112   113   115     0    52 10100

  ALT     CT SPEED    DIR S DIR     W     SW     SU     SV INVMI  DTDZ

  108    290   807    256     2    15     17     45     32 -9999   -11
  103    295   795    256     2    14     13     43     30 -9999   -10
   98    300   781    256     2    13      8     42     28 -9999    -8
   93    305   770    256     2    13      3     41     26 -9999    -5
   88    310   757    256     2    13      2     38     26 -9999    -4
   83    315   741    256     2    13      4     34     27 -9999    -4
   78    320   721    256     2    13      6     28     30 -9999    -5
   73    325   699    256     3    13      7     25     31 -9999    -6
   68    309   676    255     3    13      7     26     31 -9999    -7
   63    282   652    255     3    12      5     31     28 -9999    -5
   58    255   632    254     2    11      3     37     26 -9999    -6
   53    228   606    254     2    10      2     43     24 -9999    -7
   48    201   585    253 -9999    10      3  -9999  -9999 -9999    -8
   43    175   563    253 -9999    10      7  -9999  -9999 -9999   -10
   38    149   542    252 -9999    11     11  -9999  -9999 -9999   -12
   33    123   522    252 -9999    11     12  -9999  -9999 -9999   -13
   28    155   502    252 -9999    10     12  -9999  -9999 -9999   -12
   23    194   484    252 -9999     9      9  -9999  -9999 -9999   -11
   18    233   465    253 -9999     8      7  -9999  -9999 -9999    -9
   13    272   445    253 -9999     8      5  -9999  -9999     0    -6
```

(a)

ALT	Altitude of measurement (m)
CT	Echo strength $(-)$
SPEED	Horizontal wind speed $(cm \cdot s^{-1})$
DIR	Wind direction (°)
SDIR	Standard deviation of the wind direction (°)
W	Vertical wind speed $(cm \cdot s^{-1})$
SW	Standard deviation of the vertical wind speed (°)
SU	Standard deviation of the horizontal wind $(cm \cdot s^{-1})$
SW	Standard deviation of the horizontal wind (cross wind) $(cm \cdot s^{-1})$
INVMI	Inversion and/or mixing height (m)
DTDZ	Lapse rate estimation $(°C \cdot km^{-1})$

(b)

Figure 3.13.: (a) Example of ASCII data file provided by the SODAR for one measurement point. Column signification is given in (b).

3.4.1.2. Data Importation from External Measurement Points

For the three other measurement platforms, raw ASCII sentences coming from the sensors are recorded into text files. The acquisition software runs automatically when the system is powered. NI modules myRIO are used for this purpose. Thanks to their WiFi feature, data are downloaded each day without wire connection, allowing the procedure to be done even when catamarans are moored, without opening the waterproof box. Raw text files are then converted into MATLAB® structure.

3.4.1.3. Synchronization and Deleting Procedure of Inappropriate Wind Data

All data coming from the different measurement points are then synchronized using absolute time provided by GPS sensors. However, part of the data can be irrelevant, for example due to the motions of the platform during the setting up step when catamarans were towed to their positions. Thus a routine for deleting these data were written, inspired from the one developed for selecting data and presented in Part 3.2.3. User has then to select the unsuitable period of time using the cursor, and delete it.

3.4.2. Weather Model Data

During this experimental work performed in the bay of Quiberon, a partnership has been contracted with the company EXWEXs, specialized in weather modeling. Therefore, a fine weather modeling of the sailing area has been conducted, and data outputted by the model are stored in text files. For one geographic output point, and for one day of modeling, the data consist of multiple files. For the post processing, the relevant data related to one day of measurement, and to one point of output, are stored into a MATLAB® structure, that can be easily accessed by other routines.

4. Fishing Boat Measurement Fieldwork

Résumé

Ce chapitre présente une campagne d'essais et de mesures menée sur un navire de pêche en Gaspésie, province du Québec, Canada, équipé d'un kite de 50 m². A la suite de contacts établis avec un institut québécois spécialisé dans la pêche, un projet de développement et d'essais de kite sur des bateaux de pêche a été mis en place. Ce projet fut porté par beyond the sea, et a mené à l'installation d'un système de lancement et de contrôle du kite sur un chalutier de 13 m et de 90 t de déplacement à pleine charge (visible Fig. 4.1). Deux périodes de tests du système ont dans un premier temps été réalisées hors du cadre de cette étude, et une troisième a été mise en place avec cette fois un objectif de mesure des performances d'un navire tracté par un kite. En effet, en plus d'un système de contrôle du kite, le bateau est équipé de plusieurs capteurs, en particulier en salle des machines, permettant de mesurer la puissance du moteur transmise à l'hélice, ainsi que la consommation de carburant. Durant cette campagne, une première partie avait pour but d'installer des capteurs supplémentaires et de mettre en route toute la chaîne de mesure, une seconde partie était dédiée aux tests des différents systèmes et à la prise en main du kite, et enfin la dernière partie était dédiée à la mesure. Cependant, la disponibilité du bateau a été très inférieure à celle initialement prévue, et sur le peu de jours restants, la météo n'a pas été favorable. Finalement un seul jour a permis des mesures avec le kite en vol statique, mais avec des conditions de vent faible. De ce fait aucune mesure d'économie de carburant n'a pu être réalisée.

Principalement les données acquises relatives à l'effort produit par le kite ont été post traitées, avec comme objectif d'estimer les performances aérodynamiques du kite. Cela a été fait en considérant le kite en permanence en vol statique, et en exprimant l'effort généré par le kite dans le repère vent relatif à l'altitude du kite. Ce repère est reconstruit à partir de la mesure du vent faite sur le bateau, et en prenant en compte l'augmentation du vent avec l'altitude, modélisée par une loi puissance. A partir de là il est alors possible de retrouver la finesse du kite et ainsi que son coefficient de portance. Cependant, les valeurs instantanées obtenues présentent des extrêmes importants et peu réalistes, au cours d'une période d'enregistrement (Fig. 4.10). Ces extrêmes sont probablement la conséquence des hypothèses réalisées, et pas vérifiées en permanence : le vol parfaitement statique et le gradient du vent suivant une loi puissance. De ce fait seul les valeurs moyennes sont considérées au cours de quatre périodes. Les trois premières périodes montrent des résultats cohérents avec ce qui a déjà été publié, mais la quatrième présente un angle de finesse moyen irréaliste dans le cadre d'ailes de kite à boudins (Tab. 4.2). Aucune explication précise n'a été trouvés pour justifier ce problème, la plus probable étant une erreur sur l'estimation de l'angle de vent relatif à l'altitude du kite.

Au final, peu de données ont été acquises pendant cette campagne et aucune en lien avec l'objectif initial, à savoir les économies de carburants. Cependant, cette action a été particulièrement riche en termes de retour d'expérience et a permis d'identifier les problèmes à prendre en compte pour les travaux suivants.

4.1. Fieldwork Presentation

4.1.1. Genesis

A few years ago, during an exchange between French and Canadian laboratories, contacts were made with a Québec Institute named Merinov. This institute, mandated by local government to assist fisheries, has a very large scope of missions, going from fishing resource management, to boats and fishing gears improvements or fish packing plant optimization. At the time, a fisherman and the institute were interested in wind-assisted propulsion, and they were looking for a company developing such a technology. The beyond the sea project was not even launched, but the Ph. D. thesis done by Leloup (2014) was ongoing, and Yves Parlier and his team had already a prototype of kite to put on a boat. An agreement was found to mount on the fishing boat a kite control and launching system, and to perform trials. These type of action can only be carried out at the end of spring or at the beginning of autumn. Indeed,during winter, all boats are out of the water because navigation is not possible due to severe weather conditions, with possible ice packs surrounding the coast. During summer, boats are dedicated to fishing activities. The Québec fishing system is almost exclusively based on master-owner instead of fishing fleet owned by companies and manned by employees. Each master-owner has a fishing license allowing him to catch a certain amount of a specific specie, at a given period of the year, in a given area. With this system, the incomes for a master-owner is limited by the total value of his fishing quota, and then to maximize benefit, the master-owner must reduce costs. The expense items are: crew member salaries, boat and fishing gear amortization, fishing license amortization and of course fuel cost. The first three items are incompressible, but fuel expense can be reduced by improving boat and /or fishing gear efficiency, and then reducing fuel consumption.

Guy Le Blanc, the fisherman interested in kite, is the master-owner of a trawler, named Steven Paul (visible in Fig. 4.1(a)), and is allowed to fish 500 000 pounds of shrimp per year. He is a very curious man, always interested in any new possibility to improve his boat and his trawls. In this context, the addition of a kite on his boat to reduce consumption matched perfectly with his ideas. System assembly and trials have been then carried out during two periods, in October 2014 and May 2015. At the end of the second period, a 50-square-meter kite (see Fig. 4.1(b) and Fig. 4.2) was set up over the boat and a few tacks were done with kite operated in automatic static flight. However this was only a technology demonstration and not a concept validation, and no measurement were done. Therefore it has been decided to complete a real measurement fieldwork using the existing set up. Moreover, at the time the Merinov institute had already mounted on the boat a few sensors, as a fuel flow sensor, a tachometer on propeller shaft and a torque sensor also on propeller shaft. This boat was therefore the ideal platform for measuring effects of kite on propulsion of a professional boat, and particularly the associated fuel savings. This fieldwork was scheduled after the 2015 fishing season, in September 2015.

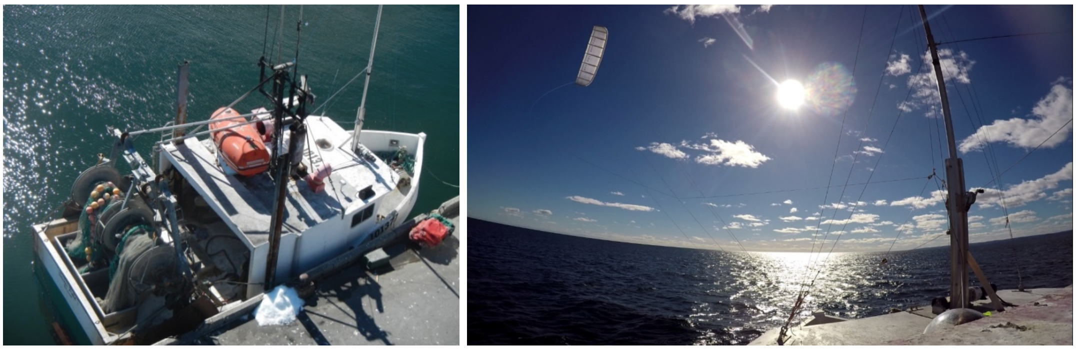

(a) (b)

Figure 4.1.: Pictures of the Steven Paul moored and at sea with a kite.

Figure 4.2.: Picture of the kite of 50 m² used during the trials.

4.1.2. Overview of the Boat

The Steven Paul is a 13-meter long and 4-meter large trawler, with a displacement at full charge of 90 metric tons. The side view is given in Fig. 4.3, with some specific location denoted with marker. In addition to the captain, the boat is manned with 2 crew members. As many boats of the area, the Steven Paul has two stabilizers to reduce roll motion and then to improve living and working conditions. These stabilizers are pulled up along the hull when the boat is moored to a wharf to reduce size impact, but they are deployed as soon as the boat leave the harbor, independently of sea state. The boat is powered by a Caterpillar 480 hp engine and a ducted propeller with a diameter of 1.26 m and four blades. Moreover a grid is protecting propeller from unidentified floating objects or from fishing ropes in case of problem during trawling operation. These features are shown in Fig. 4.4.

A brief overview of a fishing session is given in this paragraph to bring some details and then be able to discuss the significance of a kite on a trawler boat. A fishing session is about 4 or 5 days at sea, and depends on catch quantity, because the objective is to fill the fish hold. It depends also on fishing area that can be far from port (up to 24 h of transit

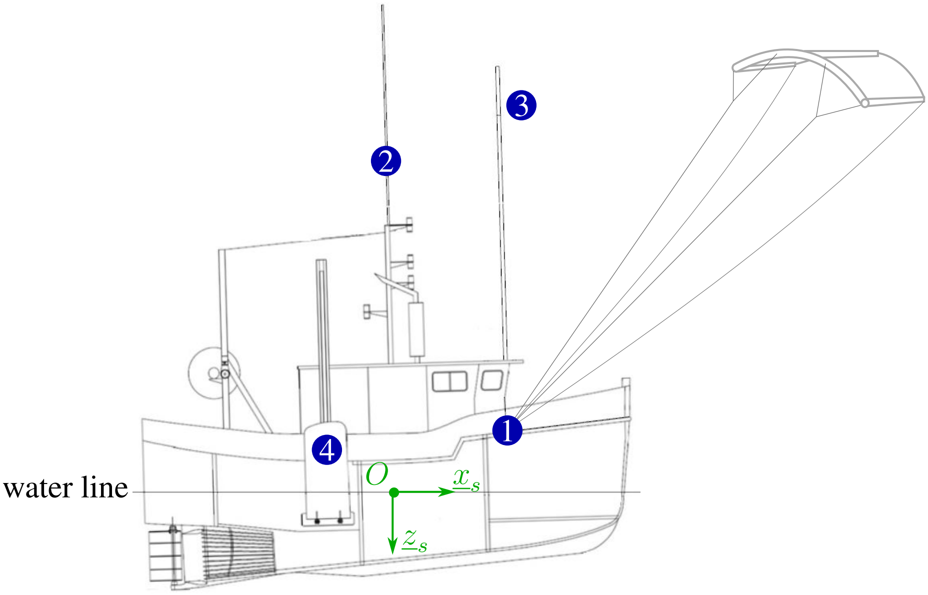

Figure 4.3.: Side view of the Steven Paul with the waterline as it was during trials. Marker 1 denotes the kite attachment point as well as the position of the 3D load cell described in part 2.3.1. Marker 2 shows the position of the anemometer (part 2.6). Marker 3 notes the launching mast used for launching and recovering kite. Marker 4 notices the drawing of the starboard stabilizer. Kite size and tether length are not true to scale.


(a) (b)

Figure 4.4.: Pictures of some specific parts of the boat. Picture (a) shows the propeller of the boat, and picture (b) shows the hydraulic winch for winding the four tethers of the kite. The two external tethers are the back ones, whereas the center tethers are the front ones, with bigger diameter.

at a cruising speed at about 7 kt) or very close (under a couple of hour of transit). Once on site, the trawl is deployed, and 6-hour-runs are done, at a trawling speed at about 2 kt. The fuel consumption during trawling operations is about 70 L per hour. After the run, the trawl is brought back, and shrimps need to be extracted and sorted from the bycatch, and stored with ice in the hold. It takes about 2 hours and half to the crew to get the trawl back, extract catch, re-deploy it and sort shrimps. An average catch during a 6-hour run is about 4 000 pounds of shrimp, and an exceptional one is up to 10 000 pounds. During trawling operations, only minor heading change can be made (maximum 2 °).

4.1.3. Overview of the Kite and Kite Control System

The kite used during trials has an area of 50 square-meters, with an inflatable leading edge, and 9 inflatable battens (see Fig. 4.2). The mass of the deflated kite with bridles is 21 kg. Four 60-meter-tethers linked the kite to the boat. The attachment point of the tethers is located just ahead the forward bulkhead of the wheelhouse, as it can be seen in Fig. 4.3. The tether system is close from the one presented in Chap. 2, but with a specific arrangement to allow the winding of tether on a powered winch. Therefore, for launching and recovering procedures, all tethers are wound on the same hydraulic winch, visible in Fig. 4.4(b), and named Launching Winch in Fig. 4.5. For control purpose, each back tethers goes through a specific pulley system, whose length is adjustable using electric winches, denoted in Fig. 4.5 as Control Winch. These winches, the encoders and the power card associated, are identical to the ones presented in Chap. 2. When all tethers are almost out of the launching winch, a measure front leader line is put in place between the two front tethers and the hoisting eye fixed on the 3D load cell. Then the hydraulic winch is totally unwound, and kite force passes through the measure front leader line. The other leader line coming from the hydraulic winch is slack. Back tether leader lines are still taut. The two front tethers are made with 5 mm Dyneema, whereas back tethers are 3 mm Dyneema ropes.

The control system for control winches has been developed by the beyond the sea® company. It is running on a PC, also with LabVIEW. The program allows only two modes of control: automatic static flight or manual. The automatic one maintains the kite on a specified stationary position, using a small Inertial Measurement Unit (IMU) attached on the kite to get a feedback on kite position and orientation. This autopilot was only able to ensure static flight, which means that the kite could only fly on the wind window edge. However, as it has been developed out of the scope of this study, no more details will be given here. At the time, the automatic pilot for dynamic flight presented in Chap. 3 was not yet developed. Because the whole control system was already onboard before these measurement trials, the kite control system was fully independent from the data acquisition system. The later has already been introduced in Chap. 3.

The launch and recover procedure of the kite are carried out thanks to a fifth tether attached on the middle of the inflatable leading edge, and a launching mast, highlighted in

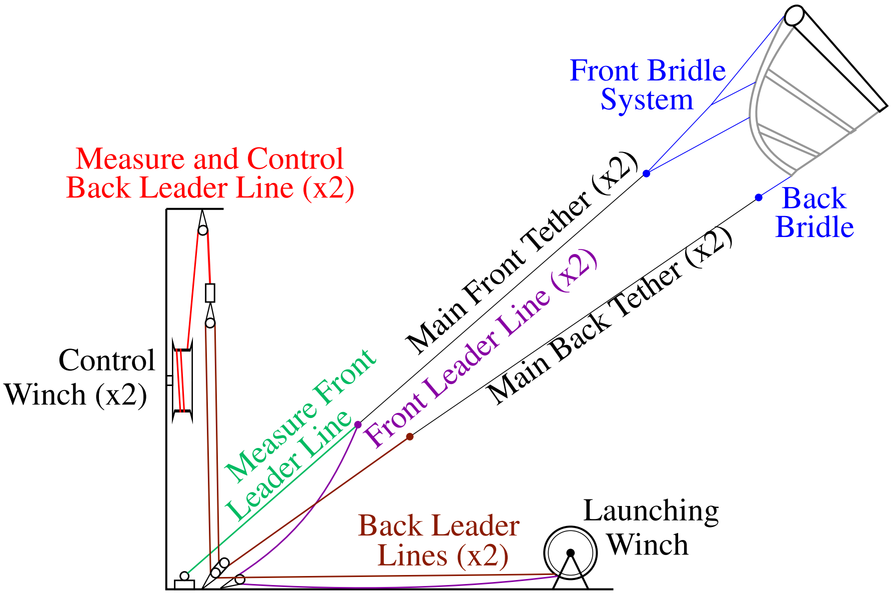

Figure 4.5.: Drawing of the kite attachment and control bridles on boat. Kite side drawing is generic and does not represent faithfully the real kite bridle setting.

Fig. 4.3 with the marker 3, and also visible in Fig. 4.1. The fifth tether was wound on another electric winch located on the top of the roof of the wheelhouse. It is not used for launching, only for recovering. To launch the kite, this one is first hoisted to the top of the launching mast, being hold by the middle of the leading edge, and then the leading edge is inflated. From there, the kite has its own shape and is able to support its own weight. During this moment when the kite is attached to the mast, big oscillations of the kite around the vertical axis were observed. These oscillations could have been damageable for the mast and perhaps for the kite too, and should be taken into account for further work involving launching mast. Then the kite is released from the mast with a quick-release hook activated from the bottom of the mast. From this moment the kite is flying by its own, and tethers could be unwound. As soon as the kite is free, oscillations stop immediately, and only little actions on control winches are required to keep the kite on a zenith position. The unwinding of tethers needs to be slow and controlled to avoid front tethers to become totally slack. Indeed in this case, the kite becomes totally out of control and falls down into the water, with absolutely no possibility to recover a normal flight situation. This phenomena, named frontal fall, occurred one time, not during a launch procedure but during a static flight, probably due to an important wind disturbance.

4.1.4. Proceedings of the Fieldwork

The fieldwork was scheduled on a three week period, and trials should have initially been carried out off the coast of Grande Rivière, a small town of the south shore of Gaspésie (a region of Quebec, located in the south of the gulf of St Lawrence). Grande Rivière is perfectly suited for these type of trials, as the Merinov insitute has its facilities directly on the port, with for example a hangar where kites can be inflated, or workshops. The selected weeks were the last of September 2015 and the first two of October, normally far after the fishing season, the later usually ending in the last days of August. The program for these three weeks was as follows: one week for sensors assembly ans settings, one week for testing all systems and being comfortable with kite launching and control procedures, and the last week dedicated to measurements.

However in 2015 the fisherman did not finished his fishing quota on time, and thus the boat was not fully available for the kite project trials. The mounting work was done nevertheless during the first week as planned, during a couple of days where the boat was in the port between two fishing sessions. However this was done at Mont Louis, in the north shore of Gaspésie, because this was the port for the unloading of shrimps during the season. During the second week, we embarked a first time with the fishermen, but technical problems with the launching mast and the control winches stopped any attempt of launching. We tried again two days after for another session of 3 days and 4 nights of fishing. However, this was finally not possible in spite of several trials, due to the launching system we had on the boat. Indeed for unwinding the first meters of tethers, the boat must stay perfectly downwind, otherwise the kite collides antennas mounted on the top of the wheelhouse. Unfortunately during trawling, the heading of the boat can not be changed, and the heading of the trawling run is ruled by the need to follow an isobath. During the session, the wind was never well oriented or strong enough to launch the kite. Moreover, the boat captain advised us that, in case of kite crash during trawling, the boat could not be stopped, and kite should have to be brought back onboard using the hydraulic winch. This could be very damaging for the kite, and the risk was not taken in order to preserve the equipment for the last week.

Five days before the end of the period, the shrimp quota was finally completed, and the boat was fully available for kite trials. At first, we convoyed the boat from Mont-Louis to Grande Rivière (20h), expecting some wind to do trials, but the wind never exceeded 5 kt. Finally, only two days of trials were achieved, but the first one was lost due to a tether breakage leading to a violent kite crash ending the day prematurely without relevant data. The second day was better and a few runs with kite in static flight were done, however the wind was quite low (about 12 kt) and the kite force was small in comparison with boat size and weight. Moreover no comparative runs with and without kite were done to bring out fuel savings. Despite a very promising set up, few measurements were finally achieved. Therefore the following post processing will only focus on kite performance instead of kite impact on propulsion as intended initially.

4.2. Available Data

Kite data measured during experiments were the force and direction of the front tether, denoted by $\underline{F}_m$, the forces in the left and right back tethers, respectively F_{bl} and F_{br}. Wind data came from one measurement point 9.01 m above mean sea level giving the measured wind velocity vector $\underline{V}_{WM}$. Kinematic boat related data were the boat velocity vector $\underline{V}_s$, the true heading angle ψ of the boat, the roll and pitch angles ϕ_s and θ_s, the rotation speed vector of the boat $\underline{\Omega}_s$, and the boat absolute position Lat and Lon. The engine related data were the rotation speed of the propeller shaft ω, the torque on the propeller shaft Q and the fuel consumption of the engine C. Some videos were taken using GoPro cameras mounted on the top of the wheel house or on the kite.

At the beginning of the last day, maneuverability tests were carried out, taking the opportunity of very low wind period to reduce the effects of boat windage on measurements. These tests are based on ITTC guidelines ITTC (2002). These tests were turning circles at different speed, in both direction, with and without the use of stabilizers. One zig zag test has also been carried out, but a incorrect interpretation of the guidelines led to a non-standard test. Finally a power test has been done to measure boat speed at various engine rpm. All these measurements were used to build and validate a maneuverability and sea keeping model of the Steven Paul. This work was carried out by Bigi et al. (2016) and is out of the scope of this thesis, therefore no result dealing with these tests will be presented.

Finally the only day of measurement we had led to four clean phases with kite in static flight, for a total duration of 23 minutes. These phases have been processed using the equations, assumptions and simplifications presented in the next section. These four periods are presented in Fig. 4.6. During launching procedure, boat was going backward, to have all the foredeck leeward, and to increase the relative wind on kite an then help the launching phase, which was very critical due to wind disturbance created by the boat. The time with no record between Period 2 and 3 is due to an actuator control failure, leading to a kite crash and requiring a complete control system reboot. The time with no record between Period 3 and 4 is due to a power black-out affecting recording system.

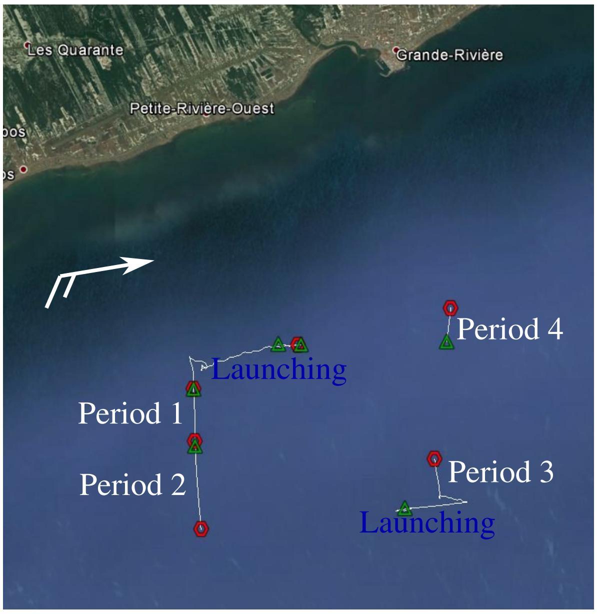

Figure 4.6.: GPS tracks of the measurement runs. The green markers denote the beginning of a record, whereas the red ones denote the end. The white arrow denotes the average wind during all the runs.

4.3. Post processing

Vectors are expressed into the boat reference frame R_ψ, unless otherwise noted. Velocities are given with respect to the Earth, unless otherwise noted.

4.3.1. Boat Related Equations

The velocity of the ship is defined as the the velocity of a point O, with respect to the Earth. This point O is located in the center plane of the boat, at mid-ship, and at the level of the sea surface. The velocity of the ship can be obtained from the velocity of the point U (coming from the measurements of the IMU):

$$\underline{V}_s = \underline{V}_U + \underline{OU} \wedge \underline{\Omega}_s \tag{4.1}$$

The rotation speed vector of the boat$\underline{\Omega}_s^{(s)}$ (expressed in the ship reference frame R_s) is directly the measurement of the turn rates (p, q, r) provided by the inertial measurement unit. Thus $\underline{\Omega}_s$ expressed in R_ψ can be obtain using the following transfer matrices:

$$\underline{\Omega}_s = (\underline{\underline{M}}_{\theta_s} \underline{\underline{M}}_{\phi_s}) \underline{\Omega}_s^{(s)} \tag{4.2}$$

4.3.2. Wind Related Equations

The onboard wind measurement are first computed in the heading reference frame:

$$\underline{V}_{WM} = (\underline{\underline{M}}_{\theta_s}\underline{\underline{M}}_{\phi_s})(\underline{\underline{M}}_{\psi_w}\underline{\underline{M}}_{\theta_w}\underline{\underline{M}}_{\phi_w})\underline{V}_{WM}^{(ws)} \tag{4.3}$$

Then, the relative wind velocity at the altitude of the measurement point z_0 can be computed, taking account velocity of wind sensor with respect to the point O belonging to the boat:

$$\underline{V}_{WR,z_0} = \underline{V}_{WM} - \underline{V}_{W/O} = \underline{V}_{WM} + \underline{OW} \wedge \underline{\Omega}_s \tag{4.4}$$

From there, the true wind speed at measurement point can be calculated:

$$\underline{V}_{WT,z_0} = \underline{V}_{WR,z_0} + \underline{V}_s \tag{4.5}$$

And also the true wind speed at any other altitude z, and so at kite altitude $|Pz|$, using ITTC (2014) formula.

$$\underline{V}_{WT,z} = \left(\frac{z}{z_0}\right)^{1/7} \underline{V}_{WT,z_0} \tag{4.6}$$

$$\underline{V}_{WT} = \left(\frac{|Pz|}{z_0}\right)^{1/7} \underline{V}_{WT,z_0} \tag{4.7}$$

The relative wind at the kite altitude can be obtained by subtracting the velocity of the kite attachment point $\underline{V}_A$ to the true wind speed at kite altitude (because tethers are considered as perfectly straight, attachment point motions are entirely transmitted to the kite):

$$\underline{V}_A = \underline{V}_s + \underline{AO} \wedge \underline{\Omega}_s \tag{4.8}$$

$$\underline{V}_{WR} = \underline{V}_{WT} - \underline{V}_A \tag{4.9}$$

4.3.3. Kite Related Equations

At first, forces into front tether are computed in the heading reference frame instead of the frame of the boat, otherwise, boat motions are visible on 3D load cell measurement :

$$\underline{F}_f = \underline{\underline{M}}_{\theta_s}\underline{\underline{M}}_{\phi_s}\underline{F}_m \tag{4.10}$$

Then, back tether forces are added to front tether vector, to create the total kite force vector $\underline{F}_k$ at kite attachment point A on the boat:

$$\underline{F}_{k,A} = \frac{\underline{F}_f}{\|\underline{F}_f\|}(\|\underline{F}_f\| + F_{bl} + F_{br}) \tag{4.11}$$

With the hypothesis of perfectly straight tethers with constant length, the total kite force vector at attachment point on the boat is equal to the opposite of the force generated by the kite at kite position (see Fig. :

$$\underline{F}_k = -\underline{F}_{k,A} \tag{4.12}$$

With the same assumption, the kite position $\underline{P}_k$ can also be computed:

$$\underline{P}_k = \frac{\underline{F}_f}{\|\underline{F}_f\|}L_t \tag{4.13}$$

Considering the zero-mass model, as introduced in Chap. 1, the aerodynamic force $\underline{F}_a$ generated by the kite is directly equal to the opposite of the force generated by the kite at kite position:

$$\underline{F}_a = -\underline{F}_k \tag{4.14}$$

However, the weight of the kite can be considered, in the previous equation, even if kite accelerations are neglected because the flight was almost static. Therefore, the previous equation becomes:

$$\underline{F}_a + \underline{F}_k + \underline{p}_k = \underline{0} \tag{4.15}$$

The diagram of forces associated with this equation is given Fig. 4.7.

The definition of the relative wind vector$\underline{V}_{WR}$ allows us to define the relative wind reference frame R_{wr} as explained in the Reference Frames chapter. Therefore aerodynamic kite force can be expressed in this reference frame as follows:

$$\underline{F}_a^{(wr)} = \underline{\underline{M}}_{\zeta_{wr}}^{-1}\underline{\underline{M}}_{\chi_{wr}}^{-1}\underline{F}_a \tag{4.16}$$

With the hypothesis that the kite is always in static flight, as defined Part 1.3.1.2, the apparent wind on the kite equals the relative wind at kite altitude. Therefore, the aerodynamic reference frame and the relative wind reference frame are equal, and lift and drag vectors can be easily obtained:

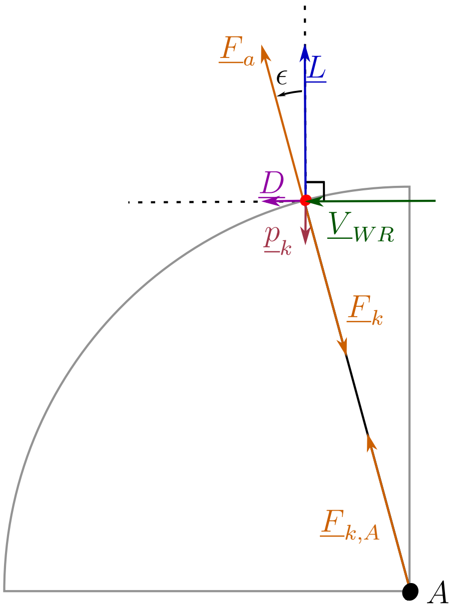

Figure 4.7.: Force diagram of the model used for processing data, associated with Eq. 4.15. For the simplicity of the diagram, kite force, kite weight and relative wind velocity vector are drawn in the same plane, however this is a particular case.

$$\underline{D} = F_{a,1}^{(wr)} \underline{x}_{wr} \tag{4.17}$$

$$D = F_{a,1}^{(wr)} \tag{4.18}$$

$$\underline{L} = F_{a,2}^{(wr)} \underline{y}_{wr} + F_{a,3}^{(wr)} \underline{z}_{wr} \tag{4.19}$$

$$L = \sqrt{F_{a,2}^{(wr)2} + F_{a,3}^{(wr)2}} \tag{4.20}$$

Finally lift to drag ratio and lift coefficient follow on.

$$f = \frac{L}{D} = \frac{\sqrt{F_{a,2}^{(wr)2} + F_{a,3}^{(wr)2}}}{F_{a,1}^{(wr)}} \tag{4.21}$$

$$C_l = \frac{\sqrt{F_{a,2}^{(wr)2} + F_{a,3}^{(wr)2}}}{\frac{1}{2}\rho A_k V_{WR}^2} \tag{4.22}$$

4.3.4. Neglected Elements and Simplification

The rotation rates of the boat (p, q, r) during measurement runs were below 0.03 rad/s. With an anemometer located 9 m above the surface, the induced velocity of the measurement point in the heading reference frame is under 0.3 m/s. This value is under the sensor sensitivity which is equal to 0.5 m/s. Therefore, $\underline{OW} \wedge \underline{\Omega}_s$, the last term of Eq. 4.4 is taken equal to 0. In the same way, the velocity of kite attachment point $\underline{V}_A$with respect to the point O is taken equal to zero, and the velocity of the ship $\underline{V}_s$ is taken equal to the velocity outputted by the IMU $\underline{V}_U$. Moreover, the ship velocity $\underline{V}_s$ is considered as being all the time contained in the horizontal plane. Furthermore, the anemometer is only 2D, therefore the change of reference frame, from the ship one to the heading one, is also neglected. In other words, θ_s and ϕ_s are taken equal to 0 in Eq. 4.3 and the associated matrices equals the identity matrix. Without this simplification, the boat motions, and change of the reference frame associated, will induce vertical components, which will be normally added and eventually compensated by measurements in case of a 3D anemometer. However, with our 2D anemometer this is not possible. Lastly, the anemometer was mounted on the boat with an angle ψ_w equals to $\pi/2$, and the two other angles equal 0. Thus the relative wind at kite altitude can be simplified and written in this way:

$$\underline{V}_{WR} = \left(\frac{|Pz|}{z_0}\right)^{1/7} \left(\underbrace{\overbrace{\underline{\underline{M}}_{\psi_w} \underline{V}^{(ws)}_{WM}}^{\underline{V}_{WR,z_0}} + \underline{V}_s}_{\underline{V}_{WT,z_0}} \right) - \underline{V}_s \tag{4.23}$$

With this equation, thanks to the previous simplifications, the relative wind vector is contained in the horizontal plane, leading to the z_{wr}-axis identical to the z_{ψ}-axis, and the ζ_{wr} angle equals 0. Consequently, the weight of the kite can be easily expressed in the relative wind reference frame, and then taken into account in the lift to drag ratio and lift coefficient calculations:

$$f = \frac{\sqrt{F_{k,2}^{(wr)2} + (F_{k,3}^{(wr)} + p_k)^2}}{F_{k,1}^{(wr)}} \tag{4.24}$$

$$C_l = \frac{\sqrt{F_{k,2}^{(wr)2} + (F_{k,3}^{(wr)} + p_k)^2}}{\frac{1}{2}\rho A_k V_{WR}^2} \tag{4.25}$$

4.4. Results

Main averaged values for the four cases considered in this study are presented in Tab. 4.1. The duration of each run t_r is given in the second column.

Case Name	t_r (s)	$\mu_{\overrightarrow{V_s}}$ (m/s)	$\mu_{\overrightarrow{V_{WT}}}$ (m/s)	$\mu_{\overrightarrow{\beta_{WR}}}$ (°)	$\mu_{\overrightarrow{F_k}}$ (N)	C_k (-)
Period 1	400	2.2	6.9	70	661	0.45
Period 2	568	2.4	7.1	76	787	0.51
Period 3	209	2.6	8.0	-38	774	0.40
Period 4	190	2.9	6.9	-60	537	0.36

Table 4.1.: Summary table of average results for the 4 runs studied.

From there, as defined in the Nomenclature, an over-right-arrowed quantity denotes a time series, and the associated time line is the one related to the result of the conditional phase averaging method. The letter μ denotes the average value of a time series. Thus, the last column presents the value of the kite coefficient, and defined as follows:

$$C_k = \frac{\mu_{\overrightarrow{F_k}}}{\frac{1}{2}\rho A_k \left(\mu_{\overrightarrow{V_{WR}}}\right)^2} \tag{4.26}$$

It can be noticed that the kite force is about 700 N, for a kite weight of 225 N. Therefore kite weight is not negligible in comparison with kite force and taking account weight in Eq. 4.25 and 4.27 is important.

4.4.1. Impact of Boat Motions on 3D Load Cell Measurement

If the boat motions have been neglected for the wind calculations, this is not possible for kite force data coming from the 3D load cell measurements. This is visible in Fig. 4.8, where measurements of the kite elevation angle are given in the ship reference frame R_s and in the heading reference frame R_ψ. These kite elevation angles are obtained by transforming cartesian coordinates into polar coordinates as presented in Fig. 7. The boat pitch motion is also plotted in the right axis. It appears that the elevation angle in the ship reference frame evolves in line with the pitch motion. That shows the importance of the change of reference frame associated with Eq. 4.10.

4.4.2. Kite Position Signals during the Four Periods

Kite positions has been computed in the relative wind reference frame for the 4 periods, and results are plotted in 3D in Fig. 4.9. The boat position is denoted by a red triangle, and the orientation of the boat is defined using the average value of the relative wind relative angle. Indeed, the position of the boat in the relative wind reference frame is usually not a time-constant. The first two cases show the boat sailing on starboard tack whereas the two others are related to the boat sailing on port tack.

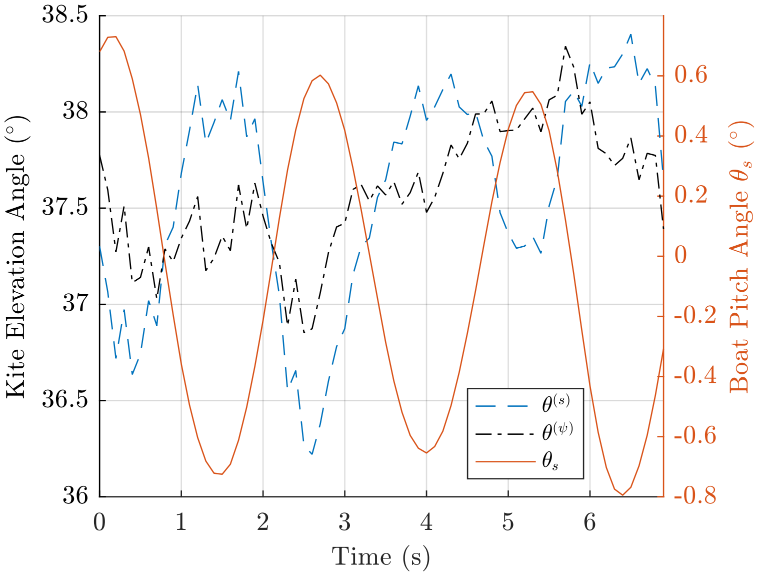

Figure 4.8.: Impact of boat motion on kite position measurement during a static flight period. The blue line shows the evolution of the kite evolution angle expressed in the boat reference frame, and this evolution is in line with pitch motion of the boat (orange line). The black dash dotted shows the evolution of the kite elevation angle expressed in the heading reference frame.

The kite positions are spread out on the wind window, and create in fact a cloud of points. If the kite flight is perfectly static, as defined in Part 1.3.1.2, only one point should be visible for each case of Fig. 4.9, instead of a cloud of points. But in fact, wind relative reference frame is estimated from a measurement over the boat, and from a power formula to catch the evolution along the altitude. Thus, real relative wind has no chance to be equal to the estimation at all time. Moreover, when the kite undergoes wind variations, the angle of attack of the kite evolves, then the lift to drag ratio of the kite evolves too, and the position of the wind window edge moves consequently. Therefore, at the new angle of attack, the kite is no longer located on the wind window edge, and needs to move towards the new one. These induced motions can be forward or backward, and generate a kite velocity which will also affect the angle of attack. Little control actions to keep the kite at a given elevation angle also lead to drift motion. These various elements explain why the kite position is not a single point during a static run. Therefore the lift to drag ratio and the lift coefficient cannot be constant during a run, and only an average value will be finally considered.

A specific attention needs to be brought to the fourth case. Indeed, the cloud of points is much closer from the wind window edge than the others, with some points with negative coordinate along the x_{wr}-axis. This means the kite at these moments creates a negative drag. This is of course not realistic, and points out a measurement issue that will be discussed later. Moreover, very low drags generate very high lift to drag ratios, and this

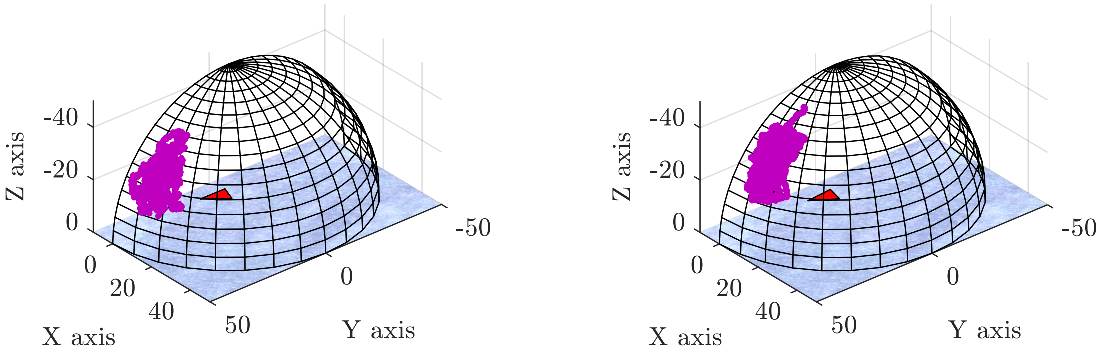

(a) Period 1

(b) Period 2

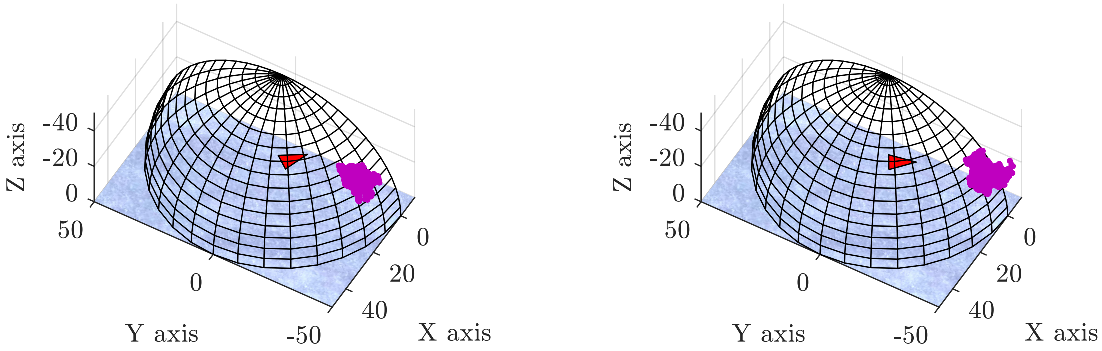

(c) Period 3

(d) Period 4

Figure 4.9.: Evolution of kite position expressed in the relative wind reference frame for the 4 considered cases. The red triangle denotes the boat position, and her orientation depends on the average relative wind vector at kite altitude during the run.

makes lift to drag ratio signals difficult to analyze. Therefore the lift to drag angle ϵ will be preferred as defined by the following equation:

$$\epsilon = \arctan(\frac{D}{L}) = \arctan\left(\frac{F_{k,1}^{(wr)}}{\sqrt{F_{k,2}^{(wr)2} + (F_{k,3}^{(wr)} + p_k)^2}}\right) \tag{4.27}$$

4.4.3. Example of Lift to Drag Angle and Lift Coefficient Signals

Figure 4.10 presents the evolution of the lift to drag angle and the lift coefficient during the Period 1. Important variations are observed, and these variations do not reflect the real evolution of the kite parameters. Indeed no kite settings, and specially trim, were

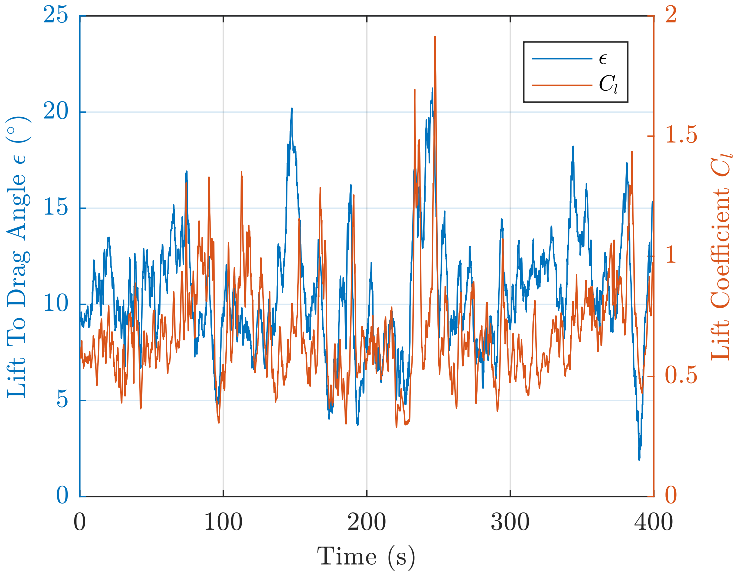

Figure 4.10.: Signals of the lift to drag angle and lift coeffcient of the kite during Period 1, calculated respectively from Eq. 4.27 and Eq. 4.25.

modified during run, and neither between the four periods. These variations are probably induced by the incorrect estimation of the wind at kite altitude.

4.4.4. Average values of Lift to Drag Ratio and Lift Coefficient Signals during the 4 runs

Table 4.2 provides summary results on the lift to drag angle and the lift coefficient for the 4 cases. Data are almost consistent between cases, except for the fourth one, with a lift to drag angle more than two times lower than the other cases (equivalent to a lift to drag ratio about 14). This is not really surprising regarding kite position during Period 4 presented in Fig. 4.9(d). This result is not realistic for leading edge inflatable kites, and seems to confirm a measurement issue already introduced in the subsection 4.4.2. Moreover, the standard deviation associated to this period is consistent with the other runs.

Otherwise, results are in agreement with other ones published in the literature, for example by Dadd (2012), or by Fagiano et al. (2014). Therefore, the average lift to drag angle for the first three cases, weighted by the duration of each period, is found equal to 10.6°, corresponding to a ratio of 5.3, and the lift coefficient is found equal to 0.70. For a 3-square-meter kite with an aspect ratio AR of 4.9, Dadd got a lift coefficient of 0.78 and a lift to drag ratio of 6.07. To estimate drag coefficient and so lift to drag ratio of other kites with other aspect ratios, Dadd uses Prandtl's formula as presented in Abbott and Von Doenhoff (1959) and given by Eq. 4.28, assuming both kites are trimmed to produce

Case Name	$\mu_{\overrightarrow{\epsilon}}$ (°)	$\sigma_{\overrightarrow{\epsilon}}$ (°)	$\mu_{\overrightarrow{C_l}}$ (°)	$\sigma_{\overrightarrow{C_l}}$ (°)
Period 1	10.6	3.1	0.68	0.21
Period 2	10.4	3.0	0.76	0.26
Period 3	11.4	2.6	0.59	0.17
Period 4	4.1	3.0	0.59	0.26

Table 4.2.: Summary table presenting lift to drag angle and lift coefficient average values the 4 runs studied, and their standard deviations.

the same lift coefficient C_l, equals in the case of the present study to 0.70. Applying this method to the kite used for the present study (aspect ratio of 5.5), the expected lift to drag ratio should be 6.34.

$$C'_d = C_d + \frac{C_l}{\pi}\left(\frac{1}{AR'} - \frac{1}{AR}\right) \tag{4.28}$$

4.4.5. Effect of the Kite on Propulsion

Due to the unexpected unavailability of the boat as already explained, the assessment of the effects of the kite towing force on the propulsion chain could not be achieved.

Nevertheless, a comparison can be done between power supplied by the kite, and power delivered by the engine to the propeller thanks to the sensors that were installed on-board. For example for the Period 2, on the engine side, the average rotation speed of the propeller shaft ω is 3.4 revolutions per second (21.3 rad/s), and the average torque on the propeller shaft Q is 1800 Nm. The total power provided by the engine to the propeller is then 38 kW. On the kite side, the average propulsive force generated by the kite $F^{(s)}_{k,1}$ is 505 N, the average speed of the boat is 2.4 m/s, so the average power is 1.2 kW. Assuming a propulsive efficiency of 50% for the boat (Bigi et al. (2016)), the kite therefore provides almost 6 % of the propulsive power, with only 6.1 m/s of true wind speed, and in static flight condition.

4.5. Discussion

As it has been introduced, the fourth case is really problematic, with a not realistic estimation of the lift to drag angle, in comparison to the other cases, or to other published results. The most probable issue comes from the wind estimation at the kite altitude. Indeed, in the theoretical case of a kite in static flight, therefore located on the wind window edge, with no mass, the position of the kite in the relative wind reference frame is ruled by the Eq. 1.4. From there, the azimuth angle can be calculated, knowing the lift to drag angle and the elevation angle:

$$\phi_{WR} = \arccos\left(\frac{\sin(\epsilon)}{\cos(\theta_{WR})}\right) \tag{4.29}$$

To get a lift to drag angle equals to a relevant value according to the other periods, for example 11°, the azimuth angle should be equal to 77° (with an elevation angle of 30°, which is an average value during the Period 4). However, in the present case, the azimuth angle is about 85°. Therefore a deviation of 8° of the azimuth angle with respect to the relative wind reference frame is necessary to retrieve consistent data. These deviation can be seen as a measurement error of the relative wind angle β_{WR}, since this angle defines the wind relative reference frame.

This deviation of 8° is far above the sensitivity of the sensor. However it is not a large value and three possible explanations exist: the wind at the sensor level was disturbed by an element of the boat, the true wind was twisted along the altitude or the angle of the sensor with respect to the boat has changed. There is no evidence that can favor one hypothesis among the others, and no conclusion of this issue can be brought.

The amount of data obtained during this work is very low, with respect to the time spent for preparing and carrying out these sea trials. Indeed the scientific results which has been presented regarding the lift to drag ratio and the lift coefficient, are simply a validation of already known elements. Moreover no measurement of fuel savings could have been achieved, in spite of an engine room well equipped with sensors. However, this work has been a very valuable learning experience, and the feedback has been used to prepare and carry out the other experimental works that are presented in the following chapters. In particular, emphasis has been placed on wind measurements and wind estimation at kite altitude. Moreover, a new strategy has been considered to get an experimental platform suitable for sea trials fully available.

5. Onshore Measurement Fieldwork

Résumé

L'un des objectifs de cette action de recherche est de réussir à estimer les paramètres aérodynamiques du kite le long de sa trajectoire, en particulier sa finesse et son coefficient de portance. Jusqu'à présent aucune évolution de ces paramètres n'est prise en compte dans le modèle zero-mass développé par Leloup (2014) et présenté au Chap. 1. En effet, cela peut être un problème car les amplitudes d'efforts induits par les variations des caractéristiques aérodynamiques peuvent être plus grandes que celles prédites par le modèle. Cela peut donc impacter le dimensionnement structurel des actionneurs, des lignes, des tissus, tant au niveau des efforts maximums possibles qu'au niveau de la fatigue. Par ailleurs, une forte amplitude d'effort peut aussi affecter la stabilité du navire. Au regard de la déformation du kite en vol pendant un virage, visible Fig. 5.1, il est fort possible que des variations de ces caractéristiques existent.

Pour estimer cela, une campagne de mesure à terre a été réalisée, avec le système expérimental présenté aux deux chapitres précédents, déployé dans un champ à une position fixe. La campagne de mesure précédente réalisée sur un bateau de pêche a montré l'importance de la mesure du vent pour pouvoir remonter aux caractéristiques du kite, et en particulier l'importance de connaître le vent a l'altitude du kite. Cependant cela n'est pas une donnée facilement accessible, avec un kite pouvant évoluer entre 10 et 70 m d'altitude. Pour régler ce problème, un profileur vertical a été utilisé, basé sur une technologie sonore. Grace à cela, le profil du vent au-dessus du site de mesure pouvait être connu, en étant moyenné toutes les 5 min. Le pilote automatique du kite a permis de réaliser de nombreux enregistrement de vol dynamique, avec un kite réalisant des trajectoires en huit de façon répétables. Ainsi, au cours des 15 jours où les conditions météo étaient propices à la réalisation de mesures, de nombreuses phases de vols de 10 min ont été enregistrées, avec un kite à boudins de 5 m². Aucune mesure n'a pu être effectuée dans un vent supérieur à 11 m/s.

Un post traitement particulier a dû être mis en place pour traiter les données, car la période moyenne des trajectoires est d'environ 6 s, mais l'évolution du vent donnée par le profileur vertical n'est pas disponible à cette fréquence. Un post traitement par moyenne de phase a donc été utilisé, afin de rappporter statistiquement toutes les trajectoires d'un enregistrement à une seule trajectoire moyenne et à une variance. Ceci permet de gommer l'influence des variations du vent à l'échelle d'une trajectoire. Lors du processus de moyenne de phase une détection conditionelle, basée sur l'intercorrélation des signaux entre eux, a été exploitée pour discriminer les trajectoires et supprimer de l'analyse celles trop extrêmes. Les signaux issus de ce processus sont ainsi très lissés (Fig. 5.9), et permettent un calcul des caractéristiques aérodynamiques du kite.

Les données ont été dans un premiers temps regardées de façon générale. Les résultats obtenus permettent de confirmer en partie des valeurs utilisées jusqu'à présent par le consortium, comme par exemple la distribution de chargement entre lignes avants et lignes arrières, ou la quasi linéarité de la commande par rapport au taux de rotation du kite. La charge alaire typique de 1 kN/m² n'a en revanche pas été atteinte, car des phénomènes de flambement importants des boudins sont apparus avant (Fig. 5.12).

Pour calculer le coefficient de portance et la finesse du kite, une première hypothèse a été utilisée : les lignes sont considérées comme parfaitement droite et de tailles constantes. De ce fait, la position du kite est calculée directement en connaissant la mesure de l'angle des lignes au niveau du sol. Par ailleurs, l'analyse préliminaire des données a montré que le kite subissait au cours des trajectoires en huit des accélérations pouvant générer des forces inertielles non négligeables. De ce fait, un nouveau modèle physique du kite a été introduit, et comparé au modèle zero-mass. Ce modèle considère le kite comme ayant une masse concentrée en un point. La comparaison des deux modèles a montré que les accélérations ont en effet une influence sensible dans le calcul des caractéristiques aérodynamiques du kite (Fig. 5.15). Ce modèle a donc été conservé par la suite. Le post traitement a bien mis en évidence des variations de la portance et de la finesse le long de la trajectoire en huit (Fig. 5.16 et 5.18), et les valeurs moyennes obtenues pour ces caractéristiques sont cohérentes avec la littérature (Dadd (2012);Fagiano et al. (2014)). Cependant, il n'a pas été possible de lier ces variations avec le taux de rotation du vecteur vitesse du kite, car les différents cas considérés ne convergent pas vers un schéma standard (Fig. 5.17 et 5.19). De plus un problème de symétrie du kite a été mis en évidence, ce qui vient perturber les mesures et l'analyse des résultats ou l'interprétation.

Une analyse théorique des incertitudes a été conduite, et montre une importante marge d'erreur sur le calcul des caractéristiques du kite (Fig. 5.21). De nouvelles phases de mesures seraient pertinentes à mener, en portant une attention particulière au problème de symétrie, et en travaillant à réduire les incertitudes, sur la base de ce qui a été déjà fait. De cette façon de meilleurs résultats pourraient être obtenus, et une tendance plus nette concernant l'évolution des caractéristiques aérodynamiques pourrait peut-être être mise en évidence. Cependant, une loi linéaire d'évolution est tout de même proposée, basée sur les meilleures phases de mesure.

5.1. Fieldwork Presentation

5.1.1. Genesis

One of the objectives of the research action is to experimentally benchmark average kite performances predicted by modeling approaches presented in Chap. 1, and to refine the evolution of kite specifications along an 8-pattern trajectory. Indeed, these variations are not taken into account with the zero-mass model developed by Leloup (2014) and presented in Chap 1. However, regarding the deformation of the structure of the kite during a turn, as shown in Fig. 5.1, it is very probable to get a variation of these specifications, with respect to the turn rate of the kite for example.

To the question of the best strategy required to achieve these objectives, the answer of an experimental work carried out onshore has become rapidly obvious. Indeed, kite performance assessments can be disconnected from boat motions, which is useful to stay focused on the kite itself. Moreover, onshore experiments are easier to achieve, with less consideration about sea water robustness of the experimental set up, and less human and material resources required.

The onboard experimental fieldwork held before this one and presented in Chap. 4 highlighted the importance of wind measurements, and particularly the wind measurement at kite altitude. However this measurement is a complex one to obtain, with a kite flying between 10 m and up to 70 m high. The built of a wind measurement mast is not a reliable option regarding costs and authorization required to put up such a device. Moreover, a 70-meter mast and associated rigging could affect seriously the wind leeward the mast, and then be detrimental to good kite flight conditions. Thus, the option of wind profilers has been explored, with two possibilities : the one using sonic technology (SODAR), and the other based on laser (LIDAR). These types of devices are not usual, and thus the choice between the two possibilities was made according to which device was available locally.

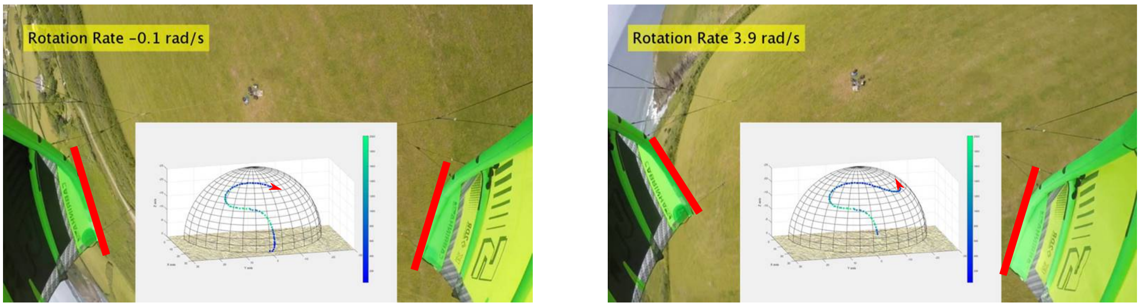

(a) (b)

Figure 5.1.: Kite's structure deformation during a kite turn (b) with high rotation rate, in comparison with quasi straight trajectory (a) with low rotation rate.

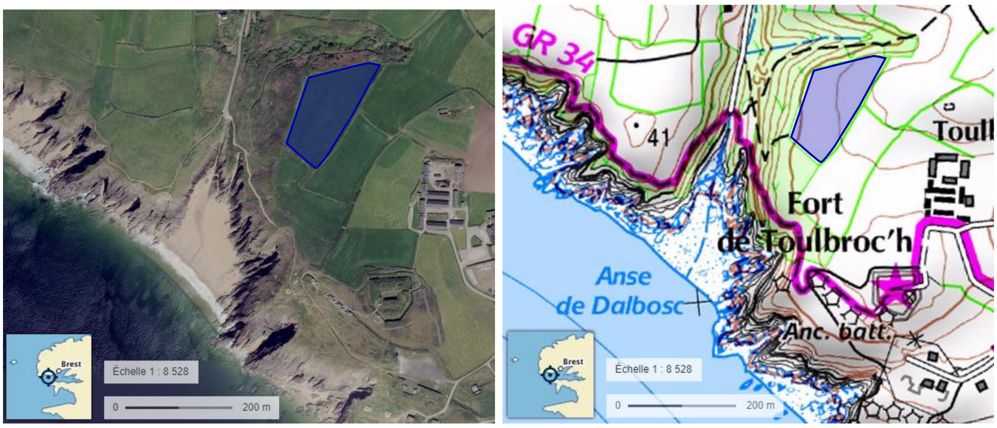

(a) (b)

Figure 5.2.: Geographic situation and topographic map of the field where experimental onshore measurements took place, denoted with a blue overlay (image source www.geoportail.gouv.fr/).

A local company owning a SODAR wind profiler was contacted, and a rental agreement was signed for one month of measurement, including setting-up and dismounting of the device. For a proper functioning, the SODAR needs to be set-up perfectly horizontally, and needs 24 hours of auto calibration. Thus the SODAR could not be mounted and dismounted every day, and a field had to be found, adapted to kite experiments, and available for one whole month.

5.1.2. Measurement Site Situation

With the help of a the company providing the SODAR, a field has been found near Brest, large enough to allow kite launch and measurements for any wind orientation, with 80-meter tether length. The geographic situation of the field is given in Fig. 5.2, together with the topographic map. As shown in the figure, this field is near the sea, and with a wind orientation of south-west (the dominant wind), the field receives wind directly from the sea. Thus the wind profile when the wind arrives on the shoreline should reasonably not be too far from the wind profile occurring offshore, and then relatively smooth and not to disturbed by interactions between flow and rough and irregular surface. However, although the field is relatively flat, it is located about 55 m above mean sea level, as mentioned on the topographic map given in Fig. 5.2. This leads to an alteration of the wind profile, with the possible appearance of a non-negligible vertical component of the wind. This point will be discussed later with the support of SODAR data.

The SODAR was located near the middle of the field, as shown in the satellite picture given in Fig. 5.3. Depending on wind orientation and tether length configuration (up to 80m), the ground station was deployed around the SODAR position to ensure enough space for the take off and landing of the kite.

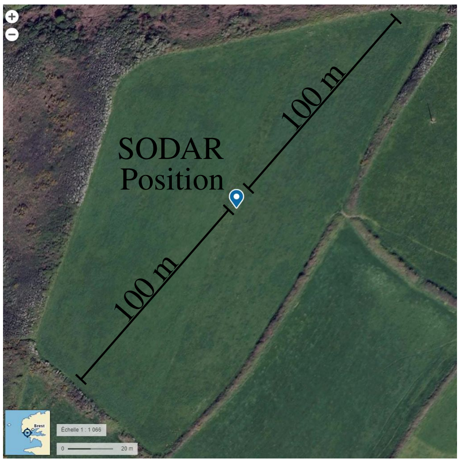

Figure 5.3.: Field size and SODAR position (image source www.geoportail.gouv.fr/).

5.1.3. Proceedings of the Fieldwork

The SODAR was in place from the 1st of June 2016 to the 8th of July 2016, ensuring measurement from 6am to 20pm UTC (measurements were stopped during night to avoid disruption of local residents, as SODAR generates sounds which can be annoying). Depending on weather conditions of the day, and especially wind intensity, the decision to go to the measurement site was taken. The minimum wind intensity to ensure a proper flight of the kite was 8 kt. To get an overview of the current wind on site, several means were available, as the network of anemometers is spread over Finistère department (Diabox[1]), but the most useful was the possibility to access to the SODAR data stored on an FTP server, through the mobile phone network. Once the measurement team (at least two people, one for launching the kite and the other to control the actuators, the autopilot and the data acquisition) was on site, the ground station was deployed according to wind direction, and data acquisition could be started. The objective was to realize as many 8-pattern trajectories as possible, with a good reproducibility. Various autopilot settings were then tried to achieve this purpose. Depending on wind conditions and kite behavior, it was not always possible to get a fair reproducibility, leading to data with very limited interest. Thus, the first days of the fieldwork were more focused on autopilot setting optimization, and then relevant data were more stemmed from the last week of measurement. At the end of the day of measurements, data were downloaded from the system, and a report presenting data and the most important facts of the day was written. Some videos have been made during the month of experiments, and can be watched on YouTube[2].

---

[1] http://pubs.diabox.com/?page=survey

[2] https://www.youtube.com/watch?v=77FKwKODCcA


(a) (b)

Figure 5.4.: The two 5 m² kites used during the onshore fieldwork: (a) is the North Rebel and (b) is the Cabrinha Switchblade.

5.1.4. Kites Involved during the Fieldwork

The fieldwork started with the kite used for first trials, namely a 2013 North Rebel 5 m² with five battens, and the autopilot development. However this kite was worn out by the numerous crashes that it underwent during the development period, and it broke on the 3rd day of measurement. It has been repaired but a second kite was bought to realize measurement with a brand new kite. Thus the second is a Cabrinha Switchblade 2016 5 m², also with five battens. Both are visible in Fig. 5.4. The choice of the size of the kites was ruled by the range of the load cells, assuming that kites can generate up to 1 kN per square meter of area.

5.2. Available Data

Kite data measured during experiments are the force and the direction of the front tether, denoted by $\underline{F}_m$, the forces in the left and right back tethers, respectively F_{bl} and F_{br} , and the variable part of the length of the back tethers, which accounts for the position of actuators $\lambda 1$ and $\lambda 2$. The wind data are measured from three different devices, presented in Part. 2.6.2. However, the CV7 anemometer was only at an altitude of 4 m and was then very disturbed by ground proximity. Moreover, a damage of the device has been found at the end of the fieldwork leading to a false wind direction outputted by the sensor. Thus, data from this device are not taken into account in the following work. The two other wind measurements come from the SODAR and the METEK, but the second one was only in place the last two days. An example of a measurement done with the SODAR is given in Fig. 5.5. Some videos and pictures have also been taken using camera such as GoPro, reflex or hybrid camera. Fifteen days of measurement have been carried out, generating more than 15 hours of kite flight recording, and identified as potential relevant data.

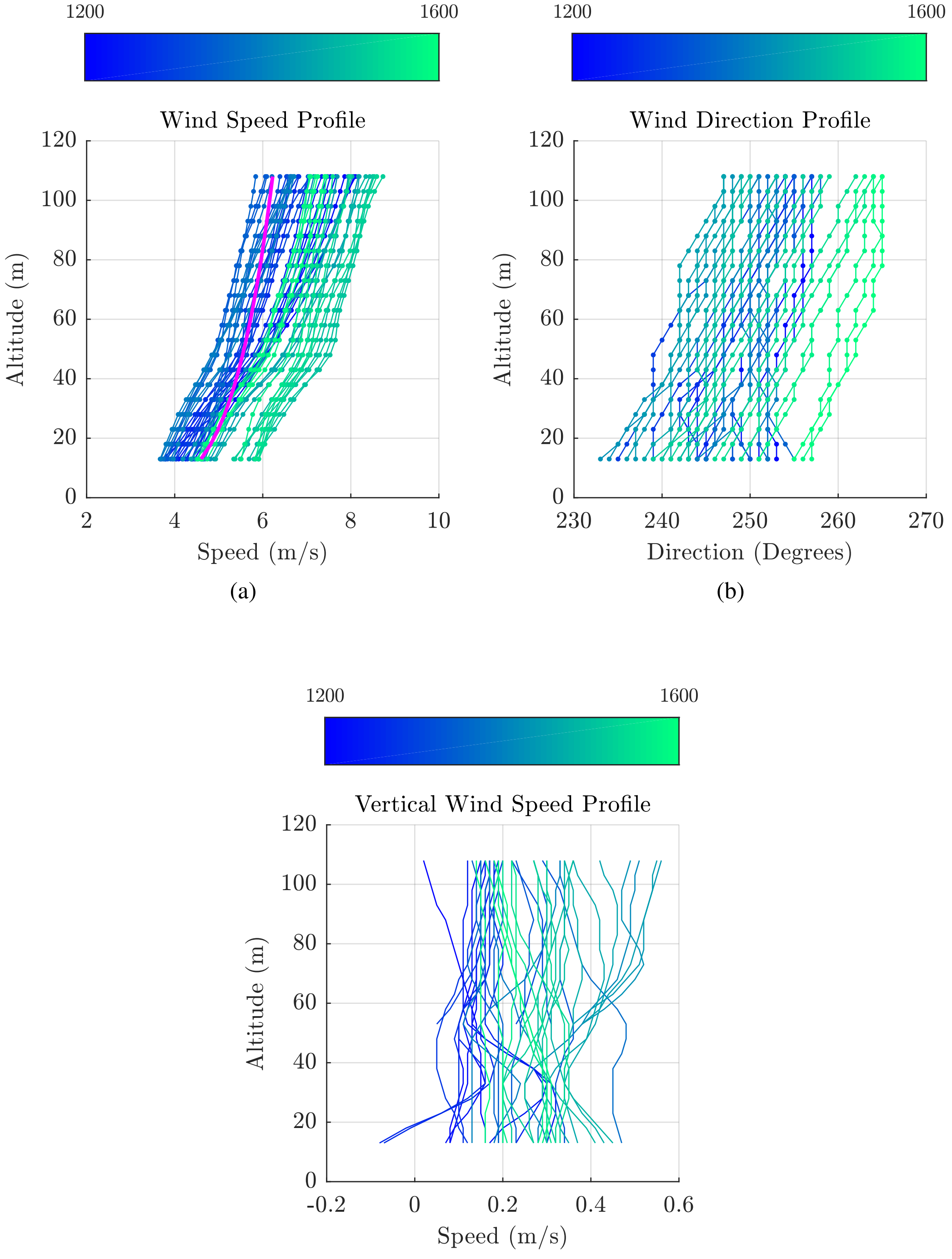

(a)

(b)

(c)

Figure 5.5.: Example of wind speed profile (a), wind direction profile (b) and vertical wind speed profile (c) measured by the SODAR during the 8th of July between 12:00 and 16:00 UTC (time of each profile depends on color, and is denoted by the colorbar). The magenta line on plot (a) denotes the ITTC profile from Eq. 1.17, calculated from the average wind measured at 13 m during the period.

5.3. Post processing

The main objectives of the post processing are to obtain estimation of lift to drag ratio and lift coefficient along an eight-pattern trajectory. For this purpose the following equations are computed, and a phase averaging method has been developed, to deal with the low frequency of the SODAR wind measurements.

5.3.1. Main Equations

Vectors are expressed into the heading reference frame R_ψ, as defined in the Reference Frames presentation, unless otherwise noted. All velocities are given with respect to the Earth. At first, forces into front tether are computed in the heading reference frame instead of the frame of the ground station:

$$\underline{F}_f = \underline{\underline{M}}_{\theta_s} \underline{\underline{M}}_{\phi_s} \underline{F}_m^{(s)} \tag{5.1}$$

Then, forces into back tethers are added to the front tether vector, to create the total kite force vector $\underline{F}_k$ at kite attachment point A on the ground station :

$$\underline{F}_{k,A} = \frac{\underline{F}_f}{\|\underline{F}_f\|}(\|\underline{F}_f\|+F_{bl} + F_{br}) \tag{5.2}$$

With the hypothesis of perfectly straight tethers with constant lengths, the total kite force vector at attachment point on the ground station is equal to the opposite of the force generated by the kite at kite position:

$$\underline{F}_k = -\underline{F}_{k,A} \tag{5.3}$$

With the same assumption, the kite position $\underline{P}_k$ and the kite velocity $\underline{V}_k$ can also be computed:

$$\underline{P}_k = \frac{\underline{F}_f}{\|\underline{F}_f\|} L_t \tag{5.4}$$

$$\underline{V}_k = \frac{d\underline{P}_k}{dt} \tag{5.5}$$

With the hypothesis of the zero-mass model, the aerodynamic force $\underline{F}_a$ generated by the kite is directly equal to the opposite of the force generated by the kite at kite position:

$$\underline{F}_a = -\underline{F}_k \tag{5.6}$$

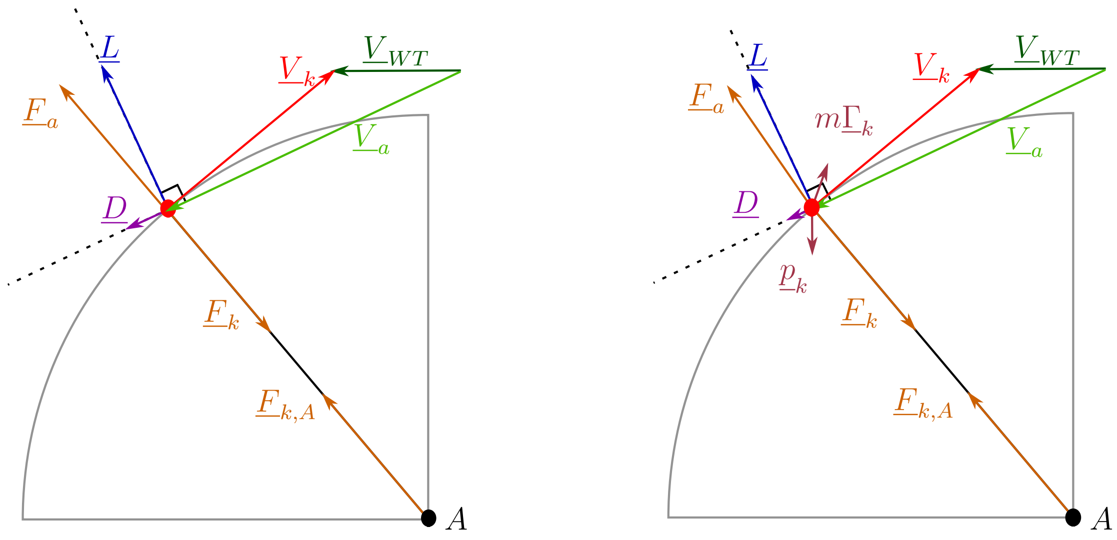

(a) Zero-mass model

(b) Point-mass model

Figure 5.6.: Force diagrams of the zero-mass model (a) and the point-mass model (b), respectively defined by Eq. 5.6 and Eq. 5.7.For the simplicity of the diagrams, kite force, kite velocity vector, wind velocity vector and kite weight vector are drawn in the same plane, however this is a particular case.

The force diagram presenting the zero-mass model is given in Fig. 5.6(a). However, a second model can be also used, the so called point-mass model. In this case, the weight of the kite $\underline{p}_k$ and inertial forces are taken into account. Impacts on model choice will be discussed in Part 5.4. The force diagram presenting the Point-mass model is given in Fig. 5.6(b).

$$\underline{F}_a = m\underline{\Gamma}_k - \underline{F}_k - \underline{p}_k \tag{5.7}$$

Where $\underline{\Gamma}_k$ is the kite acceleration vector, obtained from time derivative of kite speed vector $\underline{V}_k$, and m is the mass of the kite.

$$\underline{\Gamma}_k = \frac{d\underline{V}_k}{dt} \tag{5.8}$$

In the current case of onshore measurements with a fixed ground station without velocity, the relative wind vector $\underline{V}_{WR}$ is equal to the true wind vector $\underline{V}_{WT}$, and can be get by an axis-system change from the onshore wind measurement reference frame $R_{ws}$to the heading reference frame R_{ψ}. In our case, for all wind measurement devices, z-axis of R_{ws} reference frame was coincident with the vertical, meaning that ϕ_{ws} and θ_{ws}equals 0.

$$\underline{V}_{WT} = \underline{V}_{WR} = (\underline{\underline{M}}_{\psi_{ws}} \underline{\underline{M}}_{\theta_{ws}} \underline{\underline{M}}_{\phi_{ws}}) \underline{V}_{WM}^{(ws)} \tag{5.9}$$

Knowing the true wind speed and the kite velocity, the apparent wind on the kite $\underline{V}_a$ can be computed as follows:

$$\underline{V}_a = \underline{V}_{WT} - \underline{V}_k = \underline{V}_{WT} - \frac{d\underline{P}_k}{dt} \tag{5.10}$$

This apparent wind vector allows to define the aerodynamic reference frame R_a, as detailed in the Reference Frames chapter. Drag vector $\underline{D}$ can be get by projecting $\underline{F}_a$ on $\underline{x}_a$and lift vector $\underline{L}$ is then the difference between $\underline{F}_a$and $\underline{D}$:

$$\underline{D} = (\underline{F}_a \cdot \underline{x}_a)\underline{x}_a \tag{5.11}$$

$$\underline{L} = \underline{F}_a - \underline{D} \tag{5.12}$$

The lift to drag ratio f is then obtained by computing the ratio of the norm of the lift and drag vector:

$$f = \frac{L}{D} = \frac{\|\underline{L}\|}{\|\underline{D}\|} \tag{5.13}$$

Finally the lift coefficient C_l is also get, with A_k the kite area, and ρ the density of the air.

$$C_l = \frac{\|\underline{L}\|}{\frac{1}{2}\rho A_k V_a^2} \tag{5.14}$$

5.3.2. Time Derivative of Experimental Data

To compute $\underline{V}_k$ and $\underline{\Gamma}_k$, time derivative is necessary. A simple centered first-order Euler method is used, as following, where X denotes a given signal sampled with a Δt time step:

$$\frac{dX(t + \frac{\Delta t}{2})}{dt} = \frac{X(t + \Delta t) - X(t)}{2\Delta t} \tag{5.15}$$

The derivative signal is then interpolated on the initial time vector to get all signals on the same base time. However with experimental data, and particularly using directly the sampling period, this process generates a noise more or less important depending on the quality of the initial signal. Thus a filtering step needs to be added to get relevant results. A zero-phase digital filter built from MATLAB® dedicated tools is then applied, and an example of filtering effects is given in Fig. 5.7.

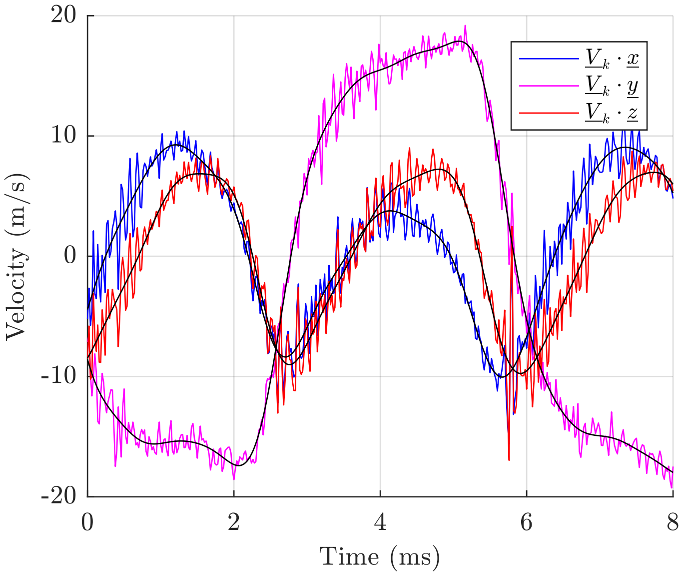

Figure 5.7.: Example of raw (colored) and filtered (black) signals for each component of the kite velocity vector.

5.3.3. Wind Estimation at Kite Altitude

As detailed before, the wind at kite altitude can be estimated by two means: the wind measurement done by the METEK sensor, at high frequency at 8 m above the surface (when available) or the wind profile given by the SODAR, but at low frequency. These two wind sources have been used to compute the post processing, and differences induced in the results are discussed in Part 5.4 (see Fig. 5.15(a) for example). For the METEK case, the wind at measurement point is considered as being equal to the wind at kite altitude. A power law formula, as the one proposed by the ITTC (2014) (Eq. 1.17), could have been used to model the wind gradient, however variability along the altitude was far from the ITTC profile, as shown in Fig 5.5(a). Moreover, the ITTC formula does not predict wind variations in direction and vertical speed, whereas these variations also exist in Fig. 5.5. In the case of the SODAR, wind at kite altitude is linearly interpolated in time and space from data provided by the SODAR.

5.3.4. Phase Averaging Method

The autopilot described in Part 3.1.5 is able to perform repeatable 8-pattern trajectories. Nevertheless, due to the variability of the boundary conditions of such full scale outdoor experiments, small variations around a mean periodic trajectory are observed during measurements of several minutes. Therefore, for the analysis of each runs, a conditional phase averaging procedure of the recorded data is applied in order to determine the mean trajectory and all the associated time sampled mean characteristics along it (environmental condition, kite control parameters and tensions of the tethers), but also their standard deviations. The present conditional phase averaging process is directly inspired by well known statistical analysis techniques, which are widely used theoretically or experimentally in the very general field of turbulent flows (Sagaut (2006, Chap.1, Sec. 1.4);Wernert and Favier (1999);Yu et al. (2010)).

The chosen detection signal S_d is the components of $\underline{P}_k$ along the main axis of the cloud of points composed from the whole eight-pattern trajectories of the run. To identify the axis, the co-variance matrix $\underline{\underline{M}}_{cov}$ is built from the cloud of points (Eq. 5.17 and Eq. 5.18), and then this matrix is diagonalized. The eigen vector associated with the biggest eigen value denotes the main axis of the cloud of points, meaning the main axis of the average 8-pattern. This axis is then defined as the x-axis of a new reference frame R_8. The two other eigen vectors complete the reference frame. Each elementary 8-pattern trajectory is then a specific pattern visible on this signal. By centering the signal, each pattern can be isolated by detecting when the signal is crossing zero and becoming positive (Fig. 5.8 Step 1).

$$S_d = \underline{P}^{(8)}_{k,1} \tag{5.16}$$

$$\forall \overline{X}, \overline{Y} \in \mathbb{R}^n,\ cov(\overrightarrow{X}, \overrightarrow{Y}) = \frac{1}{n-1} \sum_{i=1}^{n} (X_i - \mu_{\overrightarrow{X}})(Y_i - \mu_{\overrightarrow{Y}}) \tag{5.17}$$

$$\underline{\underline{M}}_{cov,i,j} = cov(\overrightarrow{P}_{k,i}, \overrightarrow{P}_{k,j}) \tag{5.18}$$

From there a set of pieces of the detection signal is available, with as many pieces of signal as the number of patterns initially existing during the run. The average period of the eight-pattern can be computed by averaging the duration of each piece of signal.

Then the detection signal is windowed with the following process: the first point of each window comes from the detection signal and the window length is set equal to the average period of the trajectory. This leads to a set of elementary signals of equal lengths, each associated with one elementary 8-pattern trajectory of the run (Fig. 5.8 Step 2.1). A representative one of these elementary signal is chosen as the reference one (Fig. 5.8 Step 2.2), and the cross correlation of each window with that reference is finally calculated (Fig. 5.8 Step 3.1). This leads to a set of maximum correlation levels and a set of small time shift for each window to reach this maximum, which are used to slightly correct the beginning of the corresponding windows.

This whole process of the detection signal being achieved, all the simultaneously sampled signals recorded in the considered run can be windowed using the obtained final set of the

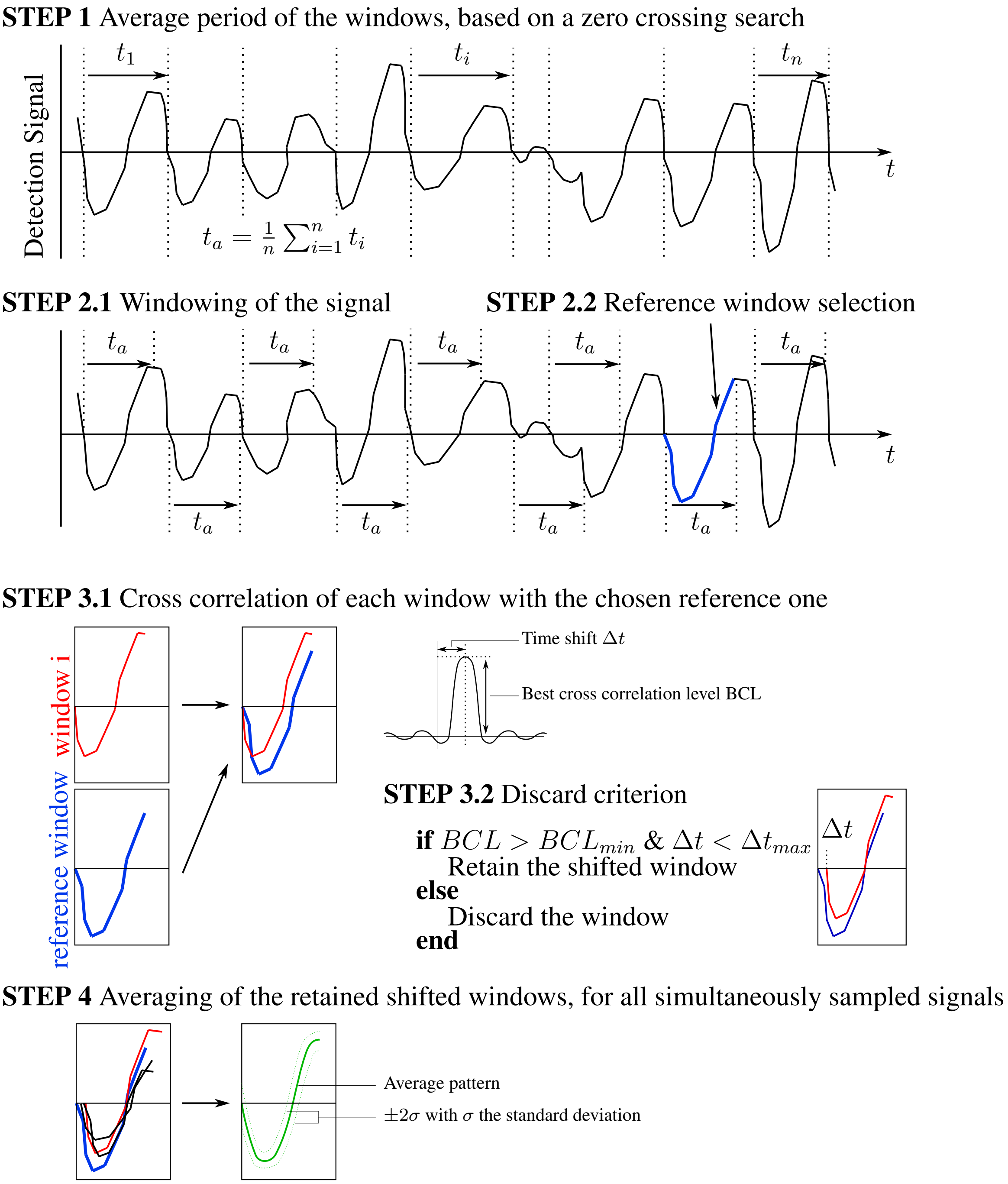

Figure 5.8.: Schematic diagram of the phase averaging method.

starting time index and ending time index. Finally for each signals, for each sampled instant of the period, a mean value and a standard deviation value can be calculated from the set of corresponding values in each elementary window (Fig. 5.8 Step 4). Moreover, as the cross correlation process returns a level of best correlation for each detected window, it is possible to introduce a conditional criterion to remove corrupted patterns from the set (Fig. 5.8 Step 3.2). A limit has been defined to only keep windows for which detection patterns have a cross correlation level of 70% of the level of the auto correlation of the reference detection pattern. This cross-correlation check is done simultaneously on the three components of the front tether force. Thus, not only the geometry of the trajectory is investigated but also the intensity of the force. To ensure a fair comparison, these checks are done on the centered signals normed by the standard deviation of the signals. Moreover, the quality of wind signal is checked, and particularly the SODAR signals. Indeed, some parts of the SODAR signals can be missing, and replaced by NaNs (Not a Number, numeric representation of undefined value). Thus an additional limitation has been introduced to discard all patterns with more than 5% of NaN in the SODAR signals.

The choice of the reference pattern is important and needs to be detailed. In the case of a perfect periodic signal, this choice will have no effect, however the detection signal is rather pseudo periodic with a few extreme events. Therefore a random choice have to be avoided, because the reference pattern could be then an extreme one, and the cross correlation may discard the majority of all other patterns. The option which was finally chosen is to manually select a pattern that seems to be centered in relation to the others. An example of the effect of the phase averaging process is given in Fig. 5.9(a), with all the patterns of the runs superimposed on the same plot, for the y-axis component of $\underline{F}_f$. The result of the method applied on kite position is shown in Fig. 5.9(b).

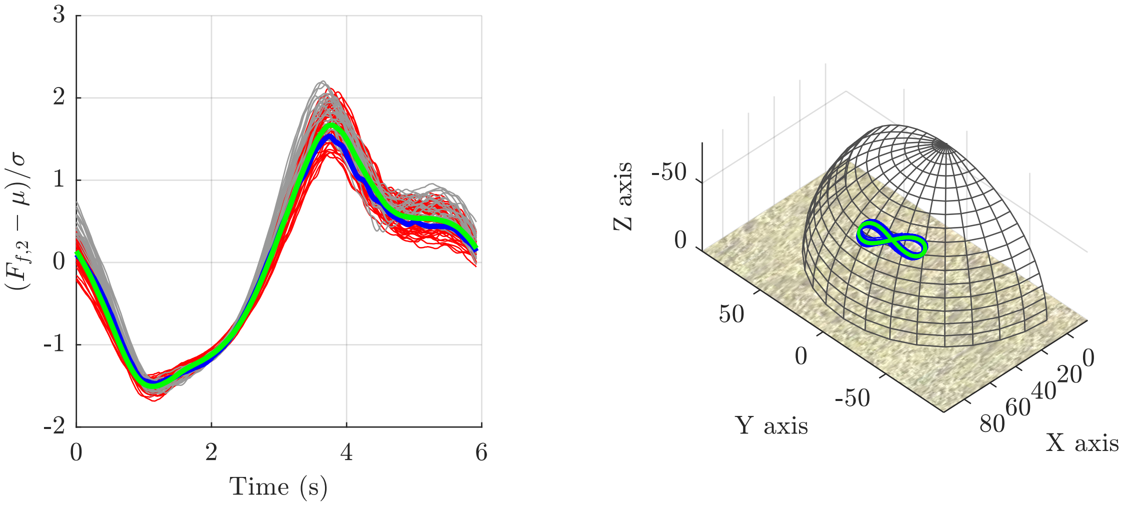

(a)

(b)

Figure 5.9.: Plot (a) shows all the pattern of the run, with colored in blue the reference one, in red patterns that have been selected, in gray the discarded ones and in green the resulting pattern after averaging. Plot (b) shows all the positions of the kite during the run in blue, and the average track resulting from the phase averaging process in green (in the true wind reference frame).

5.4. Results

The conditional phase averaging procedure has been applied to all data recorded and identified as being potentially relevant, leading to a set a 25 cases, plus some specific cases. Therefore, each run leads to one average 8-pattern. All these runs were done with the Cabrinha kite, but three different tether lengths were used. Global average data for these runs are given in the Tab. 5.1. These results are analyzed in the following subsections along several main lines. When a specific plot needs to be shown to illustrate a fact relatively common for all cases, a reference case is then used, colored in blue in Tab. 5.1. This case has already been used in Fig. 5.9. From there, as defined in the Nomenclature, an over-right-arrowed quantity denotes a time series, and the associated time line is the one related to the result of the conditional phase averaging method. The letter μ denotes the average value of a time series.

To compare easily a case to another, the kite force coefficient C_k is computed, from the average value of each case:

$$C_k = \frac{\mu_{\overrightarrow{F_k}}}{\frac{1}{2}\rho A_k \left(\mu_{\overrightarrow{V_{WT}}}\right)^2} \tag{5.19}$$

The back tether ratio r_b represents the part of the force supported by back tethers. The value given in Tab. 5.1 is the average value $\mu_{\overrightarrow{r_b}}$ over a pattern.$\mu_{\overrightarrow{F_k}}$

$$r_b = \frac{F_{bl} + F_{br}}{F_k} \tag{5.20}$$

The amplitude ratio r_a is the amplitude of force along the trajectory.

$$r_a = \frac{\max(\overrightarrow{F_k}) - \min(\overrightarrow{F_k})}{\mu_{\overrightarrow{F_k}}} = \frac{\triangle \overrightarrow{F_k}}{\mu_{\overrightarrow{F_k}}} \tag{5.21}$$

The trajectory width $\triangle traj$ is the azimuth amplitude of the trajectory, given in meter, and calculated as follows:

$$\triangle\, traj = L_t \triangle \overrightarrow{P^{(8)}_{k,1}} \tag{5.22}$$

5.4.1. Kite Loading

5.4.1.1. General case

As visible in Tab. 5.1, the average force generated by the kite is between 400 and 1300 N, leading to a wing load per square meter under 300 N, so far under the initially expected value of 1 kN/m². However this is the average value on a pattern, and the instantaneous value along the trajectory is far from constant, as displayed in the last column of the table: the variation is about 100% of the average value of the run. This is also illustrated in Fig. 5.10(a). The maximum kite force values occur generally at the end of the straight part of the trajectory, whereas the minimum values are located at the end of the turn, as shown in the 3D plot presented in Fig. 5.10(b).

5.4.1.2. Extreme loads observed

During all phases of experiments, higher loading conditions occurred sometimes on the kite at specific moments, as at launch for example. These moments can not be processed as it has been done it the previous subsection because in that case kites were not doing a regular pattern. However since loads generated during these moments are so much higher than during other phases it definitely has to be investigated. Two cases have been identified, one for each kite.

With the North kite, load exceeded 2500 N during three peaks for a total duration of 4 s (for a period duration of 12s), with a maximum force reaching 3 700 N, with an average

Run Name	L_t (m)	$\mu_{\overrightarrow{V_{WT}}}$ (m/s)	$\mu_{\overrightarrow{F_k}}$ (N)	C_k (-)	$\triangle traj$ (m)	r_b (%)	r_a (%)
C25_1	25	6.4	508	4.0	38.6	19.0	99.5
C25_2	25	6.3	448	3.6	39.0	18.7	107.7
C25_3	25	6.1	459	3.8	37.9	18.7	110.5
C25_4	25	6.1	454	3.8	35.8	19.3	102.1
C25_5	25	6.4	454	3.5	33.2	19.5	93.1
C25_6t	25	5.6	432	4.3	33.2	18.9	85.6
C50_1	50	6.4	605	4.7	59.2	21.3	83.3
C50_2	50	5.1	795	9.8	49.5	24.1	78.3
C50_3	50	7.0	1271	8.3	72.1	27.6	104.1
C50_4	50	7.8	1274	6.7	81.0	27.1	111.0
C50_5	50	5.5	1169	12.3	54.3	25.8	69.4
C50_6	50	4.6	1057	15.6	62.0	26.0	76.3
C50_7	50	4.4	1031	16.5	55.7	26.7	60.6
C50_8	50	5.4	976	10.5	60.3	26.3	76.0
C50_9	50	5.7	659	6.5	60.6	21.9	120.1
C50_10	50	5.3	516	5.8	60.1	21.3	134.1
C50_11	50	5.3	641	7.2	62.2	22.6	100.8
C50_12	50	5.1	669	8.1	61.5	23.0	102.8
C50_13	50	5.0	621	7.9	59.9	22.8	99.6
C50_14	50	4.8	500	6.8	59.9	22.3	119.2
C80_1	80	5.1	942	11.4	56.1	27.5	74.2
C80_2	80	5.3	877	9.8	56.1	27.8	75.3
C80_3	80	5.0	834	10.3	55.2	27.9	80.9
C80_4	80	5.6	1124	11.3	82.7	30.1	70.9
C80_5	80	6.0	1077	9.4	94.4	30.2	72.9

Table 5.1.: Summary table of average results for the 25 runs studied. The blue row denotes the reference case (C80_3).

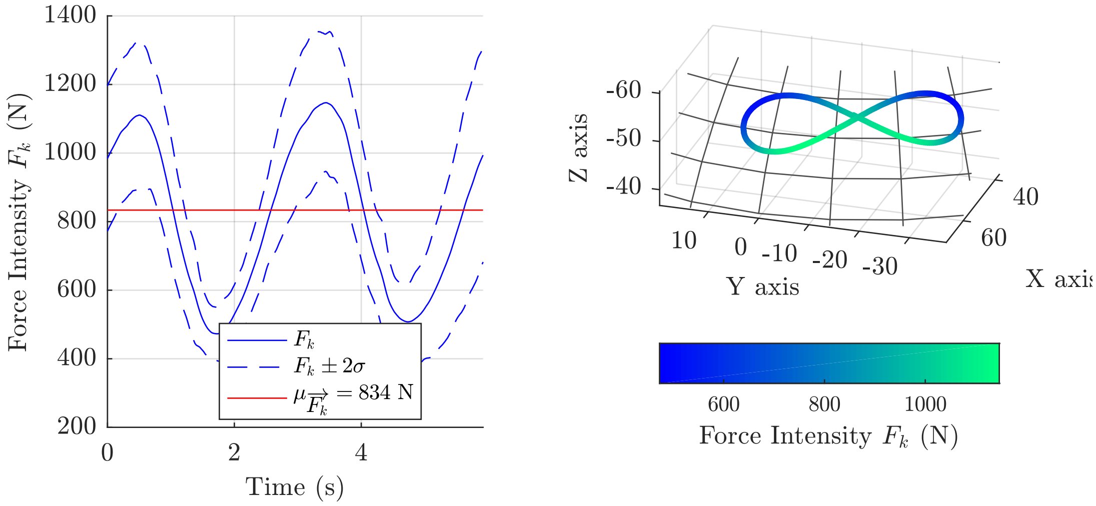

(a) (b)

Figure 5.10.: Evolution of kite load F_k along a eight-pattern trajectory, for the reference case (see Tab. 5.1). Plot (a) shows variation of the time over the time, with the associated standard deviations computed thanks to the phase averaging method. Plot (b) shows the same data but according to the position of the kite along the trajectory.

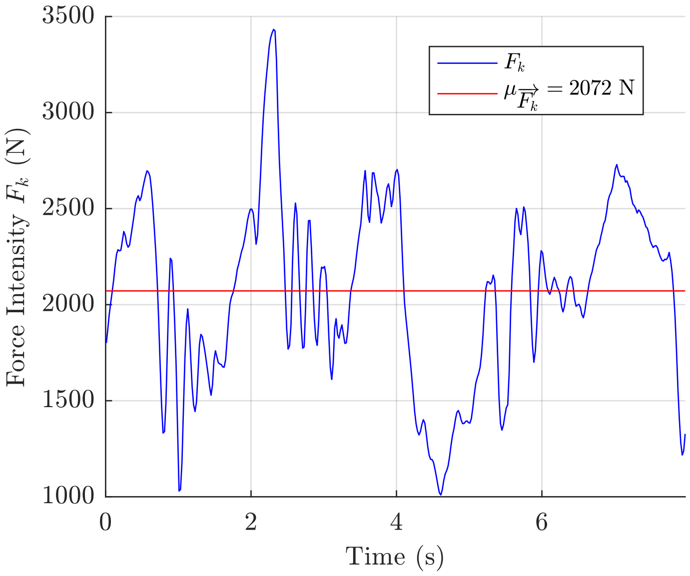

Figure 5.11.: Maximum effort recorded for Cabrinha kite during fieldwork.

true wind speed during the period of 9.02 m/s. This maximum value is equivalent to a wing load equal 0.74 kN/m².

With the second kite (Cabrinha), only one peak was observed reaching 3 400 N, however the average load during the 7 s period was slightly above 2 000 N , with an average true wind speed during the period of 10.92 m/s. The evolution of the load during this period is given in Fig. 5.11.

5.4.1.3. Buckling Phenomena

None of the cases presented in Tab. 5.1 show a true wind speed higher than 8 m/s. Nevertheless, such wind conditions occurred during the month of measurement, as it can be seen with the observation of extreme loading cases. However, no run suitable for the phase averaging method could be achieved with these wind conditions. This is due to buckling phenomena occurring on the inflatable leading edge of the kite and also on battens. When the amplitude of the phenomena was limited, it has no important effects, but when the wind speed increased, the amplitude also increased, generating losses of performance and control problems of the kite. Thus, the autopilot was no longer able to draw perfect eight-pattern trajectories, leading to kite tracks appearing like a succession of unpredictable loops with no identifiable pattern. In extreme case, the autopilot was even not able to maintain kite in flight, leading to the crash of the kite, often violently. Examples of instantaneous observations of buckling phenomena are given in Fig. 5.12. Picture (a) presents a very classic case with a little bending at the end of the leading edge. Pictures (b), (c) and (d) show the same phenomena, propagating to the last and middle battens, and affecting also the leading edge at wider scale. Finally, picture (e) presents a case where the kite was totally collapsed, during approximately 150 ms.

Another example of buckling phenomenon can be seen on force records presented in Fig. 5.11. Indeed the force oscillations observed between 0.8 s and 1.6 s and between 2.5 s and 3.3 s are typical of a buckling issue: when load reaches a certain threshold, buckling appears leading to a significant loss of performance of the kite. Then, when kite load is sufficiently low, the kite retrieves a better shape, and load can raise up again, until a new partial collapse. These oscillations continue until the kite reach a reduced power area, like the wind window edge. According to the data, in this case, oscillations occur at approximately 3 Hz. During this type of events, autopilot or manual pilot have almost no control of the kite. The other force oscillations observed just before the 4th second and around the 6th second are also probably buckling phenomena, but as no video data are available for this case it is then difficult to conclude.

Parameters ruling the threshold levels of buckling appearance are complex and not predictable from what we know. Indeed, still in Fig. 5.11, buckling affects load for the first time around 2 600 N, whereas one second later the load reaches 3 400 N before being

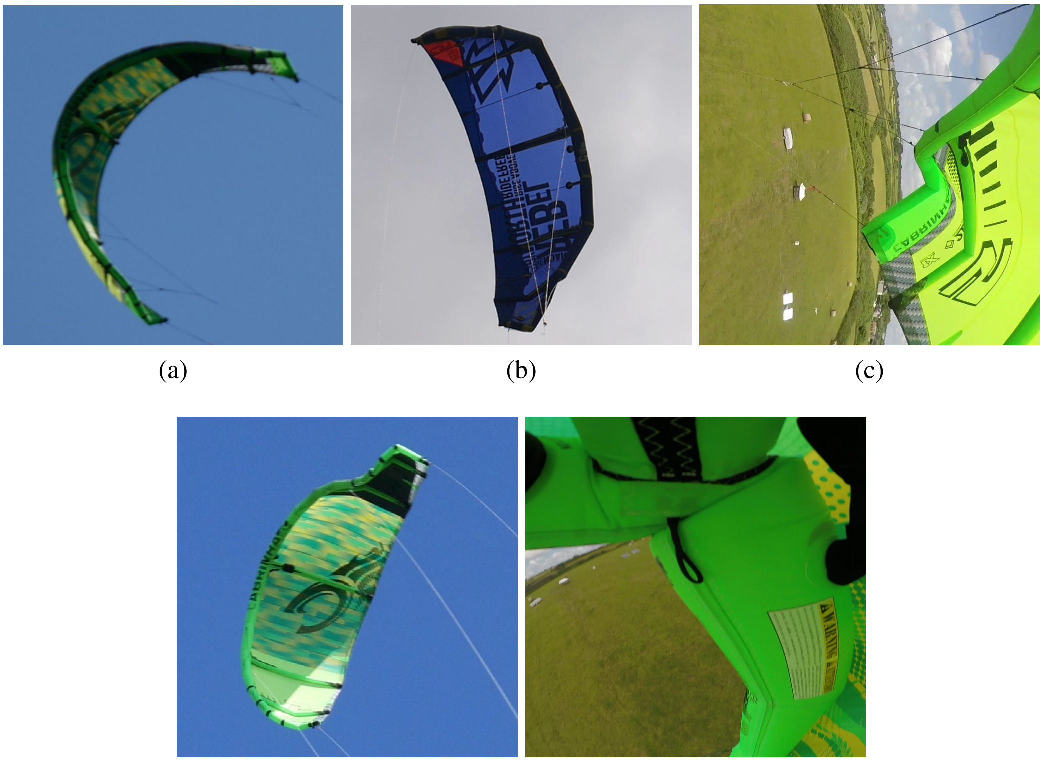
(a) (b) (c) (d) (e)

Figure 5.12.: Pictures of buckling phenomena, with several levels of deformation . Picture (e) shows the junction between the inflatable leading edge and the central batten (the camera was mounted on the central batten, shooting forward).

affected. However, two elements have a clear influence on buckling threshold: the pressure of the leading edge and the bridle structure. Pressure effect was clearly observed during fieldwork: when the kite lost pressure due to little holes in the inflatable part, it was more exposed to buckling after a few minutes of flight than just after take off. Bridle structure is more complicated to modify and no test was carried out in that way. But it is obvious that these types of kite are not designed to be used onshore by being permanently attached to the ground. Indeed, under normal conditions, a 75 kg kite-surfer can not hold out against a force of 1500 N. Then, he will move towards the kite generating a velocity of the attachment point. This velocity will cause a decrease of the angle of attack on the kite and then will reduce the load consequently.

5.4.2. Ratio between Forces into Back Tether and Total Force

For the purpose of commercial development of kite control systems, the part of effort supported by the back tethers is an interesting element to analyze. Indeed this information is essential to size correctly the power of the actuators and to define back tether section

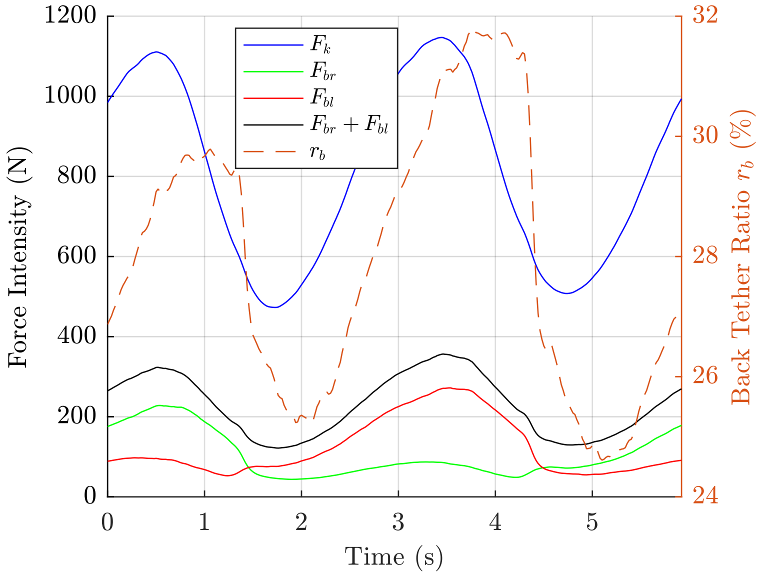

Figure 5.13.: Back tether load versus total load during the reference case.

and material. As it can be seen in Fig. 5.13, the ratio between the sum of contributions of the back tethers and an the total kite force, as defined in Eq. 5.20, varies between 25% and 30% along the trajectory of the reference case. The average values for the complete eight-patterns presented in Tab. 5.1 are between 18% and 30%.

5.4.3. Impact of Trim

The trim τ of the kite was defined as the length difference between back and front tethers. Thus, if front tethers were directly connected to the attachment point, the trim value should be the distance between real start of back tethers and attachment point. Indeed back tether are all the time longer than front ones. And this distance is measured thanks to the optical encoders. However, between real start of front tether and attachment point, a front leader line was rigged (as shown in Fig. 2.4), and the length of this leader line was not measured precisely. Moreover, this leader line was replaced several times due to important friction at attachment point. Thus trim values can not be compared from one day to another. This entails that kites were not rigorously set in the same way all the time, and therefore absolute performances can not be really compared.

However a record was done to analyze the effect of the trim on kite performances. Thus during a run, with no change of any other parameters, three trim values were tested during a few minutes. Average results are given in Tab. 5.2, and these trim values are expressed relatively to the first one. This measurement was done with the North kite rigged with 52 m tethers.

Case Name	t_r (s)	V_{WT} (m)	$\mu_{\overrightarrow{F_{k,A}}}$ (N)	C_k (-)	r_b (%)	$\triangle\tau$ (cm)
BC1	350	6.2	959.4	7.8	21	0
BC2	58	6.4	1729.7	13.2	25	-4
BC3	290	6.5	1654.9	12.2	25	-5

Table 5.2.: Impact of trim on kite performances

Differences between the case 2 and 3 are significant, but trim difference is only 1 cm, and case 2 deals with a time window 5 times shorter. However the comparison between case 1 and case 3 is more appropriate (same period length). Therefore, a trim reduction of 5 cm leads to an increase of kite force about 72%. On the same time the back tether ratio goes from 21% to 25%.

5.4.4. Steering versus Rotation Rate of Velocity Vector

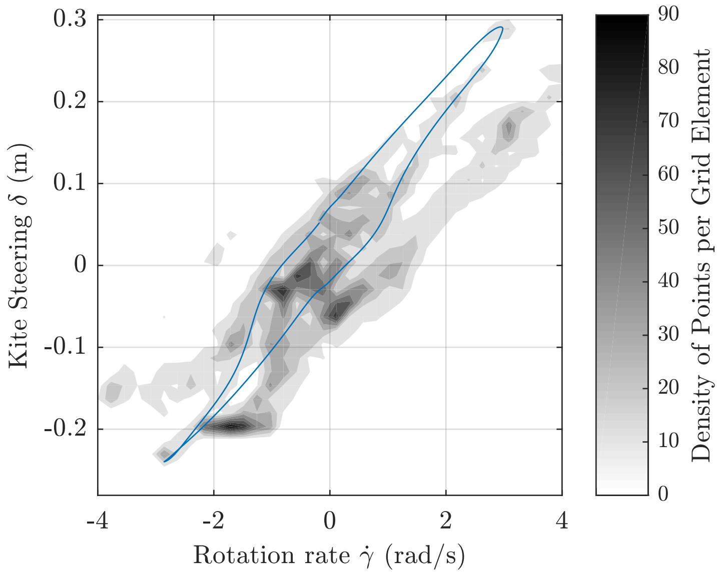

Figure 5.14.: Density plot of the steering command versus the rotation rate of the velocity vector, for all cases in Tab. 5.1, centered on average value of the command. The blue line is the evolution of the reference case.

The density plot for all cases giving the evolution of steering δ versus the rotation rate of the velocity vector around tether axis$\dot{\gamma}$ is shown in Fig. 5.14. This value is the time derivative of the angle γ, defined in Part 3.1.5. The relation can be at first sight almost linear. However, looking at the blue line which is the evolution for the reference case, it shows the presence of a delay between steering action and effect on rotation rate. Indeed the blue line denotes a loop, and not a single line.

5.4.5. Apparent Wind Speed versus True Wind Speed

When kite is flying in dynamic mode, the kite velocity increases the apparent wind seen by the kite. And this is one of the major advantage of kites in comparison with classic sail. Thus, it is interesting to analyze the factor between the relative wind speed, equals in the current fieldwork to the true wind speed, with the apparent wind. Therefore, this average factor was computed for each of the 25 cases presented in Tab. 5.1, and then averaged again for all cases. Finally, the average factor is 3.1. Because forces are related to the square of the apparent wind speed, this value shows that kites used in our study are almost 10 times more powerful than a classic sail with the same size. But this is only true when the kite is operated in dynamic flight. In static flight, the apparent wind is equal to the true wind, and kites in this case are equivalent to sails, with usually poorer performances due to their soft structures.

5.4.6. Kite Model Impact on Post Processing

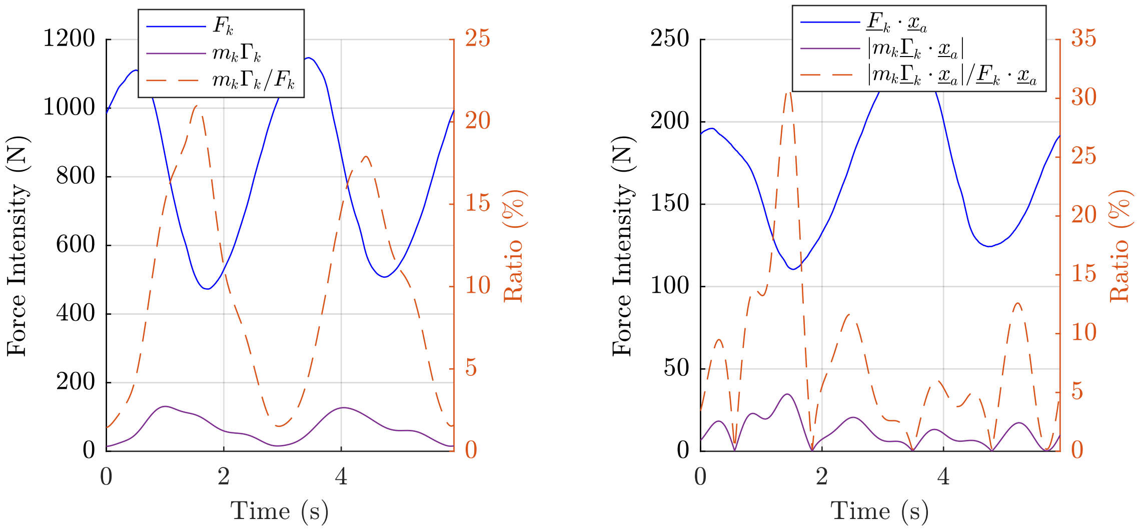

(a)

(b)

Figure 5.15.: Comparison between the total kite force and inertial forces, during the reference case. Plot (a) deals with the norm of these forces, whereas plot (b) is a focus on the projection of these forces on the apparent wind axis.

Two different models have been presented in Eq. 5.6 and Eq. 5.7 to estimate the aerodynamic force of the kite. The first one is the zero-mass model assuming the kite has no mass and then no inertial effect exists. The second model is the point-mass model, assuming the kite mass is concentrated at point K. This entails the apparition of inertial forces. In Fig. 5.15(a), the total kite force is plotted with the calculated inertial force. The ratio between these two values is printed on the right axis. Even if the inertial force remains low, it can reach nonetheless 20% of the kite force value. When projected on the wind apparent axis $\underline{x}_a$ as shown in part (b) of Fig. 5.15, the inertial force amounts as much as 30% of the total kite force projected on x_a-axis, in other words, the drag of the zero-mass model. Therefore, the choice of the model will particularly affect the drag calculation, and so the lift to drag ratio result. This will be confirmed by the computation of the lift to drag ratio and the lift coefficient with one of the two models in the two following subsections.

5.4.7. Lift to Drag Ratio

The lift to drag ratio has been computed for all cases using Eq. 5.13, and the time evolution of lift to drag value along the trajectory of the kite during the reference case is given in Fig. 5.16(a). Three lines are plotted. The blue one is the lift to drag ratio calculated from wind data coming from the SODAR and using the zero-mass model. The orange one uses also SODAR data, but with the point mass model. Finally the yellow one is based on METEK wind data with the zero-mass model. An important difference is observed between the last line (METEK data - yellow line) and the two others (SODAR data - blue/orange line). This can be easily explained regarding average wind speed given by the two different devices: thus the wind measured by the SODAR (and expressed at kite altitude) is about 5.0 m/s whereas the wind measured at the time by the METEK sensor with no profile compensation was 3.3 m/s. This shows how important it is to know as well as possible the wind at kite altitude for post-processing lift to drag ratio. The average value of the lift to drag ratio computed with the point mass model is 4.74. Plot (b) of Fig. 5.16 shows the same lift to drag data, but plotted in relation to the rotation speed of the velocity vector of the kite $\underline{V}_k$ around tethers axis. According to what was discussed before, the line with METEK data is not plotted. What is striking on this plot is that the lift to drag ratio is really not symmetrical. Indeed we could expect the same behavior when the kite turns to the left (meaning positive $\dot{\gamma}$) and to the right (negative $\dot{\gamma}$), but this is not the case. The origin of this default of symmetry could be the misalignment between eight-pattern center and wind axis. Indeed, the kite load is almost symmetrical (see Fig. 5.10(a)), the kite trajectory is also almost a perfect symmetrical eight-pattern (see Fig. 5.10(b)), but the pattern center is not aligned with the wind axis, as visible in Fig. 5.9(b), where the kite position is plotted according to the true wind reference frame, and then the true wind axis corresponds to the x-axis of the plot. However the cause of this misalignment has not been identified so far. Furthermore, the lift to drag ratio seems to become lower during kite turn, which makes sense: control action leads to kite structure's deformations, and these deformation are detrimental for performances. The aim of the following paragraph is then to confirm these trends with the 24 other cases.

The average values of lift to drag ratio for each case have been computed leading to various results, which is quite natural because the kite trim was no identical from one case to another (see part 5.4.3). All these values have been then averaged once again, leading to a mean result for the lift to drag ratio of our kite equal to 4.70. Because we

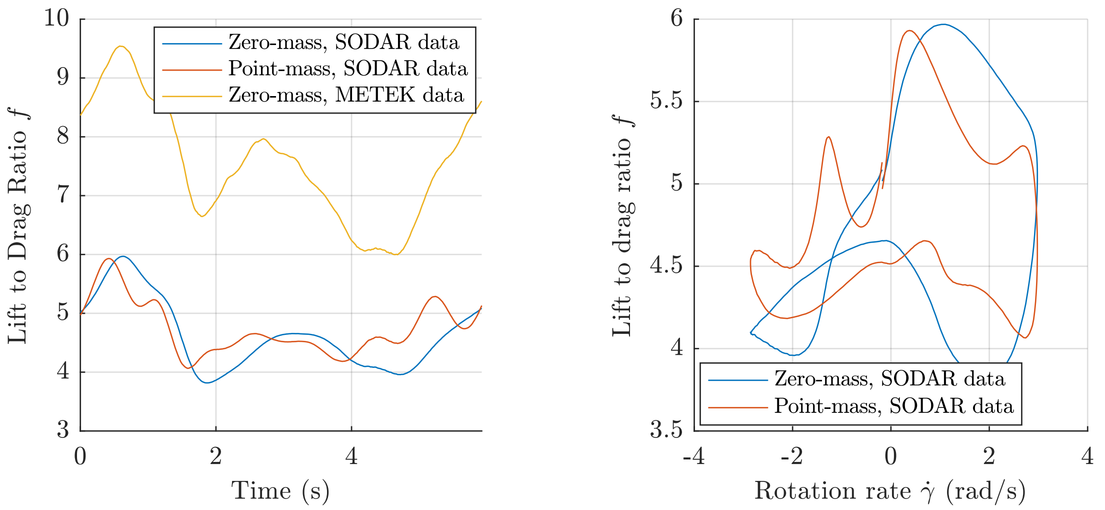

(a) (b)

Figure 5.16.: Evolution of the lift to drag ratio along the trajectory, for the reference case. Plot (a) gives the time evolution, and plot (b) gives the evolution of the ratio according to the rotation speed of the kite velocity vector around the tether axis.

are interesting only in the evolution of the lift to drag ratio and not in the absolute value, all cases have been re-centered on this value, and the cloud of points obtained from all cases is then used to plot a density graph, presented in Fig. 5.17. Unfortunately, the trends which have been identified on our reference case do not seem to be confirmed, with no clear drop at high turn rate. Nevertheless, even if the cloud of points has been centered on an average value coming from all cases, the effect of trim may still impact the results. Indeed, the trim was not precisely recorded leading to possible variations from a case to another (see Sec. 5.4.3). Consequently, if the value of the trim impacts the way the the lift to drag ratio vary along a trajectory, it becomes more complicated to get a density plot showing a clear trend. This hypothesis of a trim affecting the variation of the lift to drag ratio seems to make sense. Indeed the trim can be seen as a way to adjust the angle of attack of the kite, and it is well known that the lift to drag ratio of a wing strongly depends on its angle of attack, with a non-linear relation (Abbott and Von Doenhoff (1959)).

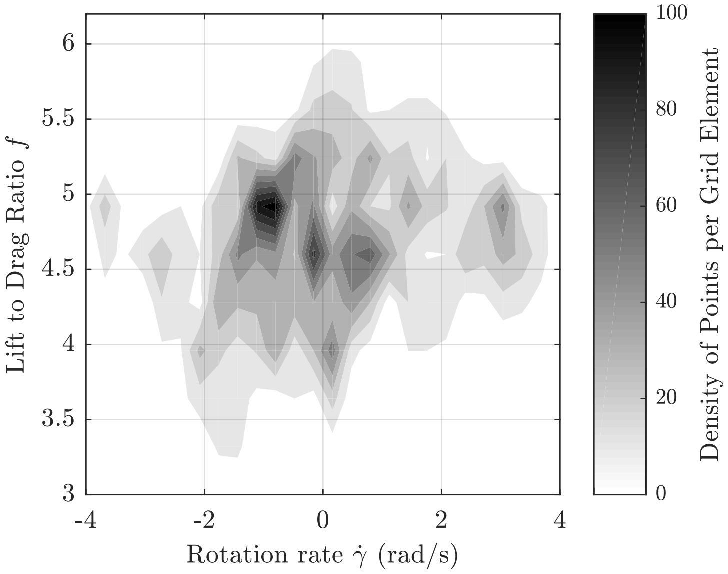

Figure 5.17.: Density plot of lift to drag ratio versus $\dot{\gamma}$, for all cases, centered on the average value of the lift to drag ratio of all cases.

5.4.8. Lift Coefficient

The lift coefficient of the kite computed using Eq. 5.14 has been processed in the same way as for the lift to drag ratio. Thus, time evolution of lift coefficient is given in Fig. 5.18(a), and the evolution related to $\dot{\gamma}$ is given in plot (b). It is interesting to notice that true wind speed value has less influence for lift coefficient computation than for the lift to drag ratio. Indeed, difference between results with METEK data and SODAR data are minimum. Here again, the symmetrical issue is very visible on plot (b), but, as for the lift to drag ratio, the lift coefficient is getting lower at high turn rate, positive or negative . The average value for the whole period is 0.83.

The density graph has also been plotted for the lift coefficient in Eq. 5.19, centered also on the average value of lift coefficient for all cases, and was found equal to 0.76. Again, the trends predicted with the reference case are not confirmed with the density plot, but the trim problem can also affect the lift coefficient, as for the lift to drag ratio.

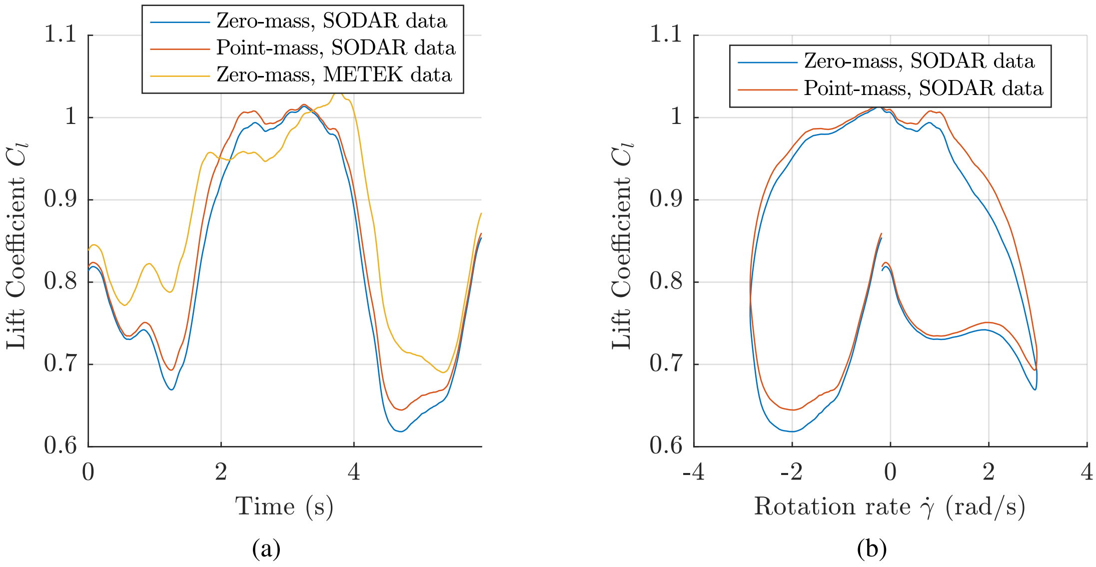

Figure 5.18.: Evolution of the lift coefficient along the trajectory, for the reference case. Plot (a) gives the time evolution, and plot (b) gives the evolution of the coefficient according to the rotation speed $\dot{\gamma}$ of the kite velocity vector around the tether axis.

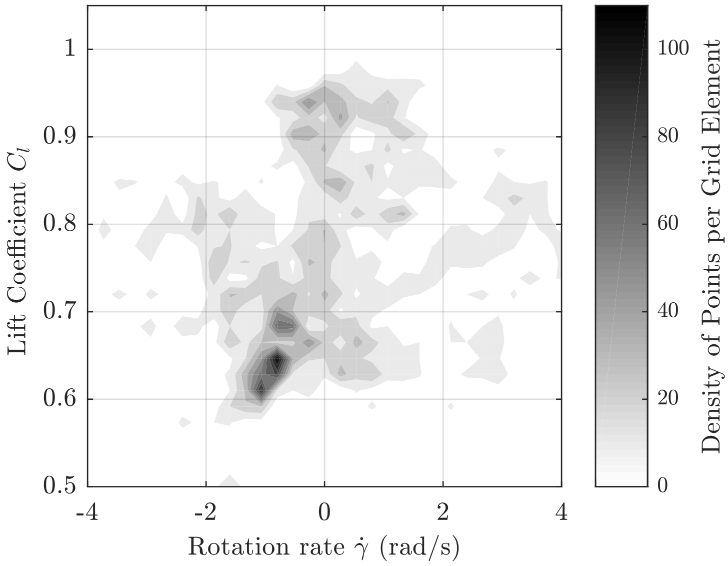

Figure 5.19.: Density plot of lift coefficient versus the rotation rate of the velocity vector, for all cases of Tab. 5.1, centered on the average value computed from all cases.

5.5. Uncertainties

Average values for lift to drag ratio and lift coefficient obtained during this fieldwork are consistent with results of previous experimental studies, as Dadd (2012). However, it seemed important to carry out an uncertainty calculation to find out how measurement errors of the various sensors affect the final result. Moreover, this study could provide an answer to the symmetrical problem noticed previously.

5.5.1. Equations

In the following equations, red colored parts of equations stand for elements that need to be differentiated, whereas blue colored parts stand for known uncertainties from sensor specification sheets. Only results of calculation are presented in following subsections, calculation details are given in Appendix D.

5.5.1.1. Lift

$$\frac{d\|\underline{L}\|}{\|\underline{L}\|} = \frac{1}{\|\underline{L}\|^2}(\underline{L} \cdot d\underline{F}_a - \underline{L} \cdot d\underline{D}) \tag{5.23}$$

5.5.1.2. Drag

$$\frac{d\|\underline{D}\|}{\|\underline{D}\|} = \frac{1}{\|\underline{D}\|}(\underline{x}_a \cdot d\underline{F}_a + d\underline{x}_a \cdot \underline{F}_a) \tag{5.24}$$

$$d\underline{D} = \underline{x}_a \underline{x}_a^T d\underline{F}_a + (\underline{x}_a \underline{F}_a^T + \underline{x}_a \cdot \underline{F}_a \underline{I}_{\mathbb{R}^3}) d\underline{x}_a \tag{5.25}$$

5.5.1.3. Aerodynamic Force

The calculation of the aerodynamic force implies the choice of one of the two kite model. Because the time differentiation is a delicate problem in such calculations, as it will be shown in subsection 5.5.1.7, it has been decided to use only the zero mass model, and then avoid a second time differentiation to get $\underline{\Gamma}_k$. Therefore, with still the assumption of straight lines with constant length, the aerodynamic force is directly as follows:

$$\underline{F}_a = \frac{\underline{F}_f}{\|\underline{F}_f\|}(\|\underline{F}_f\| + F_{bl} + F_{br}) \tag{5.26}$$

.

$$d\underline{F}_a = \frac{\underline{\underline{\alpha}}}{\|\underline{F}_f\|} d\underline{F}_f + \frac{\underline{F}_f}{\|\underline{F}_f\|} dF_{bl} + \frac{\underline{F}_f}{\|\underline{F}_f\|} dF_{br} \tag{5.27}$$

With $\underline{\underline{\alpha}} = -\frac{(F_{bl}+F_{br})}{\|\underline{F}_f\|^2} \underline{F}_f \underline{F}_f^T + (\|\underline{F}_f\| + F_{bl} + F_{br}) \underline{\underline{I}}_{\mathbb{R}^3}$

5.5.1.4. Front Tether Force

$$d\underline{F}_f = \frac{\partial \underline{\underline{M}}_{\theta_s}}{\partial \theta_s} \underline{\underline{M}}_{\phi_s} \underline{F}_m^{(s)} d\theta_s + \underline{\underline{M}}_{\theta_s} \frac{\partial \underline{\underline{M}}_{\phi_s}}{\partial \phi_s} \underline{F}_m^{(s)} d\phi_s + \underline{\underline{M}}_{\theta_s} \underline{\underline{M}}_{\phi_s} F_m \frac{d\underline{F}_m^{(s)}}{F_m} \tag{5.28}$$

5.5.1.5. Apparent Wind Vector

$$d\underline{x}_a = \left(\underline{\underline{I}}_{\mathbb{R}^3} - \underline{x}_a \underline{x}_a^T \right) \frac{1}{\|\underline{V}_a\|} d\underline{V}_a \tag{5.29}$$

The true wind speed vector is get from the axis system change from wind measurement reference frame to heading reference frame. Thus the three Euler angles $(\psi_{WS}, \theta_{WS}, \phi_{WS})$ are part of the transfer matrix. However, the SODAR was assumed perfectly horizontal, and no uncertainties were known on the two quantities θ_{WS} and ϕ_{WS}, which are not considered here and then taken equal to 0. Moreover, the uncertainties on θ_{WS} and ϕ_{WS} can be seen as redundant to the ones of θ_s and ϕ_s. Indeed, the purpose of these angles are to get all the measurement vectors (force and wind) in the same reference frame. In principle, only one set of three Euler angles is necessary for that, but for simplicity of presentation, it has been decided to use an intermediate reference frame R_ψ. Finally, three Euler angles are in use as a matter of fact, with their associated uncertainties : ψ_{WS}, θ_s and ϕ_s. Apparent wind vector can be then calculated as follows :

$$d\underline{V}_a = \frac{\partial \underline{\underline{M}}_{\psi_{WS}}}{\partial \psi_{ws}} \underline{V}_{WM}^{(ws)} d\psi_{ws} + V_{WM} \underline{\underline{M}}_{\psi_{ws}} \frac{d\underline{V}_{WM}^{(ws)}}{V_{WM}} - d\underline{V}_k \tag{5.30}$$

5.5.1.6. Kite Position Vector

$$\underline{P}_k = \frac{\underline{F}_f}{\|\underline{F}_f\|} L_t = \underline{x}_k L_t \tag{5.31}$$

$$d\underline{P}_k = L_t \left(\underline{\underline{I}}_{\mathbb{R}^3} - \underline{x}_k \underline{x}_k^T \right) \frac{1}{\|\underline{F}_f\|} d\underline{F}_f \tag{5.32}$$

For clarity reasons in followings parts, new elements are introduced:

$$d\underline{P}_k = \underline{p}_1 d\theta_s + \underline{p}_2 d\phi_s + \underline{\underline{p}}_3 \frac{d\underline{F}_m^{(s)}}{\|\underline{F}_m^{(s)}\|} \tag{5.33}$$

With:

$\underline{p}_1 = L_t \left(\underline{\underline{I}}_{\mathbb{R}^3} - \underline{x}_k \underline{x}_k^T \right) \frac{1}{\|\underline{F}_f\|} \frac{\partial \underline{\underline{M}}_{\theta_s}}{\partial \theta_s} \underline{\underline{M}}_{\phi_s} \underline{F}_m^{(s)}$
$\underline{p}_2 = L_t \left(\underline{\underline{I}}_{\mathbb{R}^3} - \underline{x}_k \underline{x}_k^T \right) \frac{1}{\|\underline{F}_f\|} \underline{\underline{M}}_{\theta_s} \frac{\partial \underline{\underline{M}}_{\phi_s}}{\partial \phi_s} \underline{F}_m^{(s)}$
$\underline{\underline{p}}_3 = L_t \left(\underline{\underline{I}}_{\mathbb{R}^3} - \underline{x}_k \underline{x}_k^T \right) \underline{\underline{M}}_{\theta_s} \underline{\underline{M}}_{\phi_s}$

5.5.1.7. Kite Velocity vector

The kite velocity vector $\underline{V}_k$ is obtained by finite difference on kite position $\underline{P}_k$. At first, we can consider that, for all $i \in [\![0, 3]\!]$ $|\Delta V_{k,i}| \leqslant \frac{2}{\Delta t} |\Delta P_{k,i}|$. Thus,

$$|\Delta V_{k,i}| \leqslant \frac{2}{\Delta t} \left(|p_{1,i} \Delta\theta_s| + |p_{2,i} \Delta\phi_s| + \sum_{j=1}^{3} |p_{3,ij}| \left| \frac{\Delta F_{m,j}^{(s)}}{F_m} \right| \right) \tag{5.34}$$

However, with the 3D load cell used for this study, with for example 80-m tethers, the absolute position error is about one meter. But with a time step of 20 ms, this will lead to an error on velocity of 100 m/s, which is not workable in comparison with our kite speed always under 30 m/s. A solution is to assume the position error as a sum of low frequency variations errors, and a dynamic error. With the finite difference process, the absolute position error disappears from the kite velocity error, and only the dynamic position error remains. The dynamic error can be far under the absolute error. Indeed, in case of the 3D load cell the error is 0.5% of full scale, meaning about 22 N. However the white noise amplitude of signals under a static load was about 1 N. Moreover the filtering process presented in part 5.3.2 can be seen as an increase of the time step used for differentiation. Therefore the time step used for uncertainties computations will be 500 ms. But as it will be shown, even with these assumptions, velocity error will have a significant impact on lift to drag ratio and lift coefficient.

$$\Delta\underline{V}_k \leqslant \frac{2}{\Delta t} \left(\left\lceil \underline{p}_1 \right\rfloor \Delta\theta_{dyn/s} + \left\lceil \underline{p}_2 \right\rfloor \Delta\phi_{dyn/s} + \left\lceil \underline{\underline{p}}_3 \right\rfloor \frac{\Delta\underline{F}_{m/dyn}^{(s)}}{F_m} \right) \tag{5.35}$$

5.5.1.8. Lift to Drag ratio

Finally, the lift to drag ratio uncertainty can be maximized by the sum of contributions of each measurement uncertainties, denoted from C_1 to C_8 for plotting convenience. C_1 concerns the measurement of the 3D load cell. C_2 and C_3 deal with the back tether measurement. C_4, C_5 and C_6correspond to the axis changes to get all data in the same reference frame. C_7 is the contribution of the wind measurement. At last, C_8 denotes the influence of the kite velocity.

$$f = \frac{\|\underline{L}\|}{\|\underline{D}\|} \tag{5.36}$$

$$\begin{aligned}\frac{\Delta f}{f} \leqslant & \overbrace{\left\lceil \underline{c}_1^T \right\rfloor \frac{\Delta \underline{F}_m^{(s)}}{F_m}}^{C_1} + \overbrace{|c_2| \frac{\Delta F_{bl}}{F_{bl}}}^{C_2} + \overbrace{|c_3| \frac{\Delta F_{br}}{F_{br}}}^{C_3} + \overbrace{|c_4| \, \Delta\theta_s}^{C_4} \\ & + \overbrace{|c_5| \, \Delta\phi_s}^{C_5} + \overbrace{|c_6| \, \Delta\psi_{ws}}^{C_6} + \overbrace{\left\lceil \underline{c}_7^T \right\rfloor \frac{\Delta \underline{V}_{WM}^{(ws)}}{V_{WM}}}^{C_7} \\ & \overbrace{+ \frac{2}{\Delta t} \left\lceil \underline{c}_8^T \right\rfloor \left(\left\lceil \underline{p}_1 \right\rfloor \Delta\theta_{dyn/s} + \left\lceil \underline{p}_2 \right\rfloor \Delta\phi_{dyn/s} + \left\lceil \underline{\underline{p}}_3 \right\rfloor \frac{\Delta \underline{F}_{m/dyn}^{(s)}}{F_m} \right)}^{C_8}\end{aligned} \tag{5.37}$$

With:

$\underline{c}_1^T = \underline{\beta}^T \underline{\underline{\alpha}} \, \underline{\underline{M}}_{\theta_s} \underline{\underline{M}}_{\phi_s}$

$c_2 = \underline{\beta}^T \frac{\underline{F}_f}{\|\underline{F}_f\|} F_{bl}$

$c_3 = \underline{\beta}^T \frac{\underline{F}_f}{\|\underline{F}_f\|} F_{br}$

$c_4 = \underline{\beta}^T \frac{\underline{\underline{\alpha}}}{\|\underline{F}_f\|} \frac{\partial \underline{\underline{M}}_{\theta_s}}{\partial \theta_s} \underline{\underline{M}}_{\phi_s} \underline{F}_m^{(s)}$

$c_5 = \underline{\beta}^T \frac{\underline{\underline{\alpha}}}{\|\underline{F}_f\|} \underline{\underline{M}}_{\theta_s} \frac{\partial \underline{\underline{M}}_{\phi_s}}{\partial \phi_s} \underline{F}_m^{(s)}$

$c_6 = \frac{\underline{\gamma}^T}{\|\underline{V}_a\|} \left(\underline{\underline{I}}_{\mathbb{R}^3} - \underline{x}_a \underline{x}_a^T \right) \frac{\partial \underline{\underline{M}}_{\psi_{ws}}}{\partial \psi_{ws}} \underline{V}_{WM}^{(ws)}$

$\underline{c}_7^T = \frac{\underline{\gamma}^T}{\|\underline{V}_a\|} \left(\underline{\underline{I}}_{\mathbb{R}^3} - \underline{x}_a \underline{x}_a^T \right) V_{WM} \underline{\underline{M}}_{\psi_{ws}}$

$\underline{c}_8^T = -\frac{\underline{\gamma}^T}{\|\underline{V}_a\|} \left(\underline{\underline{I}}_{\mathbb{R}^3} - \underline{x}_a \underline{x}_a^T \right)$

$\underline{\beta}^T = \frac{\underline{L}^T}{\|\underline{L}\|^2} \left(\underline{\underline{I}}_{\mathbb{R}^3} - \underline{x}_a \underline{x}_a^T \right) - \frac{1}{\|\underline{D}\|} \underline{x}_a^T$

$\underline{\gamma}^T = -\frac{\underline{L}^T}{\|\underline{L}\|^2} (\underline{x}_a \underline{F}_a^T + \underline{x}_a \cdot \underline{F}_a \underline{\underline{I}}_{\mathbb{R}^3}) - \frac{1}{\|\underline{D}\|} \underline{F}_a^T$

5.5.1.9. Lift coefficient

As it has been done for the lift to drag ratio, the lift coefficient is maximized by the quantity $\sum_{i=1}^{8} D_i$, with each contribution D_i being associated to the same uncertainty measurement than the C_i contributions used in the case of the lift to drag ratio.

$$C_l = \frac{\|\underline{L}\|}{\frac{1}{2}\rho A_k V_a^2}$$

$$\begin{aligned}\frac{\Delta C_l}{C_l} \leqslant\ & \overbrace{\left\lceil \underline{d}_1^T \right\rfloor \frac{\Delta \underline{F}_m^{(s)}}{F_m}}^{D_1} + \overbrace{|d_2| \frac{\Delta F_{bl}}{F_{bl}}}^{D_2} + \overbrace{|d_3| \frac{\Delta F_{br}}{F_{br}}}^{D_3} + \overbrace{|d_4|\, \Delta\theta_s}^{D_4} \\ & + \overbrace{|d_5|\, \Delta\phi_s}^{D_5} + \overbrace{|d_6|\, \Delta\psi_{ws}}^{D_6} + \overbrace{\left\lceil \underline{d}_7^T \right\rfloor \frac{\Delta \underline{V}_{WM}^{(ws)}}{V_{WM}}}^{D_7} \\ & \overbrace{+ \left\lceil \underline{\nu}^T \right\rfloor \frac{2}{\Delta t} \left(\left\lceil \underline{p}_1 \right\rfloor \Delta\theta_{dyn/s} + \left\lceil \underline{p}_2 \right\rfloor \Delta\phi_{dyn/s} + \left\lceil \underline{\underline{p}}_3 \right\rfloor \frac{\Delta \underline{F}_{m/dyn}^{(s)}}{F_m} \right)}^{D_8}\end{aligned} \tag{5.38}$$

With:

$$\begin{aligned}\underline{d}_1^T &= \underline{\kappa}^T \underline{\underline{\alpha}}\, \underline{\underline{M}}_{\theta_s} \underline{\underline{M}}_{\phi_s} \\ d_2 &= \underline{\kappa}^T \frac{\underline{F}_f}{\|\underline{F}_f\|} F_{bl} \\ d_3 &= \underline{\kappa}^T \frac{\underline{F}_f}{\|\underline{F}_f\|} F_{br} \\ d_4 &= \underline{\kappa}^T \frac{\underline{\underline{\alpha}}}{\|\underline{F}_f\|} \frac{\partial \underline{\underline{M}}_{\theta_s}}{\partial\theta_s} \underline{\underline{M}}_{\phi_s} \underline{F}_m^{(s)} \\ d_5 &= \underline{\kappa}^T \frac{\underline{\underline{\alpha}}}{\|\underline{F}_f\|} \underline{\underline{M}}_{\theta_s} \frac{\partial \underline{\underline{M}}_{\phi_s}}{\partial\phi_s} \underline{F}_m^{(s)}\end{aligned}$$

$$\begin{aligned}d_6 &= \underline{\nu}^T \frac{\partial \underline{\underline{M}}_{\psi_{ws}}}{\partial\psi_{ws}} \underline{V}_{WM}^{(ws)} \\ \underline{d}_7^T &= \underline{\nu}^T \|\underline{V}_{WM}^{(ws)}\| \underline{\underline{M}}_{\psi_{ws}} \\ \underline{\kappa}^T &= \frac{\underline{L}^T}{\|\underline{L}\|^2} (\underline{\underline{I}}_{\mathbb{R}^3} - \underline{x}_a \underline{x}_a^T) \\ \underline{\nu}^T &= -\frac{\underline{L}^T}{\|\underline{L}\|^2} \left[(\underline{x}_a \underline{F}_a^T + \underline{x}_a^T \underline{F}_a \underline{\underline{I}}_{\mathbb{R}^3})(\underline{\underline{I}}_{\mathbb{R}^3} - \underline{x}_a \underline{x}_a^T) \frac{1}{\|\underline{V}_a\|} \right. \\ & \left. - \frac{2}{\|\underline{V}_a\|^2} \underline{V}_a^T \right]\end{aligned}$$

5.5.2. Results

Uncertainties were calculated for lift to drag ratio and lift coefficient with the following sensor errors:

$$\begin{aligned}\Delta \underline{F}_m^{(s)} &= \begin{pmatrix} 22.0 \\ 22.0 \\ 22.0 \end{pmatrix} N \\ \Delta F_{bl} &= 10\, N \\ \Delta F_{br} &= 10\, N \\ \Delta\theta_s &= 1.7 \cdot 10^{-3}\, rad \\ \Delta\phi_s &= 1.7 \cdot 10^{-3}\, rad \\ \Delta\psi_{ws} &= 1.7 \cdot 10^{-3}\, rad\end{aligned}$$

$$\begin{aligned}\frac{\Delta \underline{V}_{WM}^{(ws)}}{V_{WM}} &= \begin{pmatrix} 0.02 \\ 0.02 \\ 0.02 \end{pmatrix} \\ \Delta \underline{F}_{dyn/m}^{(s)} &= \begin{pmatrix} 1.00 \\ 1.00 \\ 1.00 \end{pmatrix} N \\ \Delta\theta_{dyn/s} &= 1.7 \cdot 10^{-4}\, rad \\ \Delta\phi_{dyn/s} &= 1.7 \cdot 10^{-4}\, rad \\ \Delta t &= 0.5\, s\end{aligned}$$

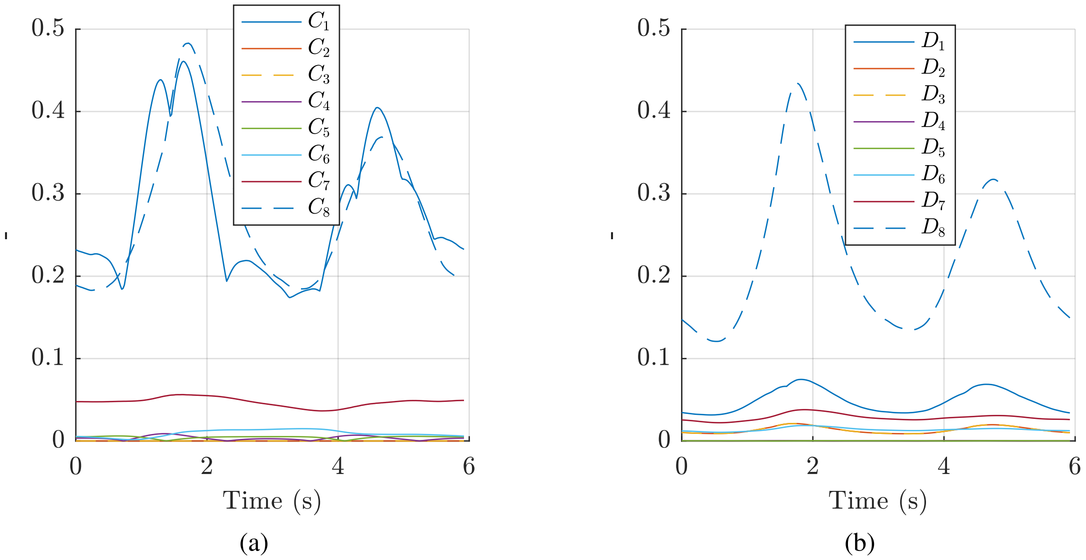

Figure 5.20.: Contribution of each uncertainty in the total error calculation of the lift to drag ratio (a) and lift coefficient (b) along the eight-pattern trajectory of the reference case (blue row in Tab. 5.1). Each line corresponds to a part of Eq. 5.38 and Eq. 5.37.

To have a quick overview of which elements will be prominent for final uncertainties, they are all plotted in Fig. 5.20(a) for the case of the lift to drag ratio and (b) for lift coefficient. One of the visible fact is that C_2 and C_3 (Eq. 5.37) are extremely low, and have then no effect in lift to drag uncertainty computation. More generally, the back tether force measurements have no effect on lift to drag processing. Not surprisingly, C_1 and C_8, ruling the effects of the 3D load cell error (static and dynamic), are the parameters with the most important contribution, followed by the uncertainties on wind measurements (C_7). The lift coefficient uncertainty follows the same rule, but with an uncertainty on position D_1 of less significance with respect to the uncertainty on the kite velocity D_8.

Results are shown in Fig. 5.21. The average relative uncertainty for the lift to drag ratio is 62$\%$ with peak value over 100$\%$, that is very questionable. For the lift coefficient, relative uncertainty is a bit lower but still large, with an average of 40$\%$ and peak over 60$\%$.

5.6. Discussion

With the results of uncertainty calculations, the evolution of kite parameters along a trajectory is very questionable. Indeed, with the error window presented in Fig. 5.21, the solution of no variation along a trajectory will fit between the two error lines. However,

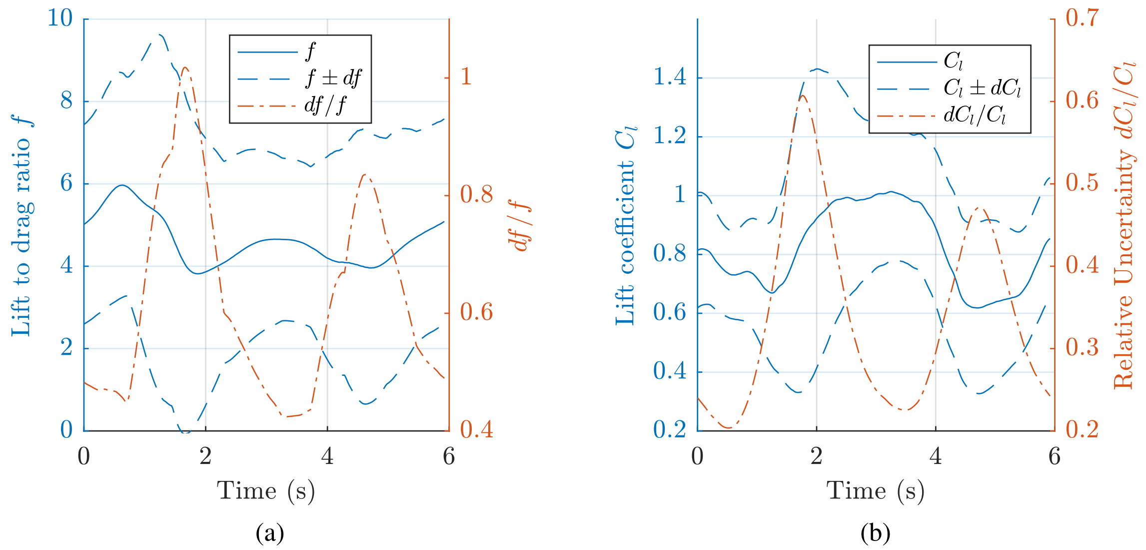

(a) (b)

Figure 5.21.: Evolution of uncertainties on the lift to drag ratio (a) and lift coefficient (b) along the eight-pattern trajectory of the reference case (blue row in Tab. 5.1).

the lift to drag ratio and the lift coefficient plotting in Fig. 5.21 are the result of the phase averaging method, leading to data coming from 43 eight-patterns (regarding the reference case) and averaged to get only one pattern. Therefore the observed variations have a physical signification and cannot be the result of sensors errors. Nevertheless, better results could be expected in the future, with a new set of data, and a systematic variation of kite specifications could be highlighted, with respect to the rotation rate of the velocity vector of the kite around tether axis, or with respect to other quantities.

Consequently, these future work should have to focus on several points. At first the symmetry issues have to be considered carefully, with a rigorous verification of all elements that can lead to potential symmetry issue. For example tether lengths should be carefully checked, and particularly the lengths of left and right tethers. These measurements must be carried out at various loads. For that, the two tethers are fixed on one side, and the other sides of the two tethers are linked using a leader line. This leader line goes through a return pulley, and a load is applied to the pulley. Therefore, the load is equally split between the two tethers. When the applied load rises, the length difference should not change if the two tethers have experienced the same history. However, when operating the kite, during a hard turn or during a crash, a tether could be slightly damaged, and then the elongation under load can be different from the one of the other tether. To identify symmetry issues the data post processing should be done quickly. Indeed, during trials the symmetry problem was identified, but did not seem to be so important.

Secondly, new sensors could be added to bring more information about the kite position and kite attitudes. For example, IMUs could be embedded on the kite again, but only for estimating the yaw angle of the kite, and compare this value to the angle γ related to the velocity vector. The yaw angle of the kite could also be obtain using video tools, by filming the kite from the ground, and performing an image analysis. This solution could also lead to a measurement of the flying shape, if several camera are used, associated with a photogrammetry post processing. This possibility, already tested by Infanzon (2013) with limited results, can probably be improved with better cameras. Much more could also be done regarding embedded cameras, to get a finest understanding of phenomenon occurring during turns. For example, yarn tell-tales could be stuck on the kite, and filmed by a camera. Thus, separated flows could be observed at some locations, as it can be done for the analysis of a stall occurring on the wing of an airplane [3].

Thirdly, a simple aerodynamic modeling of the kite could be achieved, based for example on a non-linear lifting line method, to foresee kite specs during turns, and then provide a guidance on the expected variations of the aerodynamic parameters of the kite

The lift to drag ratio and the lift coefficient variations along an eight-pattern trajectory are not brought out in a perfect conclusive way by the present measurements. However, these variations exist, and lead consequently to larger amplitudes of forces than the ones predicted by the zero-mass model. These amplitude have to be considered: indeed, they can be detrimental to boat stability, actuator power or material wear if they are not taken account. Therefore it has been decided to propose an evolution law based on the average of the reference case (blue row in Tab. 5.1) and on two other similar cases (C80_1 and C80_2 in Tab. 5.1). In this way, modelings of kite and modelings of boats towed by kite could integrate these variations, and these laws will be updated when further works lead to results with better accuracy. To get rid of the symmetry issue, data over the eight pattern trajectory have been processed in order to make symmetrical. For this purpose, each signal (lift to drag ratio f and lift coefficient C_l) has been cut into two pieces of equal length, and these two pieces have then been averaged. This is only possible because the middle of the eight pattern corresponds to the middle of the time-series. Thus, for a signal S defined for $t \in [\![0, t_a]\!]$, the symmetrical signal S_{sym} is:

$$S_{sym}(t) = \begin{cases} \frac{S(t)+S(t+\frac{t_a}{2})}{2} & t \in [\![0, \frac{t_a}{2}]\!] \\ \frac{S(t-\frac{t_a}{2})+S(t)}{2} & t \in]\!]\frac{t_a}{2}, t_a]\!] \end{cases} \tag{5.39}$$

Results of this process are given in Fig. 5.22. Only positive rotation rates are plotted, because the signal is now symmetrical about the axis defined by $\dot{\gamma} = 0$ rad/s. This leads to the following linear laws:

$$f = 4.89 - 0.11|\dot{\gamma}| \tag{5.40}$$

$$C_l = 0.92 - 0.06|\dot{\gamma}| \tag{5.41}$$

---

[3] https://www.youtube.com/watch?v=WFcW5-1NP60

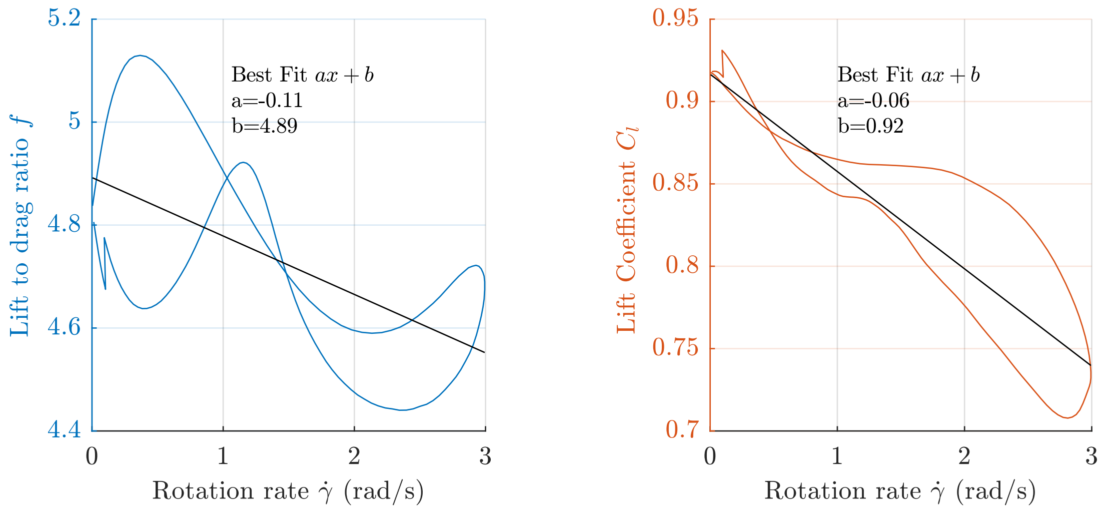

(a) (b)

Figure 5.22.: Best fit processed on symmetrical signal of the lift to drag ratio (a) and the lift coefficient (b), from an average data set coming from three best cases (C80_1, C80_2 and C80_3 in Tab. 5.1)

The symmetrical data set used for proposing these laws is also used by Bigi et al. (2018). In this work, linear laws are also proposed, but the parameters are obtained in a different way: the experimental data are compared with zero-mass model results, and the parameters are adjusted to get the best fit possible. The parameter values are close but no equal. Indeed the current value of the lift to drag ratio and the lift coefficient are computed from a point-mass model, as it is explained Part 5.4.6.

6. Sea Measurement Fieldwork: the Kiteboat Vessel

Résumé

Ce chapitre présente une campagne de mesure réalisée sur une bateau spécialement conçu est fabriqué pour être adapté à des essais de kite en mer. Le retour d'expérience des précédents travaux a montré qu'une plateforme d'essais et de mesures devait être totalement disponible pour le projet. Le dessin d'un tel bateau, de type kiteboat, a été confié à des étudiants de troisième année de l'ENSTA Bretagne, et devait respecter un cahier des charges spécifiant les caractéristiques globales du bateau. En particulier, le banc d'essais présenté dans les premiers chapitres devait pouvoir être directement embarqué, et sa place devait être ajustable pour mesurer l'influence de la position d'attache sur le comportement du navire. Par la suite, le bateau a été fabriqué en contreplaqué-époxy, par un chantier local. Après réalisation, le bateau mesure 6 m de long et 2 m de large, et a un déplacement d'environ 850 kg en pleine charge, avec trois membres d'équipages. Une photo du bateau est disponible à la Fig. 6.1. A l'issue de la construction, une première phase d'intégration des capteurs et du système de mesure et de contrôle du kite a été menée, permettant en particulier d'intégrer une centrale des mesures des mouvements du bateau, ainsi qu'un mat anémométrique équipé de trois capteurs. Une seconde phase a ensuite portée sur la prise en main du bateau. Pour cela plusieurs navigations ont été réalisées dans les environs de Brest, répondant à plusieurs objectifs. Premièrement, il s'agissait d'estimer les capacités du bateau lorsqu'il est propulsé par un kite, pour pouvoir ensuite tracer un plan d'expérience. Deuxièmement, des procédures de lancement du kite en autonomie depuis une petite plateforme ont aussi été mise en place. Enfin, ces navigations avaient pour troisième objectif de valider le fonctionnement du système de contrôle du kite lorsqu'il est déployé sur le bateau, ainsi que de vérifier le bon fonctionnement de tous les capteurs. A cette occasion, le pilote automatique présenté précédemment a été amélioré pour s'adapter au contrôle d'un kite sur une plateforme mobile.

A l'issue de cette phase de développement, une réelle campagne de mesure des performances du bateau tracté par un kite a été menée. Celle-ci s'est déroulée pendant 4 semaines en avril 2017, dans la baie de Quiberon, pour bénéficier des installations et du savoir-faire de l'Ecole Nationale de Voile et des Sports Nautiques (ENVSN). En effet, avec un site de plusieurs hectares situés en bord de mer, cette structure forme une base opérationnelle de grande qualité, permettant une mise en place rapide et optimisée. De plus le plan d'eau est relativement bien documenté, et a déjà été utilisé pour d'autres études scientifiques. Les chapitres précédents ont montré la problématique de la mesure du vent à l'altitude du kite pour post traiter finement l'évolution des performances du kite le long d'une trajectoire en huit. De ce fait une attention particulière a été apportée à la mesure du vent, et cela a mené à un dispositif contenant des points de mesures ancrés dans la baie à des positions fixes, et des mesures mobiles faites directement sur le kiteboat, ou à partir d'un semi rigide évoluant proche du bateau. De plus, un partenariat a été engagé avec une société spécialisée dans la micro-météorologie, pour avoir une modélisation fine du vent au-dessus de la zone de mesure, et pour connaitre en particulier le profil du vent en fonction de l'altitude. Le domaine plus fin de cette modélisation a une résolution spatiale de 110 m horizontalement, et de 20 m verticalement. Une journée de mesure est donnée Fig. 6.10, montrant clairement que la loi en puissance utilisée dans un chapitre précédent pour décrire le gradient de vent n'est pas suffisante.

Pendant cette campagne de mesures, des phases systématiques de navigation d'une longueur de 5 min étaient enregistrées, en conservant autant que possible tous les paramètres constants. Entre chaque phase, un élément du plan d'expérience était modifié. Les éléments les plus importants de ce plan étaient l'angle de vent réel, le type de kite, la longueur des lignes, et le type de dérives utilisé. D'autres paramètres mineurs rentraient aussi en compte. L'angle de vent réel déterminait aussi le type de pilotage du kite : pour les allures entre le travers abattu et le vent arrière, le pilote automatique du kite présenté au Chap. 3 donnait des résultats satisfaisants. Pour des angles plus serrées, le pilotage du kite se faisait par un contrôle manuel des actionneurs, et pouvait être dynamique ou statique. A l'issu de la campagne, plus de 100 phases de navigation avec kite ont ainsi été réalisées. Le post traitement des données est très similaire à ceux précédemment mis en place dans le deux autres campagnes expérimentales. Concernant l'utilisation des données, une première étape a consisté à utiliser la multiplication des capteurs, en particulier en ce qui concerne le vent, pour réaliser des vérifications croisées et ainsi valider la cohérence des données ou identifier des problèmes (Fig. 6.13 à 6.13).

Pour l'ensemble des phases de mesure sous kite, l'analyse des résultats a été faite sous deux angles d'approche : une vision moyennant toutes les informations pour chaque phase, permettant donc de dégager des tendances, et une approche plus fine utilisant la méthode de la moyenne de phase. A partir de la première approche il a par exemple été possible de tracer une polaire de vitesse du kiteboat, dans la configuration la plus utilisée (Fig. 6.17). Une courbe de résistance à l'avancement du kiteboat aussi été tracée, et peut servir de base à de futurs travaux de modélisation. (Fig. 6.18 (b)) Les mouvements du bateau en fonction de l'angle de vent réel ont aussi été mesurés (Fig 6.19) Une analyse de la puissance nécessaire pour contrôler le kite comparé à la puissance propulsive fournis par celui-ci a aussi été faite, montrant que suivant le type de kite et donc du ratio d'effort entre lignes avants et lignes arrières, la puissance pour contrôler le kite peut être supérieure à celle fournie (Fig. 6.20). Une attention particulière devra donc être accordée pour le dessin de futurs kites afin de minimiser l'effort de contrôle, ainsi que dans la réalisation des systèmes de contrôle, en utilisant des actionneurs les plus efficaces possibles. La seconde approche par moyenne de phase n'a pu être menée que sur un nombre limité de cas, car tous les bords ne présentaient pas un caractère périodique suffisant, en particulier ceux réalisés en contrôle manuel. Les résultats globaux sembles cohérents au regard du comportement attendu d'un navire tracté par un kite. Cependant, il n'a pas été possible d'identifier des évolutions typiques et répétitives des performances du kite le long d'une trajectoire, bien que ces évolutions soient toujours visibles, comme pour le chapitre précédent. Cependant, ce type d'analyse est plus discutable pour un système mis en œuvre depuis un bateau, car les mouvements de celui-ci peuvent rendre encore plus contestables certaines des hypothèses, comme celle des lignes parfaitement droites et indéformables. De façon générale, cette campagne de mesure apporte une bonne première basse de données pour la validation de modélisation d'un bateau tracté par kite, et de nombreux autres résultats peuvent encore être extraits de ce jeu de données.

6.1. Fieldwork Presentation

6.1.1. Genesis

The major feedback of the experimental work carried out on the Steven Paul, and presented in Chap. 4, was the issue with the availability of the boat for scientific trials. Therefore a thorough examination has been conducted to identify the best adapted platform for kite trials and measurements. Due to overseas location of the Steven Paul, it was not relevant to plan other projects with her, and then a local solution was sought. As it was shown, for such a project the vessel must be fully dedicated to trials, and then the purchase of a similar vessel was investigated. The cost of a professional 13-meter-long vessel refitted to be suitable for kite trials and measurements was estimated based on following elements:

- Purchase of a second hand vessel: at least 100 000 €
- Refit in a shipyard to modify the structure: at least 40 000 €
- New dedicated sensors and kite control system: 50 000 €
- Annual cost (place in the harbor, ongoing maintenance): 10 000 €

Moreover, this type of project is also really time expensive:

- Time for finding the suitable vessel to buy
- Study for the structure refit and shipyard choice
- Study for the choice of the sensors
- Sensors and kite control system development and mounting

The workload associated to all these tasks represents probably a full-time position for an engineer in addition to the Ph. D. student. However, this project was not planned in the initial program, consequently an additional engineer should have been hired. The induced cost is about 100 000 € minimum for two years. All in all, at least 300 000 € are required for completing successfully the project, with one year of development and one year of trial, but this is probably a low estimate. A such amount of money was not available and consequently this solution could not be chosen. A second solution was then considered, involving a smaller boat, and then lower costs. It was decided to build a specific platform that can be operated with three crew members, and transportable by road, like rigid inflatable boats (RIB). In this case, the experimental set up previously developed and used in the previous fieldwork could be reused. Finally, the choice was to let the design to students in their last year of naval architecture course at ENSTA Bretagne, and to subcontract the construction to a professional shipyard. In these conditions, the needful time for the team was really reduced, and most of the project could be managed by the Ph. D. student, with the temporarily help of the other members of the team. The boat resulting from this process was named KiteLab, and is presented in Fig. 6.1.

Figure 6.1.: Picture of the kiteboat used during the fieldwork, during a sailing session.

6.1.2. Kiteboat Design

As part of training of the last year of naval architecture studies, engineer students of ENSTA Bretagne have to complete projects suggested by professors or industrial partners. The duration of the exercise is one full-time month, and students can work together on the same project. Therefore, the kiteboat was fully designed by two students, in one month. The starting point for them was a list of specifications, with following requirements:

Size:	maximum length over all of 6 m, maximum width of 2 m.
Construction:	plywood-epoxy method (entails limited hull shape possibilities - only developable surface). The advantages of such a material is that it does not need any mold, and this is a good point in the case of a single prototype.
Kite Control System:	suitable for boarding the control box and the associated elements used during previous works (visible in Fig. 2.2). Moreover, the control box must be able to be attached at various longitudinal positions in the boat, and the attachment system must withstand a kite load of 5 000 N (in all directions).
Safety:	the boat must stay stable with a crew of three people, and a kite generating a force up to 5 000 N in any direction. Moreover, the boat must be able to board safely at least six people when no kite is in used.
Propulsion:	the boat must have an outboard engine with a power of 6 HP.

At the end of the exercise, the students had to provide a set of drawings, including exterior view drawings, lines drawings, plywood cutting plans and an instruction manual for the assembly of plywood pieces. Moreover, they had to write a report presenting their work

(Jubert and Leslé (2016)). The main drawings are given in App. B, and an overview of the kiteboat structure made of an assembly of multiple plywood pieces is given in Fig. 6.2. The student work ended in April 2016.

6.1.3. Kiteboat Construction

The kiteboat construction was subcontracted to a local shipyard. At first, cutting plans and a 3D modeling were sent to a carpentry specialized in digital cutting for naval industry. After one month, all plywood pieces were delivered to the shipyard. The plywood grade was marine quality .Then, in three months of time the shipyard completed the construction with the following steps: plywood assembly and gluing using epoxy for fillets, application of fiber glass when necessary, painting and light work. An overview of this process is visible thanks to the set of pictures given in Fig. 6.3.

6.1.4. Kiteboat Finalization

The kiteboat was delivered by the shipyard in early October 2016. The following steps were the sensor integration and protection from sea water. Most of the components were already integrated in the kite control box and in the two associated waterproof boxes, however a few sensors had to be fixed directly on the kiteboat. This is the case of the inertial measurement unit, which needs to be rigidly fixed to the boat, all the time at the same position. The wind measurement mast with anemometers was also integrated to the boat as well as the rudder angle sensor. For connecting these sensors to the acquisition box, wires had to be run in the internal structure of the boat, and every connection point needs to be perfectly sealed to avoid path for sea water. The various wires coming from the onboard sensors were merged into a single one with multiple cores to minimize the number of connector (as visible Fig. 6.4)., which are vulnerable elements. The wiring diagram of the kiteboat is given in App. B. Moreover, the kite control box and the two others boxes were not perfectly sealed when deployed onshore, therefore a work had to be done to seal these elements. All these tasks took 2 months and were done by the end of November 2016.

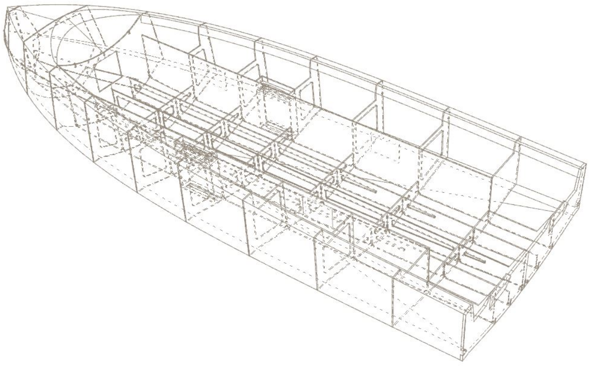

Figure 6.2.: Overview of the assembly of the plywood pieces.

(a) (b) (c)

(d) (e) (f)

Figure 6.3.: Pictures of construction steps of the kiteboat.

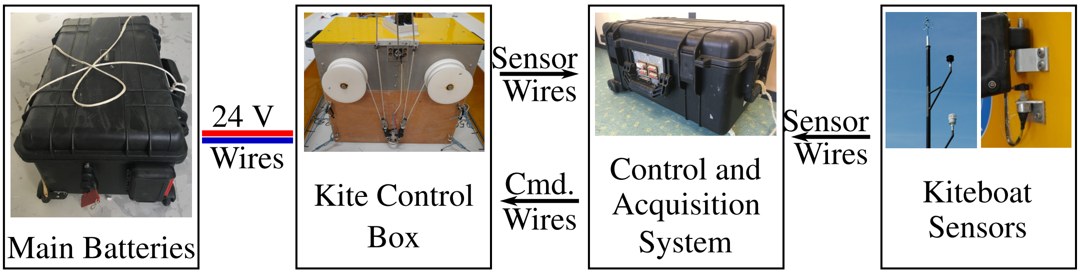

Figure 6.4.: Overview of the experimental set up when deployed on the kiteboat.

6.1.5. Testing Period

The first launching of the kiteboat took place the 30th of November 2016 in the bay of Brest, but the wind was not enough strong this day to allow the kite to fly. This first trial was followed by five other sailing sessions, with these objectives:

- Check the functioning of all sensors and systems, and verify the robustness of the whole system in a tough environment.
- Adjust the automatic pilot previously developed to a use on the kiteboat.
- Find the best suitable procedures for launching the kite from the kiteboat.
- Identify the sailing possibilities of the kiteboat to be able to draw a design of experiments

These sessions took place on the most suitable locations near Brest, depending on weather conditions, especially wind magnitude and orientation. One session required a crew of three people on the kiteboat, and a RIB with at least two people to help with kite launching when necessary, and ensure the safety of the operation in case of problem, like capsizing (which never occured).

These trials were carried out with the kite Cabrinha Switchblade 5 m², previously used in the onshore fieldwork, and shown in Fig. 5.4. It became rapidly obvious that the two daggerboards of the kiteboat (one on each side) were large enough to allow an upwind sailing, at least with a five-square-meter kite. Therefore, to optimize time on water, and so to save time of engaged persons, some sessions were arranged to be solely downwind. The starting point was then different from the arrival one. A summary of these sessions can be found on YouTube[1], and the associated GPS records are given in Fig. 6.5. One session had to be aborted due to oxidation on electric contacts of the joysticks of the remote device, leading to a complete inability to control actuators, and the kite as a consequence.

The major feedback of this trial step was the issue with upwind sailing. Therefore it was decided to buy new bigger daggerboards, and a new bigger kite, hoping to improve performances. Consequently, the sum of the two daggerboard area went from 0.683 m² to 1.265 m². The new kite was the same model (Cabrinha Switchblade), but with a larger area of 12 m² instead of 5 m².

---

[1] https://www.youtube.com/watch?v=_PRhv5hbyhU

(a) Plouguerneau (b) Lampaul-Plouarzel

(c) Bay of Brest (d) Bay of Brest

Figure 6.5.: Screen shots of GPS tracks of the trial sailing sessions. Green marker denotes the beginning of the record and red one stands for the end.

6.1.6. Proceedings of the Measurement Fieldwork

6.1.6.1. Measurement Site

The real performance measurement phase was carried out during four weeks starting by the end of March 2017. The site which was chosen for the fieldwork is the bay of Quiberon (South Brittany, France) for its various advantages. Indeed, the peninsula of Quiberon is the location of the French National Sailing School (ENVSN), and their facilities placed on the seaside are valuable, as well as the expertise of the local staff. Moreover the sailing area of the bay of Quiberon is really well known, thanks to years of studies to the benefit of the French National Sailing Team. This area had also been used for other scientific works like Roncin et al. (2005),Leloup et al. (2014). In this context, the bay of Quiberon is surrounded by several wind sensors belonging to the Wind Morbihan network[2].

6.1.6.2. Sailing Area

The objectives of this work are to measure the performance of the kiteboat at various true wind angles. Measurements have to be carried out in the area covered by the fixed-point wind sensors, presented in Fig. 2.15. In spite of the significant system deployed for measuring wind velocity, it is insufficient to get a perfect knowledge of the 3D wind field all over the sailing area. Therefore it has been decided to do systematically five-minute records at a given true wind angle, with keeping all parameters as constant as possible. This leads to size the sailing circle to a radius of 0.7 NM, to be able to complete a run of 5 minute at 12 kt (a distance of 1 NM is then necessary). A boat speed of 12 kt was the highest speed measured at the time of the design of experiments definition. The need to sail in an area with a wind as stable as possible, but not too far from shore to avoid time-consuming taxiing periods, leads to define the location of the sailing area, with the center point located at a distance of 2.5 NM from ENVSN's facilities.

6.1.6.3. Organization of a Typical Day of Measurement

At the beginning of the day, the objectives of the day were decided in accordance with the state of progress of the fieldwork and the current weather. Once the wind magnitude is sufficient (or with an optimistic forecast), the operation of the day could start. Two RIBs and their crew were in charge of mooring the fixed-point wind measurement platforms at their locations. In the same time, the kiteboat was launched, and transits towards the upwind part of the sailing area. It takes approximately one hour to complete this part.

---

[2] http://windmorbihan.com/

The crew of the kiteboat is made of three people: one helmsman, one kite pilot, and one person in charge of data acquisition and data monitoring to verify the proper functioning of all sensors. The launching procedure of the kite is carried out as follows:

1. Tethers are fastened on the leader lines of the control system.
2. Leading edge and battens of the kite are inflated.
3. Tethers are fastened on the kite bridles.
4. The kite is then released upside down on the water, with the leading edge facing the water.
5. Two members of the crew control the kite, with one tether in each hand, letting it go downwind (tether are accumulated in buckets, with one bucket for front tethers and another one for back tethers). The helmsman uses the engine to go backwards, and then keep the boat well oriented with the transom facing the wind).
6. When all tethers are out of the buckets, the kite can be taken off. This can be done with the help of the RIB, or with appropriate actions on tethers done by one crew member. During this step, the second crew member has the remote device in his hands, and he is ready to take control of the kite as soon as the take-off is completed. The helmsman still goes backwards to keep the tethers stretched, but regulating the power in accordance with the needs of the crew member in charge of the take-off of the kite.

Afterward, measurement runs can start, with always a first full downwind run to check the proper functioning of all sensors and systems. During runs, the RIB with wind measurement device on board stays near the kite. To save time, the upwind sailing is sometimes done with the second RIB towing the kiteboat at full speed (about 15 kt). When the measurement phase is over (at the end of the day, if the program is completed or in case of incident), the kiteboat goes back to the harbor, and the two RIBs bring back the wind measurement platforms. Data are then downloaded from all devices, calibrated and stored on computers.

6.1.6.4. Major Issues

Two major issues occurred during the fieldwork. The first one was relative to the roll bar shown in Fig. 6.1, supposed to protect crew members from kite tethers in the case of an uncontrolled kite flight. This case only happened once, during an upwind phase towed by the RIB, with the kite was held in static flight by one of the crew member. Unfortunately, for an unknown reason the pilot lose the control of the kite, and the later suddenly crossed the wind window, reaching very quickly the most powerful area. The kite underwent then a strong buckling phenomena, similar as the one shown in Fig. 5.12 (e) (it was the same

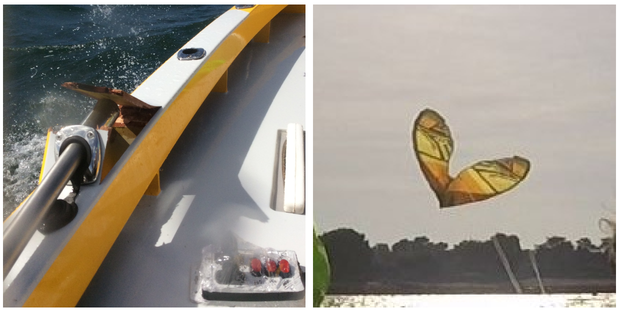
(a) (b)

Figure 6.6.: Consequences of the loss of control of the kite. (a) Damage of roll bar fixings after an uncontrolled kite flight. (b) Rollover of the kite consequently of the emergency procedure established after the incident.

kite - Cabrinha 5 m²). It became totally impossible to retrieve the control of the kite. At a moment, the tethers met the top of the roll bar, creating a force on the roll bar estimated to more than 1 500 N (estimated from other measurements). The roll bar fixings did not support such an effort and broke instantly (see Fig. 6.6(a)). Therefore, it felt down on the crew, and the kite finally crashed into the water. Fortunately, nobody was injured. The roll bar fixings were repaired, more firmly, and an emergency procedure was defined to be able to shut down rapidly the power of the kite. This procedure consists of reducing quickly the length of back tethers, or in other word, reducing the trim a lot. This can be done by pushing the trim joystick as far as possible. The consequence for the kite is quite immediate, with a rollover, as visible in Fig. 6.6(b). In this position, tension in tethers becomes very low.

The second issues was not relative to the safety of crew, but affected the measure of the heading of the boat done by the IMU Vector Nav, presented in Part 2.5.1. Indeed, to provide an accurate measurement of the heading, the device compares the position of one GPS antenna relatively to the second one. However, the distance between the two antennas needs to be accurately specified during the configuration of the device, and a margin of error has also to be entered. Unfortunately, a mistake was made at this stage, and the entered value was different from the measured one, with a gap of 6 cm. The margin of error was left to the default value equals to 2.5 cm. Thus, the entered value overshot the range of acceptable values. This issue led to incorrect values of heading, but not at all time, and the error on heading was never higher than 20°. Consequently, the complete scale of the problem was not seen during the measurement. Some unusual values were observed, but it seemed happen only at the beginning of the day, and a regular value was at all time observed before the first run (the verification was done with a classic manual compass). Finally, the importance of the problem was only noticed during the first stage of post processing carried out in the weeks after the measurement operations, when the heading data provided by the IMU was benchmarked with the heading data coming from the integrated electronic compass of the anemometer MaxiMet (see part

2.6.3). It showed than the heading error was time-varying, and could go from 0 to 20° of difference during a five-minute-run (a part is dedicated to sensor benchmark in the Results section, and this issue is shown in Fig. 6.13). The origin of the problem was then investigated, and the configuration error of the device had been found. The manufacturer was contacted, but not enough data were recorded to be able to retrieve the correct heading value. Therefore, the heading data provided by the IMU has been totally discarded, and all the post processing of the following section is only based on heading data provided by the MaxiMet. Consequently the accuracy and the frequency of the data are lower than expected.

6.1.6.5. Overview of the Achievements

The fieldwork was carried out during a four-week period. However, depending on the availability of the ENVSN's facilities and staff, only 15 days were spent on site. Then, weather conditions and technical problems reduced to 10 the number of days with useful measurements (which was the initial target).This leads to more than one hundred runs with a kite, in the sailing area. The GPS tracks of all these runs are visible in Fig. 6.7. Adding to these ones the other specific runs like seakeeping or maneuverability tests, it finally corresponds to more than 9 hours and 40 minutes of relevant recordings. This required more than 80 hours on the water taking into account all steps of the trials. These trials led to a second video available on YouTube[3].

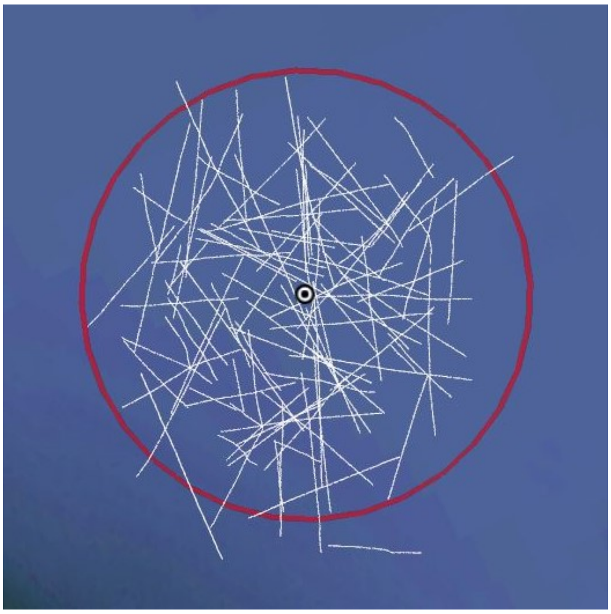

Figure 6.7.: GPS tracks of all relevant runs of the kiteboat sailing with one of the kite in the sailing area (red circle) during the fieldwork.

---

[3] https://www.youtube.com/watch?v=Zgd8KkaCavg

6.2. Design of Experiments

A set of parameters were varied during the fieldwork from one run to another, and these variations shape the experience matrix. Some of the parameters were perfectly defined and chosen, as tether lengths, whereas others were only desired, as the true wind angle, or undergone like true wind speed. The inputs of the matrix are described is the following subsections.

6.2.1. Kite

Three different kites are used: the two Cabrinha kite with area of 5 and 12 m², and a third one built especially for the kiteboat by the beyond-the-sea company. This kite has an area of 5 m², but it has been delivered only on the last two days of the sea trials. These three kites are presented in Fig. 6.8 (a) to (c).

6.2.2. Daggerboards

Two set of daggerboards are used. The first one are the set initially bought for the kiteboat and shown on drawings of App. B. These appendages are named Standard daggerboards, shorten with the letters STD when necessary. The daggerboards of the second set are custom ones, and specially ordered for the kiteboat. These appendages are named Black daggerboards, shorten with the three letters BCK when necessary. These two sets of daggerboards are presented in Fig. 6.8 (d) and (e). The main differences are the span and, to a lesser extent, the chord law. The thickness law and profiles are quite identical.

6.2.3. True Wind Angle

Numerous true wind angles are tested, from upwind sailing with true wind angles about 60°, to full downwind (180°). For each run, the desired true wind angle is defined and so the induced heading, and the helmsman does his best to keep the heading of the boat as constant as possible to obtain a run with the correct true wind angle. The objective is to cover the range of true wind angle with an increment of 20°.

6.2.4. True Wind Speed

The magnitude of the wind is obviously a parameter that can not be decided. Consequently, runs are done whatever is the wind magnitude, and they are then sorted to group together runs with similar wind magnitude.

(a) Cabrinha 5 m² (Cab 5.) (b) Cabrinha 12 m² (Cab 12.) (c) beyond-the-sea 5 m² (BTS)

(d) Daggerboard Standard (STD) (e) Daggerboard Black (BCK)

Figure 6.8.: Pictures of the kites and the daggerboards used during the measurement phase. The bracketing letters denote the short name used in legends of plots.

6.2.5. Tether Lengths

As it was done for the previous experimental study presented in Chap. 5, two set of tether are considered, with lengths equal to 50 m and 80 m.

6.2.6. Kite Flight

Various kite flight type are tested, but most of them are ruled by the true wind angle. For low true wind angles (lower than 80°), only static flight is achievable. In this case, one of the crew member is in charge of holding the kite at a given position using the control joysticks. For medium true wind angles (between 80° and 100°), the dynamic flight is possible, but not with the automatic pilot. Indeed the the kite needs to fly close to the wind window and the autopilot is not able to deal efficiently with this type of situation. Here again, one of the crew member manually controls the kite with the joysticks. For larger true wind angle (from 100° to 180°), the autopilot presented in Chap. 3 controls the kite. In this case, two trajectories are tested: down-loop and up-loop. Autopilot settings are changed as little as possible from one run to another, however it is sometimes necessary to adjust some settings to ensure a proper flight. Moreover, these settings result from manual choices, based on empirical experiences.

6.2.7. Kite Attachment Point

The longitudinal position of the kite control box can be modified, and consequently the longitudinal location of the kite attachment in the boat reference frame. Four positions equally distributed along the boat were at first defined. However it became rapidly obvious that the extreme positions initially foresaw were in fact inoperable. Finally one position was used most of the time, with a kite attachment point located at 2.68 m forward the transom. This position is named “C2bis”. A second position has been tried for a few runs, and is characterized by a longitudinal position of kite attachment point equals to 2.48 m, and named “C1bis”. The position of the crew members and additional waterproof boxes were then adapted to maintain the center of gravity at the same position at all time.

6.2.8. Propulsion

Some of the run are done with the outboard engine working. This allows upwind runs not always achievable only with the kite. It also allows to consider the effect of kites on a motor boat, which is the scope of the project. However the engine is not equipped with any sensors, therefore it becomes difficult to analyze results. The engine shaft is furthermore too short, leading to a ventilating phenomena of the propeller. When such an event occurs, the propulsion is totally ineffective, and data recorded during these runs cannot be considered.

6.3. Available Data

6.3.1. Kiteboat Data

One hundred and one runs have been achieved inside of the sailing area, with the kite, plus several other measurements done with no kite to acquire data about maneuverability and sea keeping capabilities of the kiteboat. However these specific tests are not considered in this study, and the exploitation of the associated data will be done in a future work. A run with kite consists of a five minute record, keeping all inputs of the experience matrix as constant as possible. For each run, many data were recorded, and an overview of the most important ones is given in Tab. 6.1.

6.3.2. Wind Data

Many wind data have been also recorded during these measurement works, as it has been detailed in part 2.6.4. When the source of the data needs to be precised, a subscript will

Symb.	Details
(COG)	Course Over Ground
V_s	Speed of the boat
ψ	Heading of the boat (HDG)
θ_s	Pitch angle of the boat
ϕ_s	Roll angle of the boat
δ_r	Rudder angle

(a)

Symb.	Details
$\underline{F}_m$	Front tether force vector
F_{bl}	Left back tether force
F_{br}	Right back tether force
$\lambda 1$	Position of actuator 1 (left)
$\lambda 2$	Position of actuator 2 (right)

(b)

Table 6.1.: Major variables recorded during runs. Table (a) presents information related to the boat, whereas part (b) deals with kite data.

Subscript	Source	Subscript	Source
kb	Kiteboat WindMaster	so	South Point
kws	Kiteboat WindSonic	we	West Point
kmm	Kiteboat MaxiMet	rib	RIB number 2
ctr	Center Point WindMaster	mod	EXWECs Model
cws	Center PointWindSonic	int	Interpolated
cmm	Center PointMaxiMet	extrap	Extrapolated
no	North Point		

Table 6.2.: Description of subscript used to identify the origin of wind data.

be added after a coma, in accordance with notations given in Tab. 6.2. Some subscripts can be combined, as for example “mod,extrap” to specify a data calculated from an extrapolation of the weather model.

Moreover a partnership has been engaged with the company EXWEXs specialized in weather forecast and weather models. The objective is to get a fine modeling (horizontal mesh size about 100 m, vertical mesh size of 20 m) of the wind over the sailing area, at high frequency, from 0 to 300m. A report provided by the company gives details on the models, the associated physic and outputs (Messager (2017)). The model in use is the Weather Research and Forecasting model (WRF) The strategy of modeling for such a forecast is to nest several spatial domains centered on the area of interest, from the large one with largest horizontal resolution to the smallest one with the expected resolution of 110 m. The time step of the finest domain is equal to 0.72 s. The five domains, with their topography are presented in Fig. 6.9. Because a real time forecast is not necessary, initial conditions and boundary conditions were taken from reanalyzed data, coming from the National Center for Atmospheric Research (USA). The deep understanding of this model is however totally out of the scope of this study, but the reader can refer to the technical report written by Skamarock et al. (2008) for more information. Thus, from there, only results of this model will be investigated.

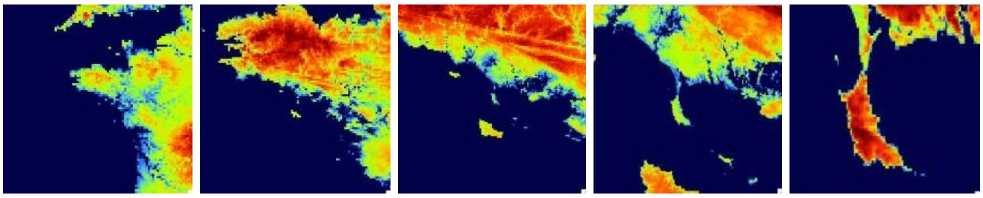

(a) Domain 1 (b) Domain 2 (c) Domain 3 (d) Domain 4 (e) Domain 5

Figure 6.9.: Spatial domains of the model used to predict the wind above the sailing area (Source: EXWEXs' report of modeling, Messager (2017)) .

The outputs of the model are weather data along the altitude (from 20 m to 300 m) for some points of the grid, for each time step. The most interesting data are the three components of the wind velocity, the temperature and the pressure. Other weather data are also outputted, but are not really relevant in the present case. Data from all points of the grid of the Domain 5 have not been outputted, because the amount of data would have been too large, and unnecessary. However some relevant points of the grid have been kept. At first, the points of the grid that are the closest from the locations of the measurement platform have been outputted. The results of a few hours of modeling outputted at the location of the center measurement platform is given in Fig. 6.10. Moreover, 222 other points were outputted, spread over the sailing area.

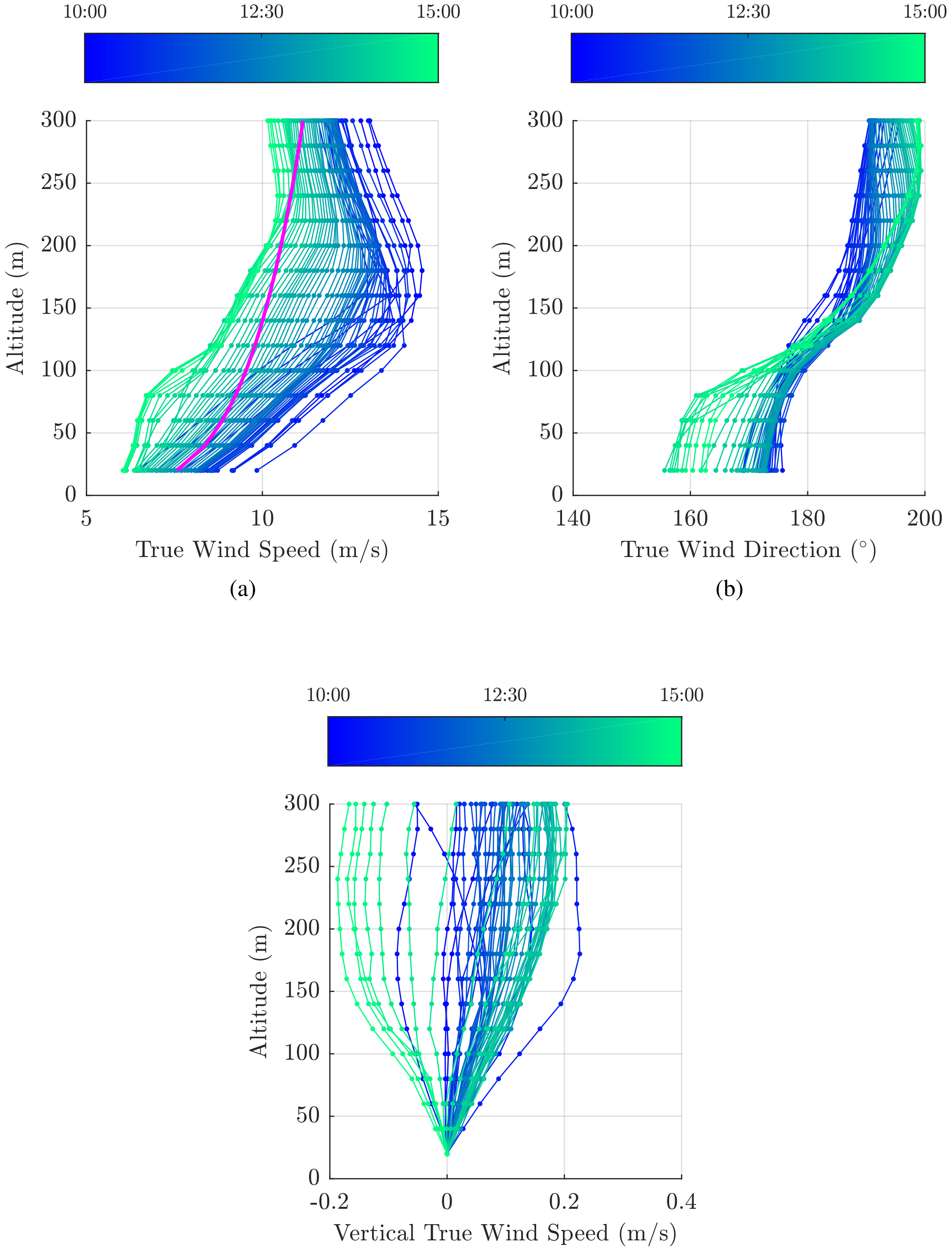

(a)

(b)

(c)

Figure 6.10.: Example of wind speed profile (a), wind direction profile (b) and vertical wind speed profile (c) calculated by the weather model during the 29th of March, and outputted at the location of the center measurement platform (time (UTC) of each profile depends on color, and is denoted by the colorbar). The magenta line on plot (a) denotes the ITTC profile, calculated from the average wind of all profile at 20 m during the period.

6.4. Post processing

The post processing of the kiteboat data is very close from the one presented in Chap. 5 and Chap 4. Some paragraphs are consequently close to other ones from other chapters, and are reproduced here for the reader's convenience. Vectors are still expressed into the heading reference frame R_ψ, unless otherwise noted. Velocities are given with respect to the Earth, unless otherwise noted.

6.4.1. Boat Related Equations

The velocity of the ship $\underline{V}_s$ is defined as the velocity of a point O, with respect to the Earth. This point O is located in the center plane of the boat, at mid-ship, and at the level of the cockpit floor (visible in App. Drawings). The velocity of the ship can be obtained from the velocity of the point U (coming from the measurements of the IMU):

$$\underline{V}_s = \underline{V}_U + \underline{OU} \wedge \underline{\Omega}_s \tag{6.1}$$

The rotation speed vector of the boat $\underline{\Omega}_s^{(s)}$ expressed in the ship reference frame R_s is directly the measurement of the turn rates (p, q, r) provided by the IMU. Thus $\underline{\Omega}_s$ expressed in R_ψ can be obtain using the transfer matrices:

$$\underline{\Omega}_s = (\underline{\underline{M}}_{\theta_s} \underline{\underline{M}}_{\phi_s}) \underline{\Omega}_s^{(s)} \tag{6.2}$$

6.4.2. Equations Related to Wind Data from Onboard Sensors

This part deals with the wind measurements carried out directly on the kite boat. The onboard wind measurement are firstly computed in the heading reference frame, going at first from the sensor reference frame R_{wm} to the ship reference frame R_s, and secondly to the heading reference frame R_ψ:

$$\underline{V}_{WM} = (\underline{\underline{M}}_{\theta_s} \underline{\underline{M}}_{\phi_s})(\underline{\underline{M}}_{\psi_w} \underline{\underline{M}}_{\theta_w} \underline{\underline{M}}_{\phi_w}) V_{WM}^{(wm)} \tag{6.3}$$

Then, the relative wind velocity at the altitude of the measurement point z_0 can be computed, taking into account velocity of wind sensor with respect to the point O belonging to the boat:

$$\underline{V}_{WR,z_0} = \underline{V}_{WM} - \underline{V}_{W/O} = \underline{V}_{WM} + \underline{OW} \wedge \underline{\Omega}_s \tag{6.4}$$

From there, the true wind speed at measurement point can be calculated:

$$\underline{V}_{WT,z_0} = \underline{V}_{WR,z_0} + \underline{V}_s \tag{6.5}$$

The estimation of the wind at any other altitude will be discussed in another section.

The relative wind at the kite altitude can be obtain by subtracting the velocity of the kite attachment point $\underline{V}_A$ to the true wind speed at kite altitude (tethers are considered as perfectly straight, therefore the translations motions of the kite attachment are entirely transmitted to the kite):

$$\underline{V}_A = \underline{V}_s + \underline{AO} \wedge \underline{\Omega}_s \tag{6.6}$$

$$\underline{V}_{WR} = \underline{V}_{WT} - \underline{V}_A \tag{6.7}$$

6.4.3. Kite Related Equations

At first, forces into front tether are computed in the heading reference frame instead of the frame of the boat:

$$\underline{F}_f = \underline{\underline{M}}_{\theta_s} \underline{\underline{M}}_{\phi_s} \underline{F}_m^{(s)} \tag{6.8}$$

Then, back tether forces are added to front tether vector, to create the total kite force vector $\underline{F}_k$ at kite attachment point A on the boat :

$$\underline{F}_{k,A} = \frac{\underline{F}_f}{||\underline{F}_f||}(||\underline{F}_f||+F_{bl} + F_{br}) \tag{6.9}$$

With the hypothesis of perfectly straight tethers with constant length, the total kite force vector at attachment point on the boat equals the opposite of the force generated by the kite at kite position:

$$\underline{F}_k = -\underline{F}_{k,A} \tag{6.10}$$

With the same assumption, the kite position $\underline{P}_k$ and the kite velocity $\underline{V}_k$ can also be computed with respect to the point A (kite attachment point):

$$\underline{P}_k = \frac{\underline{F}_f}{||\underline{F}_f||} L_t \tag{6.11}$$

$$\underline{V}_k = \frac{d\underline{P}_k}{dt} \tag{6.12}$$

With the hypothesis of zero-mass model, the aerodynamic force $\underline{F}_a$ generated by the kite is directly equal to the opposite of the force generated by the kite at kite position:

$$\underline{F}_a = -\underline{F}_k \tag{6.13}$$

With the hypothesis of point-mass model, as introduced in Chap. 5, the aerodynamic force $\underline{F}_a$ can be calculated taking into account the kite acceleration vector, computed with respect to an inertial frame, like the Earth:

$$\underline{F}_a = m\underline{\Gamma}_{K|Earth} - \underline{F}_k - \underline{p}_k \tag{6.14}$$

The kite acceleration with respect to the Earth is given in Eq. 1.24. However, the hypothesis of straight tethers with constant length (allowing the estimation of the kite position) seems very questionable regarding the acceleration of the kite. Indeed, because tethers are not infinitely stiff, the entire acceleration of the boat cannot be transmitted to the kite. Particularly, when motions of the attachment point occur at a sufficiently high frequency, they will be probably damped by the tethers. Moreover, the acceleration of the kite with respect to the Earth has been compared with the kite acceleration with respect to heading reference frame for one representative case. Results show an average difference under 1% of the norm of the acceleration vectors. For this two reasons, the heading reference frame is now considered as inertial:

$$\underline{\Gamma}_{K|Earth} = \underline{\Gamma}_k \tag{6.15}$$

$$\underline{F}_a = m\underline{\Gamma}_k - \underline{F}_k - \underline{p}_k \tag{6.16}$$

Knowing the relative wind vector at the altitude of the kite and the kite velocity, the apparent wind on kite $\underline{V}_a$ can be computed:

$$\underline{V}_a = \underline{V}_{WR} - \underline{V}_k \tag{6.17}$$

This apparent wind vector allows to define the aerodynamic reference frame R_a, and detailed in Part Aerodynamic Reference Frame. The drag vector $\underline{D}$ can be obtained by projecting the aerodynamic force $\underline{F}_a$ on $\underline{x}_a$, and the lift vector $\underline{L}$ is then the difference between $\underline{F}_a$and $\underline{D}$:

$$\underline{D} = (\underline{F}_a \cdot \underline{x}_a)\underline{x}_a \tag{6.18}$$

$$\underline{L} = \underline{F}_a - \underline{D} \tag{6.19}$$

The lift to drag ratio f is then obtained by computing the ratio of the norm of the lift and drag vector:

$$f = \frac{L}{D} = \frac{\|\underline{L}\|}{\|\underline{D}\|} \tag{6.20}$$

Finally the lift coefficient C_l is also obtained, with A_k the kite area, and ρ the density of the air.

$$C_l = \frac{\|\underline{L}\|}{\frac{1}{2}\rho A_k V_a^2} \tag{6.21}$$

6.4.4. Wind Estimation at Kite Altitude

With the large plan implemented for estimating wind variation all over the sailing area (numerous wind measurement devices presented Part 2.6.4 and 2.6.3, wind modeling introduced Part 6.3.2), several options are available to value the wind at the altitude of the kite. This part aims to list all possible options, and to chose the most suitable ones. Some of these methods will be immediately discarded, and others will only be introduced and postponed to further work. The underlying question in this context is what could be the the most appropriate solution.

6.4.4.1. Solution Based on Logarithmic or Power Laws

The method used for estimating wind above the Steven Paul and presented in Chap. 4 is based on a power law with a parameter taken equal to $1/7$. It could be reused for the current post processing, however the limits of such a method have already been pointed out (see Part. 5.3.3). Moreover the difference between the weather modeling and the power law is shown in Fig. 6.10. With the system deployed for this experimental work, a better estimation could be expected. Therefore the power law option will not be considered for this time.

6.4.4.2. Solution Based on the SODAR Data

The SODAR used during the onshore work presented in Chap. 5 was also used during this work, but with a really different purpose. Indeed, the SODAR was installed onshore, in the ENVSN's facilities, and was there to get data for the weather model (introduced in Part 6.3). Therefore the settings were really different from the ones used previously, leading to an amplitude of measurement going from 30 m to 600 m. Consequently, the lower layer has a small discretization, and is not relevant for estimating the wind in the lower layers. Moreover, because the SODAR was located onshore the lower layer was really disturbed by ground topography. Lastly, the distance between the SODAR and the center of the sailing area was large (2.5 NM). All these elements lead to discard this option for directly estimating wind at kite altitude. Therefore the weather model was considered.

6.4.4.3. Solution Based on the Profiles from the Weather Model

The first solution which is considered is to use the weather model to get a wind magnitude profile above the kiteboat, and then to scale this profile with measurements carried out on the kiteboat. In this case, no twist of the true wind direction along the altitude is assumed (which could be considered reasonable in a first approach, regarding the elevation range the kite was flying). The true wind direction is calculated with the data coming from the onboard sensors (anemometer for wind and GPS-IMU for boat velocity). However, the altitude of the onboard measurement of the wind and the altitude of the lowest point outputted by the model are not identical. Therefore, an estimation of the wind at measurement point is extrapolated from the data model. This extrapolation is a simple linear one. Consequently the scale factor can be calculated, by dividing the measured value by the extrapolated one, as presented in Eq. 6.22. This process is summarized in Fig. 6.11.

$$V_{WT}(z) = V_{WT,mod}(z)\,\overbrace{\frac{V_{WT,kb}(z_0)}{V_{WT,mod,extrap}(z_0)}}^{Scale\,Factor} \tag{6.22}$$

This approach requires the wind magnitude profile above the kiteboat, however this information is not outputted by the model at any point and at any time. The best way to obtain this profile is to find the three points (among the outputted ones) surrounding the current location of the boat, and then to compute a spatial interpolation of the profile, based on these three points. In the same way, a time interpolation needs to be achieved to get a profile between two time steps. However this method is really time consuming, if all the output points are used. Indeed the amount of data generated by the weather model is huge (more than 5 GB for a day of modeling, for the 226 output points), and the interpolation of a profile in space and time requires the loading of these data into random access memory. Another option is to only consider an average wind profile coming from a limited number of points, for example the four points of measurement, or eventually only one point. With such a method no spatial interpolation is required. The time interpolation can also be avoided by finding the nearest time step of the model. The relevance of these methods will be discussed in part 6.5.1.3, regarding the results of the weather model in comparison with measurements.

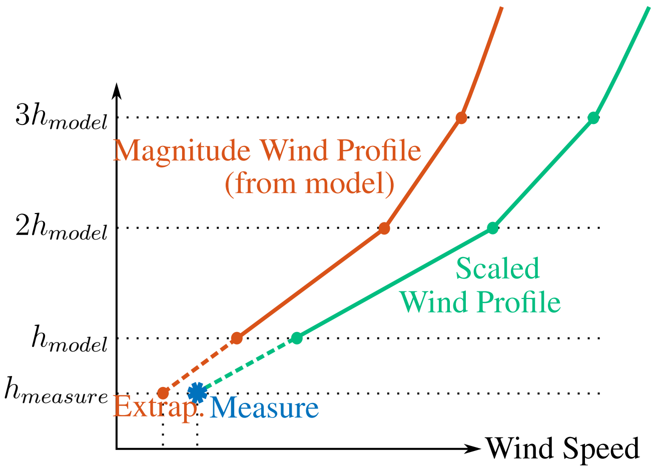

Figure 6.11.: Diagram of the procedure associating wind model data with measurement data, to obtain an estimation of the wind above the kiteboat. This corresponds to Eq. 6.22. The first output point of the model is at an altitude h_{model} of 20 m whereas the altitude of the wind measurement point $h_{measure}$ is equal to 5.5 m above the sea surface.

6.4.4.4. Solution Based only on the Data from the Weather Model

This last option is to directly interpolate the wind profile in the data provided by the model, without considering the measurements. Depending on the level of interpolation and the density of the grid of data, this method can be also very time consuming. Here again, the relevance of this method will be discussed later.

6.5. Results

During the four weeks of experiments, one hundred and one runs have been achieved, with various sailing configurations according to the experience matrix presented Part 6.2. This section aims to point out some relevant elements regarding the global objective of the project. A representative overview of the various trajectories achieved by the kite during the the 101 runs, is given in Fig. 6.12. The typical run duration t_r is five minutes. Four plots are visible, corresponding to four different true wind angles, with respect to the boat axis. The two plots at the top show the trajectories of the kite flying in dynamic mode, and steered by the auto pilot. This case is possible only for downwind and reaching conditions (true wind angle not smaller than 100°). For smaller true wind angle, the kite needs to fly very close from the wind window edge, and the autopilot is not able to deal with such a situation, at least not in a systematic way during five minutes. Therefore these types of run are achieved with a manual control. This is the case for the two plots at the bottom of the Fig. 6.12, with the left plot being a dynamic run whereas the right one is a static run.

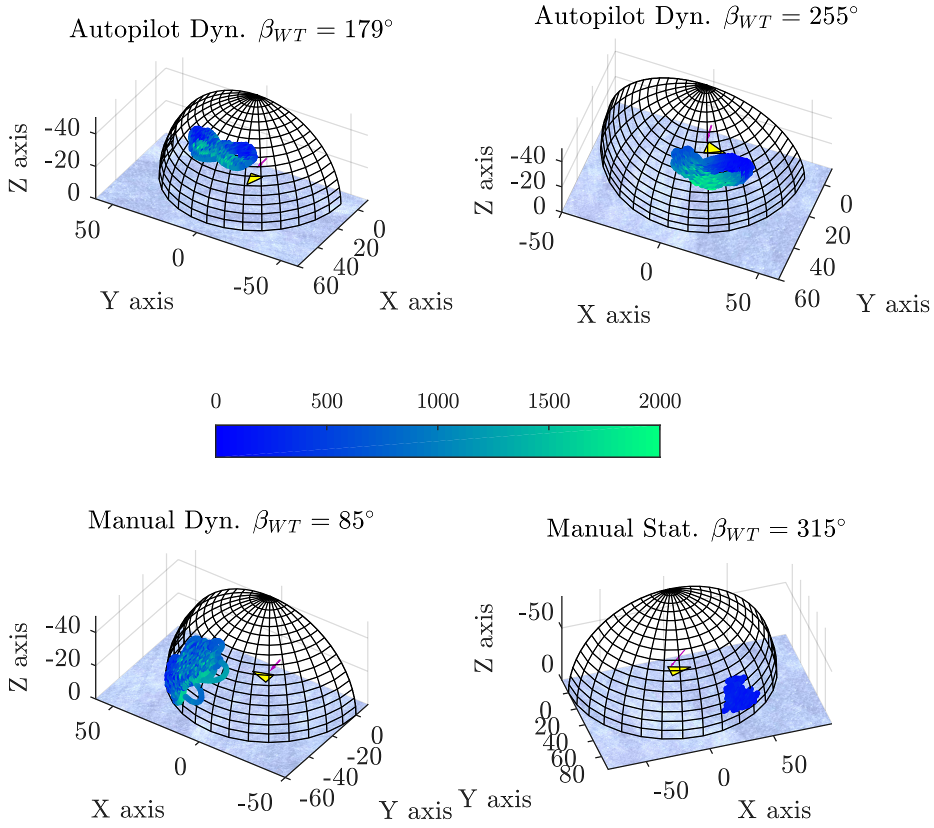

Figure 6.12.: Kite trajectories during four representative runs, with different true wind angles with respect to the boat axis. The yellow triangles denote the kiteboat positions, and the magenta arrows give the orientation of the true wind. Each plot is oriented to have the wind always coming from the top right part of the global figure. The colorbar presents the total kite force. The case name associated with App. C are, from the top to the bottom and from the left to the right: d05f4, f07f18, f10f9, d11f15.

Figure 6.12 also shows that the reproducibility of the trajectories steered by the autopilot is far much better than the trajectories steered by a crew member. The two dynamic cases (top plots) are also plotted in App. C with a full page size.

6.5.1. Benchmark of Redundant Data

With the large number of sensors deployed for this work and presented in the dedicated chapter, some data are redundant. This enables the possibility of benchmarking sensors against each other, and eventually to identify faulty ones.

6.5.1.1. Heading, Course and Speed

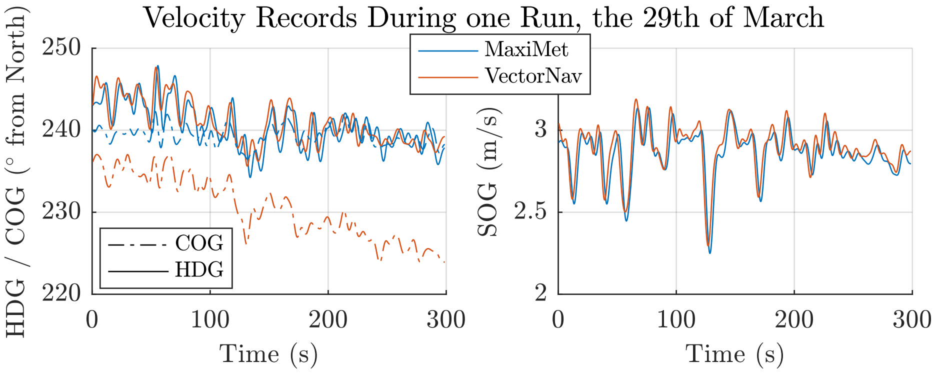

Figure 6.13.: Comparison between data from MaxiMet device (blue lines) and data from VectorNav device (orange line). The left plot shows heading data (HDG - dot-dashed lines) and Course Over Ground data (COG - solid lines), with respect to the North. The right plot presents the Speed Over Ground (SOG) data.

Two devices provide heading and course information: the IMU-GPS VectorNav and the lowest anemometer Gill MaxiMet. Therefore the data have been compared for all runs, and results from a specific run only are presented in Fig. 6.13. In this paragraph, to focus on sensor comparison, usual notations for navigation data are voluntarily used instead of the specific notations associated with the boat. These notations have nevertheless been introduced Part 3.2.2. A good agreement can be seen between GPS-based data, like the Course Over Ground (COG) and the Speed Over Ground (SOG). Minor differences observed can be easily explained regarding the location of the sensors (inside the boat for the VectorNav, on the wind measurement mast for the MaxiMet).

However, this example of data presents a large difference between heading data (HDG): the MaxiMet outputs a value close to the course over ground (COG) measurements whereas the VectorNav heading data are really different, with up to 15 degrees of difference, and increasing over time. If a constant offset can be explained by a mounting misalignment of one of the two devices, a time-variable offset is more problematic. This example is in fact an illustration of the major issue encountered with the VectorNav device and detailed in part 6.1.6.4. Consequently, the heading data that is used in the following part is only the one provided by the MaxiMet.

6.5.1.2. Onboard Anemometers

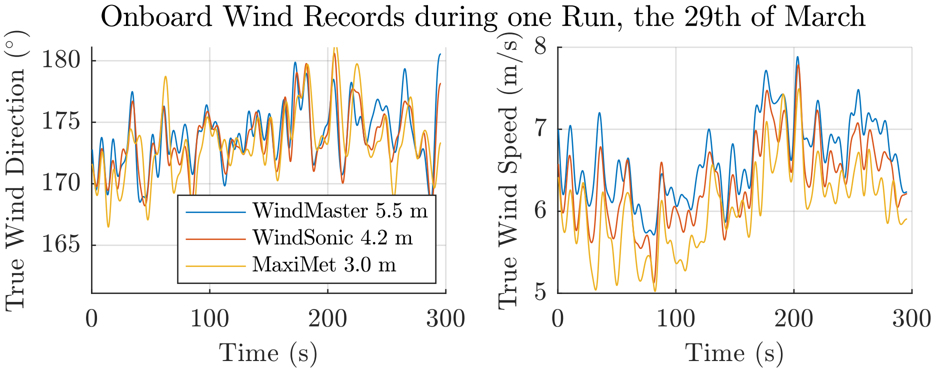

(a)

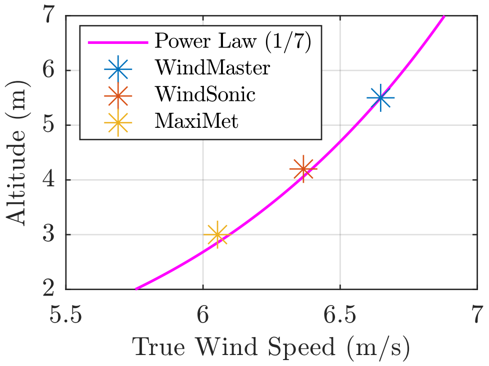

(b)

Figure 6.14.: Comparison between the wind measurements of the three onboard sensors mounted on the measurement mast at various height (a). The average value of the true wind speed during the run is plotted for the three sensors (b), and compared to the power law calculated from the WindMaster measurement at 5.5 m, with a parameter equal to 1/7.

Three anemometers are mounted on a dedicated mast, detailed in part 2.6.3, at three different heights. Data coming from these three devices have also been compared, and an example of this work is given in Fig. 6.14(a) . The correlation of the direction data (left plot) is very good. The plot of the true wind speed (right plot) shows that the uppers sensors measure stronger winds. This is perfectly consistent with boundary layer theory. Indeed, the average values of run for each sensors have been plotted with respect to the altitude of measurement and compared, with the power law profile calculated from the highest measurement, with a parameter of 1/7 already used in the previous chapter. Results are presented in part (b) of the same figure. In regard to these satisfactory agreements, the wind measured by the highest sensor (WindMaster) will be used when only one point of measurement is sufficient. Indeed, this sensor being located at the top of the mast, no wind orientation leads to the case of a sensor located in the wind shadow of the mast. Moreover this sensor has a better output rate, and provides also a measurement along the vertical direction.

6.5.1.3. Weather Model Vs. Fixed Measurements

The weather model introduced in Part 6.3.2 has been benchmarked with data coming from fixed platform set around the sailing area, and presented in Part 2.6.4. For that, a full day of measurement has been considered (29th of March), and the results of the model have been observed at the location of the fixed platform. Results of this comparison are given in Fig. 6.15. Each row corresponds to one of the fixed measurement points, the left column stands for true wind direction (with respect to the North, as defined Part 1.3.2.1), and the right column deals with true wind speed. The outputs of the model are given at an altitude of 20 m, whereas the measurement height is about 5 m, and no compensation has been added. This difference can therefore explain why the model is always estimating a stronger wind. However, the variation of the modeled true wind speed against the measured values are not perfectly in line. The wind orientation comparison does no show a perfect agreement, with a deviation of up to 20°. This deviation cannot be explained by the difference in height between measurement point and model output. Indeed such a deviation, between 5 and 20 m of altitude, relatively constant over time, is not in accordance with the theory of MABL introduced in Chap. 1. Sub-hour wind evolution is neither predicted by the model.

If this model seems to give after all encouraging results, the deviations regarding measurements are too important to consider to use only the model to estimate wind at kite altitude. Therefore, for the following works, the model is only used to define a vertical profile, but the magnitude of the wind is still based on measurements. Moreover, the direction profile in the area covered by the kite (up to 50 m in most cases) shows a variation under 5°, as visible in Fig. 6.10. This variation is far under the gap between the model at an height of 20 m and the measurements at 5.5 m, therefore it does not seem relevant to trust the direction profile neither. Consequently no direction profile is assumed to affect the true wind between 5 and 50 m, and wind direction measured by the onboard sensor will be used.

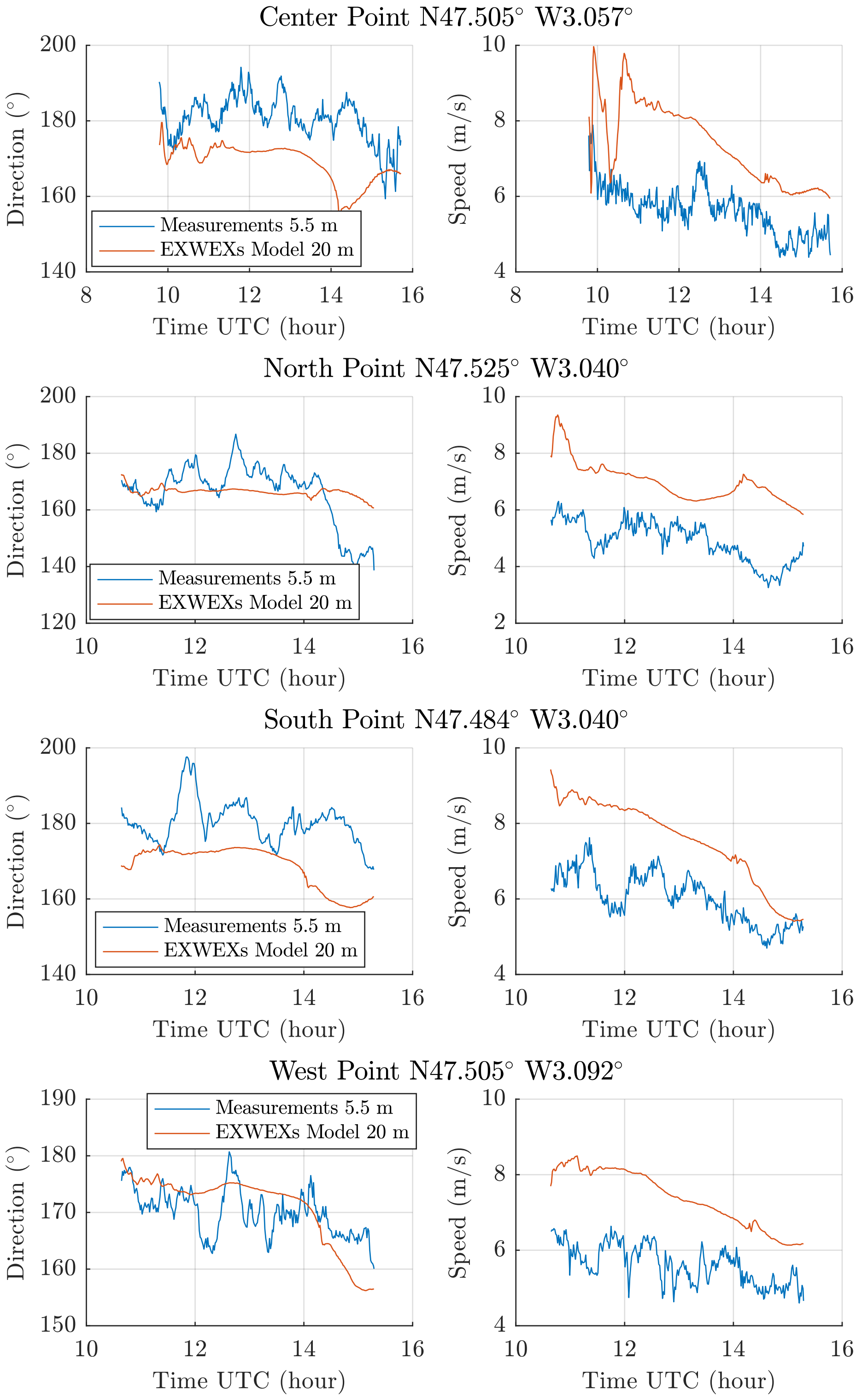

Figure 6.15.: Comparison between the wind measurements at the four fixed-points and the outputs of the model at the same locations, during the 29th of March.

6.5.2. Average Data

For each of the 101 runs, data have been averaged, and a summary table of all relevant data for all runs is given in App. C. This allows to globally analyze the effects of one or several parameters on the kiteboat performances and behavior. To keep notations as simple as possible, the fact that all data are averaged is implied and the notation μ used in previous chapter and denoting average time-series is not used in this part.

6.5.2.1. Roll and Pitch Offset Compensation

Average roll and pitch angles of the kiteboat for all runs are plotted in Fig. 6.16. These two values depend on forces applied on the kiteboat: hydrodynamic loads on the hull and appendages, kite force, and distribution of moving masses. With a kite providing the totality of the propulsive force, the hydrodynamic loads on the hull and appendages and the kite force are strongly coupled. However, the perturbation induced by a moving mass has been considered during trials, and to face it, it was decided to fix the positions of boxes and crew members, in order to keep the global center of gravity at the same position all the time. However with a crew made up to three people, it is not possible to symmetrically distribute the masses. Therefore the helmsman is permanently seat on the starboard bench, and this is visible on the average value of the roll, with an offset of +1.47°. For the following analyses, this value will be subtracted from the data to center the cloud of points on 0, and then get plots more reader friendly. The average offset on pitch values has also been subtracted from the data for the same reason.

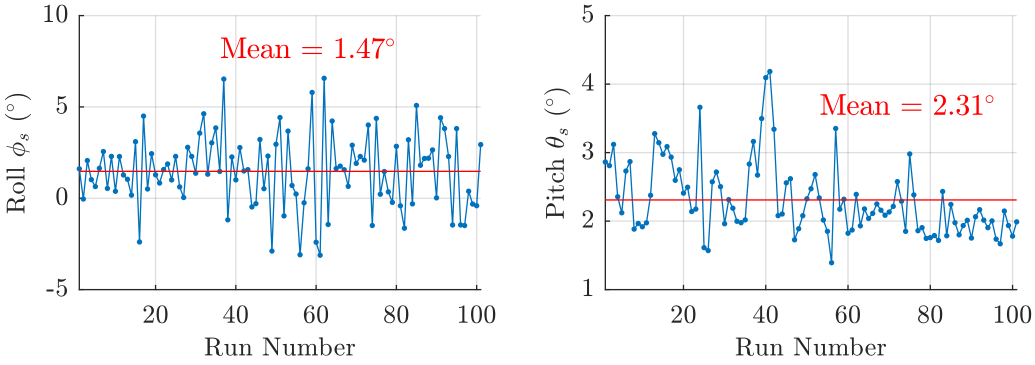

(a) (b)

Figure 6.16.: Evolution of the roll and pitch angles for all the run achieved only with the kite.

6.5.2.2. Polar Plots of the Kiteboat

The aim of this section is to draw a polar plot of the kiteboat, associating the true wind angle of the runs with the speed of the boat. To get a relevant example, cases are selected in the experience matrix, to ensure as many fixed-parameter as possible. This requires to set the kite, the length of the tethers, the daggerboard, the location of the attachment point and the propulsion. The choice of the retained cases among the given parameters is achieved by maximizing the number of runs. This leads to 54 cases, fitting these criteria:

- Kite Cabrinha 12 m²
- 50 m tethers
- Black daggerboard
- Kite attachment point at 2.48 m
- No Motor

All selected runs are shown in Fig. 6.17, with the average true wind speed of the run given thanks to the colorbar. To have a more readable plot, true wind angles for all runs are concentrated between 0 and 180°, however the portside runs (with negative TWA) are denoted with another symbol than the starboard runs. No symmetry issue between port side and starboard runs can be noticed.

Other choices can be made about the set of parameters. Thus in Fig. 6.18(a), the true wind speed has been limited to remain in the range from 4.5 to 6 m/s, and the impact of the daggerboard choice is regarded by plotting the runs done with the two types of daggerboard. Other parameters remain identical to the previous plot. It is immediately visible that the black daggerboards allow runs closer to the wind than the standard daggerboards. However, the black daggerboards generate larger drag due to their bigger size, and this added drag seems to have an non-negligible impact on boat speed during downwind runs, when no large size force needs to be withstood.

6.5.2.3. Running Resistance Curve of the Kiteboat

The running resistance curve of the kiteboat is plotted in part (b) of Fig. 6.18, based on all the runs achieved without additional power from the motor. Thus the value of the propulsive force generated by the kite (in other word the projection of the kite force F_k on the x-axis of the heading reference frame) is analyzed with respect to the boat speed. Moreover the kite in use during each run is also specified using a color code, in accordance with real color of the kites, visible in Fig. 6.8 (a) to (c). The curve obtained is really clean for outside measurements, considering the number of uncontrolled parameters, as the

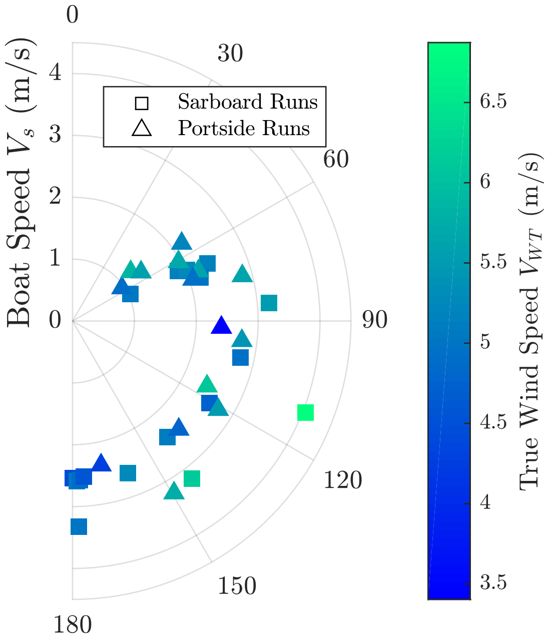

Figure 6.17.: Polar of the kiteboat in the most used configuration (Kite Cabrinha 12 m², Tether length 50 m, Black daggerboard, Kite attachment point at 2.48 m, No motor). Port side and starboard runs have been set together, but marker type (square or triangle) allows the identification.

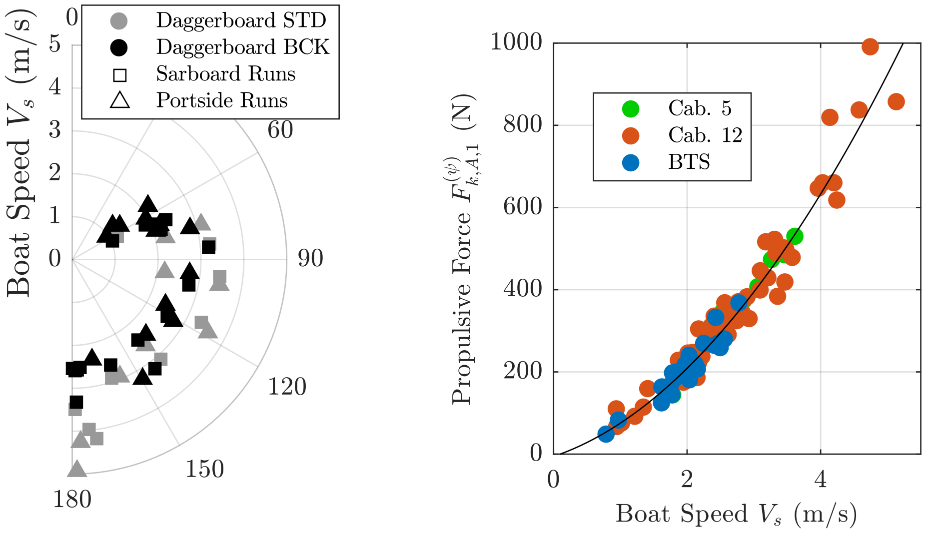

(a) (b)

Figure 6.18.: (a) Impact of the daggerboard choice on speed performances of the kiteboat regarding the true wind angle. (b) Overview of the running resistance curve of the the kiteboat built from all runs completed during the trials, with respect to the kite used during each run. The black line denotes the best quadratic fitting applied on the entire cloud of points.

wind speed, the state of the sea or the surface current. A quadratic fitting has been applied to the entire set of points, leading to the following equation:

$$F_{k,A,1}^{(\psi)} = 26.2\,V_s^2 + 54.8\,V_s - 5.7 \tag{6.23}$$

6.5.2.4. Effects of Daggerboards on Boat Motions

The impact of the daggerboard choice on boat attitudes has also been investigated. Thus, the average roll and pitch angles are plotted according to the true wind angle, the daggerboard type, and the true wind speed. No constraint has been added to reduce the number of runs, except that the motor shall not be used. Results are given in Fig. 6.19. Whatever the daggerboard choice, the absolute value of the roll angle increases when the run are closer to the wind. This can be easily explained regarding the side force generated by the kite: the side forces are much stronger in reaching conditions, and because the attachment point is located in the center plane and above the center of buoyancy of the kiteboat, these forces induce a heeling moment. The sign of the roll angle is relevant with this explanation: true wind angles between 0 and 180° are associated with starboard tacks, and induced side forces are consequently negative. The heeling moment is also negative and so the roll angle. During port tacks (TWA from 180° to 360°), side force are positive

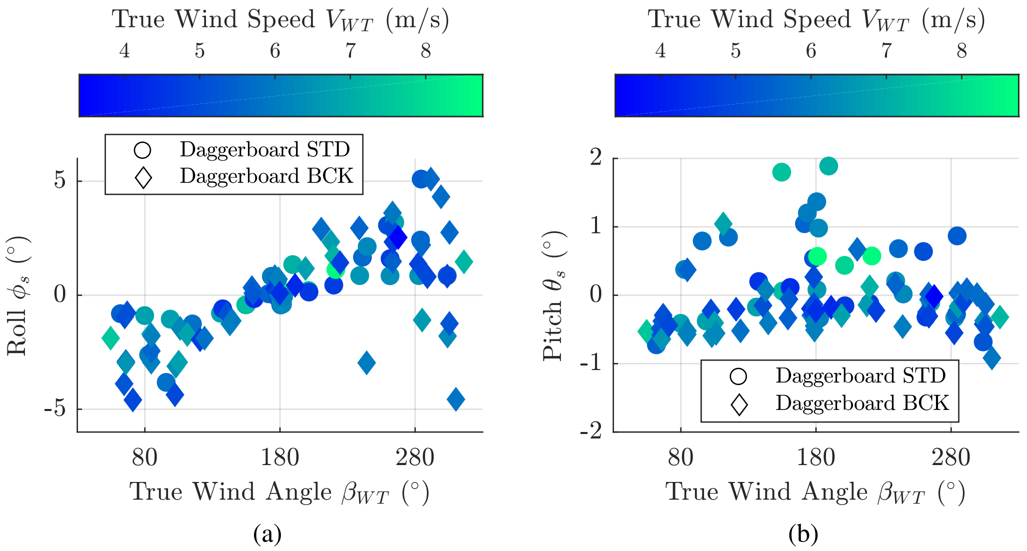

Figure 6.19.: Effects of the daggerboard choice on roll (a) and pitch (b) angles of the kiteboat, according to the true wind angle.

leading to positive roll angles. The 4 negative values associated with port tack, related to the black daggerboard, deal with runs with a kite manually steered. In this case, the crew members position may have been changed to ensure a good position of the member in charge of the kite steering. The black daggerboards, the bigger ones of the two sets, seem also lead to bigger value of the roll angle. This makes sense because, with the larger span of the black daggerboard, the center of effort of the hydrodynamic force force generated by the daggerboards is located lower than in the case of standard daggerboards, and the associated heeling moment is therefore larger.

The pitch angle is also affected by the daggerboard choice as shown in Fig. 6.19(b). Indeed amplitudes of pitch angles are limited with the black daggerboard, and this can also be explained regarding the lower position of the points of application of the hydrodynamic force on daggerboard. Plot (b) seems also to show a slight decrease of pitch when runs come closer to the wind, but this trend is more complicated to explain, and further work needs to be carried out.

6.5.2.5. Back Tether Ratio

The ratio between the force in back tethers and the total kite force has been computed, as it has been done in the previous chapter, using the following formula:

$$r_b = \frac{F_{bl} + F_{br}}{F_{k,A}} \tag{6.24}$$

Results are given in Fig. 6.20(a), with respect to the true angle of the run, and for the three kites. As expected, the ratio for the two Cabrinha kites are close to the ones obtained onshore, with an average value during all the runs achieved with these kites equal to 23% of the total force. However this ratio for the third kite is really different, with an average value for the all the runs completed with this kite equal to 40 %. The evolution of this ratio along an eight-pattern trajectory is given in the section dealing with the phase averaging processing, and presented in part 6.5.3. This difference can be explained by regarding the bridle system of the BTS kite. Indeed, on Cabrinha kites, back tethers are fixed directly at the end of the inflatable leading edge, at only one point. For the BTS kite, a bridle system exists also for back tethers, with a line linking back and front bridle system.

6.5.2.6. Power Ratio

During the last two days of measurements, the main battery voltage has been recorded as well as the intensity of each channel of the power card. Therefore the electrical power P_e consumed by actuators can be analyzed. However the data rate was low (1 Hz), consequently a fine analysis of the consumption along a trajectory can not be performed and only average values will be considered. Nevertheless, this quantity is really interesting to analyze, particularly in comparison with the propulsive power generated by the kite P_{prop}. This one is the product of the propulsive force of the kite by the speed of the boat, or in other words:

$$P_{prop} = V_s \underline{F}_{k,A} \cdot \underline{x}_{\psi}$$

The ratio of these two values is calculated, denoted r_p and named Power Ratio:

$$r_p = \frac{P_{prop}}{P_e}$$

If this ratio is lower than 1, it means that the control of the kite requires a level of power higher than the towing power provided by the kite . This ratio has been computed for the runs achieved during the two last days, when electrical data were recorded. Results are given in Fig. 6.20(b), according to the true wind angle. The efficiency limit $r_p = 1$ is plotted in red. During this two days, runs have mostly been achieved with the BTS kite, and only 4 points are existing with the Cabrinha 12 m². For runs with low true wind angles, the power ratio is close from 1 and even below for some runs. This is not really surprising, because for these points of sail, most of the kite force is along the y axis of the boat, and consequently the propulsive force is low, and so the power ratio. For greater true wind angles, the ratios increase, but remain relatively low for the BTS kite. In contrary, the power ratios of the Cabrinha 12m² seem to be much better, but more data are required with the Cabrinha kite to do a fair comparison. Nevertheless, this is consistent with the observation of larger back tether ratios with the BTS kite: a bigger part of the force goes through the actuator, and consequently more power is necessary to steer the kite.

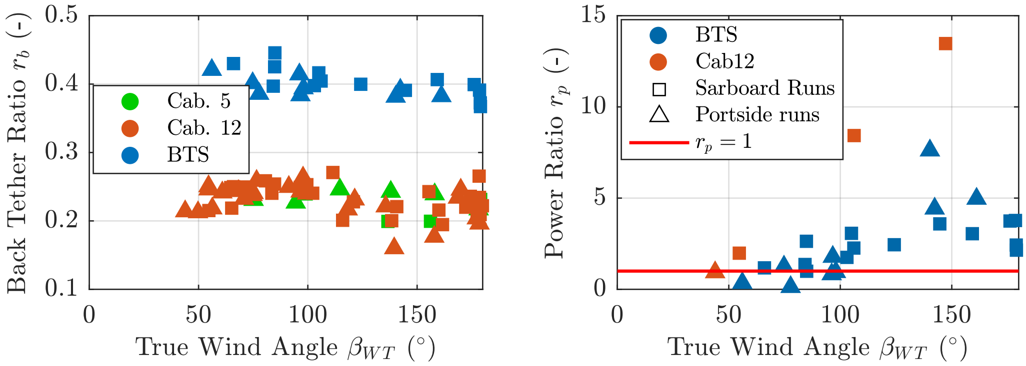

(a)

(b)

Figure 6.20.: Power ratio according to the true wind angle, for two different kites.

However, it is necessary to mention than the two runs with the Cabrinha kite having the best power ratio have been done out of the strict framework of the trials. Indeed, these runs have been conducted outside of the sailing area, during the way back to the harbor. The crew was not seated at its reference position, and the aim of the leg was to break the speed record of the boat. Thus, the heading was chosen to allow a true wind angle between 100° and 140°, and the kite was manually steered by a crew member in a dynamic mode, performing vertical eight-patterns quite close from the wind window edge. The helmsman could change the heading to take full advantage of waves.The true wind speed was 6.2 m/s, and the best recorded speed reaches 6.58 m/s, which is the best speed of the boat reached so far.

Further works have to be carried out to measure more accurately the power ratio,and with respect to the bridle system. Indeed bridles may appear to affect the power ratio, and a power ratio too low might impact considerably the possible fuel saving associated with kites. However, the present steering system was not designed with an energy efficiency approach, then much better results can be expected.

6.5.3. Phase Averaging Method

The phase averaging method presented in Part 5.3.4 of the previous chapter has been adapted to take into account the additional data induced by the boat. All the 101 runs are not suitable for the phase averaging method. Indeed, a minimum reproducibility of the trajectories is required, and some sailing configurations do not allow such trajectories, as the manual steering. Thus, several runs have been tested with the phase averaging method, and finally 10 runs have been selected. The phase averaging method is particularly suitable to analyze variations in line with the kite periodic loads. Then, the amplitudes of these variations can be estimated, which will not be possible with standard data sets, due to extreme events invariably occurring during five-minute records. In addition to the back

Case	Kite	β_{WT}	r_{prop}	r_a	r_b	r_s	$\triangle\delta_R$	$\triangle\psi$	$\triangle\phi_s$	$\triangle\theta_s$	$\triangle\delta$
d01f7	Cab. 5	137	0,76	1,28	0,20	0,13	12,1	2,4	4,7	1,3	0,75
d02f5	Cab. 12	182	0,47	0,90	0,19	0,11	8,2	3,1	1,5	0,8	0,87
d02f6	Cab. 12	182	0,67	0,96	0,20	0,10	2,9	4,2	2,0	1,0	0,85
d04f1	Cab. 12	183	0,62	0,95	0,22	0,09	4,1	3,9	1,6	0,6	0,66
d05f4	Cab. 12	179	0,69	1,12	0,20	0,11	4,2	2,8	1,9	0,5	0,92
d07f12	Cab. 12	121	0,60	2,00	0,21	0,34	7,8	4,7	3,8	1,4	0,91
d07f18	Cab. 12	263	0,31	1,80	0,23	0,31	12,0	18,6	10,7	0,8	0,97
d08f1	Cab. 12	180	0,80	1,34	0,22	0,16	4,7	1,4	1,5	0,7	1,07
d10f8	BTS	220	0,72	1,18	0,38	0,15	7,2	4,0	3,3	1,1	0,70
d11f4	BTS	106	0,49	1,22	0,40	0,14	12,9	6,2	4,0	1,9	0,73

Table 6.3.: Relevant quantities taken out from the ten runs suitable with the phase averaging method. Angles are given in degree, and the steering amplitude is given in meter. The blue rows denote the cases which are plotted in Fig. 6.21 to 6.24. The 3D plots of these cases are given in App. C.

tether ratio r_b and the amplitude ratio r_a already defined and used in the previous chapter, two others ratio are introduced: the propulsive ratio r_{prop} and the amplitude speed ratio r_s. The first one denotes the part of the kite load useful for propulsion, and is the projection of the kite force on the x_ψ-axis:

$$r_{prop} = \frac{\underline{F}_{k,A} \cdot \underline{x}_{\psi}}{F_{k,A}} \tag{6.25}$$

The amplitude speed ratio denotes the maximum speed variation during the kite eight pattern in comparison with the average speed:

$$r_s = \frac{\max(\overrightarrow{V_s}) - \min(\overrightarrow{V_s})}{\mu_{\overrightarrow{V_s}}} = \frac{\triangle\overrightarrow{V_s}}{\mu_{\overrightarrow{V_s}}} = \tag{6.26}$$

Moreover, other quantities are introduced denoting the variation of some parameters, as the amplitude of the rudder angle $\triangle\delta_r$, the amplitude of the heading angle $\triangle\psi$, the amplitude of the roll angle $\triangle\phi_s$, the amplitude of the pitch angle $\triangle\theta_s$ and the amplitude of the steering command $\triangle\delta$ (given in meter). All these quantities are given for each of the 10 runs in Tab. 6.3, with the first three columns denoting the short name of the case, the kite used and the true wind angle β_{WT}.

Among them, four cases have been selected for their relevancy to the present study. Some pieces of data are plotted for each of the four runs in Fig. 6.21 to 6.24, and the 3D plots are given in App. C. The first case deals with one of the only runs achieved with the small Cabrinha kite during the trials. The two next cases concern the Cabrinha 12 m² , with one run achieved in downwind condition, and the other in reaching condition. Finally the last case shows a run with the BTS kite, in reaching conditions.

For each case, the plot (a) deals with the position of the kite with respect to the heading reference frame. Thus, the kite elevation and the kite azimuth angles, as defined in Fig. 7, are given according to the time vector of the average eight pattern. Elevation angles (blue line) are at all times positive, and near zero values denote a kite flying very close from the surface of the sea. When the eight-pattern trajectory is symmetrical and horizontal, the elevation angle curve looks like a sine function. Depending on the true wind angle of the run, the azimuth angle (green dot-dashed line) can be mainly under zero (case of a starboard run, with TWA below 180°), or mainly over 0 (case of a portside run, with TWA bigger than 180°). The variation of the propulsive force $F_{k,A,1}$ and the side force $F_{k,A,2}$ along the trajectory is given in plot (b), respectively in blue and red lines. The back tether ratio is given on the right axis, denoted by an orange dashed line. The lift to drag ratio and the lift coefficient computed from Eq. 6.20 and 6.21 are shown in plot (c), respectively on the left axis (blue line) and on the right axis (orange dot-dashed line). The plot (d) deals with the kiteboat data. The boat speed is plotted on the right axis, and denoted by a pink line. Four specific angles are plotted on the left axis: the roll angle ϕ_s with a solid black line, the pitch angle θ_s with a black dashed line, the rudder angle δ_R with a black dot-dashed line and the centered yaw angle with a black dotted line.

The variations of the lift to drag ratio and the lift coefficient along the trajectories are still not easy to generalize,with no repeatable scheme: some cases show maximum value of the lift coefficient before a turn, or after, and sometimes it seems to depend on the direction of the turn.

The speed of the boat seems to correlate with the propulsive force with a little phase shift, and this makes sense. However, the last case (Fig. 6.24) does not follow the same scheme, with a best speed observed not when the propulsive reach is maximum, but just after a second local maximum. Moreover, this moment corresponds to the maximum side force. Therefore, the location of the best speed is hard to explain. However, an interesting analysis can be achieved on this case, regarding the rudder angle, the heading angle and the kite force: between 2 and 4 s, the rudder angle becomes positive, going from about -2° to +5°. This leads to a raise of the yaw angle over 6°, corresponding to a decrease of the true wind angle (this is true only for starboard tacks). Therefore the boat motion is done against the kite and this seems to induce an increase of the tension in the tethers.

The variations of the roll angle are clearly in line with the side force intensity. Moreover, the more strong the side force is, the larger the amplitude of the roll angle is, and such large side forces occur in reaching sailing condition. Thus, during case 3 (Fig. 6.24), with a true wind angle of -97° (or 263°), the side force is almost permanently bigger than the propulsive force, and reaches more than 1500 N. This leads to an amplitude of roll motion over 10°. This trend makes sense with all the phase averaging data presented in Tab. 6.3, and with the average values of the roll for all runs given in Fig. 6.16(a). Concerning the pitch angles, no clear trend can be identified.

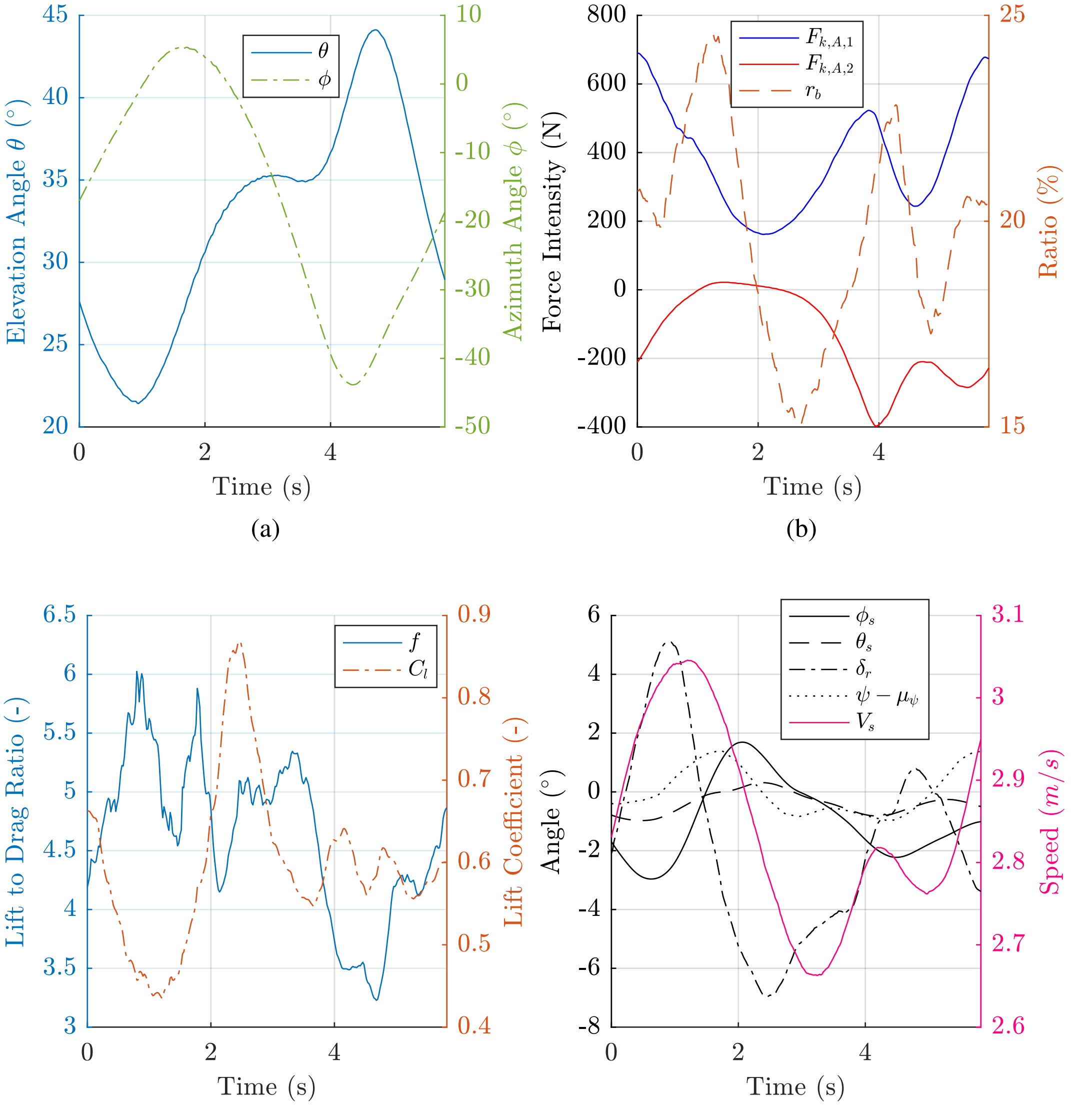

(a) (b)

(c) (d)

Figure 6.21.: Results of the phase averaging process applied to a starboard run with the kite Cabrinha 5 m², at an average true wind angle equals to 137°, and an average true wind speed equals to 6.8 m/s (Index of the case: d01f7).

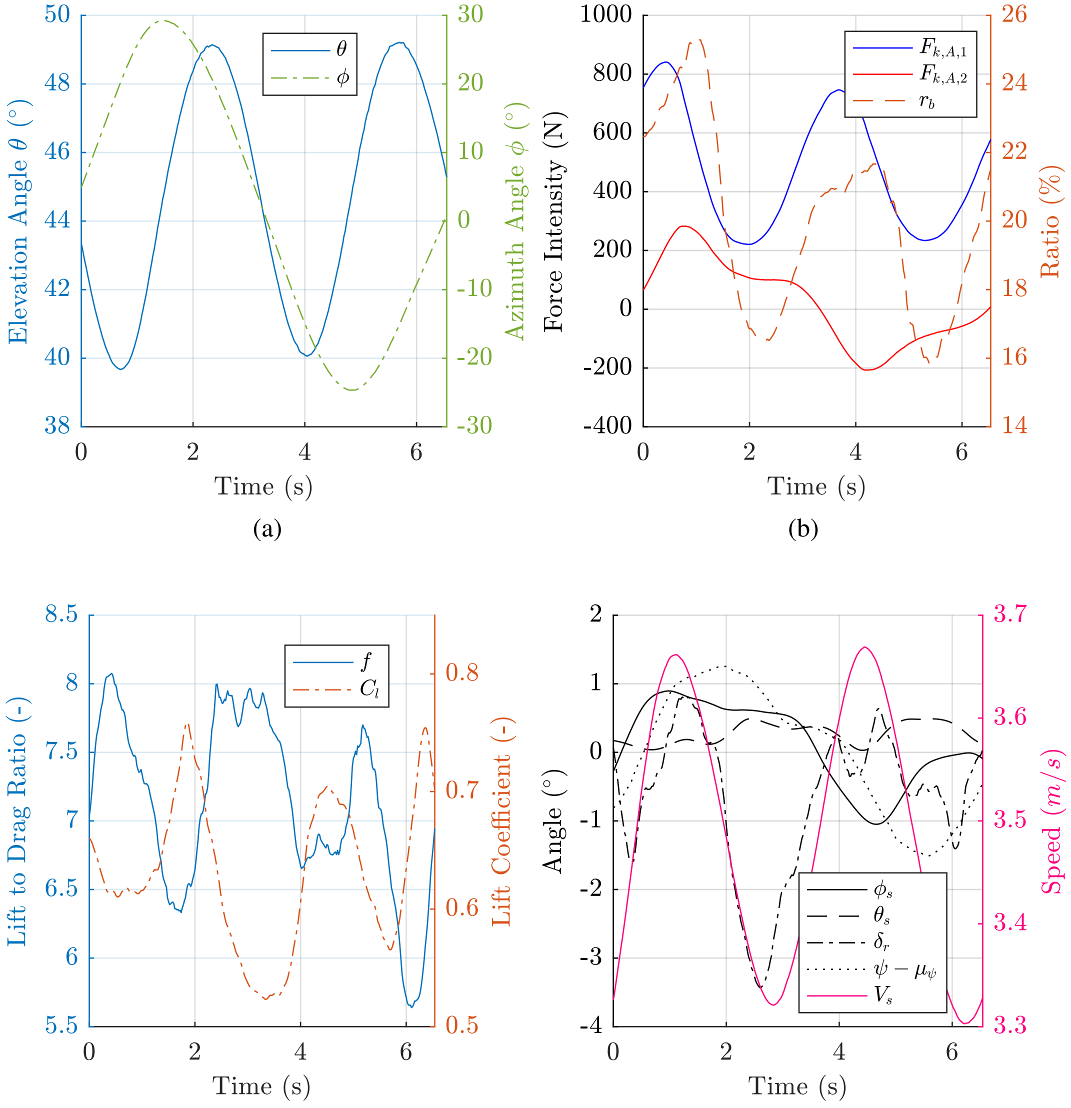

(a) (b)

(c) (d)

Figure 6.22.: Results of the phase averaging process applied to a downwind run with the kite Cabrinha 12 m², at an average true wind angle equals to 179°, and an average true wind speed equals to 5.2 m/s (Index of the case: d05f4).

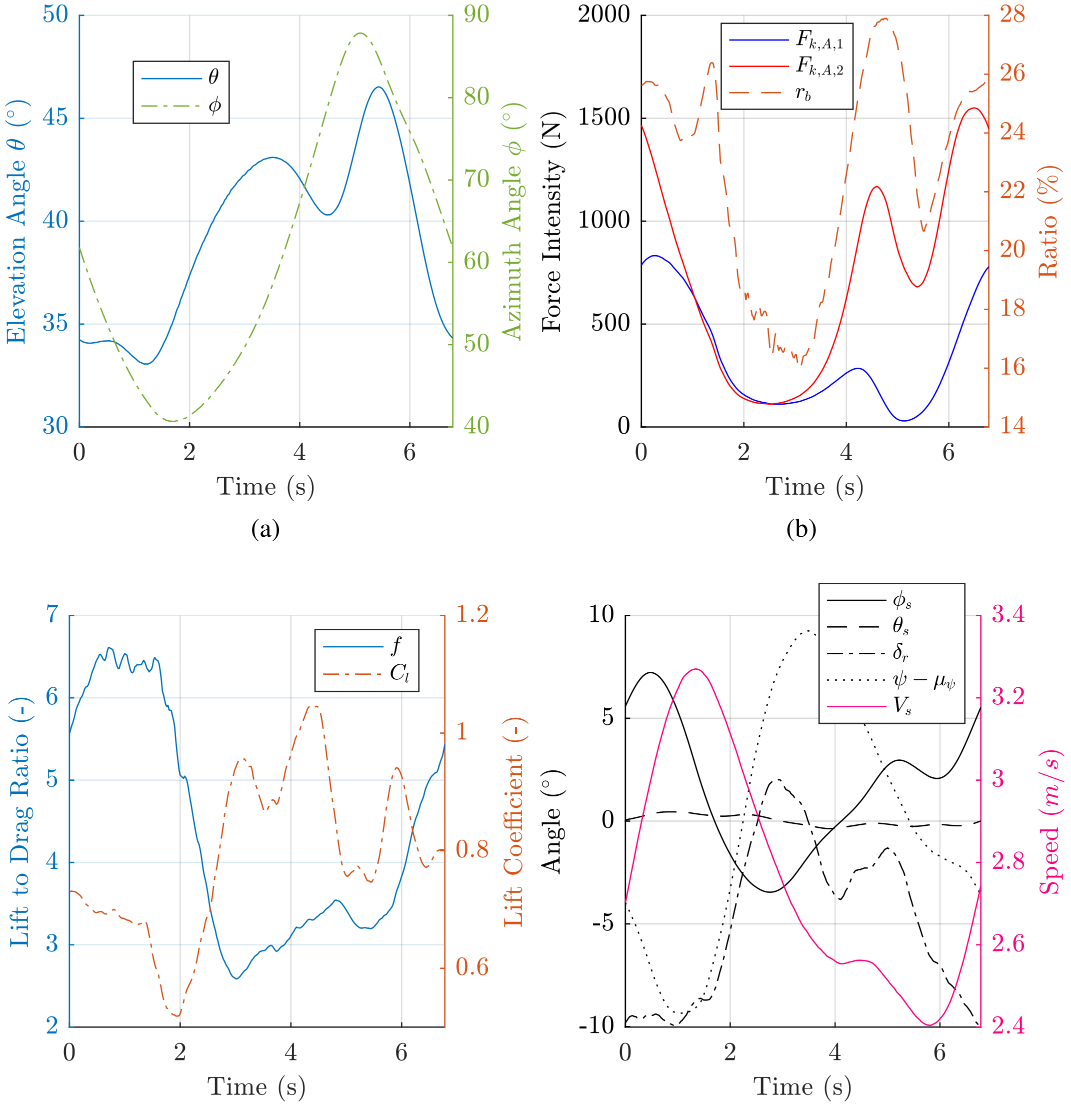

(a) (b)

(c) (d)

Figure 6.23.: Results of the phase averaging process applied to a portside run with the kite Cabrinha 12 m², at an average true wind angle equals to 263°, and an average true wind speed equals to 5.5 m/s (Index of the case: d07f18).

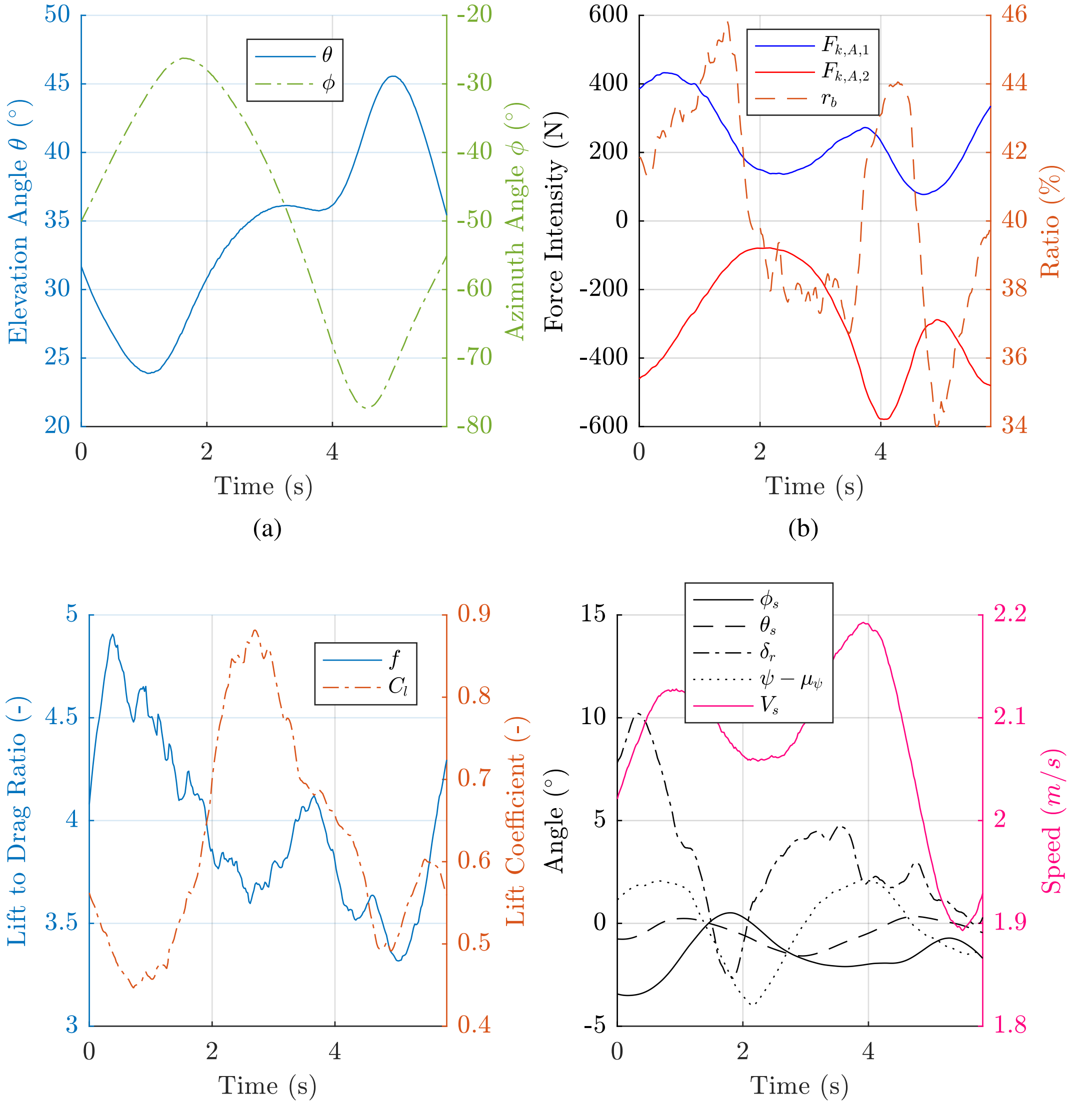

(a) (b)

(c) (d)

Figure 6.24.: Results of the phase averaging process applied to a starboard run with the kite BTS 5 m², at an average true wind angle equals to 106°, and an average true wind speed equals to 6.3 m/s (Index of the case: d11f4).

6.6. Discussion

The objective of this experimental study carried on a boat is to acquire relevant data to analyze the behavior of a boat towed by a kite, and more generally for benchmarking numerical models suitable for achieving this type of analyses. In this context a large amount of data has been obtained, and the first analyses show sensible data, regarding the expected behavior of a ship towed by a kite. However the entire set of data acquired during this work is not fully processed, and a future work could be focused on a finest analysis of the cross-influence of each parameter. The estimation of the wind at a given point of the sailing area could also be improved, by using more data coming from the various tools deployed during the trials. Otherwise, in addition to maneuverability tests that have been achieved but not considered in this study, other tests will be probably necessary to fully validate a modeling of the kiteboat.

Variations of kite specs according to the position of the kite along an eight trajectory are still not easy to identify. Indeed, no repeatable trend has been highlighted, but these variations seem all the time linked to the position along the trajectory. An improvement of the weather model, by integrating wind data measurements carried out over the sailing area could enhance the estimation of the true wind speed at kite altitude, but this will probably not resolve the whole problem. Such analyses are far more complex to achieve on a moving platform, and it seems more relevant to carry out this type of study with an onshore fieldwork. Indeed the analysis of the data has shown that the boat motions seems to impact the tether tension. However, there is for the moment no clue allowing to conclude if this increase of the tether tension impacts also the kite position, or if this variation is absorbed by a deformation of the tethers. However, this work on the lift to drag ratios and the lift coefficients allows nevertheless to corroborate the amplitudes of the variations that have been pointed out in Chap. 5.

General Conclusion and Perspectives

Conclusion

The aim of this study was to carry out an experimental study of kites, and particularly kites dedicated to wind-assisted ships. Three main experimental campaigns were achieved. Two of its were dedicated to sea trials involving two very different boats: a fishing vessel and a specific boat specially designed. The other experimental work was carried out onshore. All these works were focused on leading edge inflatable kites, which are the scope of the beyond the sea project.

An important element in such a study is naturally the experimental set-up, and the later had to be developed specially to be suitable to full scale outside measurements. This set-up was improved all along this study, taking into account feedback of the various trials. One of the main part of this set-up was the kite control system, made of actuators. An automatic pilot was implemented, largely inspired by works published in the literature, and this pilot was able to perform eight-pattern trajectories in a very repeatable way. In addition to kite control, the experimental set up was naturally in charge of acquiring various data, coming from numerous sensors. The most important ones were the load cells for measuring kite forces, and the sensors dedicated to wind measurements. Some other data were also recorded depending on the experimental campaign. With the large amount of data generated by the system, specific tools were developed to automate the data processing and post processing as much as possible.

The design of experiments to perform the whole experimental study was not precisely defined at the beginning, and it evolved over the time depending on results obtained at each step. The first experimental work carried out on a fishing vessel in fall 2015 was the result of the partnership between the beyond the sea company and a fisherman motivated to try kites on his 13-meter boat. Therefore a kite control system was already onboard, and also a kite launching mast, the whole system being suitable for a kite up to 50 m². Moreover, the engine room of the boat was also equipped with valuable sensors, and this campaign was therefore a great opportunity to assess the impact of a kite on the propulsive chain of a fishing vessel. At the time, fuel saving measurements were expected, which could have been used for benchmarking a numerical tool previously developed in the scope of the global beyond the sea project, to predict fuel savings associated with kites. However, the campaign finally did not allow to perform in an extensive manner such measurements, due to an unexpected unavailability of the boat, delayed in the fishing season. Instead of a set of ten days of measurements initially expected on a two-week period, only one was actually possible. Thus only a few runs with the 50 m² kite flying in static mode were achieved, and this by low wind conditions. Finally, the little data which were recorded were post processed, and an estimation of kite specs was achieved. By the way it was also possible to have an ever first assessment regarding power savings provided by the 50m² kite on that fishing vessel. Results of this work showed kite specs making sense with other experimental works carried out by other teams focused on kite uses, and a promising power saving regarding the poor wind conditions encountered. This campaign also showed the importance of wind measurement quality to assess kite specs such as the lift to drag ratio and the lift coefficient, and particularly the importance of the estimation of the wind measurement at kite altitude. Nevertheless, the work carried out on the fishing vessel was a very valuable learning experience, and this experience steered next experimental campaigns, drawing two major guidelines. The first one was to design experiments involving systems fully available and dedicated for scientific actions. The second one was to reinforce the part of the experimental devices dedicated to the wind measurement in order to obtain a better estimation of the wind at kite altitude.

The second experimental campaign took place during the beginning of the summer 2016 and was dedicated to the estimation of the variation of kite aerodynamic performances along an eight-pattern trajectory. This experimental work was consequently carried out onshore, as no boat is needed for this type of measurement. Additionally, a boat would lead to more complex results with coupled effects between boat and kite, and then add unwanted complexity for thedata analysis. For the estimation of aerodynamic specs of the kite, as the lift to drag ratio and the lift coefficient, the wind at the kite position needs to be known. However such a measurement cannot be performed, and only estimation can be achieved. Moreover, the wind is generally increasing with the altitude, and it makes this estimation difficult. To improve this, a wind profiler was used, based on sonic technology. With this device the profile of the wind was obtained, but poorly-time resolved, with only a very low frequency of one point per period of five minutes. Consequently, the estimation of the wind at kite position could not account for rapid evolution of the wind, and this was detrimental for instantaneous data post processing and then for the estimation of aerodynamic performances. Therefore, a conditional phase averaging method was established in order to obtain an average evolution of data along an average eight-pattern trajectory. This process was applied to kite flight records containing about hundred consecutive eight-patterns with a good reproducibility thanks to the autopilot, and a conditional analysis ensured the good correlation of all trajectories. After this average process, data were post processed to retrieve the lift to drag ratio and the lift coefficient, using two different kite models. The first one is the zero-mass model and the second is the point-mass model. By considering a kite mass, accelerations of the kite lead to inertial forces, and these forces were then taken into account. The two models were compared, and even if the inertial forces were low in comparison with the total kite force, they affected the post processing and particularly the lift to drag calculation. Therefore this model was preferred. The evolution of theses aerodynamic parameters was analyzed with respect to the rotation rate of the kite velocity vector around the tether axis. Some cases showed evolution making sense, with a decrease of performances during turns, however a standard scheme of evolution could no be pointed out when considering all cases. An uncertainty analysis was also performed, but the number of processing steps between measurement and final values of the lift to drag ratio and the lift coefficient are plentiful, and consequently the final uncertainty is large. However this analysis showed clearly that kite position measurement and kite velocity measurement are the dominating sources of uncertainty. Moreover, a symmetry issue was observed, and this participated to make the analysis of the results complicated. Finally, linear evolution laws of the aerodynamic parameters were proposed, based on three relevant cases, by applying a specific process to get rid of the symmetry issue.

The last experimental campaign was again focused on sea trials, but with a different objective than the first one. To have an experimental platform fully available for trials and measurements, a dedicated boat was designed and built. This boat is six-meter long and two-meter wide, and was operated by three crew members. After a period of sensors installation, a first period of trials was carried out to test and validate the whole experimental set-up and also to assess the performances of the boat towed by kite. The collected data were used to draw a design of experiments associated with the kiteboat, in accordance to kiteboat performances and possibilities. The real measurement campaign was carried out in April 2017 in the bay of Quiberon, South Brittany, in a sailing area well known and defined, surrounded by mooring platforms fitted with wind measurement sensors. Moreover, a partnership was contracted with a specialized company to get a fine modeling of the 3D wind field over the sailing area. Ten full days of measurements were achieved, leading to numerous recorded runs, one run being a five-minute record, keeping all parameters as fixed as possible. Various configurations of sailing were tried, using different kites, different lengths of tethers, different daggerboards, different points of sail and so various true wind angles. All these data were at first analyzed using only average values for each run. This led to an overview of the kiteboat performance, and this allowed also to study the impact of some elements of the boat, as for example the daggerboards, or to study the impact of true wind angles on boat motions. The electrical power required to control the kite was also checked with respect to the propulsive power provided by the kite. Results showed that in some configurations the power provided by the kite was not really greater than the power used for control purpose. The conditional phase averaging method, developed for the post processing of the previous experimental campaign, was adapted to the data coming from the kiteboat, and ten cases were found as being suitable for such a method, with a sufficient reproducibility of the eight pattern trajectories. The analysis of the results of the phase averaging method allowed to observe the influence of the kite on the boat, and specifically the influence of the kite flying in dynamic mode, and consequently generating a periodic load on the boat. However, the entire set of data acquired in the scope of this campaign could not have been fully post processed, and a lot of work is still achievable. Nevertheless, this first analysis of the results made on the data showed nevertheless that the data acquired are sensible, and they constitute a good database for the benchmarking of numerical models.

Perspectives

The last two experimental campaigns led to the acquisition of a large amount of data, and all data have not been fully analyzed or used yet. The first step of a future work would be to pursue further these analysis and post processing works, by adding benchmarks of numerical models. For example a non linear lifting line method could be implemented for instance to deal with the evolution of the aerodynamic parameters of the kite along a trajectory, and the results of the model could be compared with experimental data. Such a model could be also useful to refine the protocol of future onshore measurements.

Indeed, the current study pointed out symmetry issues in the set-up, and the value of the trim was not enough considered. Therefore new onshore measurements could be carried out, focusing on this point, and by post processing data immediately thanks to the methods presented here. Thus, potential problems like tether length variations could be corrected in real time, or at least from one day to another. Other load cells could be also added, particularly to measure the tension in each front tethers.

Video tools could also be used at a wider scale. At first, cameras could be embedded on the kite more often. The aim will be for example the observation of phenomena occurring during turns, as the potential flow separation of some sections of the kite, using yarn telltales as it is done for planes or sails. In the same time, the buckling issue could be also recorded. However, to complete such experiments, a particular attention should be given to the time synchronization between video means and the kite control and measurement set up.

The use of several cameras located on ground should be investigated, for photogrammetry analyses. Indeed with cameras fitted with suitable lens, and set to the same field-of-view, the 3D flying shape of the kite could be obtained at the moment the kite flies through the field-of-view, if all devices are well time synchronized. If this type of measurement gives good results, cameras could be mounted on motorized gimbal systems, and then track the kite position using data provided by the kite control system.

Concerning the kiteboat, the next step is to model the boat and then to compare simulation data with experiments. Depending on comparison results, a new measurement campaign could be planned, focusing on some specific points, identified as relevant. The kite control system could also be improved, particularly the automatic pilot. Indeed eight pattern trajectories were defined manually, in the range of the capabilities of the autopilot. Consequently, the autopilot should be modified to increase the range of possible trajectories, and in the meantime, the trajectory definition could be made automatic, based on the result of an optimization process aiming to maximize the propulsive force.

Appendix

A. Sensors Data Sheets

This appendix includes the relevant specification sheets of sensors used for the current study, summarized in the following table:

Nbr.	Sensors	Manufacturer
1	3D Load Cell	Michigan Scientific
2	1D Load Cell	Futek
2	VN 300 GPS/INS	VectorNav

Square Three Axis Load Cell

Model TR3D-B-*

- 250 lb, 1,000 lb, 4,000 lb, 4,500 lb, and 16,000 lb capacities
- Measures forces in three perpendicular directions
- Environmentally protected
- Temperature compensated
- Rugged construction

Description

Michigan Scientific *TR3D-B-* Square Three Axis Load Cells* are ideal for applications that require force measurements in three perpendicular directions. Available in 250, 1000, 4000, 4500 and 16000 lb capacities, these compact transducers are configured for easy adaptation to a variety of applications.

High grade stainless steel or aluminum material, in addition to weatherproof sealing, combine to provide excellent resistance to corrosion and environmental conditions. Temperature compensation of the transducers ensures stable output throughout a wide temperature range.

Specifications

	TR3D-B-250	**TR3D-B-1K**	**TR3D-B-4K**	**TR3D-B-4500**	**TR3D-B-16K**
Maximum Load Capacity (per channel)	250 lbs (1.1 kN)	1,000 lbs (4.4 kN)	4,000 lbs (17.8 kN)	4,500 lbs (20 kN)	16,000 lbs (71 kN)
Maximum Moment Capacity (per channel)	12 lb-ft (16 N.m)	48 lb-ft (65 N.m)	165 lb-ft (220 N.m)	130 lb-ft (175 N.m)	1300 lb-ft (1.7 kN.m)
Full Scale Output	3.5 mV/V, nominal, all channels	4.5 mV/V, nominal, all channels		3.0mV/V nominal,Fx,Fy 4.0mV/V nominal, Fz	4.5 mV/V, nominal, all channels
Sensor	3 Four-arm strain gage bridges				
Nonlinearity	<0.5% of full scale output				
Hysteresis	< 0.5% of full scale output				
Temperature Range, Compensated	75°F to 200°F (24°C to 93°C)				
Temperature Effect on Zero	<0.2% full scale				
Temperature Range, Useable	-40°F to 300°F (-40°C to 149°C)				
Excitation Voltage, Maximum	10V DC or AC rms				
Standard Cable Length	10 ft (3.05 m) shielded, open-ended leads				

05-15-17
Rev. A

FUTEK
ADVANCED SENSOR TECHNOLOGY, INC.

MODEL LCM200

Miniature Threaded In Line Load Cell

FEATURES

- Minimal mounting clearance
- 17-4 stainless-steel construction
- For use in both tension and compression
- Adheres to RoHS directive 2011/65/EU
- Accessories and related instruments available

🟦 **Non-loading surface, do not contact**

🟨 **Active End**

⬛ **Fixed End**

+ Output (tension)
– Output (compression)

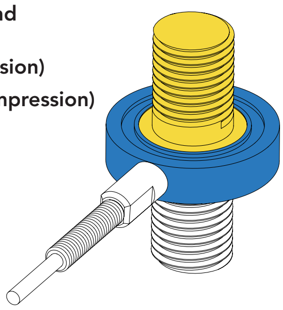

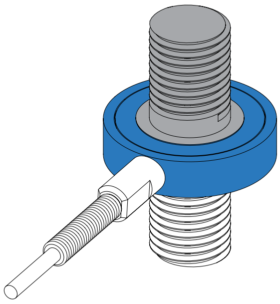

SPECIFICATIONS	
PERFORMANCE	
Nonlinearity	±0.5% of RO
Hysteresis	±0.5% of RO
Nonrepeatability	±0.1% of RO
ELECTRICAL	
Rated Output (RO)	1 mV/V nom (250 lb) 2 mV/V nom
Excitation (VDC or VAC)	15 max
Bridge Resistance	350 Ohm nom
Insulation Resistance	≥500 MOhm @ 50 VDC
Connection	#29 AWG, 4 conductor, spiral shielded Teflon cable 10 ft [3 m] long
Wiring/Connector Code	WC1
MECHANICAL	
Weight (approximate)	0.6 oz [17 g]
Safe Overload	150% of RO
Deflection	0.001 in [0.025 mm] nom
Material	17-4 PH stainless-steel
IP Rating	IP64
TEMPERATURE	
Operating Temperature	–60 to 285°F (–51 to 140°C)
Compensated Temperature	60 to 250°F (15 to 121°C)
Temperature Shift Zero	±0.01% of RO/°F (±0.018 of RO/°C)
Temperature Shift Span	±0.02% of Load/°F (±0.036 of Load/°C)
CALIBRATION	
Calibration Test Excitation	10 VDC
Calibration (standard)	5-pt Tension
Calibration (available)	5-pt Compression
Shunt Calibration Value	60.4 kOhm, 100 kOhm (250 lb)
CONFORMITY	
RoHS	2011/65/EU
CE	EN55011:2009; EN61326-1:2006

VECTORNAV
Embedded Navigation Solutions

DUAL ANTENNA GPS-AIDED
INERTIAL NAVIGATION SYSTEM

VN-300 Dual Antenna GPS/INS

High-Performance Embedded Navigation

PRODUCT OVERVIEW

VectorNav Technologies introduces the VN-300, the world's smallest and lightest high-performance Dual Antenna GPS-Aided Inertial Navigation System (GPS/INS). Building on the architecture of the currently available VN-100 line of IMU/AHRS as well as the VN-200 line of GPS/INS, the VN-300 enables a wider range of applications through the incorporation of GPS-compass techniques. The VN-300 is ideal for applications that require a highly accurate inertial navigation solution under both static and dynamic operating conditions, especially in environments with unreliable magnetic heading and good GNSS visibility.

Incorporating the latest solid-state MEMS sensor technology, the VN-300 combines 3-axis accelerometers, gyros, magnetometers, a barometric pressure sensor, two GNSS receivers, and a low-power micro-processor into a rugged aluminum enclosure or surface mount package. The VN-300 couples measurements from the onboard GNSS receivers with measurements from the onboard inertial sensors to provide position, velocity, and attitude estimates of higher accuracies and with better dynamic performance than a standalone GPS or GNSS receiver or AHRS.

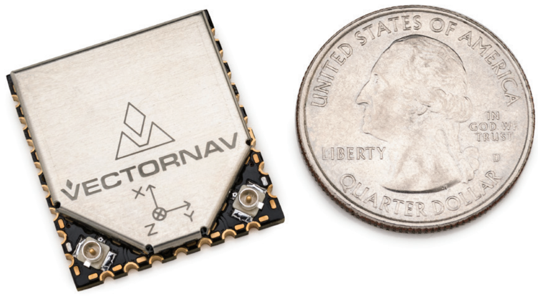

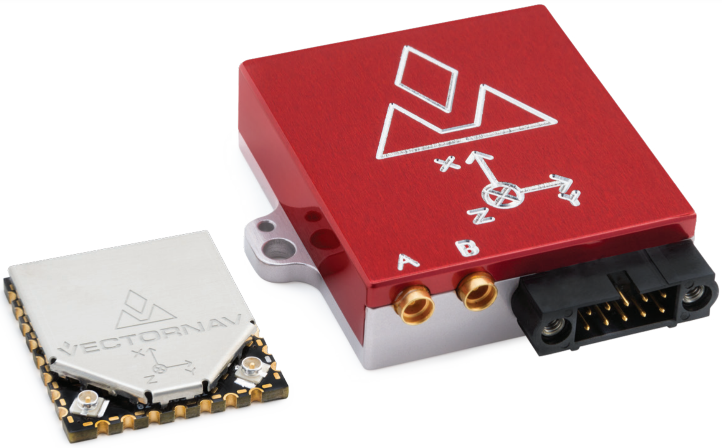

HIGHLIGHTS

- Coupled position, velocity, & attitude estimates
- Static accuracy better than 0.3° heading, 0.5° pitch & roll
- Dynamic accuracy better than 0.3° heading, 0.1° pitch & roll
- Dual 72 Channel GNSS receivers
- Built-in Extended Kalman Filter running at 400 Hz
- Automatic and seamless transition between magnetic heading (AHRS) mode (used on start-up and in GPS-denied environments), INS operation in dynamic conditions, and GPS-compass in static conditions
- True INS filter - no mounting orientation requirements
- Real-time gyro & accelerometer bias compensation
- Raw pseudorange, Doppler, & carrier phase outputs
- Individually calibrated for bias, scale factor, misalignment, and temperature over full operating range (-40°C to +85°C)
- Miniature self-locking MMCX connectors for GPS antennas
- Coning & sculling integrals (ΔV's, ΔΘ's)
- User configurable messages using VectorNav binary protocol
- Rugged aluminum package (10-pin Harwin connector)
  Dimensions: 45 x 44 x 11 mm; Weight: 30 grams
- Surface mount package (30-pin LGA)
  Dimensions: 24 x 22 x 3 mm; Weight: 5 grams

APPLICATIONS

- UAVs, UAS, Manned Aircraft, VTOL Aircraft, Aerostats
- Marine Antenna Stabilization
- Camera / Platform Stabilization
- SATCOM, SOTM, VSAT
- Ground Vehicles / Robotics
- Weapons Training / Warfare Simulation
- Heavy Machinery Monitoring
- Automated Agriculture
- Direct Surveying




DEVELOPMENT KITS

VN-300 Rugged and Surface Mount Development Kits:

- USB & Serial Adapter Cables
- Two GNSS Antennas
- Software Development Kit
- Carrying Case

DEVELOPMENT TOOLS

- **Sensor Explorer GUI**: Powerful and user-friendly GUI allows you to display sensor output as a 3D object, graph inertial data, configure sensor settings, perform data-logging, & more.
- **Software Development Kit**: Interface via C/C++, .NET & MATLAB development environments.
- **Online Library**: A large collection of inertial navigation knowledge and application notes is available on our website to help maximize VN-300 performance for your application.
- **Engineering Support**: Dedicated and responsive engineering support team with combined experience in sensing, guidance, navigation, and controls.
- **Custom Solutions Available**: Application-specific modeling & algorithm development; controls & closed-loop navigation solutions; custom form-factors & packaging; integration with other external sensors; displays, GUIs & other software packages; tailored calibrations; custom communication protocols.

TECHNICAL SPECIFICATIONS

Navigation

Horizontal Position Accuracy:	2.5 m RMS
Horizontal Position Accuracy (w/SBAS):	2.0 m RMS
Vertical Position Accuracy:	5.0 m RMS
Vertical Position Accuracy (w/Barometer):	2.5 m RMS
Velocity Accuracy:	±0.05 m/s
Dynamic Accuracy (Heading, True Inertial):	0.3 ° RMS
Dynamic Accuracy (Pitch/Roll):	0.1 ° RMS
Static Accuracy (Heading, GPS Compass)[1]:	0.3 ° RMS
Static Accuracy (Heading, Magnetic)[2]:	2.0 ° RMS
Static Accuracy (Pitch/Roll):	0.5 ° RMS
Angular Resolution:	< 0.05 °
Repeatability:	< 0.1 °
Max Output Rate (IMU Data)[3]:	400 Hz
Max Output Rate (Navigation Data):	400 Hz

Gyro

Range:	±2000 °/s
In-Run Bias Stability:	< 10 °/hr
Linearity:	< 0.1 % FS
Noise Density:	0.0035 °/s /√Hz
Bandwidth:	256 Hz
Alignment Error:	±0.05 °

Accelerometer

Range:	±16 g
In-Run Bias Stability:	<0.04 mg
Linearity:	< 0.5 % FS
Noise Density:	0.14 mg/√Hz
Bandwidth:	260 Hz
Alignment Error:	±0.05 °

Magnetometer

Range:	±2.5 Gauss
Linearity:	< 0.1 %
Noise Density:	140 μGauss/√Hz
Bandwidth:	200 Hz
Alignment Error:	±0.05 °

GNSS

Receiver Type:	72 Channels, L1, GNSS
Solution Update Rate:	5 Hz
Time-to-First-Fix (Cold/Warm Start):	26 s
Time-to-First-Fix (Hot Start):	< 1 s
Altitude Limit:	50,000 m
Velocity Limit:	500 m/s

Pressure Sensor

Range:	10 to 1200 mbar
Resolution:	0.042 mbar
Accuracy:	±1.5 mbar
Error Band:	±2.5 mbar
Bandwidth:	200 Hz

Environment

Operating Temp:	-40°C to +85°C
Storage Temp:	-40°C to +85°C

Electrical:	SMD	Rugged
Input Voltage:	3.2 V to 5.5 V	3.3 V to 14 V
Current Draw[4]:	185 mA @ 3.3 V	250 mA @ 5 V
Max Power Consumption[4]:	1.2 W	1.5 W
Digital Interface:	Serial TTL, SPI	Serial TTL, RS-232

Physical:	SMD	Rugged
Size:	24 x 22 x 3 mm	45 x 44 x 11 mm
Weight:	5 g	30 g
Connector:	30-pin LGA	10-pin Harwin
GNSS Antenna Connectors:	U.FL	MMCX

[1] With one (1) meter baseline, clear view of GNSS satellites and good multipath environment.

[2] With proper magnetic declination, suitable magnetic environment and valid hard/soft iron calibration.

[3] Contact VectorNav for higher IMU data output rates.

[4] Not including active antenna power consumption.

B. Drawings

This appendix includes the relevant drawings made for the current study, summarized in the following table:

Nbr.	Drawing Name	Author
1	Kite Control Box	Behrel
2	Kiteboat Exterior Views	Leslé & Jubert
2	Kiteboat Lines Drawing	Leslé & Jubert
4	Kiteboat Cabling Diagram	Behrel
5	Remote Control Device Resistor Diagram	Behrel

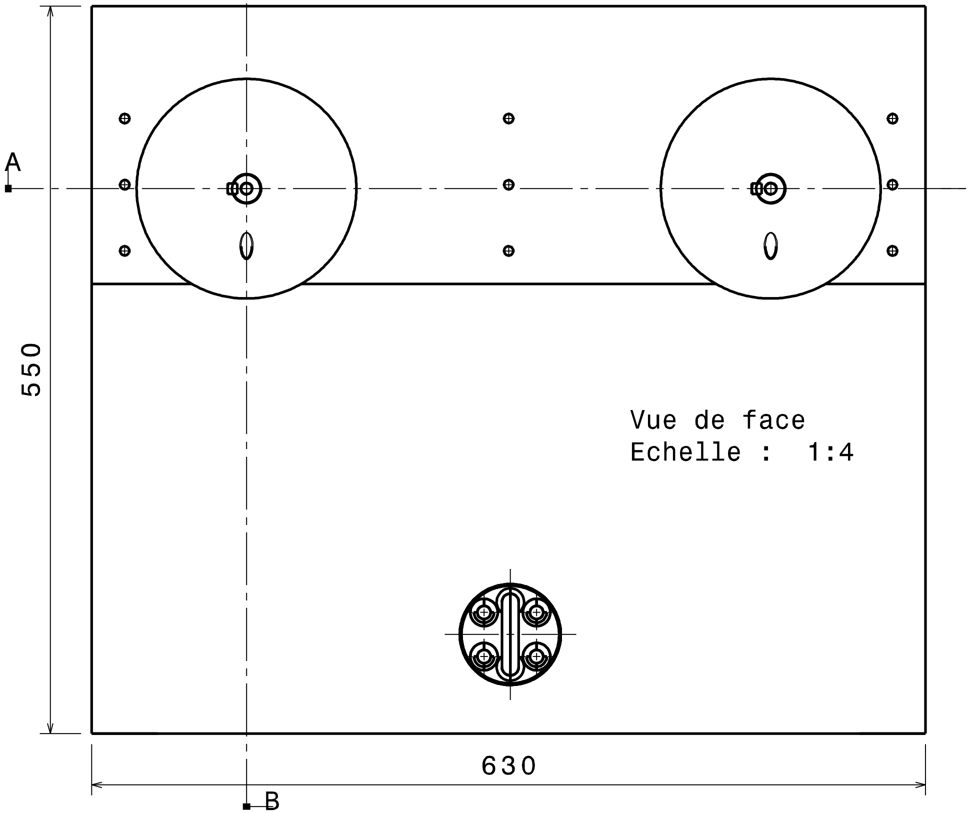

Vue de face
Echelle : 1:4

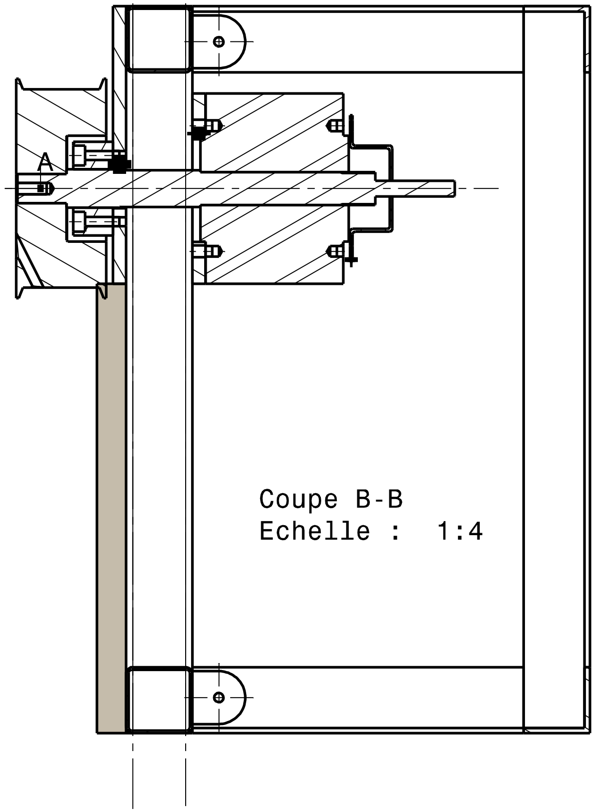

Coupe B-B
Echelle : 1:4

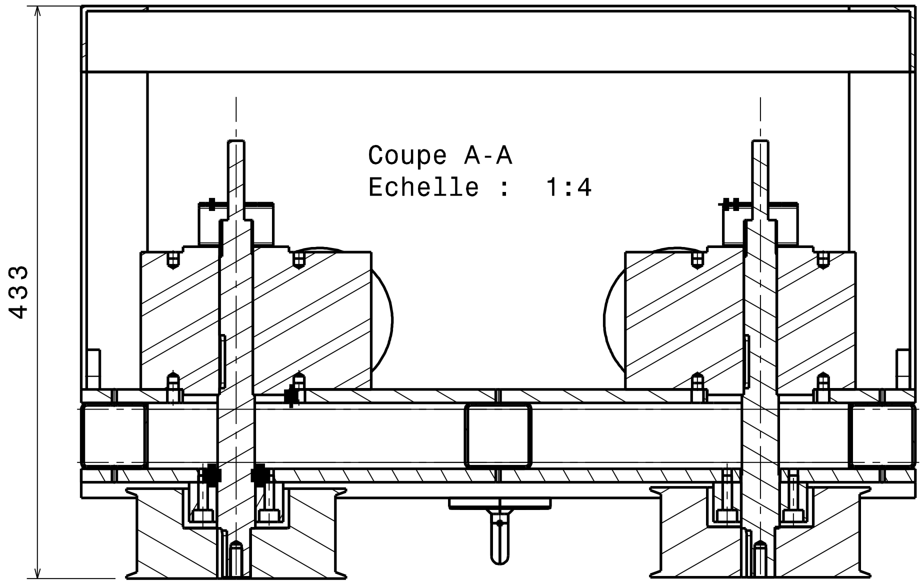

Coupe A-A
Echelle : 1:4

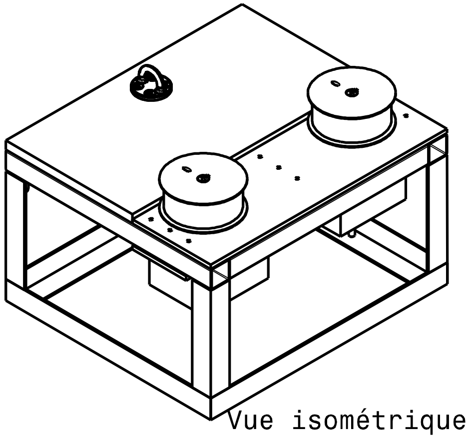

Vue isométrique
Echelle : 1:10

DESIGNED BY: M Behrel
DATE: 31/10/2014
CHECKED BY: XXX
DATE: XXX
SIZE A3
SCALE 1:4
WEIGHT (kg) XXX

Ply Name	Kite Experimental Set Up
Material	
Direction	
Thickness	
SequenceID	
GroupID	

I	_
H	_
G	_
F	_
E	_
D	_
C	_
B	_
A	_

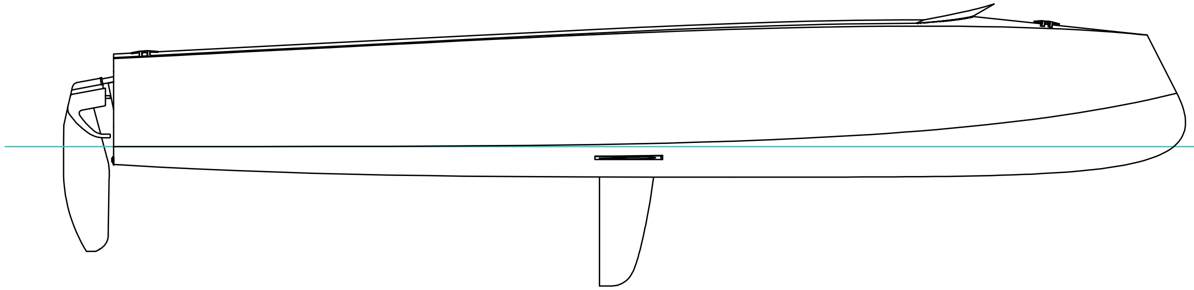

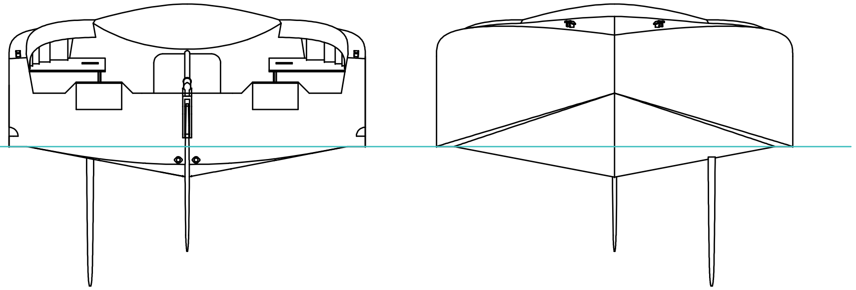

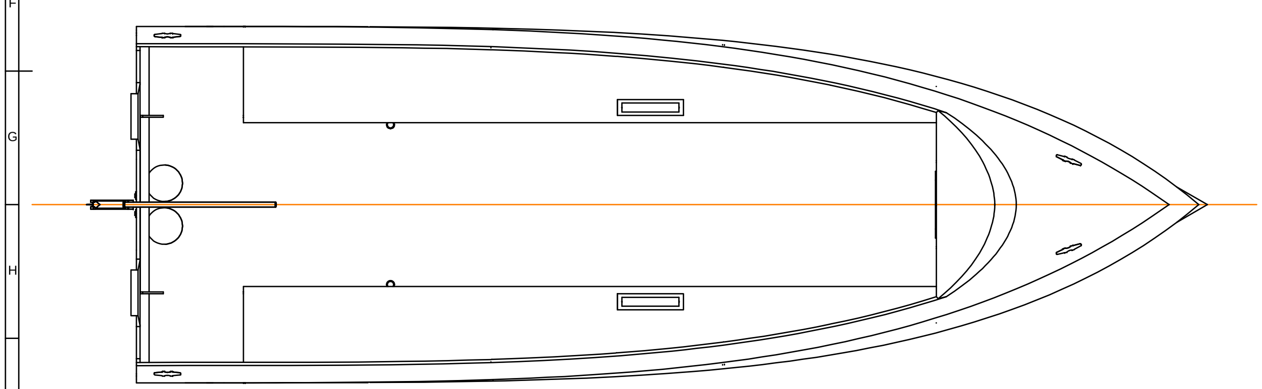

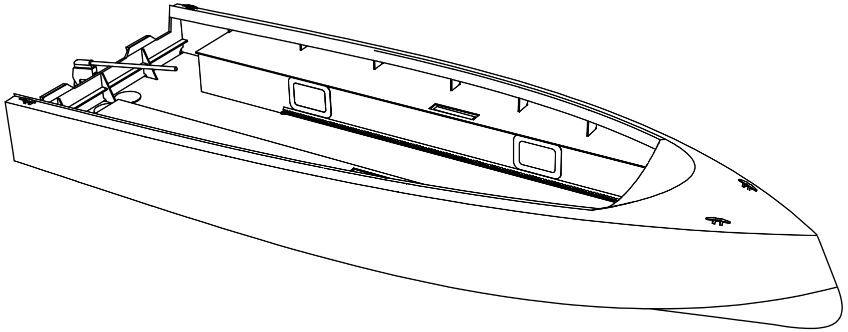

PROJET	Kite Boat	SOCIETE	ENSTA BRETAGNE
TITRE	Vues extérieures		
AUTEURS	LESLE JUBERT		
DATE	16/03/2016	Page 1/1	ETAT VALIDE
UNITE	Mètres	ECHELLE 1:30	FORMAT A3
	Contreplaqué marine 8mm		

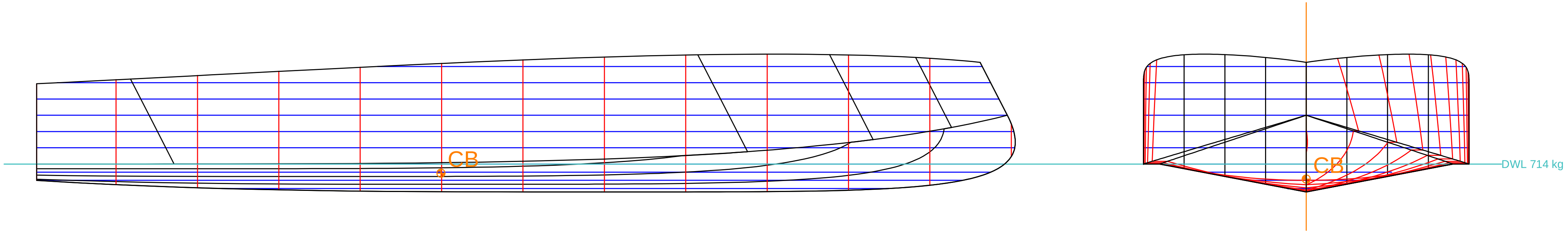

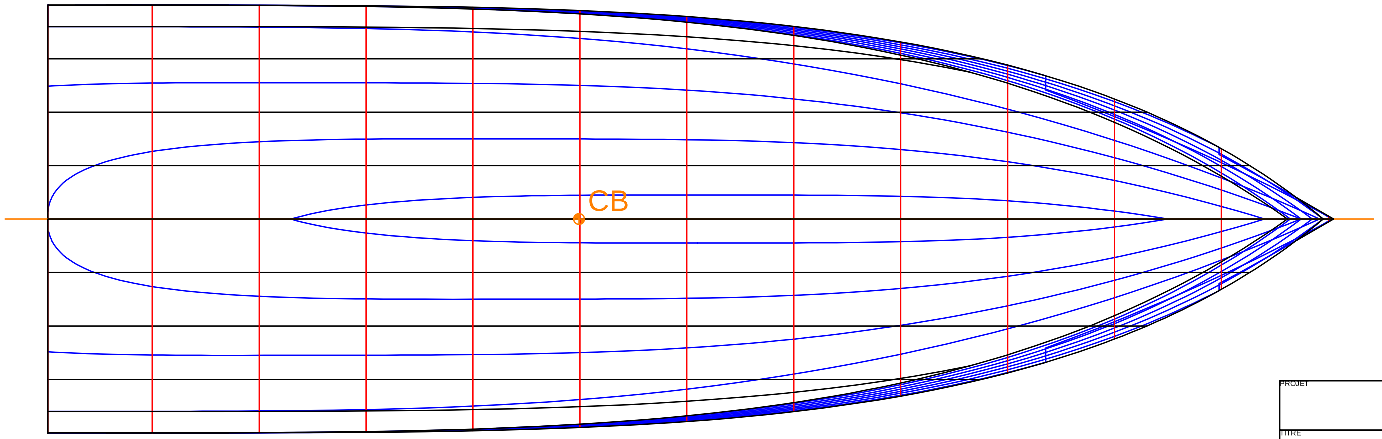

PROJET		SOCIETE
Kite Boat		ENSTA BRETAGNE
TITRE Plan de forme		
AUTEURS LESLE JUBERT		
DATE 16/03/2016	Page 1/1	ETAT VALIDE
UNITE Mètres	ECHELLE 1:25	FORMAT A3
Kite Boat LHT 6m		

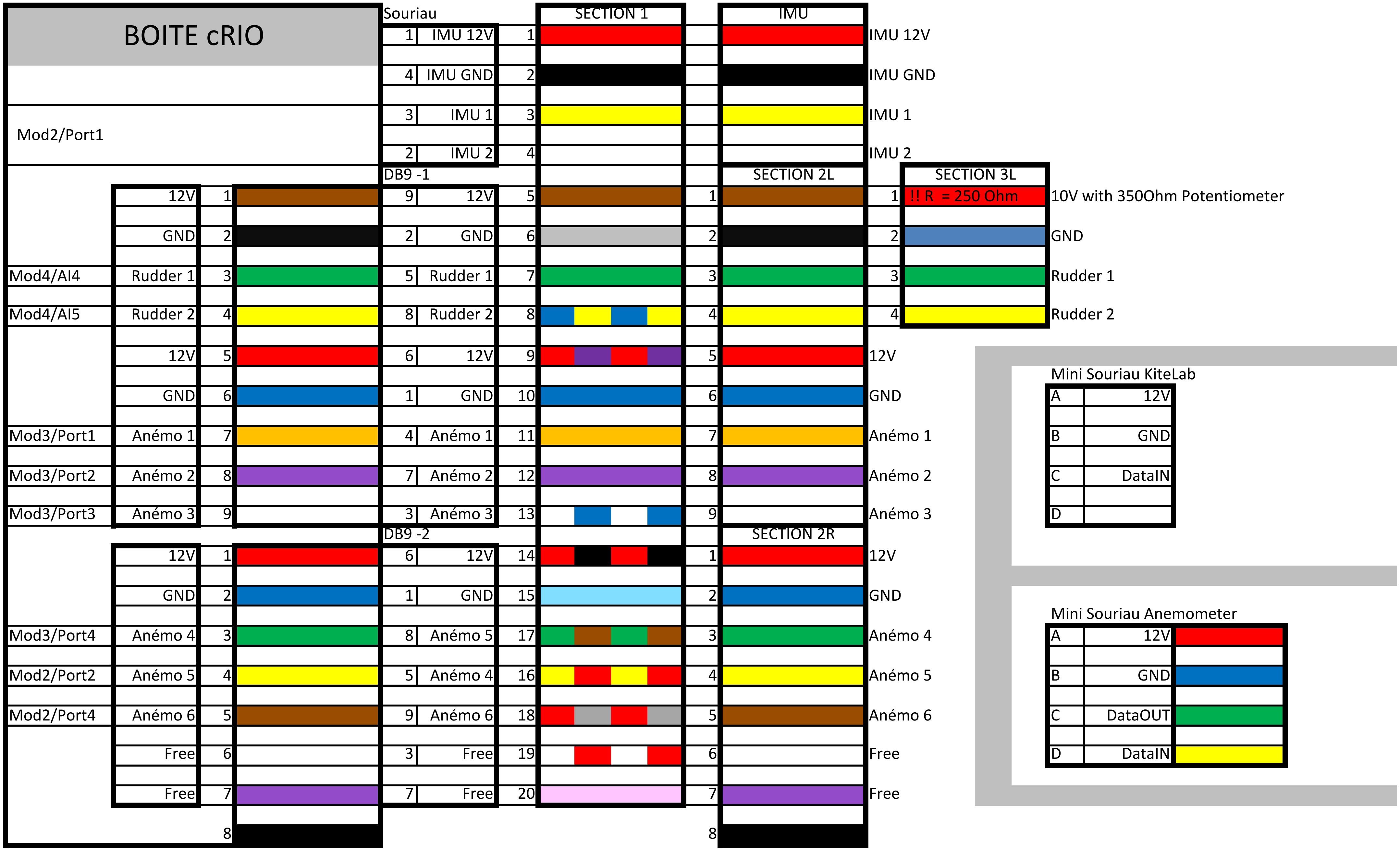
BOITE cRIO
Mod2/Port1
Mod4/AI4
Mod4/AI5
Mod3/Port1
Mod3/Port2
Mod3/Port3
Mod3/Port4
Mod2/Port2
Mod2/Port4
12V 1
GND 2
Rudder 1 3
Rudder 2 4
12V 5
GND 6
Anémo 1 7
Anémo 2 8
Anémo 3 9
12V 1
GND 2
Anémo 4 3
Anémo 5 4
Anémo 6 5
Free 6
Free 7
8
Souriau
1 IMU 12V
4 IMU GND
3 IMU 1
2 IMU 2
DB9 -1
9 12V
2 GND
5 Rudder 1
8 Rudder 2
6 12V
1 GND
4 Anémo 1
7 Anémo 2
3 Anémo 3
DB9 -2
6 12V
1 GND
8 Anémo 5
5 Anémo 4
9 Anémo 6
3 Free
7 Free
SECTION 1
1
2
3
4
5
6
7
8
9
10
11
12
13
14
15
17
16
18
19
20
IMU
SECTION 2L
1
2
3
4
5
6
7
8
9
SECTION 2R
1
2
3
4
5
6
7
8
IMU 12V
IMU GND
IMU 1
IMU 2
12V
GND
Anémo 1
Anémo 2
Anémo 3
12V
GND
Anémo 4
Anémo 5
Anémo 6
Free
Free
SECTION 3L
1 !! R = 250 Ohm
2
3
4
10V with 350Ohm Potentiometer
GND
Rudder 1
Rudder 2
Mini Souriau KiteLab
A 12V
B GND
C DataIN
D
Mini Souriau Anemometer
A 12V
B GND
C DataOUT
D DataIN

Kite Control Remote Device : Analogic Case Selector

Author : M Behrel

U	5	V
R0	120	Ohm
R1	470	Ohm
R2	270	Ohm
R3	690	Ohm
1/R3	1.4E-03	Ohm-1
R4	270	Ohm

	Cases							
Switch 0	0	1	0	0	1	1	0	1
Switch 1	0	0	1	0	1	0	1	1
Switch 2	0	0	0	1	0	1	1	1
1/R0	0.0E+00	8.3E-03	0.0E+00	0.0E+00	8.3E-03	8.3E-03	0.0E+00	8.3E-03
1/R1	0.0E+00	0.0E+00	2.1E-03	0.0E+00	2.1E-03	0.0E+00	2.1E-03	2.1E-03
1/R2	0.0E+00	0.0E+00	0.0E+00	3.7E-03	0.0E+00	3.7E-03	3.7E-03	3.7E-03
S1/R	1.45E-03	9.78E-03	3.58E-03	5.15E-03	1.19E-02	1.35E-02	7.28E-03	1.56E-02
Req (Ohm)	690.0	102.2	279.6	194.1	84.0	74.1	137.4	64.0
U2 (V)	1.4	3.6	2.5	2.9	3.8	3.9	3.3	4.0
I (mA)	5.2	13.4	9.1	10.8	14.1	14.5	12.3	15.0

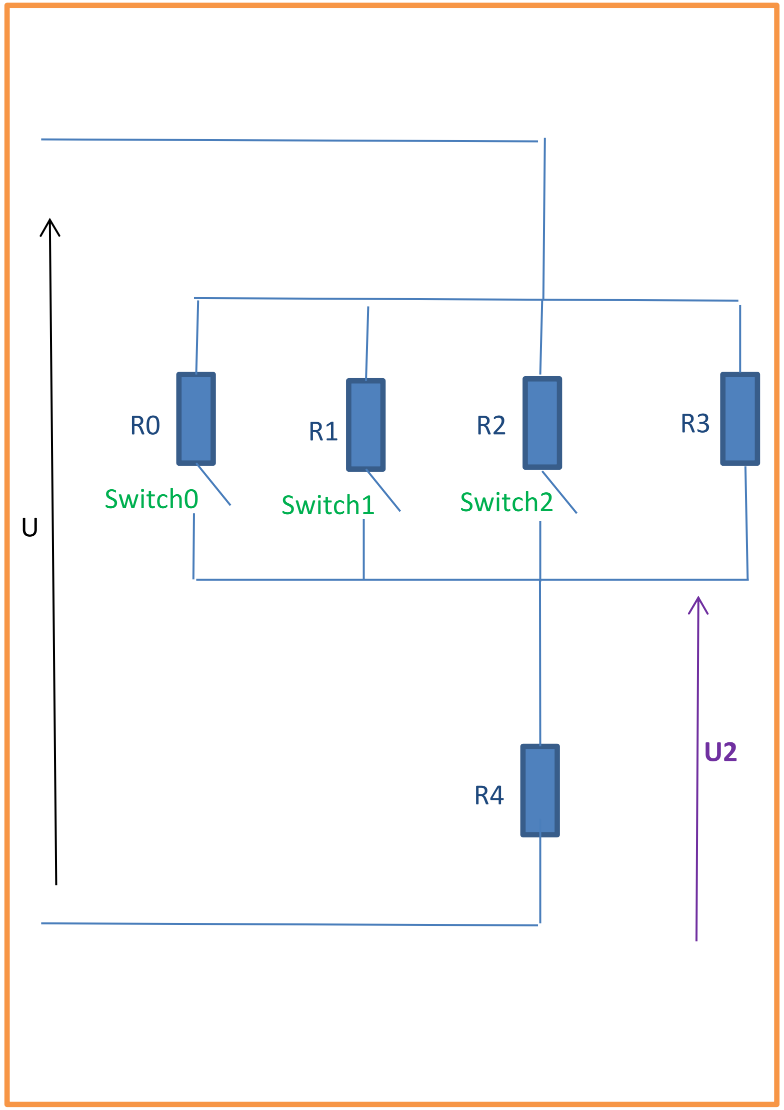

C. Result Compilation

This appendix includes results coming from various measurements, and summarized in the following table:

Nbr.	Work Name
1	Kiteboat Averaged Results
2	Kiteboat 3D plots of 2 runs
2	Kiteboat 3D plots of 4 runs processed with the phase averaging method
4	
5	

Average Result for All Runs of the Kiteboat, with Kite

Nbr	FileName	Date and Time UTC	Duration (s)	Kite Name	Kite Size	Tether Length	Centerboard	Motor	TWA (°)	TWS (m/s)	TWD (°)	SOG (m/s)	COG (°)	HDG (°)	Pitch (°)	Roll (°)	Fk,A (N)	Back Tether Ratio	Fprop (N)	Phi (°)	Theta (°)	Rudder Angle (°)	Actuator Power (W)	Propulsive Power (W)	Wing Load (N/m^2)	Pressure (hPa)	RH (%)	Temperaure (°C)
1	d01f3Cab5_C2bis_180	3/28/17 12:06	267	Cabrinha	5	50	STD	NO	181,9	8,8	225,2	3,6	38,5	43,3	2,9	1,6	709,8	0,22	527,5	3,4	40,2	-3,2	NaN	1911,4	142,0	1023,9	66,7	13,3
2	d01f4Cab5_C2bis_MOTEUR_60	3/28/17 12:21	279	Cabrinha	5	50	STD	YES	62,4	7,6	227,8	2,5	155,3	165,4	2,8	0,0	152,8	0,21	74,7	-58,6	19,0	3,5	NaN	183,5	30,6	1024,0	69,1	12,9
3	d01f5Cab5_C2bis_MOTEUR_M60	3/28/17 12:28	297	Cabrinha	5	50	STD	YES	296,7	7,0	214,9	3,2	288,6	278,2	3,1	2,1	142,1	0,20	58,7	64,3	17,5	4,4	NaN	182,3	28,4	1024,0	68,9	12,9
4	d01f6Cab5_C2bis_160	3/28/17 12:40	357	Cabrinha	5	50	STD	NO	156,1	7,4	218,6	3,1	52,9	62,5	2,4	1,0	502,2	0,20	405,0	-0,5	32,5	-2,5	NaN	1235,2	100,4	1024,0	67,3	13,3
5	d01f7Cab5_C2bis_140	3/28/17 12:48	299	Cabrinha	5	50	STD	NO	136,6	6,8	216,8	2,9	67,5	80,1	2,1	0,6	494,4	0,20	372,2	-16,7	32,7	-2,5	NaN	1040,4	98,9	1023,9	68,2	13,1
6	d01f8Cab5_C2bis_M160	3/28/17 13:20	297	Cabrinha	5	50	STD	NO	202,0	7,8	219,6	3,3	19,5	17,6	2,7	1,6	635,2	0,24	471,2	2,6	38,9	-4,3	NaN	1551,7	127,0	1023,9	67,0	13,2
7	d01f9Cab5_C2bis_M140	3/28/17 13:25	299	Cabrinha	5	50	STD	NO	222,1	8,6	217,9	3,5	2,1	355,9	2,9	2,6	710,9	0,24	482,6	19,1	38,3	-5,2	NaN	1665,2	142,2	1023,8	65,8	13,4
8	d02f1Cab12_C2bis_80	3/29/17 10:19	294	Cabrinha2	12	50	STD	NO	80,6	6,8	181,9	1,9	89,7	101,3	1,9	0,5	315,2	0,26	226,5	-34,8	28,6	1,9	NaN	428,4	26,3	1025,3	74,9	11,9
9	d02f2Cab12_C2bis_M80	3/29/17 10:26	299	Cabrinha2	12	50	STD	NO	283,5	6,5	177,9	2,2	259,7	254,4	2,0	2,3	347,0	0,26	235,4	41,0	25,2	3,1	NaN	522,9	28,9	1025,4	75,0	11,9
10	d02f3Cab12_C2bis_100STAT	3/29/17 10:31	302	Cabrinha2	12	50	STD	NO	99,5	6,8	183,6	2,1	73,8	84,1	1,9	0,4	300,3	0,25	245,0	-17,3	30,9	2,9	NaN	506,7	25,0	1025,4	74,4	12,0
11	d02f4Cab12_C2bis_M100STAT	3/29/17 10:37	299	Cabrinha2	12	50	STD	NO	262,2	6,4	178,5	2,2	283,3	276,3	2,0	2,3	261,3	0,26	222,8	19,4	24,5	2,7	NaN	475,8	21,8	1025,4	74,2	12,0
12	d02f5Cab12_C2bis_180_E65	3/29/17 12:26	296	Cabrinha2	12	50	STD	NO	181,5	6,6	173,9	3,4	354,0	352,5	2,4	1,3	808,6	0,20	381,6	5,3	59,9	-3,0	NaN	1280,3	67,4	1024,7	75,0	12,3
13	d02f6Cab12_C2bis_180_E50	3/29/17 12:33	254	Cabrinha2	12	50	STD	NO	182,7	6,3	179,7	4,3	358,8	357,0	3,3	1,0	928,7	0,20	615,7	3,8	46,2	-2,6	NaN	2604,0	77,4	1024,8	74,5	12,5
14	d02f7Cab12_C2bis_120	3/29/17 13:01	297	Cabrinha2	12	50	STD	NO	115,9	5,8	179,9	3,3	49,8	64,0	3,1	0,2	915,5	0,20	487,6	-36,6	44,6	-3,4	NaN	1599,2	76,3	1024,4	76,0	12,2
15	d02f8Cab12_C2bis_M120	3/29/17 13:51	297	Cabrinha2	12	50	STD	NO	241,8	5,6	174,6	3,6	302,9	292,9	3,0	3,1	913,6	0,22	476,2	36,4	45,1	-2,4	NaN	1695,2	76,1	1023,9	75,8	12,1
16	d02f9Cab12_C2bis_100	3/29/17 13:57	296	Cabrinha2	12	50	STD	NO	96,5	5,8	180,1	3,5	63,9	83,5	3,1	-2,4	1682,3	0,25	499,5	-61,2	46,5	-2,5	NaN	1650,3	140,2	1023,8	76,0	12,1
17	d02f10Cab12_C2bis_M100	3/29/17 14:03	320	Cabrinha2	12	50	STD	NO	260,3	5,1	171,4	3,5	280,8	271,1	2,9	4,5	1198,8	0,24	416,4	58,2	44,0	-2,8	NaN	1447,9	99,9	1023,8	76,0	12,1
18	d02f11Cab12_C2bis_MOTEUR_60	3/29/17 14:11	297	Cabrinha2	12	50	STD	YES	65,8	5,4	189,1	2,7	110,0	123,3	2,6	0,5	178,2	0,18	77,6	-62,7	18,5	5,3	NaN	199,9	14,9	1023,8	76,0	12,1
19	d02f12Cab12_C2bis_MOTEUR_M60	3/29/17 14:19	299	Cabrinha2	12	50	STD	YES	302,4	4,6	181,8	2,9	240,9	239,4	2,8	2,4	191,5	0,20	61,9	70,1	18,7	6,5	NaN	178,1	16,0	1023,6	76,0	12,1
20	d02f13Cab12_C2bis_160	3/29/17 14:34	355	Cabrinha2	12	50	STD	NO	161,6	4,4	177,7	2,9	19,1	16,1	2,4	1,3	605,8	0,19	380,4	-3,5	49,8	-1,2	NaN	1105,5	50,5	1023,6	76,0	12,1
21	d02f14Cab12_C2bis_140	3/29/17 14:40	299	Cabrinha2	12	50	STD	NO	138,4	4,6	171,5	3,1	31,5	33,1	2,5	0,8	713,2	0,20	396,9	-21,9	50,6	-1,3	NaN	1240,3	59,4	1023,5	76,0	12,2
22	d02f15Cab12_C2bis_M160	3/29/17 14:55	296	Cabrinha2	12	50	STD	NO	202,2	4,6	166,8	2,9	328,9	324,7	2,1	1,6	516,0	0,18	327,3	-0,8	47,9	-1,8	NaN	968,6	43,0	1023,4	76,0	12,1
23	d02f16Cab12_C2bis_M140	3/29/17 15:00	296	Cabrinha2	12	50	STD	NO	220,5	4,7	163,6	2,6	307,6	303,1	2,2	1,9	458,1	0,16	288,5	15,6	47,3	-1,9	NaN	777,6	38,2	1023,3	76,0	12,2
24	d03f2Cab12_C2bis_180	3/30/17 12:32	293	Cabrinha2	12	50	STD	NO	181,2	6,1	136,5	4,9	322,7	315,3	3,7	1,0	NaN	NaN	NaN	-2,3	46,9	-0,9	NaN	NaN	NaN	1018,1	65,2	13,9
25	d03f3Cab12_C2bis_M60	3/30/17 12:39	298	Cabrinha2	12	50	STD	NO	304,5	5,2	149,3	1,0	220,0	204,8	1,6	2,3	NaN	NaN	NaN	54,5	16,9	6,2	NaN	NaN	NaN	1018,0	66,8	13,7
26	d03f4Cab12_C2bis_60	3/30/17 12:45	298	Cabrinha2	12	50	STD	NO	62,7	5,5	147,0	1,2	65,4	84,4	1,6	0,6	NaN	NaN	NaN	-45,2	15,7	-4,8	NaN	NaN	NaN	1017,9	67,0	13,6
27	d03f5Cab12_C2bis_MOTEUR_60	3/30/17 12:51	298	Cabrinha2	12	50	STD	YES	55,9	5,7	141,9	3,0	69,5	86,0	2,6	0,0	NaN	NaN	NaN	-59,5	21,5	2,8	NaN	NaN	NaN	1017,8	68,4	13,3
28	d03f6Cab12_C2bis_MOTEUR_M60	3/30/17 12:59	300	Cabrinha2	12	50	STD	YES	304,1	5,7	148,9	2,8	204,8	204,8	2,7	2,8	NaN	NaN	NaN	64,0	16,7	6,4	NaN	NaN	NaN	1017,7	67,3	13,5
29	d03f9Cab5_C2bis_M120	3/30/17 13:43	249	Cabrinha	5	50	STD	NO	239,7	6,6	141,5	3,4	272,9	261,8	2,5	2,3	NaN	NaN	NaN	40,1	33,2	-3,3	NaN	NaN	NaN	1016,9	67,2	13,5
30	d04f1Cab5_C2bis_180_E50	3/31/17 10:26	300	Cabrinha	5	50	STD	NO	183,4	6,1	216,9	2,5	43,6	33,4	2,0	1,4	454,0	0,23	283,0	4,0	50,3	-1,0	NaN	683,7	90,8	1014,9	70,7	12,6
31	d04f2Cab5_C2bis_M120	3/31/17 10:32	295	Cabrinha	5	50	STD	NO	245,3	6,3	215,4	2,6	344,0	330,1	2,3	3,6	649,2	0,25	346,1	45,8	34,9	-2,8	NaN	857,5	129,8	1014,9	72,0	12,5
32	d04f3Cab5_C2bis_M100	3/31/17 10:45	297	Cabrinha	5	50	STD	NO	265,5	6,9	211,7	1,9	326,0	306,1	2,2	4,6	810,0	0,23	176,4	68,5	42,1	-1,7	NaN	313,5	162,0	1014,9	70,7	12,7
33	d05f1Cab_C2bis_180	4/5/17 9:29	299	Cabrinha	5	50	STD	NO	179,1	5,2	23,0	2,5	201,0	203,9	2,0	1,3	318,8	0,23	266,2	1,8	31,7	-1,3	NaN	668,4	63,8	1030,5	69,4	12,5
34	d05f2Cab5_C2bis_M100	4/5/17 9:36	297	Cabrinha	5	50	STD	NO	262,4	4,8	29,5	1,9	124,2	127,2	2,0	3,0	462,8	0,24	185,2	57,8	32,8	-3,2	NaN	363,7	92,6	1030,4	70,2	12,4
35	d05f3Cab12_C2bis_MANDYN_M80	4/5/17 10:15	301	Cabrinha	5	50	STD	NO	284,8	5,6	37,6	1,8	119,6	112,8	2,0	3,9	581,4	0,23	141,8	71,0	27,8	-0,8	NaN	256,5	116,3	1030,4	70,1	12,6
36	d05f4Cab12_C2bis_180_E50	4/5/17 11:17	297	Cabrinha2	12	50	STD	NO	178,8	5,2	32,1	3,5	210,4	213,3	2,8	1,5	724,9	0,21	495,6	1,9	45,1	-0,2	NaN	1733,7	60,4	1030,3	68,7	13,4
37	d05f5Cab12_C2bis_MANDYN_M80	4/5/17 11:26	315	Cabrinha2	12	50	STD	NO	285,3	5,4	48,8	3,1	114,8	123,6	3,2	6,5	1089,6	0,24	443,7	60,2	28,9	-1,8	NaN	1394,5	90,8	1030,2	68,5	13,1
38	d05f6Cab12_C2bis_MANDYN_80	4/5/17 11:35	294	Cabrinha2	12	50	STD	NO	83,5	6,1	18,2	3,2	289,7	294,6	2,7	-1,2	1075,1	0,24	426,6	-59,4	34,2	0,0	NaN	1410,5	89,6	1030,1	67,9	13,1
39	d05f7Cab12_C2bis_180_E35	4/5/17 11:45	298	Cabrinha2	12	50	STD	NO	174,3	6,0	23,2	4,0	203,0	208,9	3,5	2,3	833,7	0,24	644,6	1,3	37,3	-1,7	NaN	2541,3	69,5	1030,3	67,0	13,4
40	d05f8Cab12_C2bis_160_E35	4/5/17 12:21	299	Cabrinha2	12	50	STD	NO	155,4	7,5	16,3	4,6	218,8	220,8	4,1	1,0	1080,8	0,24	835,0	-4,6	36,1	-0,1	NaN	3860,6	90,1	1030,4	66,1	13,3
41	d05f9Cab12_C2bis_M160_E35	4/5/17 12:26	226	Cabrinha2	12	50	STD	NO	190,0	7,2	20,7	5,1	181,4	190,7	4,2	2,8	1082,3	0,25	855,0	1,6	35,8	-2,6	NaN	4317,2	90,2	1030,2	65,7	13,3
42	d05f10Cab12_C2bis_180_E35_L80	4/5/17 13:37	299	Cabrinha2	12	80	STD	NO	172,3	5,6	10,3	4,2	192,1	198,1	3,3	1,5	843,4	0,22	657,8	-0,6	37,5	-1,3	NaN	2809,3	70,3	1029,6	60,8	14,3
43	d07f11Cab12_C2bis_D2_180	4/12/17 13:35	303	Cabrinha2	12	50	BCK	NO	179,9	4,5	254,2	2,5	65,9	74,3	2,1	1,6	375,6	0,22	310,9	0,7	32,4	0,6	NaN	791,1	31,3	1022,5	58,5	14,1
44	d07f12Cab12_C2bis_D2_120	4/12/17 13:42	219	Cabrinha2	12	50	BCK	NO	120,9	4,7	256,8	2,6	126,5	135,9	2,1	-0,5	614,8	0,23	365,8	-38,8	32,8	2,9	NaN	956,0	51,2	1022,5	59,7	13,8
45	d07f13Cab12_C2bis_D2_MOT_STAT_60	4/12/17 13:55	304	Cabrinha2	12	50	BCK	YES	66,4	4,8	264,1	2,8	197,8	197,7	2,6	-0,3	167,1	0,20	78,1	-59,5	22,4	2,0	NaN	216,3	13,9	1022,4	60,9	13,5
46	d07f14Cab12_C2bis_D2_MOT_STAT_M60	4/12/17 14:02	299	Cabrinha2	12	50	BCK	YES	302,9	5,4	250,3	2,9	316,5	307,5	2,6	3,2	189,6	0,19	60,6	70,1	20,0	6,5	NaN	176,5	15,8	1022,2	60,8	13,5
47	d07f15Cab12_C2bis_D2_STAT_60	4/12/17 14:10	298	Cabrinha2	12	50	BCK	NO	65,2	5,1	266,7	1,0	193,7	201,6	1,7	0,5	124,7	0,22	73,4	-51,0	20,4	-1,6	NaN	75,1	10,4	1022,2	61,2	13,6
48	d07f16Cab12_C2bis_STAT_M60	4/12/17 14:17	310	Cabrinha2	12	50	BCK	NO	303,7	4,9	253,9	1,0	319,9	310,2	1,9	2,3	151,3	0,22	64,7	62,1	18,6	-2,6	NaN	62,0	12,6	1022,0	60,6	13,5
49	d07f17Cab12_C2bis_D2_100	4/12/17 14:27	301	Cabrinha2	12	50	BCK	NO	102,2	4,9	260,6	2,8	154,8	158,4	2,1	-2,9	1016,4	0,24	368,3	-58,6	35,5	3,9	NaN	1053,7	84,7	1021,9	60,0	13,7
50	d07f18Cab12_C2bis_D2_M100	4/12/17 14:35	285	Cabrinha2	12	50	BCK	NO	263,3	5,5	255,6	2,8	2,0	352,3	2,3	3,0	1036,6	0,24	322,2	61,0	39,5	-5,0	NaN	889,3	86,4	1021,7	60,7	13,6
51	d07f19Cab12_C2bis_D2_M120	4/12/17 14:42	295	Cabrinha2	12	50	BCK	NO	238,6	5,5	250,3	2,8	19,6	11,8	2,5	4,4	645,6	0,23	336,0	38,6	41,6	-3,7	NaN	948,8	53,8	1021,6	61,5	13,5
52	d07f20Cab12_C2bis_D2_MANDYN_80	4/12/17 14:48	294	Cabrinha2	12	50	BCK	NO	84,8	5,6	258,8	3,2	169,2	174,0	2,7	-1,0	1401,0	0,25	514,2	-63,8	25,8	3,2	NaN	1651,7	116,7	1021,5	61,7	13,5
53	d07f21Cab12_C2bis_D2_MANDYN_M80	4/12/17 14:55	300	Cabrinha2	12	50	BCK	NO	284,8	5,7	252,5	2,8	338,7	327,8	2,3	3,7	1043,8	0,24	342,4	66,4	25,9	-5,6	NaN	957,4	87,0	1021,5	61,2	13,5

Average Result for All Runs of the Kiteboat, with Kite

Nbr	FileName	Date and Time UTC	Duration (s)	Kite Name	Kite Size	Tether Length	Centerboard	Motor	TWA (°)	TWS (m/s)	TWD (°)	SOG (m/s)	COG (°)	HDG (°)	Pitch (°)	Roll (°)	Fk,A (N)	Back Tether Ratio	Fprop (N)	Phi (°)	Theta (°)	Rudder Angle (°)	Actuator Power (W)	Propulsive Power (W)	Wing Load (N/m²)	Pressure (hPa)	RH (%)	Temperaure (°C)
54	d07f22Cab12_C2bis_D2_MANDYN_60	4/12/17 15:02	299	Cabrinha2	12	50	BCK	NO	66,8	5,2	270,8	2,4	198,7	204,0	2,0	0,7	966,1	0,25	272,9	-70,3	25,4	3,2	NaN	657,7	80,5	1021,5	59,6	13,7
55	d07f23Cab12_C2bis_D2_MANDYN_M60	4/12/17 15:10	302	Cabrinha2	12	50	BCK	NO	305,4	5,2	260,2	2,2	323,2	314,7	1,9	0,2	1074,4	0,25	183,8	77,8	23,0	-7,4	NaN	401,4	89,5	1021,4	58,1	13,8
56	d07f24Cab12_C2bis_D2_STAT_60	4/12/17 15:16	300	Cabrinha2	12	50	BCK	NO	310,3	5,9	279,0	1,2	328,9	328,8	1,4	-3,1	225,2	0,21	89,6	63,7	26,3	-3,4	NaN	111,9	18,8	1021,3	56,5	13,9
57	d07f25Cab12_C2bis_D2_120	4/12/17 15:25	299	Cabrinha2	12	50	BCK	NO	111,5	6,9	287,3	4,0	168,9	175,9	3,4	-0,2	1521,4	0,27	657,8	-50,2	36,9	1,6	NaN	2683,2	126,8	1021,3	59,8	13,6
58	d08f1Cab12_C2bis_D2_180	4/13/17 13:40	298	Cabrinha2	12	50	BCK	NO	178,6	5,1	268,7	2,6	76,7	90,2	2,2	1,6	421,7	0,23	336,2	1,4	34,5	-0,7	NaN	856,9	35,1	1019,9	62,4	12,0
59	d08f2Cab12_C2bis_D2_MANDYN_M60	4/13/17 13:51	302	Cabrinha2	12	50	BCK	NO	299,1	5,7	253,7	2,0	332,9	314,6	2,3	5,8	592,9	0,24	172,6	70,6	22,8	-3,1	NaN	333,4	49,4	1019,7	62,7	11,7
60	d08f3Cab12_C2bis_D2_MANDYN_60	4/13/17 13:59	303	Cabrinha2	12	50	BCK	NO	64,7	5,2	267,8	1,9	203,5	203,1	1,8	-2,4	839,7	0,25	226,0	-71,0	25,8	2,3	NaN	440,4	70,0	1019,9	63,3	11,8
61	d08f4Cab12_C2bis_D2_MANDYN_70	4/13/17 14:05	294	Cabrinha2	12	50	BCK	NO	71,1	5,0	262,4	2,2	191,4	191,3	1,9	-3,1	963,7	0,25	302,1	-68,7	23,7	3,4	NaN	667,2	80,3	1019,8	63,8	11,8
62	d08f5Cab12_C2bis_D2_MANDYN_M70	4/13/17 14:12	295	Cabrinha2	12	50	BCK	NO	291,8	5,7	248,1	2,2	332,8	316,3	2,4	6,6	705,0	0,24	221,0	69,1	23,1	-3,2	NaN	470,2	58,7	1019,6	63,7	11,8
63	d08f6Cab12_C2bis_D2_MANDYN_65	4/13/17 14:20	284	Cabrinha2	12	50	BCK	NO	66,0	5,3	266,4	2,0	197,2	200,4	1,9	-1,4	730,3	0,25	243,5	-67,4	25,5	1,9	NaN	503,5	60,9	1019,6	63,2	11,8
64	d08f7Cab12_C2bis_D2_MANDYN_M55_court	4/13/17 14:27	169	Cabrinha2	12	50	BCK	NO	305,4	5,6	258,9	1,4	332,5	313,5	2,2	4,2	474,3	0,25	111,9	75,6	21,6	-1,6	NaN	162,2	39,5	1019,5	63,1	11,7
65	d08f8Cab12_C2bis_D2_180	4/13/17 15:01	297	Cabrinha2	12	50	BCK	NO	177,5	4,9	272,9	2,6	89,3	95,4	2,0	1,6	404,1	0,21	313,2	-1,0	36,3	-1,1	NaN	812,1	33,7	1019,3	63,4	12,3
66	d08f9Cab12_C2bis_D2_DL_180	4/13/17 15:17	296	Cabrinha2	12	50	BCK	NO	175,8	4,6	266,8	2,5	79,9	91,0	2,1	1,8	398,5	0,22	326,0	0,8	30,7	-1,4	NaN	806,8	33,2	1019,1	62,3	12,4
67	d08f10Cab12_C2bis_D2_160	4/13/17 15:42	308	Cabrinha2	12	50	BCK	NO	160,0	5,3	280,4	2,6	111,2	120,4	2,3	1,6	434,6	0,22	341,4	-6,9	34,0	-1,1	NaN	895,1	36,2	1018,9	62,8	12,2
68	d08f11Cab12_C2bis_D2_140	4/13/17 15:47	297	Cabrinha2	12	50	BCK	NO	140,7	5,1	281,8	2,4	132,8	141,1	2,2	0,7	489,8	0,22	333,2	-24,6	35,4	0,0	NaN	809,3	40,8	1018,9	63,1	12,1
69	d08f12Cab12_C2bis_D2_M140	4/13/17 16:05	296	Cabrinha2	12	50	BCK	NO	224,4	4,8	287,9	2,5	66,8	63,5	2,1	2,9	478,7	0,22	288,0	32,6	36,9	-3,8	NaN	720,9	39,9	1018,6	64,5	12,0
70	d08f13Cab12_C2bis_D2_M160	4/13/17 16:14	277	Cabrinha2	12	50	BCK	NO	191,3	4,3	291,5	2,4	93,7	100,2	2,1	1,9	383,2	0,23	309,1	10,3	31,4	-2,6	NaN	747,2	31,9	1018,6	64,0	12,2
71	d08f14Cab12_C2bis_D2_MANDYN_M90	4/13/17 16:23	205	Cabrinha2	12	50	BCK	NO	289,2	5,0	273,9	2,1	352,9	344,7	2,2	2,3	634,2	0,23	218,3	66,3	19,2	-6,0	NaN	456,5	52,8	1018,4	64,8	11,9
72	d09f5Cab12_C1bis_180	4/18/17 13:43	307	Cabrinha2	12	50	BCK	NO	178,4	5,0	56,9	3,3	235,4	238,5	2,6	2,1	635,4	0,27	520,1	2,5	32,7	-1,7	NaN	1750,9	53,0	1027,5	50,3	14,4
73	d09f6Cab12_C1bis_MANDYN_M90_COURT	4/18/17 13:51	143	Cabrinha2	12	50	BCK	NO	268,7	3,5	100,3	2,4	181,1	191,7	2,3	4,0	765,4	0,25	281,9	58,0	39,0	-6,2	NaN	705,5	63,8	1027,6	52,5	14,1
74	d09f7Cab12_C1bis_M120_FAIL	4/18/17 15:00	252	Cabrinha2	12	50	BCK	NO	243,4	6,5	55,5	2,4	176,8	171,8	1,9	-1,5	NaN	NaN	NaN	43,7	41,7	-9,5	NaN	NaN	NaN	1027,2	48,9	14,5
75	d09f8Cab12_C1bis_M140	4/18/17 15:04	303	Cabrinha2	12	50	BCK	NO	210,4	5,8	62,1	3,2	203,9	211,7	3,0	4,4	NaN	NaN	NaN	24,4	37,0	-6,5	NaN	NaN	NaN	1027,2	52,2	14,3
76	d09f9Cab12_C1bis_140	4/18/17 15:11	294	Cabrinha2	12	50	BCK	NO	142,9	6,1	54,2	3,2	273,4	271,4	2,4	0,2	NaN	NaN	NaN	-22,2	34,8	0,8	NaN	NaN	NaN	1027,3	51,5	14,2
77	d10f2Bts_C2bis_D2_180	4/19/17 12:46	282	BTS	5	50	BCK	NO	178,6	6,0	69,9	2,4	250,7	251,3	1,9	1,5	293,7	0,39	262,4	0,7	20,9	-1,3	168,8	636,9	58,7	1032,5	46,4	12,0
78	d10f3Bts_C2bis_D2_140	4/19/17 12:57	303	BTS	5	50	BCK	NO	144,6	6,1	77,0	2,3	291,4	292,4	1,9	0,4	352,6	0,39	266,9	-18,9	29,7	1,8	168,0	602,8	70,5	1032,4	47,1	12,0
79	d10f4Bts_C2bis_MANSTAT_80	4/19/17 14:17	295	BTS	5	50	BCK	NO	84,2	6,9	69,1	1,8	340,3	345,0	1,7	-0,2	420,0	0,40	165,1	-60,6	30,0	2,9	215,7	293,6	84,0	1031,8	45,0	12,8
80	d10f5Bts_C2bis_D2_MANSTAT_M80	4/19/17 14:23	350	BTS	5	50	BCK	NO	282,3	4,9	77,6	0,8	162,0	155,4	1,8	2,8	222,8	0,39	46,2	75,1	28,4	-5,6	302,4	38,5	44,6	1031,8	43,7	12,8
81	d10f6Bts_C2bis_D2_120	4/19/17 14:32	341	BTS	5	50	BCK	NO	124,2	5,8	70,5	2,1	305,0	306,3	1,8	-0,4	413,4	0,40	216,6	-41,4	35,8	2,2	191,5	468,0	82,7	1031,8	46,3	12,9
82	d10f7Bts_C2bis_D2_100	4/19/17 14:46	350	BTS	5	50	BCK	NO	103,0	6,4	69,7	1,9	321,9	326,7	1,7	-1,6	597,4	0,40	194,7	-59,3	37,4	3,8	215,9	378,2	119,5	1031,6	46,4	13,0
83	d10f8Bts_C2bis_D2_M140	4/19/17 15:20	350	BTS	5	50	BCK	NO	219,8	7,2	74,2	2,8	209,0	214,4	2,4	3,2	514,3	0,38	365,5	23,4	31,1	-5,5	133,9	1019,5	102,9	1031,4	43,6	13,3
84	d10f9Bts_C2bis_D2_MANDYN_80	4/19/17 15:32	307	BTS	5	50	BCK	NO	84,9	6,2	64,2	1,9	337,0	339,2	1,8	-0,3	477,0	0,45	197,7	-61,1	24,0	3,3	369,9	366,6	95,4	1031,2	44,3	13,4
85	d10f10Bts_C2bis_D2_100	4/19/17 15:46	295	BTS	5	50	BCK	NO	263,4	6,0	79,8	1,8	166,1	176,4	2,2	5,1	531,3	0,38	195,3	58,7	30,1	-6,8	195,1	347,6	106,3	1031,1	44,1	13,4
86	d10f11Bts_C2bis_D2_160	4/19/17 15:52	312	BTS	5	50	BCK	NO	159,2	5,5	60,5	2,0	263,6	261,3	2,0	1,8	253,9	0,41	200,2	-4,2	34,5	-1,6	133,6	407,4	50,8	1031,2	44,0	13,5
87	d11f1Bts_C2bis_D2_180	4/20/17 12:00	296	BTS	5	50	BCK	NO	179,0	6,2	64,4	2,1	242,5	245,4	1,8	2,2	221,9	0,37	178,5	2,6	32,0	-1,5	171,0	367,2	44,4	1034,3	41,6	10,8
88	d11f2Bts_C2bis_D2_DL_180	4/20/17 12:30	296	BTS	5	50	BCK	NO	178,9	6,2	56,5	2,2	233,4	237,6	1,9	2,2	256,0	0,37	204,9	0,1	33,1	-0,8	181,8	441,1	51,2	1034,2	41,1	11,2
89	d11f3Bts_C2bis_D2_M160	4/20/17 13:09	293	BTS	5	50	BCK	NO	198,9	6,8	65,2	2,5	221,1	226,3	2,0	2,6	336,9	0,38	256,7	3,4	36,9	-3,3	129,9	644,9	67,4	1033,8	40,6	11,8
90	d11f4Bts_C2bis_D2_100	4/20/17 13:24	302	BTS	5	50	BCK	NO	106,1	6,3	69,0	2,0	320,7	322,9	1,8	0,0	444,5	0,40	215,7	-49,2	33,8	2,9	191,0	431,9	88,9	1033,7	40,0	11,9
91	d11f5Bts_C2bis_D2_M100	4/20/17 13:33	299	BTS	5	50	BCK	NO	262,0	5,0	81,9	1,6	171,9	179,9	2,1	4,4	396,5	0,39	122,3	64,0	33,5	-5,3	211,0	199,6	79,3	1033,6	41,7	11,9
92	d11f6Bts_C2bis_D2_M140	4/20/17 13:38	301	BTS	5	50	BCK	NO	217,7	6,7	72,3	2,6	206,2	214,6	2,2	3,8	400,5	0,39	277,6	23,7	36,2	-5,0	159,6	706,3	80,1	1033,5	41,9	12,0
93	d11f7Bts_C2bis_D2_L80_180	4/20/17 14:22	295	BTS	5	80	BCK	NO	176,1	5,9	63,1	2,5	243,2	247,0	2,0	2,3	322,0	0,40	266,7	-1,2	32,7	1,1	176,1	659,5	64,4	1033,2	44,8	12,7
94	d11f8Bts_C2bis_D2_L80_100	4/20/17 14:30	298	BTS	5	80	BCK	NO	105,0	6,8	69,0	2,4	320,2	324,0	1,9	-1,5	784,7	0,42	330,1	-56,7	34,9	7,8	262,8	806,9	156,9	1032,9	40,8	12,6
95	d11f9Bts_C2bis_D2_L80_M100	4/20/17 14:40	301	BTS	5	80	BCK	NO	263,9	4,8	91,6	1,8	180,2	187,7	2,0	3,8	382,1	0,41	142,0	61,8	29,6	-1,8	313,3	258,8	76,4	1032,9	40,3	12,6
96	d11f10Bts_C2bis_D2_L80_MANDYN_80	4/20/17 14:47	299	BTS	5	80	BCK	NO	84,8	6,1	79,1	2,0	348,6	354,3	1,7	-1,5	646,9	0,43	237,8	-64,7	23,1	6,5	187,0	492,2	129,4	1032,7	41,0	12,8
97	d11f11Bts_C2bis_D2_L80_MANDYN_60	4/20/17 14:53	300	BTS	5	80	BCK	NO	66,0	6,6	88,1	1,6	14,2	22,1	1,7	-1,5	627,2	0,43	161,0	-72,9	19,1	6,1	225,4	265,1	125,4	1032,6	41,8	12,8
98	d11f12Bts_C2bis_D2_L80_MANDYN_M80	4/20/17 15:08	296	BTS	5	80	BCK	NO	285,3	6,6	86,0	1,8	161,2	160,8	2,1	0,4	635,5	0,40	181,9	70,8	22,0	-4,4	270,7	337,5	127,1	1032,5	43,0	12,9
99	d11f13Bts_C2bis_D2_L80_MANDYN_M60	4/20/17 15:16	298	BTS	5	80	BCK	NO	303,9	6,3	76,9	1,0	154,9	132,9	1,9	-0,3	510,5	0,42	80,4	79,5	18,1	0,6	225,8	78,2	102,1	1032,4	43,1	13,0
100	d11f14Cab12_C2bis_D2_L80_MANSTAT_60	4/20/17 15:54	298	Cabrinha2	12	80	BCK	NO	54,7	7,6	79,6	1,4	18,1	24,9	1,8	-0,4	315,9	0,22	156,9	-58,2	17,1	1,9	110,9	219,8	26,3	1032,1	43,2	13,2
101	d11f15Cab12_C2bis_D2_L80_MANSTAT_M60	4/20/17 16:01	309	Cabrinha2	12	80	BCK	NO	316,1	7,3	91,1	1,0	139,3	135,0	2,0	2,9	278,7	0,21	107,7	66,3	14,1	-1,9	110,1	102,8	23,2	1032,0	43,6	13,3
102	d11f16Cab12_C2bis_D2_L80_MANDYN_140_RETOUR	4/20/17 16:11	174	Cabrinha2	12	80	BCK	NO	147,2	6,4	75,8	4,8	293,4	288,5	5,0	-2,7	1468,4	0,26	988,7	-40,2	23,0	2,6	348,2	4690,0	122,4	1032,1	41,8	13,4
103	d11f17Cab12_C2bis_D2_L80_MANDYN_100_RETOUR	4/20/17 16:17	256	Cabrinha2	12	80	BCK	NO	106,2	6,2	79,1	4,2	332,6	332,8	4,6	-1,3	1628,4	0,33	816,9	-52,3	22,0	3,5	403,8	3403,5	135,7	1032,0	42,4	13,4

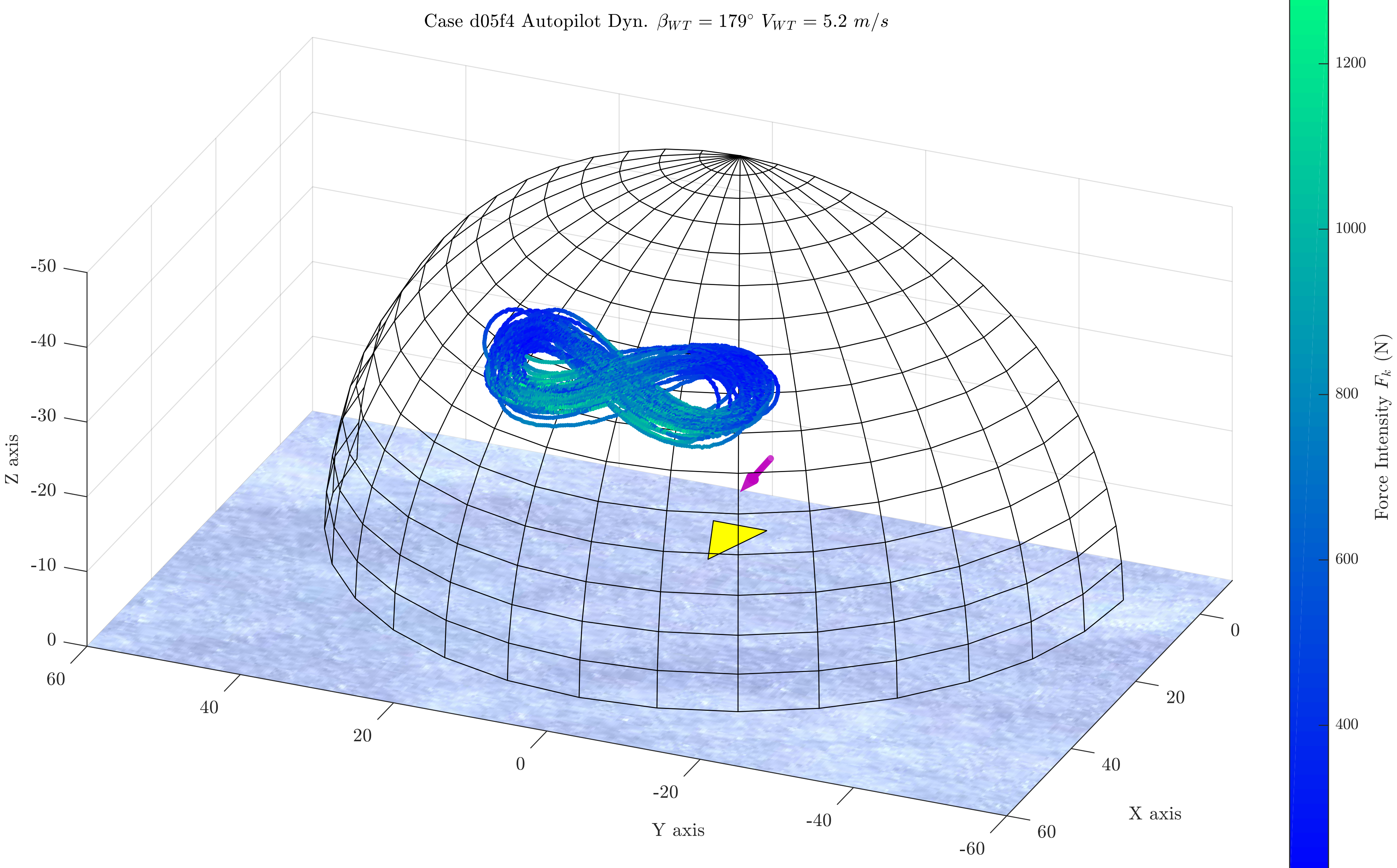
Case d05f4 Autopilot Dyn. $\beta_{WT} = 179^\circ$ $V_{WT} = 5.2\ m/s$
Z axis
-50
-40
-30
-20
-10
0
60
40
20
0
-20
-40
-60
Y axis
0
20
40
60
X axis
Force Intensity F_k (N)
1200
1000
800
600
400
200

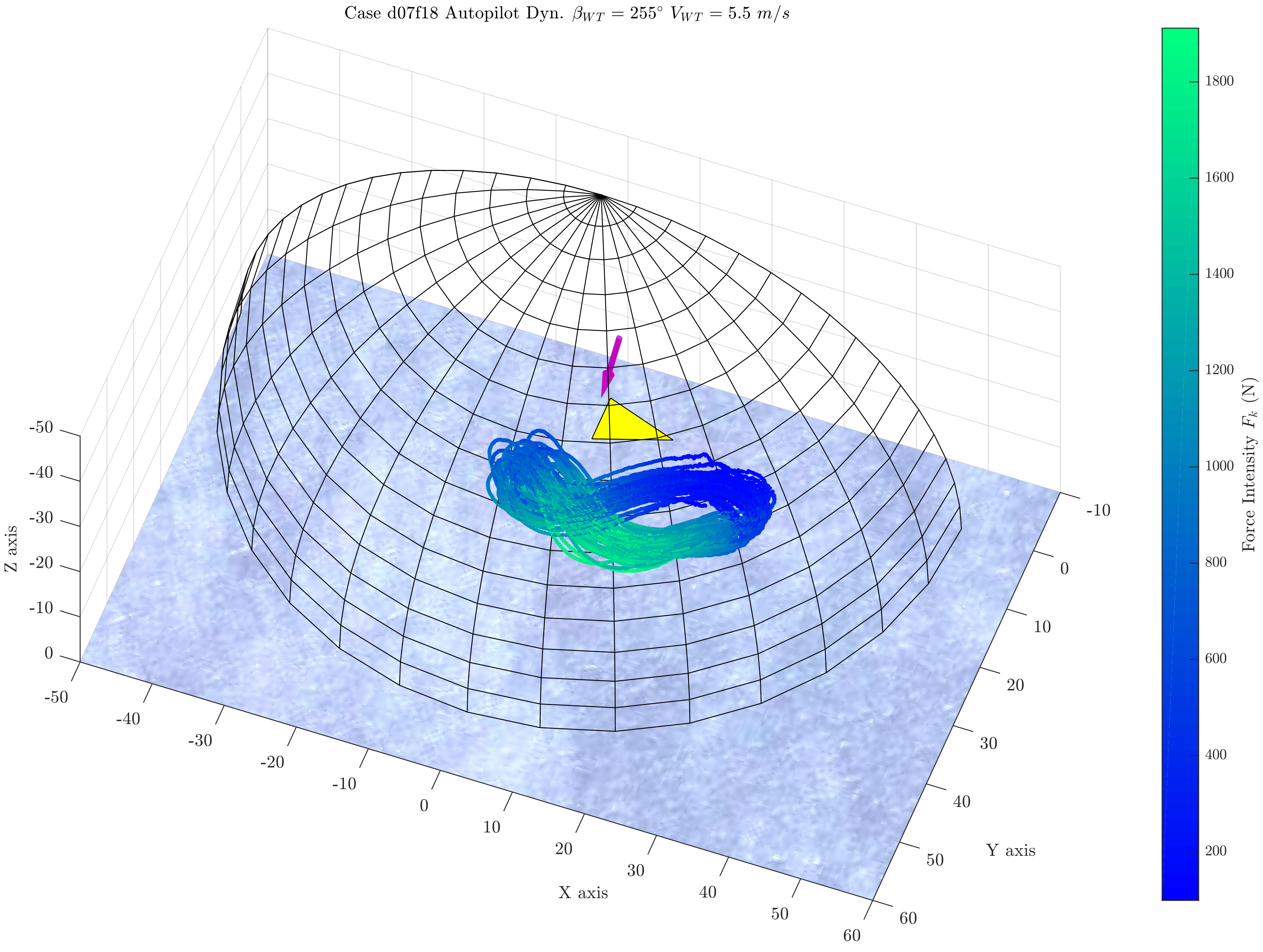

Case d07f18 Autopilot Dyn. $\beta_{WT} = 255° \; V_{WT} = 5.5 \; m/s$

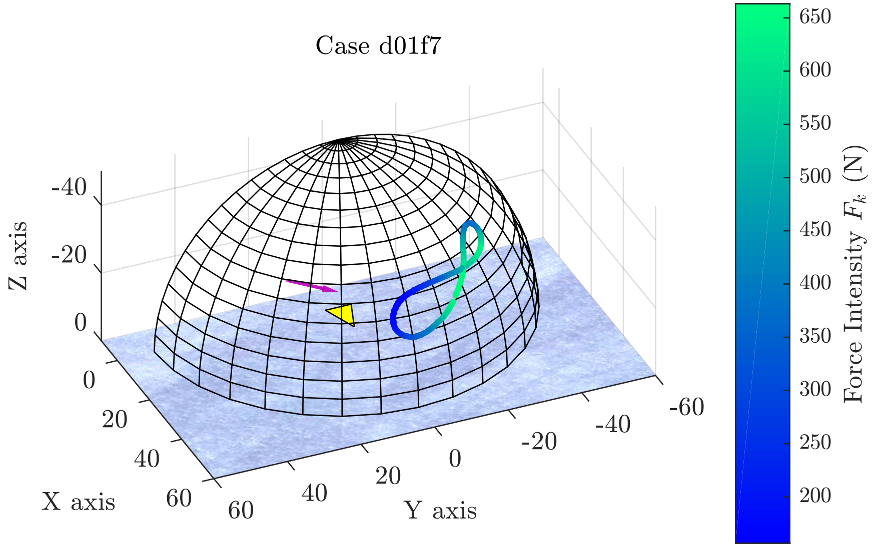
Case d01f7
Z axis
-40
-20
0
X axis
0
20
40
60
Y axis
60
40
20
0
-20
-40
-60
Force Intensity F_k (N)
650
600
550
500
450
400
350
300
250
200

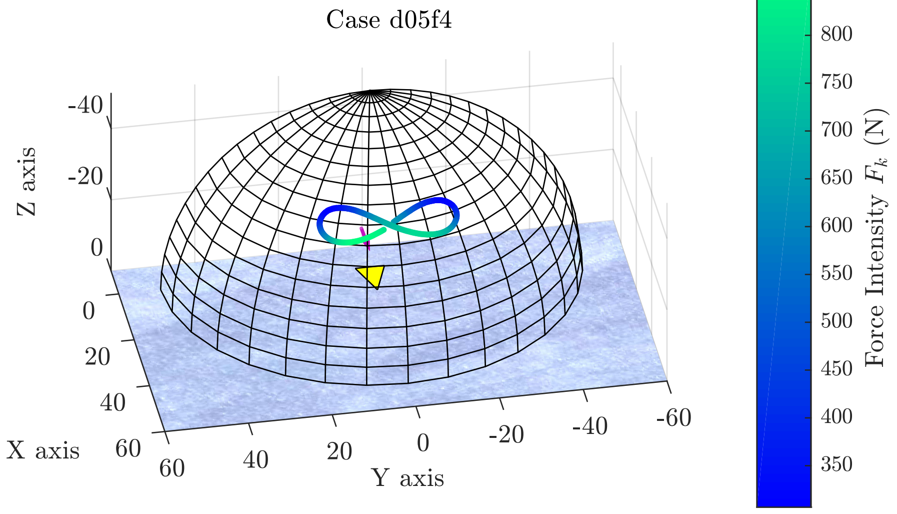
Case d05f4
Z axis
-40
-20
0
X axis
0
20
40
60
Y axis
60
40
20
0
-20
-40
-60
Force Intensity F_k (N)
850
800
750
700
650
600
550
500
450
400
350

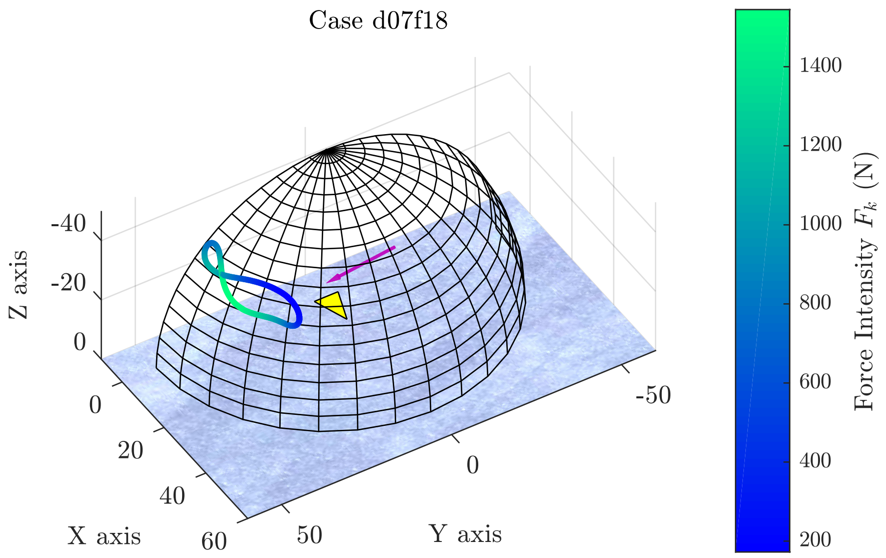
Case d07f18
Z axis
-40
-20
0
X axis
0
20
40
60
Y axis
50
0
-50
Force Intensity F_k (N)
1400
1200
1000
800
600
400
200

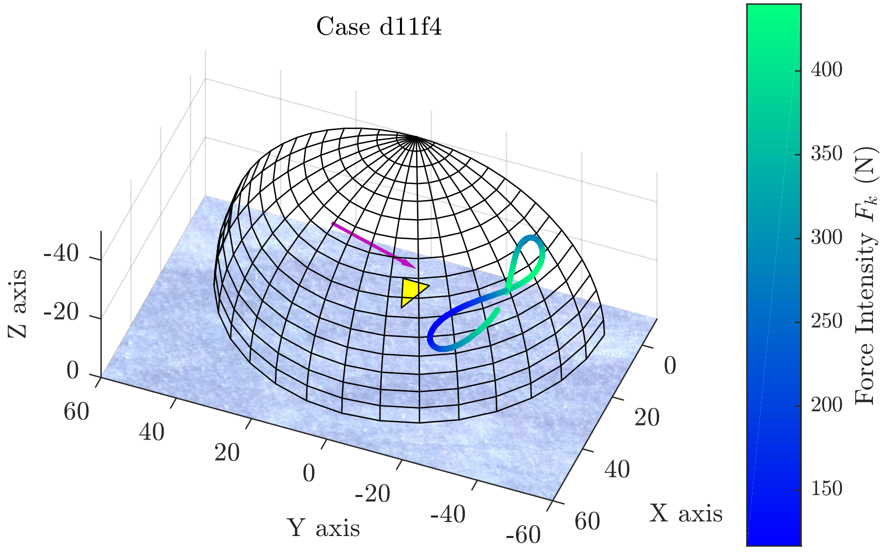
Case d11f4
Z axis
-40
-20
0
Y axis
60
40
20
0
-20
-40
-60
X axis
0
20
40
60
Force Intensity F_k (N)
400
350
300
250
200
150

D. Uncertainty Calculation Details

D.1. Elementary Equations

$$\forall\, \underline{X} \in \mathbb{R}^3,\ d\|\underline{X}\| = d\left(\sqrt{\underline{X}\cdot\underline{X}}\right) = \frac{2\underline{X}\cdot d\underline{X}}{2\sqrt{\underline{X}\cdot\underline{X}}} = \frac{\underline{X}\cdot d\underline{X}}{\|\underline{X}\|}$$

$$\forall\, \underline{X} \in \mathbb{R}^3,\ d\frac{1}{\|\underline{X}\|} = d\left(\frac{1}{\sqrt{\underline{X}\cdot\underline{X}}}\right) = -\frac{2\underline{X}\cdot d\underline{X}}{2\sqrt{\underline{X}\cdot\underline{X}}}\,\frac{1}{\|\underline{X}\|^2} = -\frac{\underline{X}\cdot d\underline{X}}{\|\underline{X}\|^3}$$

$$\forall\, \underline{X},\underline{Y},\underline{Z} \in \mathbb{R}^3,\ (\underline{X}\cdot\underline{Y})\underline{Z} = (\underline{X}^T\underline{Y})\underline{Z} = \underline{Z}(\underline{X}^T\underline{Y}) = (\underline{Z}\,\underline{X}^T)\underline{Y} = \underline{\underline{D}}(\underline{Z},\underline{X})\underline{Y}$$

$$\underline{\underline{D}}(\underline{Z},\underline{X}) = \underline{Z}\,\underline{X}^T$$

D.2. Lift

$$\|\underline{L}\| = \|\underline{F}_a - \underline{D}\|$$

$$\ln(\|\underline{L}\|) = \frac{1}{2}\ln((\underline{F}_a - \underline{D})^2)$$

$$d\ \ln(\|\underline{L}\|) = \frac{2\cdot(\underline{F}_a - \underline{D})\cdot(d\underline{F}_a - d\underline{D})}{2\,\|\,\underline{F}_a - \underline{D}\,\|^2} = \frac{\underline{L}\cdot(d\underline{F}_a - d\underline{D})}{\|\,\underline{L}\,\|^2}$$

$$d\ \ln(\|\underline{L}\|) = \frac{d\|\underline{L}\|}{\|\underline{L}\|} = \frac{1}{\|\underline{L}\|^2}(\underline{L}\cdot d\underline{F}_a - \underline{L}\cdot d\underline{D})$$

D.3. Drag

$$\underline{D} = (\underline{F}_a \cdot \underline{x}_a)\underline{x}_a$$

$$\|\underline{D}\| = |\underline{F}_a \cdot \underline{x}_a| = \underline{F}_a \cdot \underline{x}_a$$

$$d\ \ln(\|\underline{D}\|) = \frac{d\|\underline{D}\|}{\|\underline{D}\|} = \frac{1}{\|\underline{D}\|}(\underline{x}_a \cdot d\underline{F}_a + d\underline{x}_a \cdot \underline{F}_a)$$

$$\begin{aligned} d\underline{D} &= (\underline{x}_a \cdot d\underline{F}_a + d\underline{x}_a \cdot \underline{F}_a)\underline{x}_a + (\underline{F}_a \cdot \underline{x}_a)d\underline{x}_a \\ &= \underline{x}_a \underline{x}_a^T d\underline{F}_a + (\underline{x}_a \underline{F}_a^T + \underline{x}_a \cdot \underline{F}_a \underline{\underline{I}}_{\mathbb{R}^3})d\underline{x}_a \end{aligned}$$

D.4. Aerodynamic Force

Assumptions: Zero-mass model and straight lines with constant length: $\underline{F}_a = \frac{\underline{F}_f}{\|\underline{F}_f\|}(\|\underline{F}_f\| + F_{bl} + F_{br})$

$$\begin{aligned} d\underline{F}_a = &-\frac{\underline{F}_f \cdot d\underline{F}_f}{\|\underline{F}_f\|^3}\underline{F}_f(\|\underline{F}_f\| + F_{bl} + F_{br}) \\ &+ \frac{1}{\|\underline{F}_f\|}d\underline{F}_f(\|\underline{F}_f\| + F_{bl} + F_{br}) \\ &+ \frac{1}{\|\underline{F}_f\|}\underline{F}_f\left(\frac{\underline{F}_f \cdot d\underline{F}_f}{\|\underline{F}_f\|} + dF_{bl} + dF_{br}\right) \end{aligned}$$

$$\begin{aligned} d\underline{F}_a = &\left(-\frac{(\|\underline{F}_f\| + F_{bl} + F_{br})}{\|\underline{F}_f\|^2}\underline{F}_f\underline{F}_f^T + (\|\underline{F}_f\| + F_{bl} + F_{br})\underline{\underline{I}}_{\mathbb{R}^3} + \frac{1}{\|\underline{F}_f\|}\underline{F}_f\underline{F}_f^T\right)\frac{d\underline{F}_f}{\|\underline{F}_f\|} \\ &+ \frac{\underline{F}_f}{\|\underline{F}_f\|}dF_{bl} + \frac{\underline{F}_f}{\|\underline{F}_f\|}dF_{br} \end{aligned}$$

$$
\begin{aligned}
d\underline{F}_a &= \overbrace{\left((-\frac{(F_{bl}+F_{br})}{\|\underline{F}_f\|^2}\underline{F}_f\underline{F}_f^T + (\|\underline{F}_f\|+F_{bl}+F_{br})\underline{\underline{I}}_{\mathbb{R}^3})\right)}^{\underline{\underline{\alpha}}}\frac{d\underline{F}_f}{\|\underline{F}_f\|} + \frac{\underline{F}_f}{\|\underline{F}_f\|}dF_{bl} + \frac{\underline{F}_f}{\|\underline{F}_f\|}dF_{br} \\
&= \frac{\underline{\underline{\alpha}}}{\|\underline{F}_f\|}d\underline{F}_f + \frac{\underline{F}_f}{\|\underline{F}_f\|}dF_{bl} + \frac{\underline{F}_f}{\|\underline{F}_f\|}dF_{br}
\end{aligned}
$$

D.5. Front Tether Force

$$
\underline{F}_f = \underline{\underline{M}}_{\theta_s}\underline{\underline{M}}_{\phi_s}\underline{F}_m^{(s)}
$$

$$
\begin{aligned}
d\underline{F}_f &= d\underline{\underline{M}}_{\theta_s}\underline{\underline{M}}_{\phi_s}\underline{F}_m^{(s)} + \underline{\underline{M}}_{\theta_s}d\underline{\underline{M}}_{\phi_s}\underline{F}_m^{(s)} + \underline{\underline{M}}_{\theta_s}\underline{\underline{M}}_{\phi_s}d\underline{F}_m^{(s)} \\
&= \frac{\partial\underline{\underline{M}}_{\theta_s}}{\partial\theta_s}\underline{\underline{M}}_{\phi_s}\underline{F}_m^{(s)}d\theta_s + \underline{\underline{M}}_{\theta_s}\frac{\partial\underline{\underline{M}}_{\phi_s}}{\partial\phi_s}\underline{F}_m^{(s)}d\phi_s + \underline{\underline{M}}_{\theta_s}\underline{\underline{M}}_{\phi_s}F_m\frac{d\underline{F}_m^{(s)}}{F_m}
\end{aligned}
$$

$$
\frac{\partial\underline{\underline{M}}_{\theta_s}}{\partial\theta_s} = \begin{pmatrix} -\sin(\theta_s) & 0 & \cos(\theta_s) \\ 0 & 0 & 0 \\ -\cos(\theta_s) & 0 & -\sin(\theta_s) \end{pmatrix}
$$

$$
\frac{\partial\underline{\underline{M}}_{\phi_s}}{\partial\phi_s} = \begin{pmatrix} 0 & 0 & 0 \\ 0 & -\sin(\phi_s) & -\cos(\phi_s) \\ 0 & \cos(\phi_s) & -\sin(\phi_s) \end{pmatrix}
$$

D.6. Apparent Wind Vector

$$
\begin{aligned}
d\underline{x}_a &= d\left(\frac{\underline{V}_a}{\|\underline{V}_a\|}\right) = \frac{d\underline{V}_a}{\|\underline{V}_a\|} - \frac{d\underline{V}_a\cdot\underline{V}_a}{\|\underline{V}_a\|^3}\underline{V}_a \\
&= \left(\underline{\underline{I}}_{\mathbb{R}^3} - \frac{1}{\|\underline{V}_a\|^2}\underline{V}_a\underline{V}_a^T\right)\frac{d\underline{V}_a}{\|\underline{V}_a\|} \\
&= \left(\underline{\underline{I}}_{\mathbb{R}^3} - \underline{x}_a\underline{x}_a^T\right)\frac{1}{\|\underline{V}_a\|}d\underline{V}_a
\end{aligned}
$$

$$
\underline{V}_{WT} = (\underline{\underline{M}}_{\psi_{ws}}\underline{\underline{M}}_{\theta_{ws}}\underline{\underline{M}}_{\phi_{ws}})V_{WM}^{(ws)}
$$

θ_{WS} and $\phi_{WS}$are not considered here and thus taken equal to 0.

$$\begin{aligned} d\underline{V}_a &= d\underline{V}_{WT} - d\underline{V}_k \\ &= \frac{\partial \underline{\underline{M}}_{\psi_{WS}}}{\partial \psi_{ws}} \underline{V}_{WM}^{(ws)} d\psi_{ws} + V_{WM} \underline{\underline{M}}_{\psi_{ws}} \frac{d\underline{V}_{WM}^{(ws)}}{V_{WM}} - d\underline{V}_k \end{aligned}$$

$$\frac{\partial \underline{\underline{M}}_{\psi_{WS}}}{\partial \psi_{ws}} = \begin{pmatrix} -\sin(\psi_{ws}) & -\cos(\psi_{ws}) & 0 \\ \cos(\psi_{ws}) & -\sin(\psi_{ws}) & 0 \\ 0 & 0 & 0 \end{pmatrix}$$

D.7. Kite Position Vector

$\underline{P}_k = \frac{\underline{F}_f}{\|\underline{F}_f\|} L_t = \underline{x}_k L_t$

$$\begin{aligned} d\underline{P}_k &= -\frac{\underline{F}_f \cdot d\underline{F}_f}{\|\underline{F}_f\|^3} \underline{F}_f L_t + \frac{d\underline{F}_f}{\|\underline{F}_f\|} L_t \\ &= L_t \left(\underline{\underline{I}}_{\mathbb{R}^3} - \frac{\underline{F}_f \underline{F}_f^T}{\|\underline{F}_f\|^2} \right) \frac{d\underline{F}_f}{\|\underline{F}_f\|} \\ &= L_t \left(\underline{\underline{I}}_{\mathbb{R}^3} - \underline{x}_k \underline{x}_k^T \right) \frac{1}{\|\underline{F}_f\|} d\underline{F}_f \end{aligned}$$

$$\begin{aligned} d\underline{P}_k = L_t \left(\underline{\underline{I}}_{\mathbb{R}^3} - \underline{x}_k \underline{x}_k^T \right) \frac{1}{\|\underline{F}_f\|} \\ * \left(\frac{\partial \underline{\underline{M}}_{\theta_s}}{\partial \theta_s} \underline{\underline{M}}_{\phi_s} \underline{F}_m^{(s)} d\theta_s + \underline{\underline{M}}_{\theta_s} \frac{\partial \underline{\underline{M}}_{\phi_s}}{\partial \phi_s} \underline{F}_m^{(s)} d\phi_s + \underline{\underline{M}}_{\theta_s} \underline{\underline{M}}_{\phi_s} F_m \frac{d\underline{F}_m^{(s)}}{F_m} \right) \end{aligned}$$

$$d\underline{P}_k = \underline{p}_1 d\theta_s + \underline{p}_2 d\phi_s + \underline{\underline{p}}_3 \frac{d\underline{F}_m^{(s)}}{F_m}$$

With:
$\underline{p}_1 = L_t \left(\underline{\underline{I}}_{\mathbb{R}^3} - \underline{x}_k \underline{x}_k^T \right) \frac{1}{\|\underline{F}_f\|} \frac{\partial \underline{\underline{M}}_{\theta_s}}{\partial \theta_s} \underline{\underline{M}}_{\phi_s} \underline{F}_m^{(s)}$
$\underline{p}_2 = L_t \left(\underline{\underline{I}}_{\mathbb{R}^3} - \underline{x}_k \underline{x}_k^T \right) \frac{1}{\|\underline{F}_f\|} \underline{\underline{M}}_{\theta_s} \frac{\partial \underline{\underline{M}}_{\phi_s}}{\partial \phi_s} \underline{F}_m^{(s)}$
$\underline{\underline{p}}_3 = L_t \left(\underline{\underline{I}}_{\mathbb{R}^3} - \underline{x}_k \underline{x}_k^T \right) \underline{\underline{M}}_{\theta_s} \underline{\underline{M}}_{\phi_s}$ because $\|\underline{F}_f\| = \|\underline{F}_m\| = F_m\|$

D.8. Kite Velocity vector

The kite velocity vector $\underline{V}_k$ is obtained by finite difference on kite position $\underline{P}_k$. Thus, for all $i \in [\![0, 3]\!]$ $|\Delta V_{k,i}| \leqslant \frac{2}{\Delta t} |\Delta P_{k,i}|$.

$$
\begin{aligned}
|\Delta V_{k,i}| &= \frac{2}{\Delta t} \left| p_{1,i} \Delta\theta_s + p_{2,i} \Delta\phi_s + \left(\underline{\underline{p}}_3 \frac{\Delta \underline{F}_m^{(s)}}{F_m} \right)_i \right| \\
&\leqslant \frac{2}{\Delta t} \left[|p_{1,i} \Delta\theta_s| + |p_{2,i} \Delta\phi_s| + \left| \left(\underline{\underline{p}}_3 \frac{\Delta \underline{F}_m^{(s)}}{F_m} \right)_i \right| \right] \\
&\leqslant \frac{2}{\Delta t} \left[|p_{1,i} \Delta\theta_s| + |p_{2,i} \Delta\phi_s| + \sum_{j=1}^{3} |p_{3,ij}| \left| \frac{\Delta F_{m,j}^{(s)}}{F_m} \right| \right]
\end{aligned}
$$

D.9. Lift to Drag ratio

$$
f = \frac{\|\underline{L}\|}{\|\underline{D}\|}
$$

$$
\frac{df}{f} = \frac{d\|\underline{L}\|}{\|\underline{L}\|} - \frac{d\|\underline{D}\|}{\|\underline{D}\|}
$$

$$
\begin{aligned}
\frac{df}{f} &= \frac{d\|\underline{L}\|}{\|\underline{L}\|} - \frac{d\|\underline{D}\|}{\|\underline{D}\|} \\
&= \frac{1}{\|\underline{L}\|^2} (\underline{L} \cdot d\underline{F}_a - \underline{L} \cdot d\underline{D}) - \frac{1}{\|\underline{D}\|} (\underline{x}_a \cdot d\underline{F}_a + d\underline{x}_a \cdot \underline{F}_a) \\
&= \frac{1}{\|\underline{L}\|^2} \left(\underline{L} \cdot d\underline{F}_a - \underline{L} \cdot \left(\underline{x}_a \underline{x}_a^T d\underline{F}_a + (\underline{x}_a \underline{F}_a^T + \underline{x}_a \cdot \underline{F}_a \underline{\underline{I}}_{\mathbb{R}^3}) d\underline{x}_a \right) \right) \\
&\quad - \frac{1}{\|\underline{D}\|} (\underline{x}_a \cdot d\underline{F}_a + d\underline{x}_a \cdot \underline{F}_a)
\end{aligned}
$$

$$\begin{aligned}\frac{df}{f} = &\overbrace{\left[\frac{\underline{L}^T}{\|\underline{L}\|^2}\left(\underline{\underline{I}}_{\mathbb{R}^3} - \underline{x}_a \underline{x}_a^T\right) - \frac{1}{\|\underline{D}\|}\underline{x}_a^T\right]}^{\underline{\beta}^T} d\underline{F}_a \\ &\underbrace{+ \left[-\frac{\underline{L}^T}{\|\underline{L}\|^2}(\underline{x}_a \underline{F}_a^T + \underline{x}_a \cdot \underline{F}_a \underline{\underline{I}}_{\mathbb{R}^3}) - \frac{1}{\|\underline{D}\|}\underline{F}_a^T\right]}_{\underline{\gamma}^T} d\underline{x}_a\end{aligned}$$

$$\frac{df}{f} = \underline{\beta}^T d\underline{F}_a + \underline{\gamma}^T d\underline{x}_a$$

$$\frac{df}{f} = \underline{\beta}^T \left(\frac{\underline{\underline{\alpha}}}{\|\underline{F}_f\|} d\underline{F}_f + \frac{\underline{F}_f}{\|\underline{F}_f\|} dF_{bl} + \frac{\underline{F}_f}{\|\underline{F}_f\|} dF_{br}\right) + \underline{\gamma}^T \left(\underline{\underline{I}}_{\mathbb{R}^3} - \underline{x}_a \underline{x}_a^T\right) \frac{1}{\|\underline{V}_a\|} d\underline{V}_a$$

$$\begin{aligned}\frac{df}{f} = &\underline{\beta}^T \frac{\underline{F}_f}{\|\underline{F}_f\|} F_{bl} \frac{dF_{bl}}{F_{bl}} + \underline{\beta}^T \frac{\underline{F}_f}{\|\underline{F}_f\|} F_{br} \frac{dF_{br}}{F_{br}} \\ &+ \underline{\beta}^T \frac{\underline{\underline{\alpha}}}{\|\underline{F}_f\|} \left(\frac{\partial \underline{\underline{M}}_{\theta_s}}{\partial \theta_s} \underline{\underline{M}}_{\phi_s} \underline{F}_m^{(s)} d\theta_s + \underline{\underline{M}}_{\theta_s} \frac{\partial \underline{\underline{M}}_{\phi_s}}{\partial \phi_s} \underline{F}_m^{(s)} d\phi_s + \underline{\underline{M}}_{\theta_s} \underline{\underline{M}}_{\phi_s} F_m \frac{d\underline{F}_m^{(s)}}{F_m}\right) \\ &+ \frac{\underline{\gamma}^T}{\|\underline{V}_a\|} \left(\underline{\underline{I}}_{\mathbb{R}^3} - \underline{x}_a \underline{x}_a^T\right) \left(\frac{\partial \underline{\underline{M}}_{\psi_{WS}}}{\partial \psi_{ws}} \underline{V}_{WM} d\psi_{ws} + V_{WM} \underline{\underline{M}}_{\psi_{WS}} \frac{d\underline{V}_{WM}^{(ws)}}{V_{WM}} - d\underline{V}_k\right)\end{aligned}$$

$$\frac{df}{f} = \underline{c}_1^T \frac{d\underline{F}_m^{(s)}}{F_m} + c_2 \frac{dF_{bl}}{F_{bl}} + c_3 \frac{dF_{br}}{F_{br}} + c_4 d\theta_s + c_5 d\phi_s + c_6 d\psi_{ws} + \underline{c}_7^T \frac{d\underline{V}_{WM}^{(ws)}}{V_{WM}} + \underline{c}_8^T d\underline{V}_k$$

With:
$\underline{c}_1^T = \underline{\beta}^T \underline{\underline{\alpha}}\, \underline{\underline{M}}_{\theta_s} \underline{\underline{M}}_{\phi_s}$
$c_2 = \underline{\beta}^T \frac{\underline{F}_f}{\|\underline{F}_f\|} F_{bl}$
$c_3 = \underline{\beta}^T \frac{\underline{F}_f}{\|\underline{F}_f\|} F_{br}$
$c_4 = \underline{\beta}^T \frac{\underline{\underline{\alpha}}}{\|\underline{F}_f\|} \frac{\partial \underline{\underline{M}}_{\theta_s}}{\partial \theta_s} \underline{\underline{M}}_{\phi_s} \underline{F}_m^{(s)}$
$c_5 = \underline{\beta}^T \frac{\underline{\underline{\alpha}}}{\|\underline{F}_f\|} \underline{\underline{M}}_{\theta_s} \frac{\partial \underline{\underline{M}}_{\phi_s}}{\partial \phi_s} \underline{F}_m^{(s)}$
$c_6 = \frac{\underline{\gamma}^T}{\|\underline{V}_a\|} \left(\underline{\underline{I}}_{\mathbb{R}^3} - \underline{x}_a \underline{x}_a^T\right) \frac{\partial \underline{\underline{M}}_{\psi_{ws}}}{\partial \psi_{ws}} \underline{V}_{WM}^{(ws)}$

$$\begin{aligned}
\underline{c}_7^T &= \frac{\underline{\gamma}^T}{\|\underline{V}_a\|}\left(\underline{\underline{I}}_{\mathbb{R}^3} - \underline{x}_a\underline{x}_a^T\right) V_{WM}\underline{\underline{M}}_{\psi_{ws}} \\
\underline{c}_8^T &= -\frac{\underline{\gamma}^T}{\|\underline{V}_a\|}\left(\underline{\underline{I}}_{\mathbb{R}^3} - \underline{x}_a\underline{x}_a^T\right)
\end{aligned}$$

Finally,

$$\begin{aligned}
\left|\frac{\Delta f}{f}\right| \leqslant & \left|c_2\frac{\Delta F_{bl}}{F_{bl}}\right| + \left|c_3\frac{\Delta F_{br}}{F_{br}}\right| + |c_4\Delta d\theta_s| + |c_5\Delta\phi_s| + |c_6\Delta\psi_{ws}| \\
& + \left|\underline{c}_1^T\frac{\Delta\underline{F}_m^{(s)}}{F_m}\right| + \left|\underline{c}_7^T\frac{\Delta\underline{V}_{WM}}{V_{WM}}\right| + \left|\underline{c}_8^T\Delta\underline{V}_k\right| \\
\leqslant & \left|c_2\frac{\Delta F_{bl}}{F_{bl}}\right| + \left|c_3\frac{\Delta F_{br}}{F_{br}}\right| + |c_4\Delta\theta_s| + |c_5\Delta\phi_s| + |c_6\Delta\psi_{ws}| \\
& + \sum_{i=1}^{3}\left[|c_{1,i}|\left|\frac{\Delta F_{m,i}^{(s)}}{F_m}\right| + |c_{7,i}^T|\left|\frac{\Delta V_{WM,i}^{(ws)}}{V_{WM}}\right|\right] \\
& + \sum_{i=1}^{3}|c_{8,i}|\left|\Delta\underline{V}_{k,i}\right|
\end{aligned}$$

$$\begin{aligned}
\left|\frac{\Delta f}{f}\right| \leqslant & \left|c_2\frac{\Delta F_{bl}}{F_{bl}}\right| + \left|c_3\frac{\Delta F_{br}}{F_{br}}\right| + |c_4\Delta\theta_s| + |c_5\Delta\phi_s| + |c_6\Delta\psi_{ws}| \\
& + \sum_{i=1}^{3}\left[|c_{1,i}|\left|\frac{\Delta F_{m,i}^{(s)}}{F_m}\right| + |c_{7,i}^T|\left|\frac{\Delta V_{WM,i}^{(ws)}}{V_{WM}}\right|\right] \\
& + \frac{2}{\Delta t}\sum_{i=1}^{3}|c_{8,i}|\left[|p_{1,i}\Delta\theta_s| + |p_{2,i}\Delta\phi_s| + \sum_{j=1}^{3}|p_{3,ij}|\left|\frac{\Delta F_{m,j}^{(s)}}{F_m}\right|\right]
\end{aligned}$$

$$\begin{aligned}
\left|\frac{\Delta f}{f}\right| \leqslant & |c_2|\left|\frac{\Delta F_{bl}}{F_{bl}}\right| + |c_3|\left|\frac{\Delta F_{br}}{F_{br}}\right| + |c_6||\Delta\psi_{ws}| + \sum_{i=1}^{3}|c_{7,i}|\left|\frac{\Delta V_{WM,i}^{(ws)}}{V_{WM}}\right| \\
& + \left[|c_4| + \frac{2}{\Delta t}\sum_{i=1}^{3}|c_{8,i}|\,|p_{1,i}|\right]|\Delta\theta_s| + \left[|c_5| + \frac{2}{\Delta t}\sum_{i=1}^{3}|c_{8,i}|\,|p_{2,i}|\right]|\Delta\phi_s| \\
& + \left(\sum_{i=1}^{3}\left[|c_{1,i}| + \frac{2}{\Delta t}\sum_{j=1}^{3}|c_{8,j}|\,|p_{3,ji}|\right]\left|\frac{\Delta F_{m,i}^{(s)}}{F_m}\right|\right)
\end{aligned}$$

Or in vectorial notation:

$$\begin{aligned}
\left|\frac{df}{f}\right| \leqslant{} & |c_2|\left|\frac{\Delta F_{bl}}{F_{bl}}\right| + |c_3|\left|\frac{\Delta F_{br}}{F_{br}}\right| + |c_6||\Delta\psi_{ws}| + \lceil \underline{c}_7 \rfloor \cdot \left|\frac{\Delta \underline{V}_{WM}^{(ws)}}{V_{WM}}\right| \\
& + \left(|c_4| + \frac{2}{\Delta t}\lceil \underline{c}_8 \rfloor \cdot \left\lceil \underline{p}_1 \right\rfloor\right)|\Delta\theta_s| + \left(|c_5| + \frac{2}{\Delta t}\lceil \underline{c}_8 \rfloor \cdot \left\lceil \underline{p}_2 \right\rfloor\right)|\Delta\phi_s| \\
& + \left(\lceil \underline{c}_1 \rfloor + \frac{2}{\Delta t}\left\lceil \underline{\underline{p}}_3^T \right\rfloor \lceil \underline{c}_8 \rfloor\right) \cdot \left\lceil \frac{\Delta \underline{F}_m^{(s)}}{F_m} \right\rfloor
\end{aligned}$$

D.10. Lift coefficient

$$C_l = \frac{\|\underline{L}\|}{\frac{1}{2}\rho A_k V_a^2}$$

$$\frac{dC_l}{C_l} = d\ln C_l$$

$$\frac{dC_l}{C_l} = d\ln C_l = \frac{d\|\underline{L}\|}{\|\underline{L}\|} - 2\frac{d\|\underline{V}_a\|}{\|\underline{V}_a\|}$$

$$\begin{aligned}
\frac{dC_l}{C_l} &= \frac{1}{\|\underline{L}\|^2}(\underline{L} \cdot d\underline{F}_a - \underline{L} \cdot d\underline{D}) - \frac{2}{\|\underline{V}_a\|^2}\underline{V}_a \cdot d\underline{V}_a \\
&= \frac{1}{\|\underline{L}\|^2}\underline{L}^T d\underline{F}_a - \frac{1}{\|\underline{L}\|^2}\underline{L}^T\left(\underline{x}_a\underline{x}_a^T d\underline{F}_a + (\underline{x}_a\underline{F}_a^T + \underline{x}_a \cdot \underline{F}_a \underline{\underline{I}}_{\mathbb{R}^3}) d\underline{x}_a\right) \\
&- \frac{2}{\|\underline{V}_a\|^2}\underline{V}_a^T d\underline{V}_a \\
\frac{dC_l}{C_l} &= \frac{\underline{L}^T}{\|\underline{L}\|^2} d\underline{F}_a - \frac{\underline{L}^T}{\|\underline{L}\|^2}\left(\underline{x}_a\underline{x}_a^T d\underline{F}_a + (\underline{x}_a\underline{F}_a^T + \underline{x}_a \cdot \underline{F}_a \underline{\underline{I}}_{\mathbb{R}^3})(\underline{\underline{I}}_{\mathbb{R}^3} - \underline{x}_a\underline{x}_a^T)\frac{1}{\|\underline{V}_a\|} d\underline{V}_a\right)) \\
&- \frac{2}{\|\underline{V}_a\|^2}\underline{V}_a^T d\underline{V}_a \\
\frac{dC_l}{C_l} &= \underbrace{\frac{\underline{L}^T}{\|\underline{L}\|^2}(\underline{\underline{I}}_{\mathbb{R}^3} - \underline{x}_a\underline{x}_a^T)}_{\underline{\kappa}^T} d\underline{F}_a \\
&+ \underbrace{\left[-\frac{\underline{L}^T}{\|\underline{L}\|^2}\left[(\underline{x}_a\underline{F}_a^T + \underline{x}^T{}_a\underline{F}_a\underline{\underline{I}}_{\mathbb{R}^3})(\underline{\underline{I}}_{\mathbb{R}^3} - \underline{x}_a\underline{x}_a^T)\frac{1}{\|\underline{V}_a\|}\right] - \frac{2}{\|\underline{V}_a\|^2}\underline{V}_a^T\right]}_{\underline{\nu}^T} d\underline{V}_a
\end{aligned}$$

$$\begin{aligned}\frac{dC_l}{C_l} &= \underline{\kappa}^T d\underline{F}_a + \underline{\nu}^T d\underline{V}_a \\ &= \underline{\kappa}^T \left(\frac{\underline{\underline{\alpha}}}{\|\underline{F}_f\|} d\underline{F}_f + \frac{\underline{F}_f}{\|\underline{F}_f\|} dF_{bl} + \frac{\underline{F}_f}{\|\underline{F}_f\|} dF_{br} \right) \\ &+ \underline{\nu}^T \left(\frac{\partial \underline{\underline{M}}_{\psi_{ws}}}{\partial \psi_{ws}} \underline{V}_{WM} d\psi_{WS} + \|\underline{V}_{WM}\| \underline{\underline{M}}_{\psi_{ws}} \frac{d\underline{V}_{WM}^{(ws)}}{V_{WM}} - d\underline{V}_k \right)\end{aligned}$$

$$\begin{aligned}\frac{dC_l}{C_l} = {} & \underline{\kappa}^T \frac{\underline{\underline{\alpha}}}{\|\underline{F}_f\|} \left(\frac{\partial \underline{\underline{M}}_{\theta_s}}{\partial \theta_s} \underline{\underline{M}}_{\phi_s} \underline{F}_m^{(s)} d\theta_s + \underline{\underline{M}}_{\theta_s} \frac{\partial \underline{\underline{M}}_{\phi_s}}{\partial \phi_s} \underline{F}_m^{(s)} d\phi_s + \underline{\underline{M}}_{\theta_s} \underline{\underline{M}}_{\phi_s} F_m \frac{d\underline{F}_m^{(s)}}{F_m} \right) \\ & + \underline{\kappa}^T \frac{\underline{F}_f}{\|\underline{F}_f\|} F_{bl} \frac{dF_{bl}}{F_{bl}} + \underline{\kappa}^T \frac{\underline{F}_f}{\|\underline{F}_f\|} F_{br} \frac{dF_{br}}{F_{br}} \\ & + \underline{\nu}^T \left(\frac{\partial \underline{\underline{M}}_{\psi_{ws}}}{\partial \psi_{ws}} \underline{V}_{WM} d\psi_{ws} + \|\underline{V}_{WM}\| \underline{\underline{M}}_{\psi_{WS}} \frac{d\underline{V}_{WM}^{(ws)}}{V_{WM}} - d\underline{V}_k \right)\end{aligned}$$

$$\frac{dC_l}{C_l} = \underline{d}_1^T \frac{d\underline{F}_m^{(s)}}{F_m} + d_2 \frac{dF_{bl}}{F_{bl}} + d_3 \frac{dF_{br}}{F_{br}} + d_4 d\theta_s + d_5 d\phi_s + d_6 d\psi_{WS} + \underline{d}_7^T \frac{d\underline{V}_{WM}^{(ws)}}{V_{WM}} + \underline{\mu}^T d\underline{V}_k$$

With:
$\underline{d}_1^T = \underline{\kappa}^T \underline{\underline{\alpha}}\, \underline{\underline{M}}_{\theta_s} \underline{\underline{M}}_{\phi_s}$
$d_2 = \underline{\kappa}^T \frac{\underline{F}_f}{\|\underline{F}_f\|} F_{bl}$
$d_3 = \underline{\kappa}^T \frac{\underline{F}_f}{\|\underline{F}_f\|} F_{br}$
$d_4 = \underline{\kappa}^T \frac{\underline{\underline{\alpha}}}{\|\underline{F}_f\|} \frac{\partial \underline{\underline{M}}_{\theta_s}}{\partial \theta_s} \underline{\underline{M}}_{\phi_s} \underline{F}_m^{(s)}$
$d_5 = \underline{\kappa}^T \frac{\underline{\underline{\alpha}}}{\|\underline{F}_f\|} \underline{\underline{M}}_{\theta_s} \frac{\partial \underline{\underline{M}}_{\phi_s}}{\partial \phi_s} \underline{F}_m^{(s)}$
$d_6 = \underline{\nu}^T \frac{\partial \underline{\underline{M}}_{\psi_{ws}}}{\partial \psi_{ws}} \underline{V}_{WM}^{(ws)}$
$\underline{d}_7^T = \underline{\nu}^T V_{WM} \underline{\underline{M}}_{\psi_{ws}}$

Finally,

$$\begin{aligned}\left|\frac{\Delta C_l}{C_l}\right| &\leqslant \left|d_2\frac{\Delta F_{bl}}{F_{bl}}\right| + \left|d_3\frac{\Delta F_{br}}{F_{br}}\right| + \left|d_4\Delta\theta_s\right| + \left|d_5\Delta\phi_s\right| + \left|d_6\Delta\psi_{ws}\right| \\ &+ \left|\underline{d}_1^T\frac{\Delta\underline{F}_m^{(s)}}{F_m}\right| + \left|\underline{d}_7^T\frac{\Delta\underline{V}_{WM}^{(ws)}}{\|\underline{V}_{WM}^{(ws)}\|}\right| + \left|\underline{\mu}^T\Delta\underline{V}_k\right| \\ \left|\frac{\Delta C_l}{C_l}\right| &\leqslant |d_2|\left|\frac{\Delta F_{bl}}{F_{bl}}\right| + |d_3|\left|\frac{\Delta F_{br}}{F_{br}}\right| + |d_4|\left|\Delta\theta_s\right| + |d_5|\left|\Delta\phi_s\right| + |d_6|\left|\Delta\psi_{ws}\right| \\ &+ \sum_{i=1}^{3}\left[|d_{1,i}|\left|\frac{\Delta F_{m,i}^{(s)}}{F_m}\right| + |d_{7,i}|\left|\frac{d\Delta V_{WM}^{(ws)}}{\|\underline{V}_{WM}^{(ws)}\|}\right|\right] \\ &+ \sum_{i=1}^{3}|\nu_i|\left|\Delta V_{k,i}\right|\end{aligned}$$

$$\begin{aligned}\left|\frac{\Delta C_l}{C_l}\right| &\leqslant |d_2|\left|\frac{\Delta F_{bl}}{F_{bl}}\right| + |d_3|\left|\frac{\Delta F_{br}}{F_{br}}\right| + |d_4|\left|\Delta\theta_s\right| + |d_5|\left|\Delta\phi_s\right| + |d_6|\left|\Delta\psi_{ws}\right| \\ &+ \sum_{i=1}^{3}\left[|d_{1,i}|\left|\frac{\Delta F_{m,i}^{(s)}}{F_m}\right| + |d_{7,i}|\left|\frac{d\Delta V_{WM,i}^{(ws)}}{V_{WM}}\right|\right] \\ &+ \sum_{i=1}^{3}|\nu_i|\frac{2}{\Delta t}\left[|p_{1,i}|\left|\Delta\theta_s\right| + |p_{2,i}|\left|\Delta\phi_s\right| + \sum_{j=1}^{3}|p_{3,ij}|\left|\frac{\Delta F_{m,j}^{(s)}}{F_m}\right|\right]\end{aligned}$$

$$\begin{aligned}\left|\frac{\Delta C_l}{C_l}\right| &\leqslant |d_2|\left|\frac{\Delta F_{bl}}{F_{bl}}\right| + |d_3|\left|\frac{\Delta F_{br}}{F_{br}}\right| + |d_6|\left|\Delta\psi_{ws}\right| + \sum_{i=1}^{3}|d_{7,i}|\left|\frac{d\Delta V_{WM,i}^{(ws)}}{\|\underline{V}_{WM}^{(ws)}\|}\right| \\ &+ \left(|d_4| + \frac{2}{\Delta t}\sum_{i=1}^{3}|\nu_i|\,|p_{1,i}|\right)\left|\Delta\theta_s\right| + \left(|d_5| + \frac{2}{\Delta t}\sum_{i=1}^{3}|\nu_i|\,|p_{2,i}|\right)\left|\Delta\phi_s\right| \\ &+ \left(\sum_{i=1}^{3}\left[|d_{1,i}| + \frac{2}{\Delta t}\sum_{j=1}^{3}|\nu_j|\,|p_{3,ji}|\right]\left|\frac{\Delta F_{m,i}^{(s)}}{F_m}\right|\right)\end{aligned}$$

Or in vectorial notation:

$$\begin{aligned}
\left|\frac{\Delta C_l}{C_l}\right| \leqslant{} & |d_2|\left|\frac{\Delta F_{bl}}{F_{bl}}\right| + |d_3|\left|\frac{\Delta F_{br}}{F_{br}}\right| + |d_6||\Delta\psi_{ws}| + \lceil \underline{d}_7 \rfloor \cdot \left\lceil \frac{\Delta \underline{V}_{WM}^{(ws)}}{V_{WM}} \right\rfloor \\
& + \left(|d_4| + \frac{2}{\Delta t} \lceil \underline{\nu} \rfloor \cdot \left\lceil \underline{p}_1 \right\rfloor \right) |\Delta\theta_s| + \left(|d_5| + \frac{2}{\Delta t} \lceil \underline{\nu} \rfloor \cdot \left\lceil \underline{p}_2 \right\rfloor \right) |\Delta\phi_s| \\
& + \left(\lceil \underline{d}_1 \rfloor + \frac{2}{\Delta t} \left\lceil \underline{\underline{d}}_3^T \right\rfloor \lceil \underline{\nu} \rfloor \right) \cdot \left\lceil \frac{\Delta \underline{F}_m^{(s)}}{F_m} \right\rfloor
\end{aligned}$$

Bibliography

Abbott, I. H. and A. E. Von Doenhoff (1959). *Theory of Wing Sections*. New York: Dover Publications Inc.

Arche, L. C. (2013). An Introduction to Meteorology for Airborne Wind Energy. In A. Uwe, M. Diehl, and R. Schmehl (Eds.), *Airborne Wind Energy*, Chapter 5, pp. 81–94. Springer Berlin Heidelberg.

Argatov, I., P. Rautakorpi, and R. Silvennoinen (2009). Estimation of the mechanical energy output of the kite wind generator. *Renewable Energy 34*(6), 1525–1532.

Bigi, N., M. Behrel, K. Roncin, J.-B. Leroux, A. Nême, C. Jochum, and Y. Parlier (2016). Course keeping of ship towed by kite. In *15e Journées de l'Hydrodynamique*, Brest.

Bigi, N., J.-B. Leroux, K. Roncin, A. Nême, C. Jochum, and Y. Parlier (2018). Ship towed by kite for fuel saving : investigation of the dynamic coupling. *Ocean Engineering TBC*(TBC), TBC.

Bigi, N., A. Nême, K. Roncin, J.-B. Leroux, G. Bles, C. Jochum, and Y. Parlier (2017). Analytical Tether Analysis for Static Kite Flight. In A. Uwe, M. Diehl, and R. Schmehl (Eds.), *Airborne Wind Energy II*, Chapter 3, pp. 55–76. Springer Berlin Heidelberg.

Boersma, K. F., G. C. M. Vinken, and J. Tournadre (2015). Ships going slow in reducing their NOx emissions: changes in 2005-2012 ship exhaust inferred from satellite measurements over Europe. *Environmental Research Letters 10*(7), 074007.

Bormann, A., M. Ranneberg, P. Kövesdi, C. Gebhard, and S. Skutnik (2013). Development of a Three-Line Ground-Actuated Airborne Wind Energy Converter. In U. Ahrens, M. Diehl, and R. Schmehl (Eds.), *Airborne Wind Energy*, Chapter 24, pp. 427–441. Berlin, Heidelberg: Springer Berlin Heidelberg.

Breukels, J. and W. Ockels (2008). Analysis of Complex Inflatable Structures Using a Multi-Body Dynamics Approach. *49th AIAA/ASME/ASCE/AHS/ASC Structures, Structural Dynamics, and Materials Conference
 16th AIAA/ASME/AHS Adaptive Structures Conference
 10t*, 1–10.

Cherubini, A., A. Papini, R. Vertechy, and M. Fontana (2015). Airborne Wind Energy Systems: A review of the technologies. *Renewable and Sustainable Energy Reviews 51*, 1461–1476.

Dadd, G. M. (2012). *Kite Dynamics for Ship Propulsion.* Ph. D. thesis, University of Southampton.

de Wachter, A. (2008). *Deformation and Aerodynamic Performance of a Ram-Air Wing.* Ph. D. thesis, TU Delft.

Deparday, J., P. Bot, F. Hauville, B. Augier, and M. Rabaud (2016). Full-scale flying shape measurement of offwind yacht sails with photogrammetry. *Ocean Engineering 127*, 135–143.

Diehl, M. (2013). Airborne Wind Energy. In A. Uwe, M. Diehl, and R. Schmehl (Eds.), *Airborne Wind Energy*, Chapter 1, pp. 3–22. Springer Berlin Heidelberg.

Du Pontavice, E. (2016). *Propulsion par cerf-volant : envol et pérégrinations.* Ph. D. thesis, Université de Paris Saclay.

Erhard, M. and H. Strauch (2012). Control of Towing Kites for Seagoing Vessels. pp. 1–12.

Erhard, M. and H. Strauch (2013a). Sensors and Navigation Algorithms for Flight Control of Tethered Kites. *European Control Conference (ECC)*, 998–1003.

Erhard, M. and H. Strauch (2013b). Theory and Experimental Validation of a Simple Comprehensible Model of Tethered Kite Dynamics Used for Controller Design. In U. Ahrens, M. Diehl, and R. Schmehl (Eds.), *Airborne Wind Energy*, Green Energy and Technology, Chapter 8, pp. 141–165. Berlin, Heidelberg: Springer Berlin Heidelberg.

European Commission (2016). Facts and figures on the Common Fisheries Policy. Technical report.

Fagiano, L., K. Huynh, B. Bamieh, and M. Khammash (2014). On Sensor Fusion for Airborne Wind Energy Systems. *IEEE Transactions on Control Systems Technology 22*(3), 930–943.

Fagiano, L. and T. Marks (2015). Design of a small-scale prototype for research in airborne wind energy. *166 IEEE/ASME TRANSACTIONS ON MECHATRONICS 20*(1), 166–177.

Fagiano, L. and M. Milanese (2012). Airborne wind energy: an overview. In *American Control Conference*, Montréal, pp. 3132–3143.

Fagiano, L., M. Milanese, V. Razza, and M. Bonansone (2012). High-altitude Wind energy for sustainable marine transportation. *IEEE Transactions on Intelligent Transportation Systems 13*(2), 781–791.

Fagiano, L., M. Milanese, V. Razza, and I. Gerlero (2010). Control of Power Kites for Naval Propulsion. In *American Control . . .*, pp. 4325–4330.

Fagiano, L., a. U. Zgraggen, M. Khammash, and M. Morari (2014). Automatic Crosswind Flight of Tethered Wings for Airborne Wind Energy: Modeling, Control Design, and Experimental Results. *IEEE Transactions on Control Systems Technology 22*(4), 1433–1447.

FAO (2016). The State of World Fisheries and Aquaculture. Technical report, Food and Agriculture Organization of the United Nations.

Hadi, F. A. (2015). Diagnosis of the Best Method for Wind Speed Extrapolation. *International Journal of Advanced Research in Electrical 4*(10), 8176–8183.

Henry, L. L. (1998). Kites in Polynesia: Replicative Experiments and Hawaiian Petroglyphs. *Rapa Nui Journal 12*(June), 45–47.

Hol, J. (2011). *Sensor Fusion and Calibration of Inertial Sensors, Vision, Ultra-Wideband and GPS*. Ph. D. thesis, Linköping University, Sweden.

Infanzon, R. (2013). Photogrammetry Based Investigation of a Kite ' s Flying Shape - PPT. Technical report, Australian Maritime College, University of Tasmania.

Islam, M. S., M. Shajid-Ul-Mahmud, T. Islam, M. S. Amin, and M. Hossam-E-Haider (2016). A low cost MEMS and complementary filter based attitude heading reference system (AHRS) for low speed aircraft. *2016 3rd International Conference on Electrical Engineering and Information and Communication Technology, iCEEiCT 2016*.

ITTC (2002). Recommended Procedures - Full Scale Measurements Manoeuvrability Full Scale Manoeuvring Trials Procedure. In *International Towing Tank Conference*, Venice.

ITTC (2014). IITTC Symbols and Terminology List. In *International Towing Tank Conference*, Copenhagen.

J.C. Stevenson (2003). *Traction Kite Testing and Aerodynamics*. Ph. D. thesis, University of Canterbury.

Jubert, V. and Y. Leslé (2016). Conception d'un KiteBoat. Technical report, ENSTA Bretagne, Brest.

Lansdorp, B., R. Ruiterkamp, and W. Ockels (2007). Towards Flight Testing of Remotely Controlled Surfkites for Wind Energy Generation. In *AIAA Atmospheric Flight Mechanics Conference and Exhibit*, Number August, Hilton Head, South Carolina.

Leloup, R. (2014). *Modelling approach and numerical tool developments for kite performance assessment and mechanical design; application to vessels auxiliary propulsion*. Ph. D. thesis, Université de Bretagne Occidentale.

Leloup, R., K. Roncin, M. Behrel, G. Bles, J.-B. Leroux, C. Jochum, and Y. Parlier (2016). A continuous and analytical modeling for kites as auxiliary propulsion devoted to merchant ships , including fuel saving estimation. *Renewable Energy 86*, 483–496.

Leloup, R., K. Roncin, G. Bles, J.-B. Leroux, C. Jochum, and Y. Parlier (2014). Kite and classical rig sailing performance comparison on a one design keel boat. *Ocean Engineering 90*, 39–48.

Loyd, M. (1980). Crosswind Kite Power (for large-scale wind power production). *Journal of Energy 4*(3), 106–111.

Lozano, R. (2014). *Study of the flight dynamics of a kite*. Ph. D. thesis, UNIVERSITÉ DE GRENOBLE.

Luhmann, T. (2010, nov). Close range photogrammetry for industrial applications. *ISPRS Journal of Photogrammetry and Remote Sensing 65*(6), 558–569.

Masters, G. M. (2004). *Renewable and Efficient Electric Power Systems*. Hoboken: John Wiley & Sons, Inc.

Messager, C. (2017). Rapport -2017-ENSTA-01. Technical report, EXWEXs.

National Instruments (2014). NI LabVIEW for CompactRIO Developer ' s Guide.

Peterson, E. W. and J. P. Hennessey (1978). On the Use of Power Laws for Estimates of Wind Power Potential.

Pocock, G. (1827). *A treatise on the æropleustic art, or Navigation in the air: by means of kites, or buoyant sails: with a description of the charvolant, or kite carriage*.

Podeur, V., D. Merdrignac, M. Behrel, K. Roncin, C. Jochum, Y. Parlier, and P. Renaud (2016). Simulation de voyage au long cours pour le calcul d'économies de carburant : application à la propulsion par cerf-volant. In *15e Journées de l'Hydrodynamique*, Brest, pp. 1–12.

Roncin, K., J.-m. Kobus, P. Iackine, and S. Barré (2005). Méthodologie pour la validation du simulateur de voilier par des essais en mer , une première tentative. In *Workshop Science-Voile*, Lanveoc-Poulmic, pp. 1–10.

Sagaut, P. (2006). *Large Eddy Simulation for Incompressible Flows: An Introduction* (3rd ed.).

Skamarock, W., J. Klemp, J. Dudhi, D. Gill, D. Barker, M. Duda, X.-Y. Huang, W. Wang, and J. Powers (2008). A Description of the Advanced Research WRF Version 3. Technical report, National Center for Atmospheric Research, Boulder, Colorado, USA.

Stull, R. B. (1988). *An Introduction to Boundary Layer Meteorology*. Springer Science.

TR Electronic (2005). User Manual IEx-58 Incremental.

UNCTAD (2016). Review of Maritime Transport. Technical report, United Nations.

Vlugt, R. V. D., J. Peschel, and R. Schmehl (2013). Design and experimental characterization of a pumping kite power system. In U. Ahrens, M. Diehl, and R. Schmehl (Eds.), *Airborne Wind Energy*, Chapter 23, pp. 403–425. Berlin, Heidelberg: Springer Berlin Heidelberg.

Wellicome, J. and S. Wilkinson (1984). *Ship propulsive kites : an initial study*. Ph. D. thesis, University of Southampton.

Wernert, P. and D. Favier (1999). Considerations about the phase averaging method with application to ELDV and PIV measurements over pitching airfoils. *Experiments in Fluids 27*, 473–483.

Yu, J., L. liu Shi, W. zhe Wang, and Y. zheng Liu (2010). Conditional averaging of TR-PIV measurements of wake behind square cylinder using an improved cross-correlation approach. *Journal of Hydrodynamics 22*(1), 29–34.

Zgraggen, A. U., L. Fagiano, and M. Morari (2015). Real-time optimization and adaptation of the crosswind flight of tethered wings for airborne wind energy. *IEEE Transactions on Control Systems Technology 23*(2), 434–448.

“Investigation of kites for auxiliary ship propulsion: experimental set-up, trials, data analysis and kite specs novel identification approach”

Keywords: Kite, Kiteboat, Vishing Vessel, Experimental Set-up, Onboard Measurements, Data Analysis, Phase Averaging

This study is part of the research program beyond the sea® aiming to develop kites as auxiliary propulsion devices for ships. The goal is to use the energy of the wind to save fuel and reduce harmful emissions. Such a project needs numerous developments and scientific actions, particularly to model the behavior of giant kites and associated ships. However these models must be compared to measurements to assess their validity. This study is then focus on the measurements of the interaction between kites and ships, at a limited scale in comparison to the real scope of the project. Thus measurement campaigns were carried out on a 13-meter long trawler, and on a 6-meter long experimental platform specifically designed. Another experimental campaign was also carried out onshore to assess the aerodynamic specs of the kite. Each of these three campaigns was based on a complex experimental set-up, including an automatic kite control system. In addition to provide a valuable data set for further scientific analyses, this study provided also tools which can be used by the industrial partners of the beyond the sea project®.

« Les kites comme propulsion axillaire pour les navires : système expérimental, campagnes de mesures, analyse des données et identification des performances des kites »

Mots-clefs : Kite, Kiteboat, Navire de pêche, Système expérimental, Mesures embarquées, Analyse de données, Moyenne de phase

Cette thèse s’inscrit dans le programme de recherche beyond the sea® visant à développer la traction de navire de commerce par des kites géants. Le but est d’utiliser l’énergie du vent, et ainsi de réduire la consommation de carburant des navires et réduire les émissions polluantes. Un tel projet demande de nombreux développements et actions scientifiques, en particulier pour prédire le comportement des cerfs-volants géants et des navires associés. Pour cela des modèles sont développés, mais ces modèles doivent être confrontés à des mesures pour en estimer la validité. Cette thèse a donc pour objectif de mesurer les interactions entre le kite et le navire, à une échelle limitée par rapports aux navires visés par le programme global. Des mesure ont donc été réalisées sur un navire de pêche de 13 m, puis sur un bateau expérimental de 6 m spécialement conçu à cet effet. De plus, des mesures ont aussi été menées à terre pour évaluer uniquement les performances du kite. Chacune de ces campagnes expérimentales mettait en œuvre un dispositif de mesure complexe, ainsi qu’un système automatique de contrôle du vol du kite. En plus de fournir des données de qualité à destination de la science, les outils développés au cours de cette étude peuvent être utilisés directement par les partenaires industriels du projet beyond the sea®.